UNIVERSITY OF TECHNOLOGY SYDNEY

Properties of interfacial transition zones in recycled aggregate/ waste glass concrete and its influence on the mechanical properties under complicated stress states

by Hanbing Zhao

Thesis submitted in fulfilment of the requirements for the degree of

Doctor of Philosophy

under the supervision of

A/Prof Wengui Li

Prof Hadi Khabbaz

Dr Aziz Mahmood

University of Technology Sydney

Faculty of Engineering and Information Technology

April 2024

CERTIFICATE OF ORIGINAL AUTHORSHIP

I, Hanbing Zhao declare that this thesis, is submitted in fulfilment of the requirements for the award of Doctor of Philosophy in the Faculty of Engineering and Information Technology at the University of Technology Sydney.

This thesis is wholly my own work unless otherwise referenced or acknowledged. In addition, I certify that all information sources and literature used are indicated in the thesis.

This document has not been submitted for qualifications at any other academic institution.

This research is supported by the Australian Government Research Training Program.

Signature: Production Note:
Signature removed prior to publication.

Date: 10/04/2024

ACKNOWLEDGEMENT

The three-year doctoral career is fleeting but a long and meaningful experience. I would like to express my sincere thanks to my principal supervisor, A/Prof Wengui Li for his continuous support, guidance and communication in my research and life. His extensive knowledge and sensitive insights have helped me tremendously in choosing research topic, writing thesis and being able to graduate successfully. I would also like to express my thanks to my co-supervisors Prof Hadi Khabbaz and Dr Aziz Mahmood. Their constructive comments and suggestions for my experiments and papers ensured the quality of my scientific outcomes.

I would like to give my heartfelt thanks to the financial support from the Australian Research Council and the equipment support from UTS Tech Lab, UTS MAU Lab and UTS CTRF Lab. Thanks to the enthusiastic and kind laboratory staff who provided training and assistance to me, especially Herbert Yuan, Alexander Angeloski, Muller Hailu, Ann Yan, Joe Opo etc. I greatly appreciate Prof Kejin Wang, Dr Zhiyu Luo and A/Prof Zhuo Tang who devoted much time to reading my papers and gave my many constructive comments for my research. I also have to thanks to A/Prof Yixiang Gan, Yu Chen, and Xu Wang from the University of Sydney, Prof Yunan Li, Dr Yong Hu, and Dunming Zhu from the China University of Geosciences, Prof Bin Lei and his group members from Nanchang University for their important support with experimental facilities. In addition, I need to thank to my group members including Dr Wenkui Dong, Dr Fulin Qu, Dr Peiran Li, Xiaonan Wang, Zhizhong Deng, Xuqun Lin, Xuanrui Zhang, Peimin Zhan etc, for their care and help.

Finally, I want to thank my parents. Thanks to their understanding and support to help me complete my PhD research.

LIST OF PUBLICATIONS

Published papers:

1. Zhao, H., Hu, Y., Li, Y., Wang, K., Dehn, F., Li, W., Triaxial compressive performance of recycled aggregate/glass sand concrete: Experimental study and mechanism analysis. *Journal of Cleaner Production*. 2024, 442 (25): 141006.

2. Zhao, H., Li, W., Gan, Y., Mahmood, A., Zhao, X., Wang, K. Nano/microscopic investigation on the strengthening mechanism of ITZs using waste glass powder in modelled aggregate concrete. *Journal of Materials in Civil Engineering*. 2024, 36 (4): 04024007

3. Zhao, H., Li, W., Gan, Y., Wang, K., Luo, Z. Nano/microcharacterization and image analysis on cohesion behaviour of ITZs in recycled concrete enhanced with waste glass powder. *Construction and Building Materials*. 2023, 392 (8): 131904.

4. Zhao, H., Hu, Y., Tang, Z., Wang, K., Li, Y., Li, W. Deterioration of concrete under coupled aggressive actions associated with load, temperature and chemical attacks: A comprehensive review. *Construction and Building Materials*. 2022, 322 (1): 126466.

5. Li, Y., Zhao, H., Hu, Y., Qu, F., Zhu, D., Wang, K., Li, W., Effect of pore water pressure on mechanical performance of recycled aggregate concrete triaxial compression. *Cement and Concrete Composites*. 2023, 146:105402.

6. Qu, F., Zhao, H. Wu, K., Liu, Y., Zhao, X., Li, W., 2023. Phase transformation and microstructure of in-situ concrete after 20-year exposure to harsh mining environment: A case study. *Case Studies in Construction Materials*. 2023, 19, e02287.

7. Zhao, H., Hu, Y., Yuan, M., Li, Y., Li, W., 2022. Stress-Strain Behaviours of Recycled Aggregate Concrete Under Triaxial Compression and Pore Water Pressure. *3rd International Conference on Structural Engineering Research*. 2022.

TABLE OF CONTENTS

LIST OF ACRONYMS

ANOVA	Analysis of variance
ASR	Alkali-silica reaction
BSE	Backscattered scanning electron
CH	Calcium hydroxide
C-S-H	Calcium silicate hydrate
C & M waste	Construction and municipal waste
EDS	Energy dispersive spectrometer
FDH	Frequency density distribution histrogram
FTIR	Fourier transform infrared spectroscopy
ITZ	Interfacial transition zone
LVDT	Linear variable differential transformer
MAC	Modelled aggregate concrete
MRAC	Modelled recycled aggregate concrete
NAC	Natural aggregate concrete
NCA	Natural coarse aggregate
NMR	Nuclear magnetic resonance spectrometer
NFA	Natural fine aggregate
RAC	Recycled aggregate concrete
RCA	Recycled coarse aggregate
RGC	Recycled glass concrete
RGP	Recycled glass powder
RGS	Recycled glass sand
SCM	Supplementary cementitious materials

SEM	Scanning electron microscope
SSD	Saturated surface dry
TGA	Thermogravimetric analysis
TG-DTG	Thermogravimetric-derivative thermogravimetry
XRD	X-ray diffractometer

LIST OF FIGURES

LIST OF TABLES

ABSTRACT

To alleviate the burden on natural resources, waste concrete and glass are recycled as aggregate in concrete production. The performance of concrete with recycled aggregate is normally lower than the concrete with natural aggregate. Due to the high content of amorphous silicon and alkali metal oxides in waste glass, alkali-silica reaction (ASR) is prone to occur when waste glass is recycled as aggregate in concrete. If the waste glass is further ground to powder and used to replace cement, the ASR expansion will be greatly weakened, and the glass powder possesses pozzolanic activity, which can improve the performance of concrete.

This study fully explored the influence of old mortar, glass particles and glass powder on the cohesion strength of the interfacial transition zones (ITZs) from micro-levels. The ITZ is considered to be the weakest area in concrete, and it is the key to explaining the mechanism of concrete mechanical properties and water permeability. Therefore, a variety of testing techniques were used to evaluated the microstructure, chemical composition distribution and micromechanical properties of ITZs in recycled aggregate concrete (RAC). Meanwhile, the role of glass powder and glass particles in the ITZ and adjacent matrix was also investigated. The study reveals that the new ITZ between the old and new mortars in the RAC has the largest ITZ width. Within 28 days, the microstructure and micromechanical properties of the new ITZ were weaker than those of the old ITZ bonded to natural coarse aggregate (NCA). However, as time goes by, when the curing time reached one year, the incompletely reacted cement particles in the old mortar continued to hydrate, which contributed to strengthen the bond strength between the new and old cement paste. In addition, the pozzolanic effect of glass powder

can effectively improve the bonding performance between cement paste, NCA and old mortar.

For the study of macroscopic mechanical properties, concrete cylindrical specimens containing recycled coarse aggregate (RCA) and recycled glass sand (RGS) were fabricated. RCA was used to replace NCA, and RGS was used to replace natural fine aggregate (NFA), with replacement ratio of 0%, 50% and 100%. The stress-strain curves of concrete samples under confining pressure and pore water pressure were measured. The results show that the pore water pressure accelerates the expansion of micro-cracks in the concrete specimens. On the other hand, the supporting effect of pore water pressure improved the resistance to compressive deformation of concrete specimens.

CHAPTER 1. INTRODUCTION

1.1 Background

Concrete has been playing a significant role in construction industry for more than 300 years since 1900 (Xiao, et al. 2012). As a kind of resource-intensive material, concrete production annually consumes a large amount of natural sand, stone, and Portland cement (Xuan, et al. 2017, Zaetang, et al. 2016). It is reported that approximately 48.3 billion tonnes of rock and river sand were exploited as coarse or fine aggregate in concrete in 2015, and it is expected that by 2025, this figure will increase to more than 78.7 billion tonnes (Shi 2012). Excessively exploitation has put natural resources on the edge of exhaustion. Meanwhile, cement production soared to 3.27 billion tons in 2019 (Pathan, et al. 2022). Calcination of limestone to produce cement is another important CO_2 emission source in addition to burning fossil fuels, because $CaCO_3$ decomposes to CaO and CO_2 at high temperature (Golewski & Szostak 2022, Li, et al. 2023b, Silva, et al. 2023). There is a consensus that approximately 8% of the global CO_2 emission comes from cement production (Corinaldesi & Moriconi 2009, Golewski 2023). To achieve carbon neutrality as well as save natural resources, numerous researchers attempted to recycle construction and municipal wastes as aggregate or supplementary cementitious materials (SCM) in concrete, such as crushed concrete and waste glass products (Wang, et al. 2021, Xiao, et al. 2012).

The crushed waste concrete is the major construction and demolition (C & D) waste, accounting for about 70% of the total construction solid waste (Cabrera-Covarrubias, et al. 2021, Golewski 2022). The traditional treatment of waste concrete elements is simply stacking or burying them in landfill, which will undoubtedly bring a heavy burden on the land space (Thomas, et al. 2018). Waste broken concrete can be used as coarse aggregate in new concrete after crushing and sieving, namely recycled coarse aggregate (RCA) (Tang, et al. 2020c). However, it is difficult to obtain RCA with the same quality as the original nature aggregate, because the old mortar inevitably adheres to the RCA surface (Sunayana & Barai 2020, Tam, et al. 2008, Tang, et al. 2022). According to research, the workability, mechanical properties and durability of recycled aggregate concrete (RAC) all show different degrees of decline compared with natural aggregate concrete (NAC) (Lu, et al. 2019, Medina, et al. 2014, Omary, et al. 2016, Otsuki, et al. 2003, Pedro, et al. 2017). It has to admit that the properties of RAC are worse than NAC, but its economic value and environmental benefits cannot be ignored (Liu, et al. 2020, Liu, et al. 2023). The prospect of recycling waste concrete for use on road, pavements, conduit and some non-structural components is still great (Fang, et al. 2023, Hu, et al. 2019, Jayasuriya, et al. 2018, Lei, et al. 2018).

Glass is another common municipal waste. It is estimated that approximately 1.16 million tonnes of waste glass were generated in Australia from 2018 to 2019 (Dong, et al. 2021). Glass has sufficient hardness, and waste glass can be added to concrete as fine aggregate after simple crushing (Ismail & Al-Hashmi 2009, Pan, et al. 2017). However, differences in the colour and type of waste glass represent different chemical compositions (Jiang, et al. 2019, Kong, et al. 2016). The difference in chemical composition would have a certain influence on the bonding between cement paste and glass particles (Ye, et al. 2022). In addition, glass contains a relatively high content of alkali metal oxides, which are important raw materials for alkali silica reaction (ASR) (Maddalena, et al. 2018, Nassar & Soroushian 2012, Xiao, et al. 2020). Researchers have found that using waste glass as fine aggregate in concrete would cause ASR expansion that cannot be ignored and create microcracks within concrete (Schwarz & Neithalath 2008). Although a great number of studies have concluded that the performance of concrete increased with the decrease of particle size of recycled glass sand (RGS), due to the lack of clearly definition of standard glass sand for concrete preparation, there are many contradictory conclusions in research about workability and mechanical properties of recycled glass concrete (RGC) (Xiao, et al. 2020, Ye, et al. 2022, Zidol, et al. 2021).

In contrast, more researchers prefer to further grind waste glass to below 75 μm and replace cement with it, because waste glass contains more amorphous silicon and has satisfactory pozzolanic activity (Bilondi, et al. 2018, Omran, et al. 2017, Schwarz & Neithalath 2008). For example, Pan et al. (2017), Nassar et al. (2012), and Schwarz et al. (2008) replaced traditional Portland cement with recycled glass powder (RGP), and found that RGP can effectively consume excess calcium hydroxide in concrete, improve the microstructure of concrete and enhance mechanical properties and impermeability properties. Lin et al. (2012), Xiao et al. (2020) and Bilondi et al. (2018) successfully made geopolymer composite products using RGP as precursor. Waste glass geopolymer composites exhibited satisfactory mechanical properties and durability (Lin, et al. 2012, Mejdi, et al. 2019, 2022, Mirzahosseini & Riding 2015).

Many researchers have explored the differences in mechanical properties, durability, and microstructure of concrete containing RCA, RGS, and RGP (Arabi, et al. 2019, El-Hassan, et al. 2019, Ismail & Al-Hashmi 2009, Mejdi, et al. 2022, Mirzahosseini & Riding 2015). However, most of their studies are based on simple and single conditions, for example, testing the mechanical properties under compression, bending and shearing conditions, as well as the durability under high temperature, low temperature, acid corrosion and harmful ion penetration (Bisht, et al. 2020, Dimitriou, et al. 2018, Lin, et al. 2012, Lu, et al. 2020, Mejdi, et al. 2019). In actual situations, concrete structures are often under complicated stress and aggressive conditions (Bravo, et al. 2017, Du & Tan 2017, Mohammadi & South 2016). For example, for beam-column joints, underground structures, and nuclear reactors, concrete is usually in a triaxial compression state, and the mechanical behaviour of concrete under triaxial compression is significantly different from that in a simple loading condition (Malecot, et al. 2019, Yang, et al. 2022, Zeng, et al. 2013). Among them, the compressive strength and ductility will be significantly enhanced with lateral confinement (Chen, et al. 2019, Wu, et al. 2023). In addition, the pore water in concrete is difficult to dissipate completely during service (Vu, et al. 2009, Wu, et al. 2023). When subjected to high volumetric compression deformation, the influence of pore water pressure on the mechanical properties of concrete cannot be ignored (Jiang, et al. 2023, Malecot, et al. 2019, Vu, et al. 2009). Previous studies have shown that the compressive strength of saturated concrete under high lateral confinement decreases compared with that of dry concrete, while the elastic modulus increases due to the support effect of pore water (Vu, et al. 2009, Xue, et al. 2020).

More importantly, in order to explain the failure mechanism of concrete containing RCA and waste glass under complicated stress conditions, it is necessary to analyse the performance of concrete in depth at the microscopic level, especially the microstructure, micromechanical properties and chemical composition of interfacial transition zones (ITZs) (Lyu, et al. 2019a, Lyu, et al. 2020, Zhang, et al. 2019). The density and surface area of aggregate are significantly larger than cement particles, so the coarse aggregate can be considered as a 'wall' for cement paste (Vargas, et al. 2017, Zhang, et al. 2023). Due to the 'wall effect' and bleeding of aggregate, water-cement ratio, porosity and the content of alkaline crystalline phases within ITZs are higher than mortar matrix (Nuruzzaman, et al. 2023, Rangaraju, et al. 2010, Scrivener, et al. 2004). Therefore, ITZ is usually regarded as the weakest area in concrete, which is the key to studying concrete mechanical and ion transport performance (Hosan, et al. 2021, Kunther, et al. 2017). Insufficient evaluation of the ITZs in concrete containing RCA, RGS and RGP has been observed in current research, but some simple microstructure observations or chemical element tests (Bilondi, et al. 2018, Djerbi 2018). Quantitative and statistical analysis on microscopic properties of ITZs is important to understand the performance of the sustainable concrete under complicated stress states (Diamond & Huang 2001, Kunther, et al. 2017, Zhang, et al. 2023).

Therefore, the objective of this work is to elucidate the microstructure, chemical composition and micromechanical properties of concrete ITZ containing RCA, RGS and RGP. The cohesion performance between cement paste and NCA, RCA, NFA and RGS was fully compared. RGP was used to enhance the bond strength of ITZ in concrete. Confining pressure and pore water pressure were applied to the concrete specimens containing RCA and RGS by multi-field coupled testing system, and the compressive stress-strain curves were measured. The relationship between the macroscopic mechanical properties and microscopic characteristics of RCA and RGP concrete under complex stress conditions was established.

1.2 Research gaps

(1) Nowadays, how to realise the sustainable utilisation of resources has become a hot topic in the infrastructure construction. To ease the exploitation of natural aggregate and improve the life cycle of construction materials, researchers have developed eco-friendly materials to replace traditional raw materials in concrete production such as RCA, RGS and RGP (Arabi, et al. 2019, Arulrajah, et al. 2015, El-Hassan, et al. 2019, Fang, et al. 2023). Meanwhile, the rheological, mechanical, durable and micro-structural properties of these sustainable concrete are well studied (Bogas, et al. 2016, Kim, et al. 2018, Wang, et al. 2023). It is well-known that binary mixture of waste concrete and glass can greatly improve the environmental and economic benefits of

concrete (Arulrajah, et al. 2015, Gebremariam, et al. 2021). The coexistence of multiple wastes in concrete may present a more complicated performance (Gao, et al. 2016, Tang, et al. 2020a, Zhang, et al. 2021). In order to explain these complex properties, it is necessary to explore the behaviour of the concrete ITZ and the adjacent matrix at the microscopic level. However, the research on the microstructure and micromechanical properties of concrete incorporating RCA, RGS and RGP is still limit.

(2) For underground infrastructure, military shelters and nuclear power plants, concrete is generally subjected to triaxial compression state rather than uniaxial stress state (Heukamp, et al. 2001, Jiang, et al. 2017, Lim & Ozbakkaloglu 2014). Under the influence of confining pressure, the strength and ductility of concrete can be significantly increased compared with uniaxial compression (Vu, et al. 2011, Wang, et al. 2020, Xue, et al. 2019). This can be obtained from the research of Zingg et al. (2016), Wang et al. (2020), Zhu et al. (2021), and Xu et al. (2017a) on the normal, ultra-high performance, self-compacting and recycled aggregate concrete respectively. However, it still lacks relevant study on the performance of concrete containing RCA and RGS simultaneously under multi-axial compression state.

(3) Vu et al. (2009) reported that the triaxial compressive strength of dried concrete increased obviously with confining pressure. In contrast, the upward trend of the strength slowed down when confining pressure reached a given value for saturated concrete (Vu, et al. 2009). It is well-known that hydration of cement is a time-consuming process (Richardson 2008, Skibsted & Andersen 2013, Wang, et al. 2022). A large amount of free water may remain in pore network (Kunther, et al. 2016, Li, et al. 2022b). Moreover, most of concrete structures, such as bridge piers, foundation and dams inevitably encounter water and retain a quasi-saturated or saturated state for

many years (Carvalho & Carrasco 2010, Huang, et al. 2022, Zein, et al. 2021). Although it has been reported in references that pore water pressure plays an important role, few people successfully test the strength degradation performance of concrete under the combined effect of confining pressure and a given pore water pressure.

(4) Currently, many researchers have deduced the concrete stress-strain empirical model based on the existing test results (Jiang, et al. 2017, Ren, et al. 2018, Tang, et al. 2019). However, most of these analytical models are based on the test results of ordinary concrete under simple triaxial compression, and cannot accurately predict the triaxial compression performance of concrete with different proportions of RCA, and RGS, especially the stress-strain relationship for these sustainable concrete under combined effect of confining pressure and pore water pressure (Li, et al. 2022a, Lim & Ozbakkaloglu 2014, Zeng, et al. 2013). It is important to develop an effective model that can be used to analyse the behaviour of concrete containing various waste materials under complicated mechanical conditions for realising the environmental and economic benefits of infrastructure construction industry.

(5) Microstructure performance of concrete made with waste materials such as RCA, RGS and RGP is different from that of concrete made with natural materials, due to different chemical composition and specific surface area (Dimitriou, et al. 2018, Ye, et al. 2022). The analysis of cracks, pore distribution and mineralogical composition in ITZs is contributed to better understand the failure process of concrete under complex stress states (Nuruzzaman, et al. 2023, Rangaraju, et al. 2010, Scrivener, et al. 2004). Although many attempts have been made to study the micro properties of RAC, the research on the concrete containing different types and different particle sizes of RGS and RGP is still insufficient (Djerbi 2018, Zhang, et al. 2019). No one

has successfully established a relationship between microscopic properties of ITZs and mechanical performance of sustainable concrete specimens under triaxial compression with pore water pressure (Zhang, et al. 2023).

1.3 Research objectives

The main purpose of this study is to investigate the macro-mechanical properties of sustainable concrete with RAC and RGS under triaxial compression with pore water pressure, and the performance of sustainable concrete under complicated stress states is explained from mechanism level based on the microscopic properties of ITZs.

RCA possesses a layer of hardly removed old mortar on the surface. After mixing with fresh cement mixture, two kinds of ITZs emerged in RAC: new ITZ between old mortar and new mortar and old ITZ between virgin aggregate and old mortar (Lu, et al. 2019). The difference in surface morphology and chemical activity determines the performance difference between the ITZ bonded with RGS and the ITZ bonded with NFA (Ali & Al-Tersawy 2012, Jiao, et al. 2020). When waste glass is ground to powder, the pozzolanic effect of RGP helps to improve the ITZ performance of concrete (Nassar & Soroushian 2012, Xiao, et al. 2020). For the above situations, this thesis conducts a comprehensive analysis of the microstructure, chemical composition and micromechanical properties of each ITZ. For macro-mechanical properties of sustainable concrete, cylindrical concrete specimens containing RCA and RGS were subjected to a stable confining pressure and pore water pressure to measure their compressive stress-strain curve. Based on stress-strain curves, some representative mechanical properties of sustainable concrete under complicated stress states can be obtained. The influence of RCA, RGS, confining pressure and pore water pressure on the mechanical properties of sustainable concrete such as compressive strength, ductility, elastic modulus and volumetric deformation are comprehensively analysed and discussed. With the help of research on ITZ at the microscopic level, the failure mode and mechanical performance of sustainable concrete under complex stress states can be reasonably explained from the mechanism. Finally, the mechanical performance prediction model of sustainable concrete containing RCA and WGS under constant lateral confinement and pore water pressure was established and verified. The microscopic properties of ITZ, such as porosity, elastic modulus and hardness, can also be involved in modifying the model to achieve a more accurate prediction for the mechanical properties of sustainable concrete under complicated stress states. This study helps to promote the recycling of waste crushed concrete and waste glass in construction projects, reducing construction costs and achieving a low-carbon economy.

According to the existing research gaps and questions, the specific research objectives are as follows:

Research objective 1. The first research objective is to investigate the microscopic properties of different ITZs in sustainable concrete, including the cohesion performance of ITZs bonded to NCA, RCA, NFA and RGS. BSE based-image analysis technique was used to distinguish pores, cracks, reaction products and unreacted products according to the grey threshold, and then statistically analyse the volumetric fraction of each phase. Nanoindentation/nanoscratch combined with deconvolution analysis were used to evaluate the micromechanical properties and phases distribution in ITZs. At the same time, the modification efficiency of RGP can be evaluated by chemical composition within ITZs obtained from EDS, XRD, TG, FTIR, NMR etc. test results.

Research objective 2. The second research objective is to determine the triaxial mechanical properties of concrete with different percentage of RCA and RGS. The triaxial compressive strength, peak strain, elastic modulus and volumetric strain of sustainable concrete under different confining pressure were analysed according to stress-strain curves obtained in this work. Empirical models were established and calibrated to predict mechanical properties of sustainable concrete with RAC and RGS.

Research objective 3. The third research objective is to investigate the mechanical properties of sustainable concrete with RCA and RGS under confining pressure coupling with pore water pressure. 0, 3, 7, 14 MPa confining pressure and 0, 5, 9, 13MPa pore water pressure were applied to cylinder concrete specimens. The influence of pore water pressure on triaxial mechanical properties of the sustainable concrete was analysed and discussed based on stress-strain curves obtained in the tests. Moreover, empirical models were developed and fitted the triaxial compression stress-strain curves with pore water pressure of sustainable concrete.

Research objective 4. The fourth research purpose is to comprehensively analyse the experimental data and summarize the relationship between the microscopic properties of ITZs and the macroscopic mechanical properties of the concrete specimens under complicated stress states. Try to establish a correlation prediction model between the micro-level performance (nano elastic modulus, nano hardness, porosity of ITZ and adjacent matrix) and macro-mechanical properties of sustainable concrete, including the compressive strength, ductility, elastic modulus and volumetric deformation.

1.4 Thesis outline

This thesis contains eight chapters. The studies on phases distribution, micromechanical properties and chemical composition of ITZs in RAC and RGP enhancing efficiency for ITZs are mainly given in Chapter 4 and Chapter 5. The studies on macro-mechanical properties of sustainable concrete specimens with RCA and RGS under coupling confining pressure and pore water pressure are mainly presented in Chapter 6 and Chapter

7. The analysis and discussions of experimental data runs throughout Chapter 4 to Chapter 7. The main structure of this thesis is as follows:

Chapter 1 introduces the background and research gaps of the topic of this thesis. The main research objectives in this work are given out.

Chapter 2 reviewed the research progress of rheological properties, mechanical properties and durability of research targets (concrete with RCA, RGS and RGP) in this work. The existing research results related to nano/micro-characterisation techniques and macro-mechanical properties of concrete under triaxial compression with pore water pressure are summarised.

Chapter 3 introduces main facilities and techniques used in this work. The basic information and principle of test methods are briefly described.

Chapter 4 investigates and discusses the microscopic performance of ITZs modified by RGP in NAC.

Chapter 5 investigates and discusses the microscopic properties of ITZs in NAC and RAC. The enhancing efficiency of RGP on new ITZ in RAC is comprehensively evaluated by microstructure, micromechanical properties and chemical composition in ITZs.

Chapter 6 investigates and discusses the influence of pore water pressure on the triaxial compression performance of RAC. The failure mechanism of RAC under complicated stress states is explained by micro-characterisation techniques on ITZs. The critical conditions and stress-strain curves are fitted by empirical models.

Chapter 7 investigates and discusses the mechanical properties of sustainable concrete with RCA and RGS under coupling confining pressure and pore water pressure. The stress-strain behaviour of the sustainable concrete specimens under various stress states are explained by ITZ micromechanical properties and porosity. Modifications to the existing empirical models yielded satisfactory prediction results.

Chapter 8 gives out main conclusions drawn up from this work and provides some author's suggestions for future research work.

CHAPTER 2. LITERATURE REVIEW

C & D waste and municipal waste have become a main culprit in the current pollution (Tang, et al. 2020c). Studies demonstrated that waste concrete and glass can be effectively recycled as raw materials in concrete production (Arabi, et al. 2019, Ghorbani, et al. 2021, Zhang, et al. 2022). To promote the application of above waste materials in infrastructure construction, it is necessary to clarify their performance in some complicated environment such as coupled confining pressure and pore water pressure (He, et al. 2022, Heukamp, et al. 2001). Moreover, exploring characteristics of ITZs is contributed to understanding the failure mechanism of sustainable concrete under complicated stress conditions (Liu, et al. 2017, Rangaraju, et al. 2010, Xie, et al. 1991). Currently, BSE-based image analysis technique, nanoindentation, nanoscratch etc. are the most popular techniques for quantitatively analysing the microscopic properties of cementitious materials (Sidorova, et al. 2014, Yio, et al. 2017). This chapter presents a brief review of general properties of sustainable concrete with RCA, RGS and RGP, including workability, mechanical properties durability and microstructure performance. In addition, ITZ characteristic identifying techniques and stress-strain behaviour of the sustainable concrete under triaxial compression with pore water pressure are summarized.

2.1 Recycled aggregate concrete

Waste concrete is large in volume and high in density (Bravo, et al. 2017, Jayasuriya, et al. 2018). Disposal with other wastes will greatly increase energy consumption and occupy a large amount of landfill space (Pedro, et al. 2017, Tang, et al. 2022). Driven by huge environmental and social potential benefits, extensive research activities on recycling and reusing waste concrete have been conducted, and it has been demonstrated that waste concrete can be used as coarse aggregate in new concrete after crushing and sieving (Sunayana & Barai 2020, Thomas, et al. 2018, Xiao, et al. 2013a). According to research, the workability of RAC is normally lower than that of NAC mainly due to the hard-to-remove old mortar on the surface of RCA (El-Hassan, et al. 2019, Omary, et al. 2016, Zaetang, et al. 2016). The loose and porous structure of old mortar largely improves the water absorption capacity of RCA, thus reducing the slump value of freshly mixed RAC under the same water-cement ratio (Hu, et al. 2019, Kim, et al. 2018). However, this negative effect can be solved by modifying mixing approach (Fang, et al. 2023, Xiao, et al. 2012). For example, saturated surface dry method, water compensation method and two-stage mixing approach (TSMA) can all improve the workability of RAC mixture (Tam, et al. 2008, Tang, et al. 2020d, Zhang, et al. 2022). In particular, the TSMA proposed by Tam et al. (2008) achieved a higher initial slump and successfully increased the compressive strength of RAC by 20%.

However, as illustrated in Table 2.1, more research pointed out that incorporating RCA in concrete will reduce mechanical properties of concrete due to weaker bond strength between old and new cement mortar (Liu, et al. 2023, Otsuki, et al. 2003). Omary et al. (2016) reported that the compressive strength, splitting tensile strength and elastic modulus of RAC reduced by 5.4%, 16.2% and 32.8% respectively compared to NAC. Bravo et al. (2017) also pointed out that the 28-day compressive strength, splitting tensile strength and elastic modulus of concrete specimens with 100% RCA were 34.5%, 22.5% and 47.9% respectively lower than NAC. Pedro et al. (2017) stated that the compressive strength of concrete specimens decreased by about 7.5% when NCA was replaced by RCA. The mechanical properties of concrete specimens are related to many factors, such as raw materials, water-cement ratio, curing conditions etc (Nehdi, et al. 2017, Qu, et al. 2021). For RAC, the biggest difference from NAC is that there is an extra layer of old mortar on the surface of RCA (Dimitriou, et al. 2018, Wang, et al. 2023). ITZs are known to be the weakest regions within concrete (Hosan, et al. 2021). There are two types of ITZs in RAC: old and new ITZs. The high volume of ITZs in RAC leads to a decrease in the mechanical properties (Lei, et al. 2018, Lu, et al. 2019, Xuan, et al. 2017).

Table 2.1 Effects of RCA on the mechanical properties of concrete

Ref.	Curing days	Replacement ratio	Compressive strength	Flexural strength	Splitting tensile strength	Elastic modulu s
(Omary, et al. 2016)	28	34-100%	↓	—	↓	↓
(Bravo, et al. 2017)	28	10-100%	↓	—	↓	↓
(Katz 2003)	7, 28, 90	100%	↓	↓	↓	↓
(Brand, et al. 2015)	3, 7	100%	↓	—	—	—
	28	100%	↓	↓	↓	—
(Pedro, et al. 2017)	7, 56	25-100%	↓	—	—	—
	28	25-100%	↓	—	↓	↓
(Dimitriou, et al. 2018)	7, 28, 56	50%, 100%	↓	↓	↓	↓
(Gesoglu, et al. 2015)	56	100%	↓	↓	↓	↓
(Thomas, et al. 2018)	28	25-100%	↓	↓	↓	↓

Note: ↑ represents positive effect; ↓ represents negative effect; — represents the authors did not conduct the related experiments. The same below.

A microstructure of RCA can be seen in Figure 2.1. Old and new ITZs in RAC are denoted by light and dark blue line respectively. Larger volume of ITZs means more pores and cracks (Diamond & Huang 2001, Rangaraju, et al. 2010). As a result, RAC has a higher permeability coefficient (Zhang, et al. 2019). Moreover, the old mortar on the surface of virgin aggregate easily contains a large number of micro-cracks, which can provide a path for aggressive solution penetration (Wang, et al. 2017, Xie, et al. 2019). Aliabdo (2018) reported that the water permeability of concrete increased by 13.3% and 18.8% respectively when 50% and 100% NCA was replaced by RCA. El-Hassan (2019) further pointed out that when the RCA substitution ratio increased from 10% to 20%, the permeability of concrete improved significantly. Subsequently, as the RCA content continued rising, the permeability coefficient still increased but at a milder rate (El-Hassan, et al. 2019). Liu et al. (2023) conducted a chloride intrusion experiment and confirmed that more cracks were created in the old mortar of RCA and accelerated the penetration of corrosion ions. According to references, old mortar and cohesion performance of the new ITZ is the key to determine the concrete specimens resistant to external loads and water diffusion (Liu, et al. 2023).

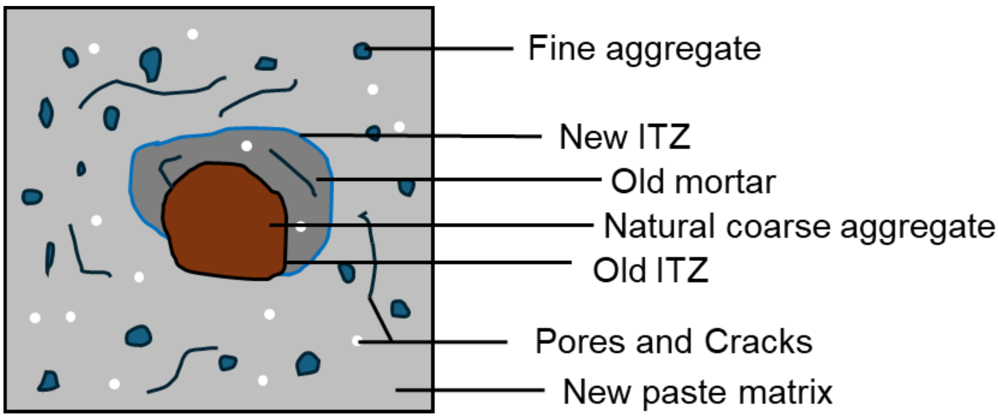

Figure 2.1 Schematic diagram of RCA in concrete (Wang, et al. 2021)

2.2 Recycled glass sand concrete

Waste glass can replace natural river sand as fine aggregate in concrete after crushing (Jiao, et al. 2020, Ye, et al. 2022). Common waste glass includes soda-lime glass, borosilicate glass, lead-silicate glass, barium glass and aluminosilicate glass (Jiang, et al. 2019). Generally speaking, these waste glass has close to zero water absorption and a smooth surface after being made into RGS, which is contributed to improve the workability of fresh cementitious mixtures (Ghorbani, et al. 2021, Ismail & Al-Hashmi 2009). On the other hand, sharper and more angular grain shapes of glass increase internal friction among aggregates and cement particles, impeding the flowability of concrete (Jiao, et al. 2020). As a result, some controversial results on the rheological performance of concrete modified by RGS were obtained in previous research (Bisht, et al. 2020, Chen, et al. 2006). It can be seen from Figure 2.2, Park et al. (2004) found that the slump of concrete dropped by 38.5-44.3% as RGS replacement ratio increased to 70%. By contrast, Terro (2006) reported that concrete containing 50% RGS showed 17.6% higher slump value than the reference concrete.

A similar phenomenon also exists in the mechanical properties of concrete with RGS (see Table 2.2). For example, Ali and Al-Tersawy (2012) found that compressive strength, splitting tensile strength, flexural strength and elastic modulus decreased by 23%, 32%, 24% and 12% respectively at 28 days when 50% of NFA was replaced by RGS. However, according to Lee et al. (2013), the 28-day compressive strength of concrete with 100% fine glass aggregate was 30.4% higher than that of reference concrete. This is because the mechanical properties of concrete modified by RGS is highly related to glass types, colours, particle sizes and replacement ratio (Lee, et al. 2013). In general, WGC with smaller particle size of RGS possess better mechanical properties (Dong, et al. 2021). Also, different type and colour of waste glass represent different chemical composition, which can influence hydration and pozzolanic reaction process within concrete (Ali & Al-Tersawy 2012, Arabi, et al. 2019, Arulrajah, et al. 2015).

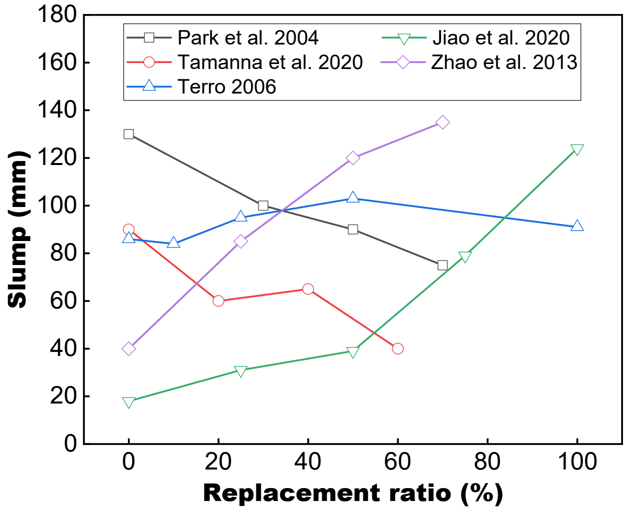

Figure 2.2 Slump values of concrete with different content of RGS as fine aggregate (Jiao, et al. 2020, Park, et al. 2004, Tamanna, et al. 2020, Terro 2006, Zhao, et al. 2013)

Table 2.2 Effects of RGS on mechanical properties of concrete

Ref.	Curing days	Particle size (mm)	Replacement ratio	Compressive strength	Flexural strength	Splitting tensile strength
(Ali & Al-Tersawy 2012)	28	0.075-5	10-50%	↓	↓	↓
(Ling, et al. 2012)	60	0.075-5	25-100%	↓	—	—
(Bisht, et al. 2020)	28, 90, 180	0.15-0.6	18-20%	↑	—	—

			21-24%	↓	—	—
(Jiao, et al. 2020)	7,14,28	0.1-0.6	25-75%	↑	No clear effect	No clear effect
			100%	↓	No clear effect	No clear effect
(Lee, et al. 2013)	28	<0.6	25-100%	↑	—	—

Regarding durability of concrete with RGS as fine aggregate, some relatively uniform conclusions were reached (Arulrajah, et al. 2015, Bisht, et al. 2020, Chen, et al. 2006). Many researchers concluded that water impermeability, chloride penetration resistance, acid resistance and fire resistance were enhanced for concrete incorporated with RGS (Ali & Al-Tersawy 2012, Arabi, et al. 2019). Figure 2.3 shows the micro-topography of ITZ of concrete with and without RGS. Concrete using RGS as fine aggregate had a denser microstructure and lesser cracks, which resulting in a satisfactory performance of concrete with WGS under some aggressive environments (Jiao, et al. 2020). Besides the above properties, another consensus is that RGS as fine aggregate in concrete increases the potential of alkali-silica reaction (ASR) due to the existence of high content of alkali metal oxides (e.g. Na_2O and GaO etc.) in glass (Park, et al. 2004, Tamanna, et al. 2020). The microcracks produced during glass crushing are the most probably sites for ASR (Tamanna, et al. 2020). In addition, concrete with green soda-lime glass fine aggregate showed lower ASR expansion because of high content of Cr_2O_3 in waste green glass (Park, et al. 2004). However, quantitative analysis of ITZ performance between RGS and cement paste is still deficient. Explaining the behaviour of concrete using RGS as fine aggregate in complicated environments from ITZs is a perspective worthy of attention.

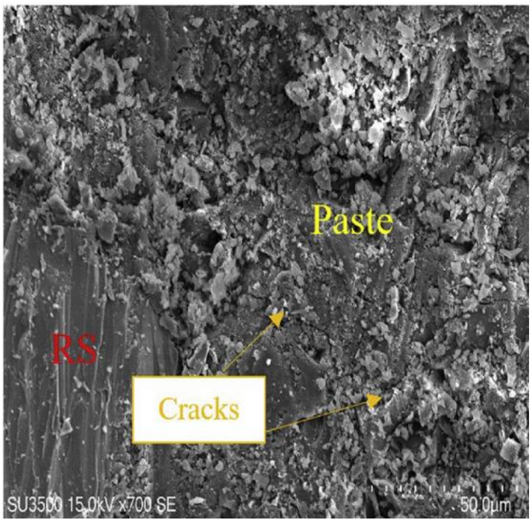

(a) Concrete with river sand as fine aggregate

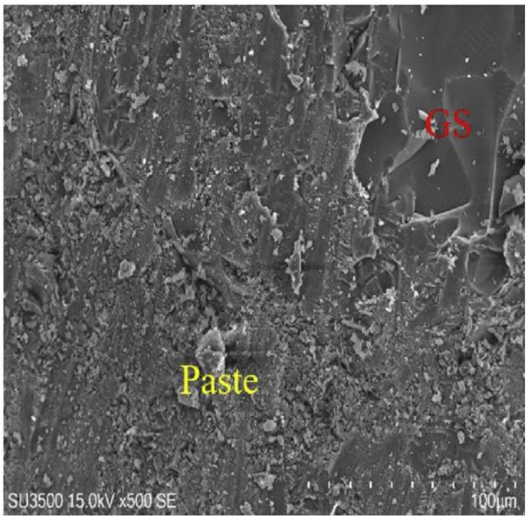

(b) Concrete with glass sand as fine aggregate

Figure 2.3 Microstructure of concrete with different fine aggregates (Jiao, et al. 2020)

There are few studies on the bonding performance of glass particles and cement paste (Du & Tan 2017, Mohammadi & South 2016). In existing studies, scholars generally believe that the bonding performance of cement paste and glass particles is weaker than that of cement paste to natural aggregates, because the former has almost no water absorption (Ke, et al. 2018). Therefore, a large amount of free water is easy to accumulate on the surface of glass particles, remaining a high local water-cement ratio and porosity (Mostofinejad, et al. 2020). However, the above conclusions all come from rough instrumental observations and lack more in-depth quantitative analysis.

2.3 Waste glass powder concrete

If waste glass particles are ground into powder, its pozzolanic reactivity will be obviously enhanced, and can be seen as an idea supplementary cementitious material (SCM) (Xiao, et al. 2020, Zidol, et al. 2021). According to studies (Pan, et al. 2017, Schwarz & Neithalath 2008, Terro 2006), the pozzolanic reactivity of RGP increases with the decrease of fineness and the effect of RGP as pozzolanic material on the mechanical properties of cementitious materials are collected in Table 2.3. Many researchers have partly replaced cement in concrete and mortar with RGP lower than 100 μm and found that the modified mixtures exhibited better mechanical properties than the counterpart especially at later ages (Nassar & Soroushian 2012, Omran & Tagnit-Hamou 2016, Omran, et al. 2017). For example, Shao et al. (2000) reported that the concrete with 30% 38μm RGP showed about 25% higher compressive strength than the reference concrete at 90 days. Du and Tan (2017, 2013) found that although reference concrete exhibited higher strength at 7 days, the compressive strength of concrete containing 15-60% RGP was higher than that of plain concrete by 27-12% averagely at 365 days. Pan et al. (2017) used RGP with an average size of 45μm as a partial replacement of cement in mortar, and found that the compressive strength ratio of 5% RGP modified mortar to reference mortar was 67% at 3 days, but this value rose to 110% at 28 days.

Table 2.3 Effects of RGP on mechanical properties of concrete

Ref.	Replacement ratio	Particle size (μm)	Curing days	Compressive strength	Flexural strength	Splitting tensile strength
(Shao, et al. 2000)	30%	38	7, 28	↓	—	—
			90	↑	—	—
(Du & Tan 2017)	15-60%	0.1-100	7	↓	—	—
			28, 365	↑	—	—
(Pan, et al. 2017)	5%	45, 60	3, 7	↓	—	—
			28	↑	—	—

(Nassar & Soroushian 2012)	20%	13	14, 56	↑	↑	—
(Omran, et al. 2017)	20%	0.3-50	28, 91	↑	↑	↑

For durability, the concrete containing RGP possesses higher impermeability, structural stability, chloride penetration resistance and freeze-thaw resistance because of pozzolanic reaction (Mohammadi & South 2016, Mostofinejad, et al. 2020). As shown in Figure 2.4, concrete with 30% glass powder had more compact ITZ than that of plain concrete. The non-expansive C-S-H gel generated by the combined action of the hydration and pozzolanic reaction can effectively modify the pore structure of concrete and improve the behaviour of concrete under aggressive environments (Mejdi, et al. 2019, 2022, Mirzahosseini & Riding 2015). Most importantly, potential harm of ASR expansion caused by waste glass can be largely alleviated by milling glass particles into powder due to high pozzolanic reactivity (Maddalena, et al. 2018, Mahmood, et al. 2022). The finer RGP can also fill harmful microcracks, where is the important channel for aggressive ions penetration (Lin, et al. 2012, Ling, et al. 2012, Lu, et al. 2020).

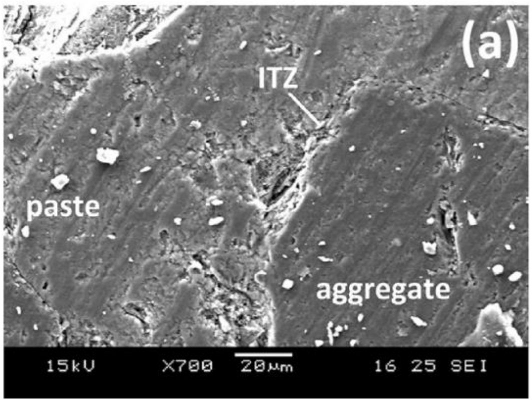

(a) Plain concrete

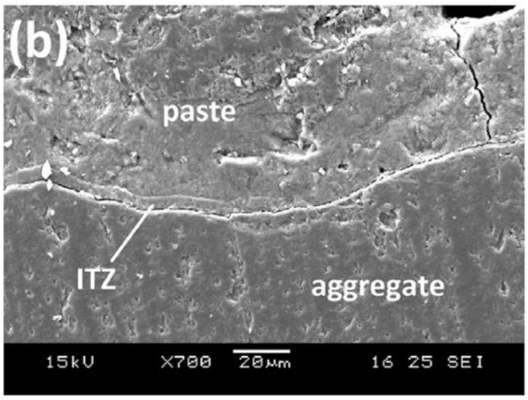

(b) Concrete with 30% glass powder

Figure 2.4 Microstructure of concrete with and without glass powder (Du & Tan 2017)

Most research on the performance of concrete containing RGP still stays on the macroscopic level, including rheological properties, mechanical properties, and durability (Jiang et al. 2019). Understanding the mechanisms responsible for these behaviours requires more in-depth research at the microscopic level. However, a small amount of research at the microscopic level is limited to simple scanning electron microscopy (SEM) image observation and identification of the changes in chemical elements and mineralogical phase between paste samples with/without RGP (Du and Tan 2017; Pan et al. 2017; Mejdi et al. 2019). In these limited studies, Du and Tan (2017) learned from X-ray diffraction (XRD) and thermogravimetric analysis (TGA) that RGP can effectively consume calcium hydroxide and generate C-S-H gel with a low Ca/Si ratio. Pan et al. (2017) found that the hexagonal plate crystals of portlandite disappeared at a high temperature of 500 °C, while the microstructure of the mortar introduced with 20 wt.% RGP was less affected by the high temperature because the glass particles consumed portlandite and filled the pores. Although Mejdi et al. (2019, 2022) recently studied the long-term hydration process of cement paste containing glass powder through thermodynamic modelling, XRD-Rietveld analysis and quantitative element distribution analysis, the investigation of concrete samples made with RGP and its interfacial transition zone (ITZ) is still insufficient, and there is a lack of in-depth analysis of large batches of test data by image analysis and mathematical statistics techniques.

2.4 Nano/micro-level properties quantitative analysis techniques

Backscattered electron (BSE) images combined with image analysis technique are usually used to quantitatively characterise the constituents of cement-based materials (Abbas, et al. 2009, Lyu, et al. 2019b, Yio, et al. 2017). Pores, cracks, hydration products and unhydrated clinkers in BSE images can be segmented and statistically analysed according to grey level thresholds (Ulsen, et al. 2022, Wong, et al. 2006). The key to image analysis is to determine the grey threshold for each phase as accurately as possible (Head & Buenfeld 2006, Wong, et al. 2009). The grey value of a BSE image is between 0-255. The dark object has a lower grey value. As shown in Figure 2.5, for a pore (black area), when the grey threshold is low, the segment area (white pixels) cannot completely cover the pore. If the grey threshold exceeds 80, the segmented area overflows the pore to the surrounding areas, resulting in a higher pore area calculated value than the real value. Therefore, there is a critical grey value for each phase in cementitious materials. Researchers (Han & Yan 2021, Hutchinson & Chen 2006, Kim, et al. 2019, Mouret, et al. 2001) proposed the inflection point method and deconvolution method based on greyscale histogram to find the critical grey value of each phase. However, it is difficult for these methods to identify the grayscale interval where each phase is located accurately. In addition, affected by brightness and contrast, the critical grey value of different BSE images may be inconsistent.

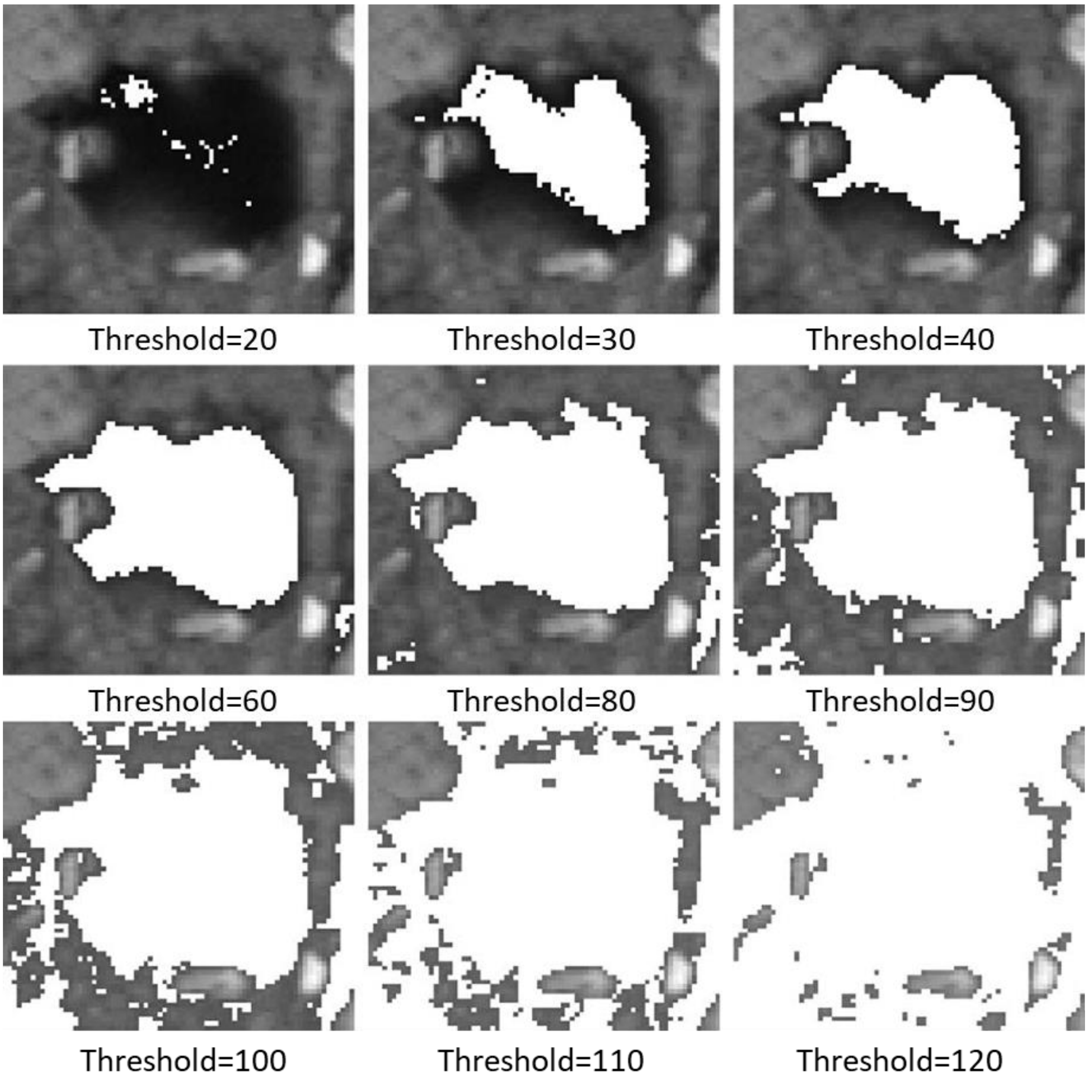

Figure 2.5 Phases segmented results at different grey threshold levels (Wong, et al. 2006)

For sustainable concrete samples with RCA, RGS and RGP in this study, determining the distribution of phases within cement paste is contributed to quantify ITZ width (Wong & Buenfeld 2006, Yang, et al. 2018). Moreover, the cohesion strength of ITZs can be inferred based on the proportion of each phase, and the microscopic performance of ITZ determines the macroscopic mechanical properties and durability of the sustainable concrete (Igarashi, et al. 2005, Mouret, et al. 2001, Wang, et al. 2015). The different surface morphologies and chemical activity of natural sand, old cement paste and RGS lead to differences in the microscopic performance of ITZs (Arabi, et al. 2019, Zhang, et al. 2021). In Djerbi's (2018) research, image analysis was performed to quantify pores and unhydrated clinkers in the new ITZ of RAC. The results show that new ITZ in recycled aggregate concrete (RAC) has a higher porosity and lower proportion of unhydrated clinkers than NAC (Djerbi 2018). Kim et al. (2019) segmented pores in ITZs of RAC and image analysis showed that bonded mortar resulted in higher porosity in ITZs and thereby affected the concrete strength. In comparison, few studies use BSE-based image analysis technique to observe the microstructure of ITZ between RGP, RGS and cement paste.

Luo et al. (2018, 2019) systematically summarised the micromechanical properties characterisation techniques of ITZs, including modulus mapping, grid nanoindentation and nanoscratch etc., among which, the latter two can be performed by a nano indenter. Xiao and Li et al. (2012, 2013b, 2013c) conducted a large number of nanoindentation tests and identified the width of old and new ITZs in RAC according to elastic modulus, which is shown in Figure 2.6. In their studies, old ITZ width ranged in 40-50 μm, whereas new ITZ width ranged in 55-65 μm with lower elastic modulus, confirming that new ITZ is the weakest region in RAC (Li, et al. 2012, Xiao, et al. 2013b, Xiao, et al. 2013c). In addition, the indentation modulus of the new ITZ is close to the paste matrix, that is, the 'wall effect' is not obvious in new ITZs (Li, et al. 2012, Xiao, et al. 2013b, Xiao, et al. 2013c). The application of nanoscratch in the study of ITZs bonded to RCA and RGS is less, and are only reported in the research of geopolymer concrete and cement paste (Li, et al. 2021, Luo, et al. 2022). Compared with grid nanoindentation, nanoscratch can obtain a series of continuous data, so the impact of uneven aggregate surface on statistical results can be mitigated (Akono & Ulm 2017, Yan, et al. 2022, Yin, et al. 2022). However, the project area of nanoscratch is larger than that of nanoindentation. When the research target is a heterogeneous material such as cement paste, the test results may be interfered by multi-phase interactions (Akono & Ulm 2014, Hoover & Ulm 2015b).

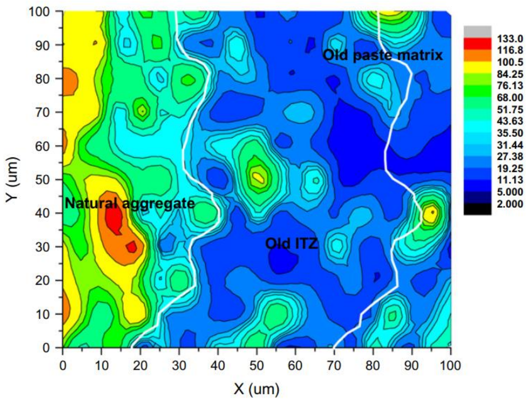

(a) Contour map of elastic modulus in Old ITZ

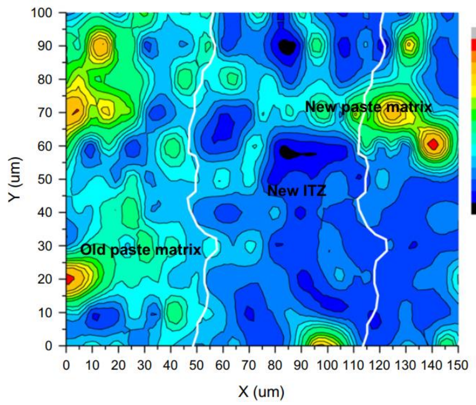

(b) Contour map of elastic modulus in New ITZ

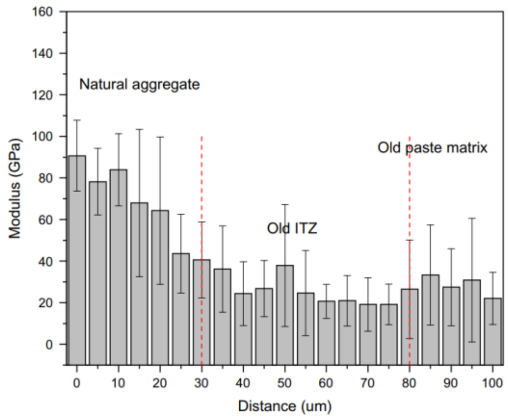

(c) Elastic modulus distribution in Old ITZ

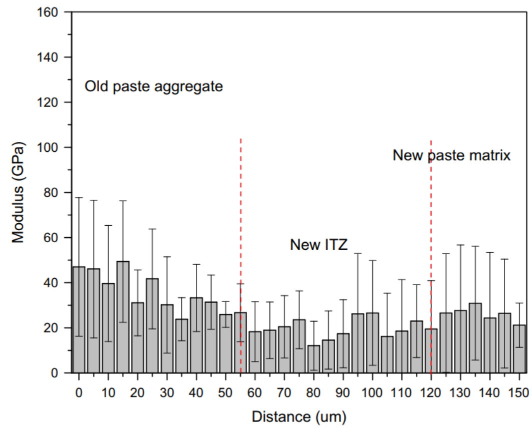

(d) Elastic modulus distribution in New ITZ

Figure 2.6 Elastic modulus of ITZs in RAC obtained from grid nanoindentation tests (Xiao, et al. 2013c)

2.5 Triaxial compression with pore pressure

Concrete structures often suffer multiaxial compression, and many researchers have conduct triaxial compression test on concrete (Jiang, et al. 2017, Lim & Ozbakkaloglu 2014, Meng, et al. 2017, Tang, et al. 2019, Zeng, et al. 2013). The triaxial compression test can be divided into two types: conventional triaxial compression and true triaxial compression (Deng, et al. 2017, He & Zhang 2014, Li, et al. 2022a). Normally speaking, the compressive strength of concrete increases with confining pressure, as shown in Figure 2.7. Xu et al. (2021b) exerted 40 MPa confining pressure on concrete and found that the average compressive strength of concrete increased by 142% and the peak strain increased by 218% compared with uniaxial compression. Wang et al. (2020) carried out triaxial compression tests on cylinder concrete specimens with confining pressure from 5-50 MPa. According to their research, triaxial compressive strength of concrete under 50 MPa of confining pressure was 198% higher than the uniaxial compressive strength of concrete (Wang, et al. 2020). The failure mode of concrete specimens damaged by triaxial compression also deserves attention. Diagonal cracks appeared on the surface of concrete specimens under triaxial compression, showing shear-type failure patterns rather than vertical cracks under uniaxial compression (Chen, et al. 2019, He, et al. 2015, Ren, et al. 2015, Zingg, et al. 2016). Under the action of lateral confinement, the failure mode of concrete changes from lateral splitting failure to shear failure mode, because the confining pressure restricts the propagation direction of micro-cracks and increases the internal friction of concrete (He, et al. 2022, Tang, et al. 2020b, Xu, et al. 2017a). Lim and Ozbakkaloglu (2014) summarized experimental results of mechanical properties of concrete specimens under triaxial compression and established a database. A unified stress-strain model was developed and successfully predicted the peak and post peak performance of concrete under active confining pressure (Lim & Ozbakkaloglu 2014). The study by Chen et al. (2019) showed that the difference in compressive strength between NAC and RAC under high confining pressure was reduced compared with the uniaxial compressive strength. This shows that the scheme of RAC applied to some structures subjected to multiaxial compression has certain feasibility (He, et al. 2022, Li, et al. 2022a, Xue, et al. 2023). In addition, the ductility and toughness of concrete under triaxial compression are enhanced, indicating that lateral confinement helps to improve the compression deformation and energy dissipation performance of concrete (Carvalho & Carrasco 2010, Chen, et al. 2017, Jiang, et al. 2023, Vu, et al. 2015).

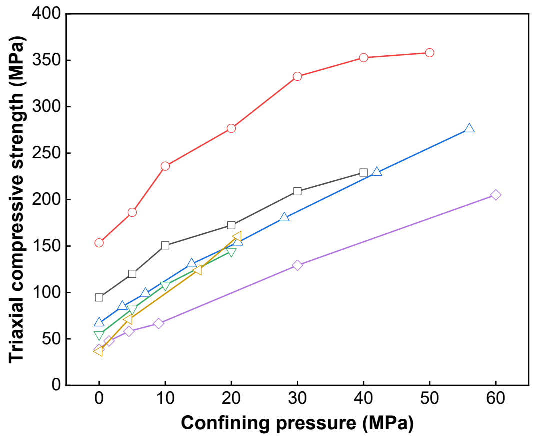

Figure 2.7 Triaxial compressive strength of concrete under different confining pressure (Lim & Ozbakkaloglu 2014, Lu & Hsu 2006, Meng, et al. 2017, Wang, et al. 2020, Xu, et al. 2021b, Zhu, et al. 2021)

It must be point out that water easily retain in pores of concrete due to capillary action and the effect of pore water pressure on the mechanical properties of concrete cannot be ignored when concrete is subjected to high confining pressure (Malecot, et al. 2019, Vu, et al. 2015). Vu et al. (2009) tested the performance of concrete with different saturation ratio under triaxial compression. They found that compressive strength of dry concrete significantly increased with confining pressure, while the increasing ratio of wet and saturated concrete remained constant over a certain confining pressure (Vu, et al. 2009). It is obvious that pore water pressure increased significantly under high lateral compression, and the axial compressive strength enhancement by confining pressure was limited (Malecot, et al. 2019, Vu, et al. 2009). Malecot et al. (2019) came to similar conclusions. The elastic modulus of concrete with high porosity and water content decreased more obviously than the counterpart in the damage process (Malecot, et al.

2019). However, all above research concerned indirect pore water pressure; the study on the relationship between mechanical properties of concrete and confining pressure with pore water pressure is still scarce (Lu & Hsu 2006, Xu, et al. 2021a, Yang, et al. 2022). In addition, the supporting effect and the crack expansion acceleration effect of pore water pressure on concrete are closely related to the porosity and micromechanical properties of ITZs (Deng, et al. 2020, He & Zhang 2014). The research on the ITZ of sustainable concrete with RCA and RGS is contributed to link the macroscopic mechanical properties and micro-level performance of concrete specimens under complicated stress states (Candappa, et al. 2001, Deng, et al. 2017, Ren, et al. 2018). Up to now, no empirical model that has been validated for predicting the stress-strain curves of concrete specimens containing RCA and RGS under confining pressure coupling with pore water pressure (Ren, et al. 2018, Wang, et al. 2020, Yang, et al. 2022).

By summarizing the existing literature, it can be found that the rheological properties, mechanical properties and durability of sustainable concrete with RCA, RGS and RGP have been comprehensively studied. However, few in-depth investigations have been made into the microstructure and micromechanical properties of ITZs within RACs containing RGS and RGP. In addition, concrete is a porous material and is often subjected to coupled pore water pressure and triaxial compression in practical engineering. Therefore, this thesis quantitatively analyses the ITZ properties within sustainable concrete with RCA, RGS AND RGP using image analysis and nanoindentation mathematical statistical techniques. Subsequently, the relationship between the microscopic properties of ITZ and the macroscopic mechanical properties of the specimens was established through the stress-strain curves of the sustainable concrete cylinder specimens under multi-dimensional stress conditions.

CHAPTER 3. INTRODUCTION OF TESTING APPRARTUS

In order to deeply study the microscopic properties of ITZ in sustainable concrete with RCA, RGS and RGP and the mechanical properties of the specimens under multi-dimensional stress, a series of advanced instruments were applied to provide data support for this thesis. This chapter describes the performance and parameter settings of each instrument. Scanning electron microscope (SEM), X-ray diffraction (XRD), Thermogravimetry analysis (TGA), Fourier transform infrared spectroscopy (FTIR) and Nuclear magnetic resonance spectrometer (NMR) are used to identify the microstructure and chemical composition of ITZs. Nanoindentation and nanoscratch are used to assess the micromechanical properties of ITZs. The Multi-field coupling testing system is used to obtain the stress-strain curves of the sustainable concrete specimens under the complicated stress states.

3.1 Scanning electron microscope (SEM)

Zeiss EVO LS15 as shown in Figure 3.1 equipped with a BSE and EDS detector was used for image analysis and element distribution observation respectively. With the help of electron microscope, nanoscale substances can be observed under a magnification over 10000 times. The instrument can apply high acceleration voltage of above 15 kV and up to 30 kV to ensure enough energy for BSE and EDS tests. Backscattered electrons are higher in energy than secondary electrons and are imaged by incident electrons being scattered by the sample. Although the resolution of the BSE image is lower than that of the SEM image, it can effectively reflect the physical phase in the cementitious materials (Gaël, et al. 2016). EDS is usually used in conjunction with SEM or BSE. The surface of the sample is bombarded by an electron beam and excited with X-rays. The elemental composition of this point can be determined based on the wavelength of the X-rays. The instrument can perform point, line scan and mapping analysis to reflect constituent distribution in concrete samples.

Figure 3.1 Zeiss EVO LS15

3.2 X-ray diffraction (XRD)

Bruker D8 Discover XRD as shown in Figure 3.2 was used for mineralogical analysis of cement paste. Diffraction occurs when an X-ray beam penetrates cement paste powder. The diffraction pattern allows the analysis of the crystal composition within the cement paste. Crystals appear as sharp peaks in the diffraction position (2θ)-intensity spectra, whereas amorphous phases appear as humps. The type and content of crystals can be determined from the diffraction position (2θ) and intensity respectively. The instrument can obtain XRD spectra with 2θ from 5° to 70° at a step size of 0.02°.

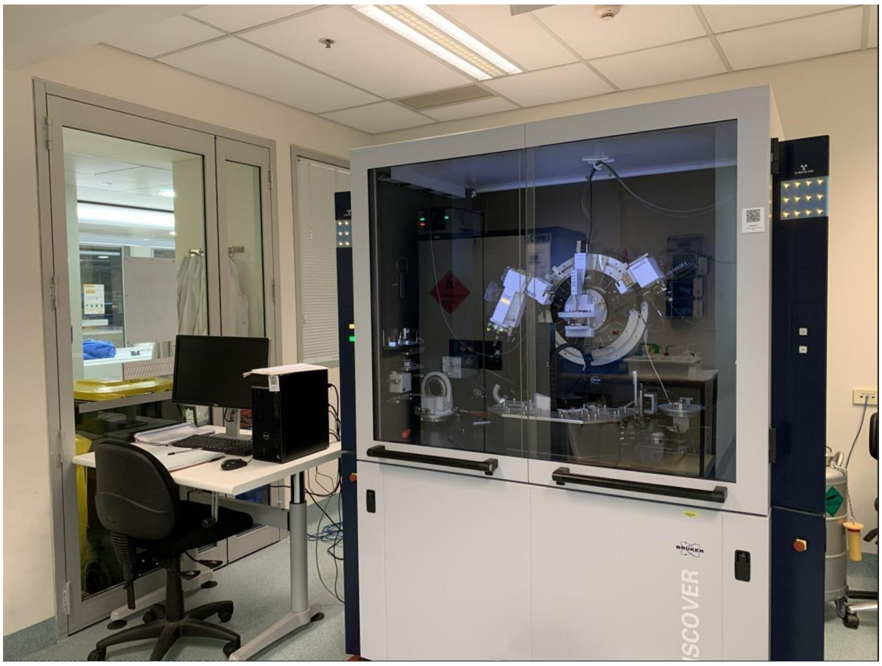

Figure 3.2 Bruker D8 Discover XRD

3.3 Thermogravimetry analysis (TGA)

STA449 F5 JUPITER was used for TGA of cement paste. The instrument is shown in Figure 3.3. The sample used for the TGA test is vacuum dried cementitious powder. Although most of the free water is removed from the vacuum dried powder, the bound water, C-S-H, calcite, portlandite, calcite etc., within the cementitious material gradually decompose and are converted to water vapour or CO_2 at elevating temperature, resulting in a loss of sample weight (Hager, et al. 2021). The content of constituents in cementitious materials can be determined from variation of sample weight. In particular, the proportions of bound water, C-S-H and portlandite are important for determining the hydration degree and the influence of waste glass on hydration (Kocaba, et al. 2012, Navarrete, et al. 2021). The instrument can heat sample powder uniformly from room temperature to 1000 ℃ under nitrogen environment and detect weight changes on the micrograms level.

Figure 3.3 STA449 F5 JUPITER

3.4 Fourier transform infrared spectroscopy (FTIR)

The Thermo Scientific Nicolet 6700 FTIR spectrometer as shown in Figure 3.4 was used to detect chemical bonds and functional groups in cementitious materials. Relative vibrations between atoms and molecular rotation absorb infrared light at specific wavelengths. The chemical bonds and functional groups in cementitious materials can be deduced from the position of the absorption peaks on the infrared spectra. The instrument analyses infrared spectral absorption information from 7400 cm^{-1} to 375 cm^{-1}, which can cover the mid-infrared region (4000 cm^{-1}-400 cm^{-1}) corresponding to inorganic substances in cementitious materials (Camposeco-Negrete 2013, Wilson, et al. 2018).

Figure 3.4 Thermo Scientific Nicolet 6700 FTIR spectrometer

3.5 Nuclear magnetic resonance spectrometer (NMR)

Agilent 500 MHz Nuclear Magnetic Resonance as shown in Figure 3.5 was used to acquire solid-state ^{29}Si spectra to identify hydration degree of cementitious materials. The main component of cementitious materials that acts as a bonding agent, C-S-H gel, is a polymeric chain consisting of basic tetrahedral units $(SiO_4)^{4-}$ (Escalante-Garcia 2003, Kunther, et al. 2016). The applied magnetic field causes the centre Si atom to absorb energy and thus jump and appear on the resonance spectrum (Chen, et al. 2004). For a high complex degree of chain, more energy is required to make the centre Si atom jump (Skibsted & Andersen 2013). The instrument is contributed to analyse hydration degree of cementitious materials combined with X-ray crystallography and microscopy.

Figure 3.5 Agilent 500 MHz Nuclear Magnetic Resonance

3.6 Nanoindentation and nanoscratch

An Agilent G200 Nano Indenter as shown in Figure 3.6 was used to conduct nanoindentation and nanoscratch tests. The Berkovich tip is usually chosen for nanoindentation tests. For nanoscratch tests, a hemispherical tip can be equipped to avoid the computational inconvenience from asymmetry. Indentation hardness and elastic modulus can be obtained from nanoindentation tests; scratch hardness and fracture toughness can be obtained from nanoscratch tests. The standard maximum normal force is 500 mN with load resolution of 50 nN and can be up to 10 N when the high-load option is selected.

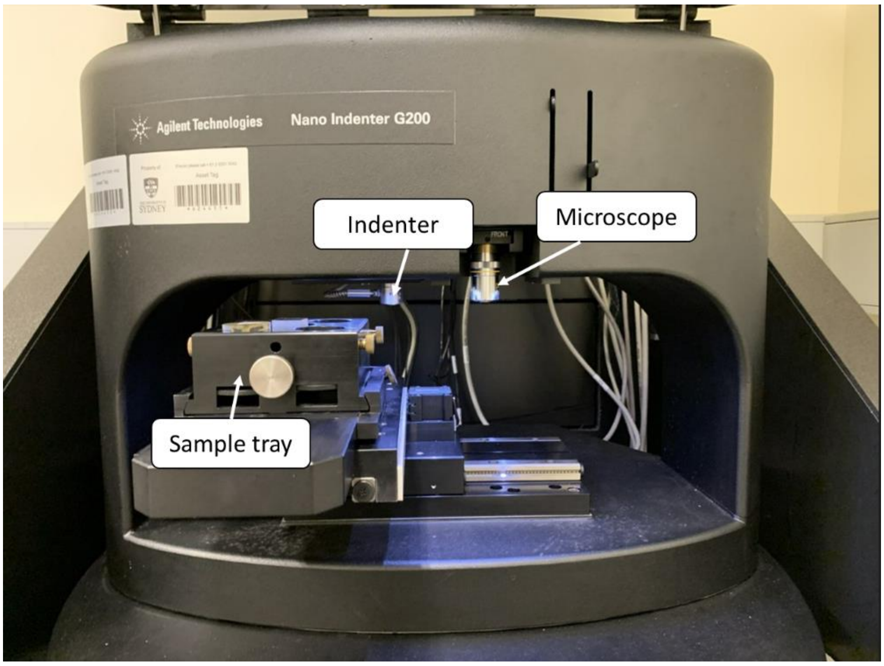

Figure 3.6 Agilent G200 Nano Indenter

3.7 Multi-field coupling testing system

As shown in Figure 3.7, the GCTS RTX-1000 multi-field coupled triaxial instrument contains two servo-controlled superchargers that can apply 70 MPa confining pressure and pore water pressure to a Φ 50 ×100 mm cylindrical sample. The maximum axial load of the system is 1000 kN with the accuracy of 0.25%. The compressive stress-strain curve of the sample can be obtained by two axial and one circumferential linear variable differential transformer (LVDT) with the same accuracy to axial load.

Figure 3.7 GCTS RTX-1000 multi-field coupled testing system

CHAPTER 4. NANO/MICROSCOPIC INVESTIGATION ON ITZS WITH RGP

4.1 Introduction

Portland cement has long been identified as an energy-intensive material, contributing to 5-7% of anthropogenic carbon emissions (Li, et al. 2023a). To reduce its carbon footprint, the use of low-carbon supplementary cementitious materials (SCMs) is well-recognised. For instance, Australian Standard AS 3972 (Australian Standard 2010) increased the allowable proportion of mineral additions (fly ash, slag, and/or limestone) from 5% to 7.5% to permit a reduction in the carbon footprint of cement manufacturing (Mohammadi & South 2016). This limit extends to more than 7.5% of fly ash and/or slag and up to 10% amorphous silica for blended cement (Type GB as per AS 3972). However, popular SCMs such as fly ash is on the decline from the rapid shift from coal-powered powerplants to sustainable alternatives, blast furnace slag processing through water quenching is a carbon-intensive process, and silica fume in high volume introduces some challenges to concrete (such as high drying shrinkage). In Australia alone, a total of 1.16 million tonnes of waste glass was generated between 2018 and 2019 (Dong, et al. 2021). As such, alternative SCMs like recycled glass, which are abundant and require reasonable processing, are to be investigated to understand their suitability to be incorporated into the mix.

ITZ forms around aggregates and is the weakest region in concrete which accounts for around 20-30% of the overall volume. As most concrete cracks along ITZ under loading, this is critical in determining the mechanical properties and durability of concrete (Fang, et al. 2023, Zhu, et al. 2023). Most studies on the microscopic properties of ITZs are based on irregular aggregate. However, rough and angular aggregate surface brings severe challenges to tests. In nanoindentation and nanoscratch tests, for example, the indenter may touch the aggregate hidden under the surface cement paste (Luo, et al. 2022). It is difficult to ensure that the same amount of data can be obtained from each region (Luo, et al. 2021). It is also difficult to determine the distance of each row of test points from the aggregate boundary (Luo, et al. 2021). Testers have to reduce indentation depth and increase the density of the grid. This greatly increases the workload and makes it difficult to achieve accurate statistical results (Luo, et al. 2018). SEM-based analysis faces a similar problem. It is well-known that the formation of ITZ is attributed to the 'wall effect' of aggregate (Diamond & Huang 2001). The uneven surface of aggregate is destined to the heterogeneity and complexity of ITZ (Luo, et al. 2021, 2022). In addition, the bleeding around the aggregate seriously affects the properties of ITZ at different locations (Tang, et al. 2019). This requires researchers to extract a large number of ITZ images at different positions to obtain a passable average result.

To solve the above problems, Shah and Winter (1966) are the first to propose a novel modelled concrete with cylindrical aggregate for analysing the inelastic mechanical properties of concrete. Subsequently, Xiao et al. (2013) extended the study of this concrete to the microscopic level. In recent years, Luo et al. (2021, 2022), Fu et al. (2020), and Zhan et al. (2020) used a similar concept to simulate ITZ by aggregate blocks and obtained satisfactory microstructure, chemical composition and micromechanical performance test results. It has to be admitted that the ITZ simulated by modelled concrete idealises the actual situation and ignores the randomness and complexity of the real ITZ (Yue, et al. 2020). However, with the help of characteristics of modelled concrete, the bonding mechanism of aggregate and mortar can be more effectively explored (Khedmati, et al. 2018, Wu, et al. 2022).

Therefore, a multi-technique holistic investigation approach including image analysis, chemical phase quantitative analysis and micromechanical tests were combined with statistical techniques to explore the changes in ITZs from the inclusion of RGP in this study. To minimise the interference of inhomogeneity of materials on test results, a simplified ITZ was simulated by modelled aggregate concrete (MAC). The efficiency and accuracy of MAC in the study of ITZs have been demonstrated in previous studies (Fu, et al. 2020, Xiao, et al. 2013b, Zhan, et al. 2020). Two pieces of natural granite stones were ground into blocks and covered with pure-cement mortar and mortar containing 20% RGP, respectively. The modification efficiency of RGP on concrete ITZs was evaluated from test results.

4.2 Raw materials

General purpose Portland cement (GP cement) conforming to AS 3972 was the main cementitious material in this study. Waste glass (soda-lime glass), preliminary composed of recycled municipal kerbside council collection, was ground to a fine powder in the laboratory to replace 20 wt% of cement as SCM. The particle size distribution (PSD) curves of cement and RGP measured by Malvern Mastersizer 3000 are shown in Figure 4.1. The RGP was ground to achieve a similar PSD to cement with a median particle size of ~20 μm. The detailed chemical compositions determined using X-ray fluorescence (XRF) are shown in Table 4.1. The loss on ignition (LOI) of RGP in Table 4.1 suggests that before supply, the glass fragments went through a furnace at a high temperature to reduce the organic content and residuals (liquid and paper tags) to a minimum. The main oxide components of cement and RGP were calcium oxide and silica, respectively. Each MAC contained a granite block as natural coarse aggregate, ground from the single aggregate particle. Naturally occurring silica sand with a fineness modulus of 1.9 was selected as the fine aggregate.

Table 4.1 Chemical composition of cement and RGP

Composition (%)	CaO	SiO_2	Al_2O_3	SO_3	Fe_2O_3	MgO	K_2O	Na_2O	LOI
Cement	64.9	18.6	4.1	3.0	3.1	1.6	0.5		4.2
RGP	10.8	68.4	0.9	0.1	0.4	1.8	0.3	13.5	3.8

Note: LOI means the loss on ignition.

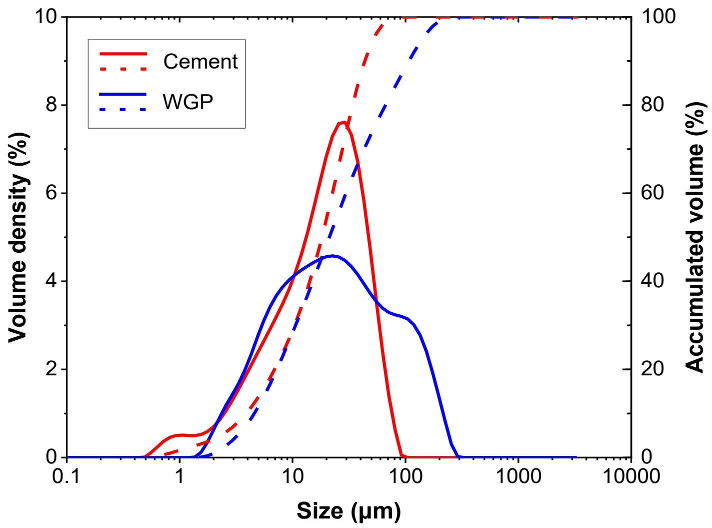

Figure 4.1 Particle size distribution of cement and RGP

4.3 Sample preparation

Modelled concrete samples were made by placing a piece of aggregate into the mortar. The mortar had a water-cement ratio of 0.45 and a sand-cement ratio (by mass) of 1.5. In one group of samples, 100% cement was used, while in the other, 20 wt.% of cement was replaced by RGP. Following previous research on modelled samples (Li, et al. 2021, Luo, et al. 2021a, Luo, et al. 2022), the MAC processing steps were designed and are shown in Figure 4.2. Firstly, the granite gravel with a suitable size was selected and ground to a 13 mm × 13 mm × 8 mm block. The granite block was further ground using a series of abrasive paper with different grits for 30 min and polished by 0.3 μm and 0.05 μm alumina slurries for 20 min. The alumina particles attached to the surface of the granite were removed in an ultrasonic bath. Subsequently, the saturated surface dried granite block was put in a Ø35 mm cylindrical mould and poured with fresh mortar. Large air bubbles were discharged by tapping. After curing in the mould for one day and being transferred and stored in a water tank at 23 ±3 °C for 3 months, the semi-finished sample was briefly ground and covered with a layer of epoxy resin to avoid damage to the ITZ during the following cutting. The sample that was cut and exposed to the ITZ was re-covered with a layer of epoxy resin in a Ø35 mm cylindrical mould. After the observation side was ground for 30 min and polished for 40 min, the sample was put in an ultrasonic bath for 2 min to remove alumina particles on the surface. Finally, the samples were put in a vacuum drying oven at 40 °C for 2 days. The MAC covered with epoxy resin was subjected to nanoindentation, nanoscratch and Backscattered Electron-Energy dispersive spectrometer (BSE-EDS) tests. Then, the mortar on the MAC was cut out and ground into powder for X-ray diffraction (XRD) and Fourier transform infrared spectroscopy (FTIR) tests. Although it is impossible to accurately measure the change of the mineral phase and chemical composition within ITZs, the pozzolanic reaction and its influence on the properties of ITZ with RGP was reasonably inferred through the analysis of the chemical composition differences between mortar matrix in MAC with and without RGP.

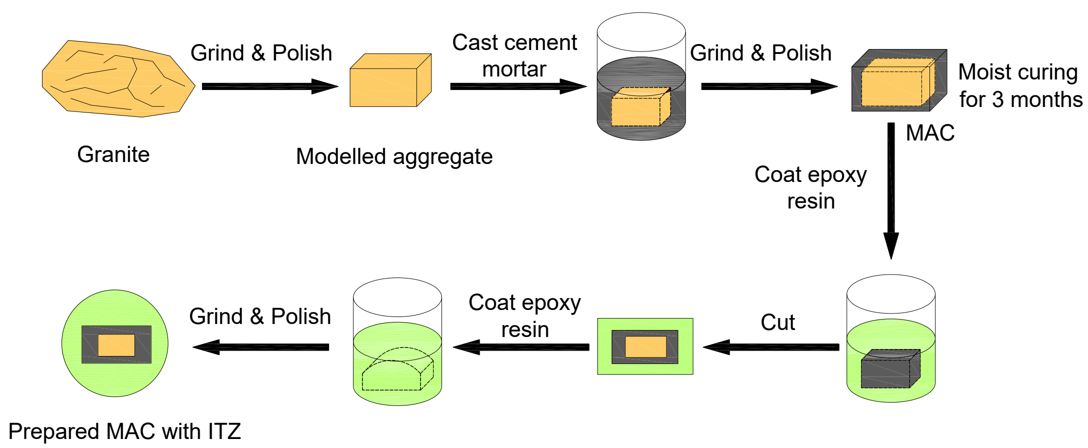

Figure 4.2 Preparation process of ITZ simulated by MAC

4.4 Testing methods

4.4.1 Microstructure examination and analysis

Thirty BSE images with a magnification of 500× were randomly extracted from the ITZs with and without RGP along the lateral boundary of the granite block. The probe current and accelerating voltage were set to 875 pA and 15 kV, respectively. The working distance was around 10 mm. To reduce unnecessary workload in subsequent analysis, the brightness and contrast during the observation process were kept consistent.

For statistical analysis of BSE images, modelled coarse aggregate can be easily identified and removed. Due to the significant difference in hardness between granite and cement paste, the grinding and polishing process may cause a height difference between the two phases (Lyu, et al. 2019a). Along the aggregate and mortar interface, this appeared as a black narrow strip, which would be mistaken for pores or cracks by image analysis software according to the grey value, but it is the shadow produced by the height difference under the electron microscope. Therefore, the shadow portion was removed together with the aggregate. The grey threshold recognition technique proposed by Wong et al. (Wong & Buenfeld 2009, Wong, et al. 2006, Wong, et al. 2009) combined with manual adjustment was adopted to distinguish pores and cracks, unreacted clinkers and hydration products in ITZ and adjacent mortar matrix. The 20 continuous strips with a width of 5 μm were taken out from the aggregate boundary to the mortar matrix. For ITZs with and without RGP, 30 BSE images were used to statistically analyse the relationship between the volume fraction of each constituent and the distance from the aggregate boundary. The width of ITZs can be easily determined by image analysis results. The processing procedure of the BSE image is shown in Figs. 4.3 and 4.4.

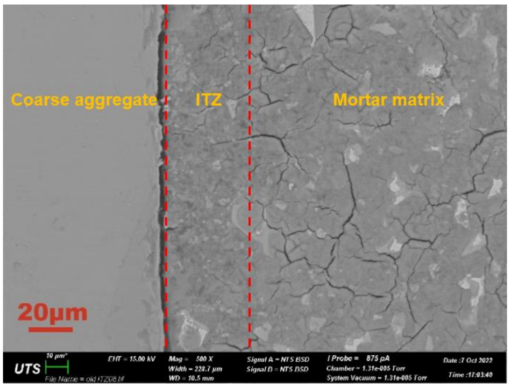

(a) BSE image of ITZ without RGP

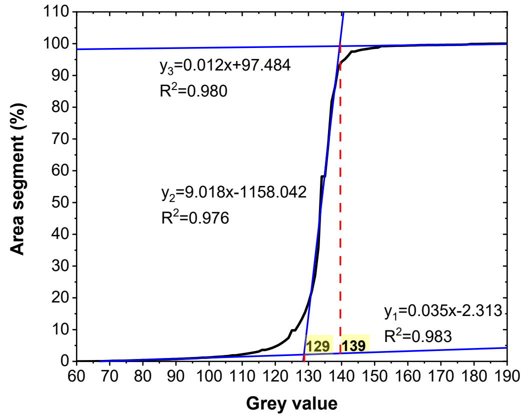

(b) Grey value threshold determination

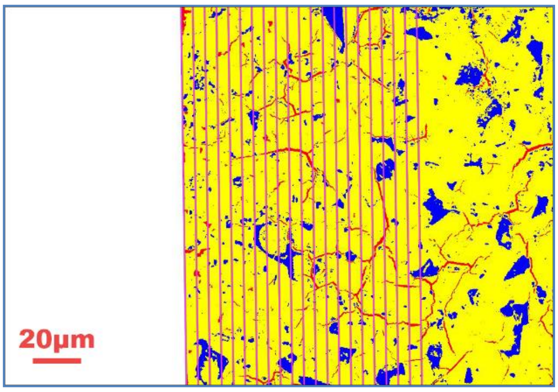

(c) Constituent segmentation

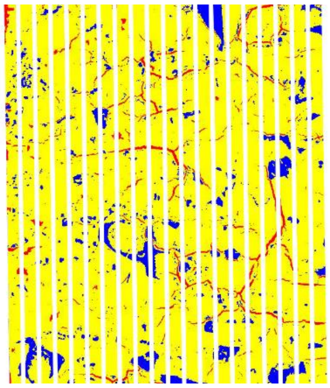

(d) Strips division

Figure 4.3 BSE image processing procedure of ITZ without RGP

Note: Yellow area means hydration products; blue area means unreacted clinkers; red area means pores and cracks.

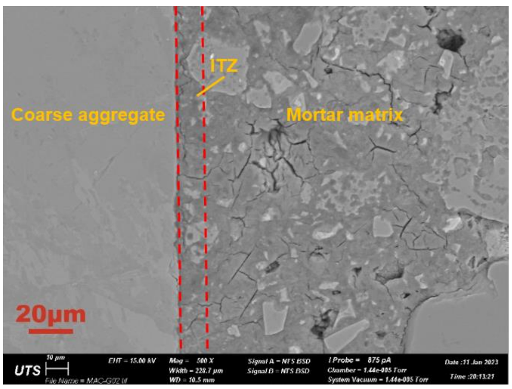

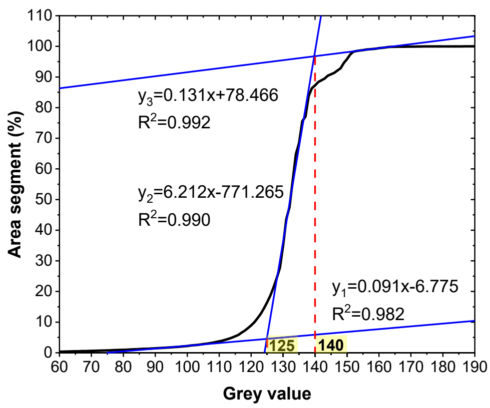

(a) BSE image of ITZ with RGP (b) Grey value threshold determination

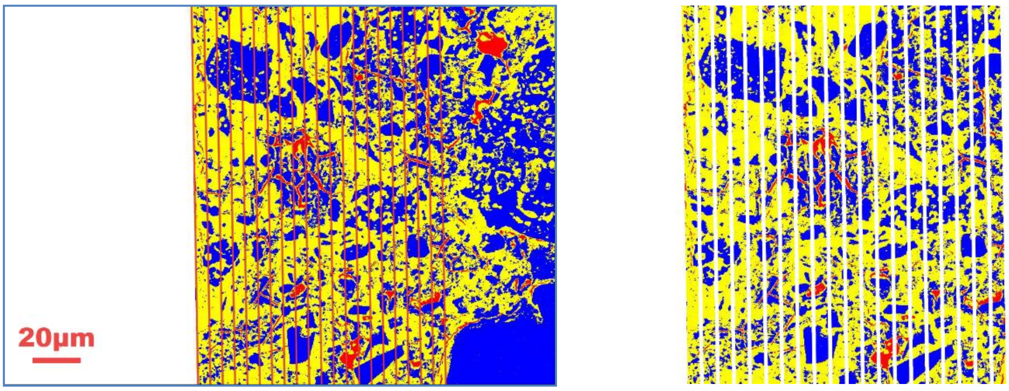

(c) Constituent segmentation (d) Strips division

Figure 4.4 BSE image processing procedure of ITZ with RGP

Note: Yellow area means hydration products; blue area means unreacted clinkers; red area means pores and cracks.

4.4.2 Nanoindentation and nanoscratch

The Agilent G200 Nano Indenter can simultaneously apply normal and lateral forces to a sample. This enables the Indenter to perform nanoindentation and nanoscratch tests, simply by choosing the appropriate tip and testing method. The schematic diagram of nanoindentation and nanoscratch tests is shown in Figure 4.5.

When conducting nanoindentation tests, a Berkovich tip with a radius of 20 nm was installed. Grid nanoindentation combined with statistical analysis was used to reveal the micromechanical properties of the ITZ and its adjacent regions, which contributed to the understanding of the bond strength between aggregate and cement paste in concrete. Concrete is a heterogeneous and multi-phase structure. Although the sample surface was ground and polished during processing, it was still difficult to ensure that the region to be tested had perfect flatness. Therefore, the nanoindentation depth was made enough to avoid the negative influence of sample surface roughness. According to previous experience (Luo, et al. 2021a), the average depth was set to 800 nm to satisfy the test accuracy as well as the number of effective testing points within the ITZs. The loading force was controlled by indentation depth. When the indentation depth was close to 800 nm, the load was maintained for 10 s to eliminate the influence of residual strain. After unloading to 10% of the peak load and maintaining for another 75s, the indenter was completely detached from the sample surface. Five regions avoiding large cracks and fine aggregate were selected for nanoindentation tests of ITZ of both with and without RGP specimens. For each nanoindentation region, as shown in Figure 4.5, 3×5 and 11×5 measuring points were conducted on the granite block and cement paste, respectively. The vertical spacing of the measuring points was 15 μm. The distance between the aggregate boundary and adjacent measuring points was 4 μm. No measuring points were arranged on the aggregate boundary. The lateral spacing of the remaining measuring points was 7 μm. Finally, the elastic modulus and harness within ITZ at different distances from the aggregate boundary can be obtained by load-indentation depth curve (P - indentation load; h - indentation depth; E_r - reduced elastic modulus), characteristics of the tip (E_i - elastic modulus; v_i - Poisson's ratio), characteristics of the sample (E - elastic modulus; v - Poisson's ratio), and projected contact area (A) according to Eqs. (4.1) to (4.3).

$$H = \frac{P_{max}}{A} \tag{4.1}$$

$$S = \frac{dP}{dh}\bigg| h = h_{max} = \frac{2}{\sqrt{\pi}} E_r \sqrt{A} \tag{4.2}$$

$$\frac{1}{E_r} = \frac{1 - v^2}{E} + \frac{1 - v_i^2}{E_i} \tag{4.3}$$

For nanoscratch tests, a hemispherical tip with a radius (r) of 5 μm and apex angle (α) of 60° was adopted to avoid the errors caused by the asymmetry of the Berkovich tip on the test results. Different from nanoindentation, nanoscratch depth (d) was controlled by the normal force. The maximum normal force (F_{Nmax}), scratch speed (v_s) and scratch distance (L) can be defined by the test method according to standards (ASTM G171-03) and previous research results (Li, et al. 2021, Luo, et al. 2022). A moderate maximum normal force can ensure relatively accurate test results while avoiding the interference of aggregate constraints (Li, et al. 2021, Luo, et al. 2022). In this study, the normal force was uniformly increased to 4 mN during the pre-scratch process, and then, the normal force was kept at peak value and 4 μm/s of scratch speed until the scratch distance obtained was 120 μm. Finally, the loading procedure entered the post-scratch stage until the tip left the sample surface. The data acquisition rate was set to 1 point/μm. A total of 20 scratches were randomly conducted along the centre of the ITZ and the matrix 30 μm away from the ITZ, respectively. Regions close to fine aggregate and large cracks were artificially avoided. The scratch hardness (HS_p) and fracture toughness (K_c) of samples were calculated based on Eqs. (4.4) to (4.7). The geometric depth (d_{gt}) and the corresponding scratch width (w_{gt}) were 2500 nm and 5 μm, respectively. The transverse force (F_T) was obtained directly from the test results.

$$HS_p = \frac{8F_{Nmax}}{\pi w^2} \tag{4.4}$$

$$K_c = \frac{2\sqrt{2}F_T}{\pi\sqrt{w^3}} \tag{4.5}$$

$$w = \begin{cases} 2\sqrt{r^2 - (r-d)^2} & d \le d_{gt} \\ w_{gt} + 2\tan\left(\frac{\alpha}{2}\right) \times \left(d - d_{gt}\right) & d > d_{gt} \end{cases} \tag{4.6}$$

$$d_{gt} = r(1 - \sin\left(\frac{\alpha}{2}\right)) \tag{4.7}$$

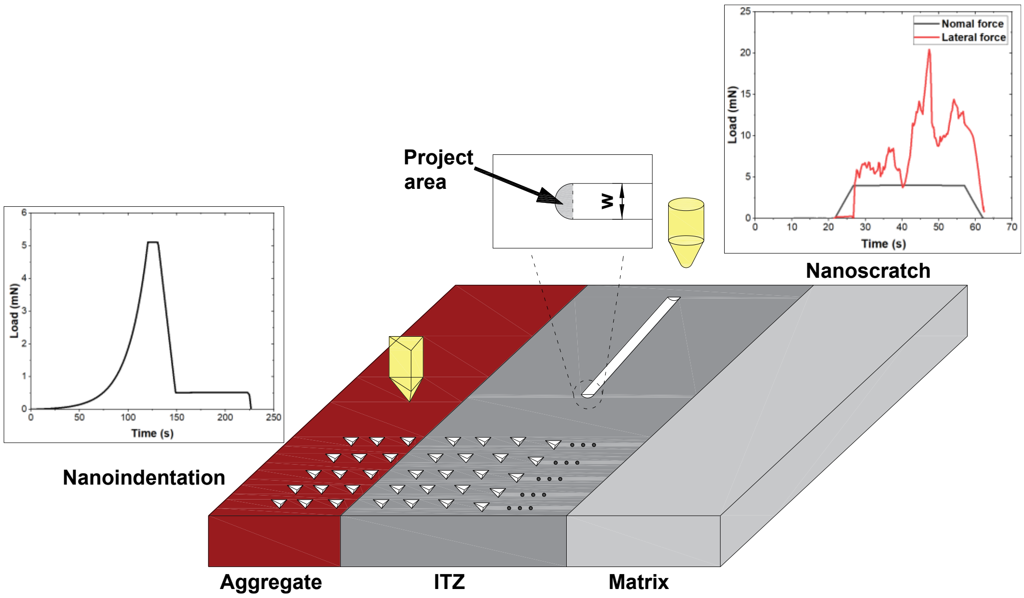

Figure 4.5 Schematic diagram of nanoindentation and nanoscratch

4.4.3 Chemical and mineralogical composition

EDS mapping analysis was used to observe the chemical elements distribution within ITZs and the adjacent regions under the background of BSE images with a magnification of 1500×. During the EDS test, the accelerating voltage and working distance remained at 15 kV and 10 mm, and the probe current was lower than that of the BSE to reduce dead time to a reasonable level. The distributions of Al, Si, Ca, and Na were observed. In addition, the atomic ratio of Si/Ca vs Si/Na was stoichiometrically quantified by a peak to the background (P/B)-ZAF correction and deconvolution of carbon.

XRD patterns of cement mortar with and without RGP were obtained by a Bruker D8 Discover diffractometer. The mineralogical characterisations of the two groups of samples were analysed at a range of 5°-70° 2θ, with a 0.02° step. CuKα radiation of wavelength 1.54 Å was applied to measure diffraction patterns. FTIR spectra of samples with and without RGP were obtained by a Nicolet 6700 FTIR spectrometer. The wavenumber ranged from 4000 to 500 cm^{-1} and a resolution of 8 cm^{-1} was adopted to analyse the contents of portlandite, ettringite, C-S-H gel etc. through chemical bonds.

4.5 Results and discussions

4.5.1 Constituent distribution within ITZs

The statistical results of image analysis in Section 4.4.1 are shown in Figure 4.6. The proportion of hydration products was directly related to unreacted clinkers. That is, when the content of hydration products increased with the distance from the aggregate boundary, the proportion of unreacted particles decreased, and vice versa. The proportion of pores and cracks was the highest near the aggregate boundary and decreased rapidly to a stable value with distance from the modelled aggregate. Due to the ‘wall effect’ on the distribution of clinkers and free water in concrete, the width of ITZ can be determined by the region where the proportion of hydration products and unreacted clinkers changed most significantly (Fang & Zhang 2020). Therefore, the ITZ widths of the modelled samples with and without RGP were approximately 10 μm and 30 μm, respectively. The ITZ and matrix in Figure 4.6 were separated by brown dash lines. The average proportions and corresponding standard deviations of phases in ITZs and the adjacent matrix are listed in Table 4.2. It can be roughly seen from the phase segmentation image in Figs. 4.3 and 4.4 that the content of unreacted clinkers in the sample with RGP was higher than that in the counterpart, and the particle size gradually increased with the distance from the boundary of the granite block. In fact, the statistical results in Table 4.2 show that the ITZ containing RGP possessed a lower proportion of unreacted clinkers and a higher proportion of hydration products compared with the ITZ without RGP, while the trends were opposite for the matrix, and the data dispersion of samples with RGP was larger. This is attributed to the nucleation effect of RGP, which offers additional space and nucleation sites for cement particles to hydrate (Hjorth, et al. 1988, Lothenbach, et al.

2011, Mahmood, et al. 2022). A similar phenomenon was also found in the analysis of the distribution of fly ash and slag clinkers in geopolymer concrete (Fang & Zhang 2020, Luo, et al. 2022). For example, Fang and Zhang (Fang & Zhang 2020) found that the diameter of grains distributed in ITZ was much smaller than that in the mortar matrix. For pores and cracks, the proportion in the ITZ with RGP was slightly higher than that in the sample without RGP, while the proportion in the matrix with RGP was significantly reduced. Part of RGP participated in the pozzolanic reaction to generate more C-S-H gels and filled gaps (Nassar & Soroushian 2012). In addition, the rough and angular surface of RGP provided a site for C-S-H nucleation reaction, which promoted cement hydration, and the rest unreacted RGP can also play the role of filler to improve the pore structure (Du & Tan 2017, Mirzahosseini & Riding 2015).

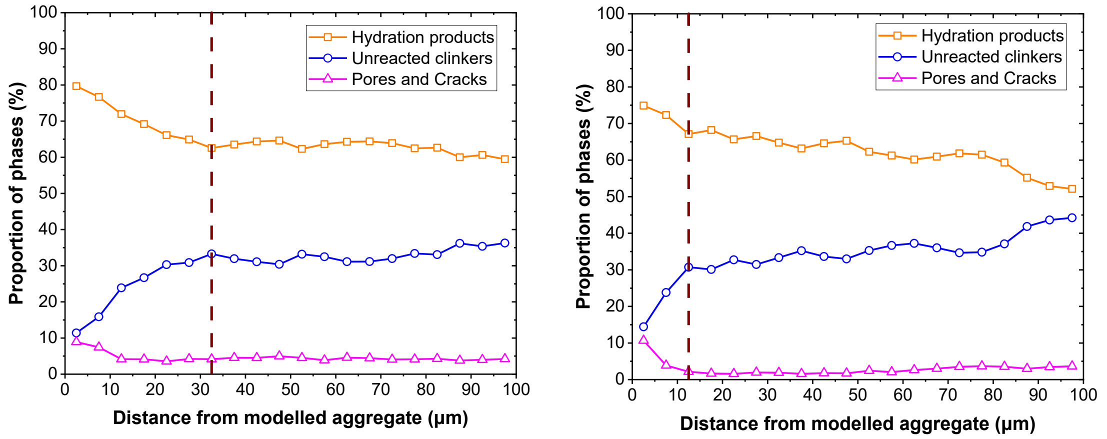

(a) Modelled sample without RGP

(b) Modelled sample with RGP

Figure 4.6 Phase distributions in ITZs and adjacent mortar matrix

Table 4.2 Average proportion of different phases in image analysis

	Hydration products (%)		Unreacted clinkers (%)		Pores and Cracks (%)	
	ITZ	Mortar matrix	ITZ	Mortar matrix	ITZ	Mortar matrix

MAC-C	70.16 ± 5.84	62.80 ± 1.68	24.61 ± 7.58	32.89 ± 1.89	5.23 ± 1.92	4.31 ± 0.32
MAC-G	71.45 ± 3.23	61.52 ± 4.44	22.99 ± 6.68	35.94 ± 3.87	5.56 ± 3.68	2.54 ± 0.79

4.5.2 Elements and mineralogical composition of ITZs

4.5.2.1 EDS analysis

GP cement and soda-lime glass powder were the main cementitious materials in this study. A BSE image was used as background, and the distributions of Al, Si, Ca, and Na are shown in Figure 4.7 by EDS mapping. The region with a relatively uniform distribution of Si and Ca was C-S-H gel. It can be understood that cement hydration in MAC with and without RGP has reached a high level. There were more Al-rich regions in the ITZ without RGP, whereas more Si- and Na-rich regions appeared in the ITZ with RGP. This is because, in the sample containing RGP, there was less cement, but a good amount of partially reacted RGP containing higher concentrations of SiO_2 and Na_2O remained within the ITZ.

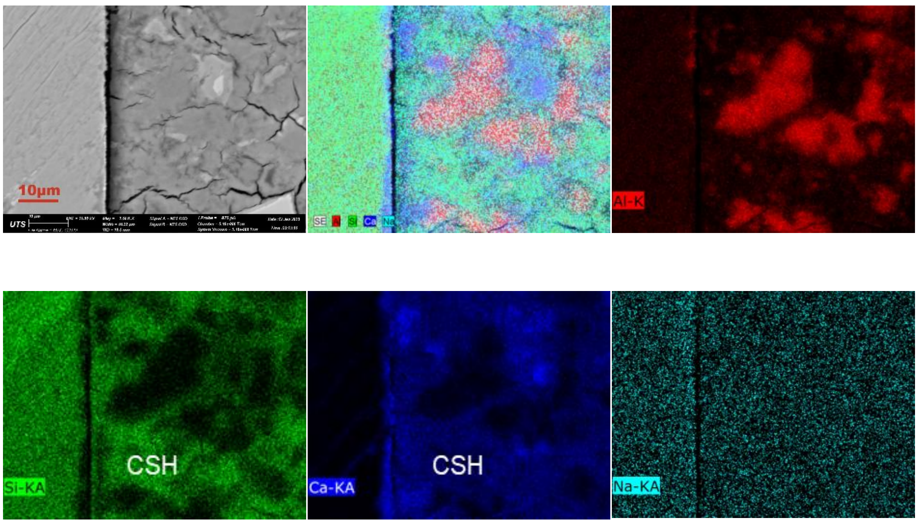

(a) Chemical elements distribution of ITZ without RGP

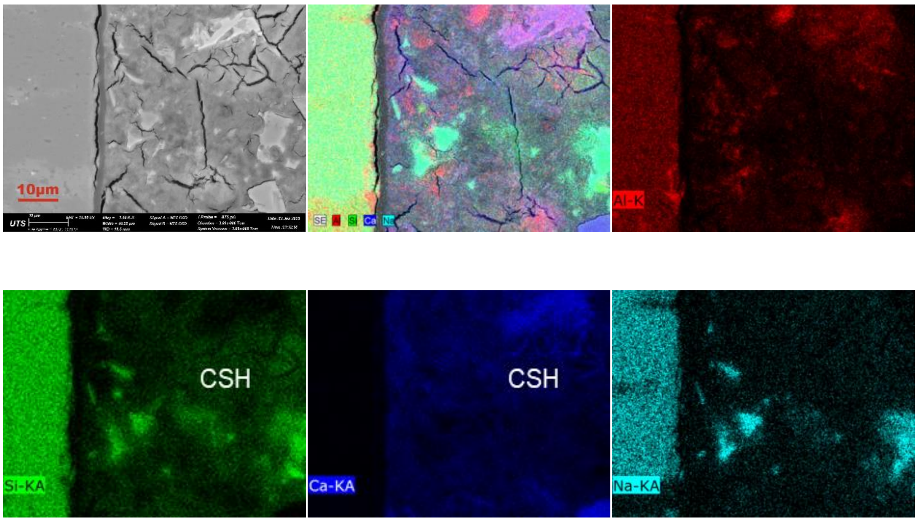

(b) Chemical elements distribution of ITZ with RGP

Figure 4.7 EDS mapping analysis of ITZs

Figure 4.8 depicts the quantitative analysis results based on EDS mapping in random regions of ITZ and matrix. The data cluster area represented C-S-H gel, except some data with Si/Ca and Si/Na close to 0 may refer to pores and cracks. The Si/Ca of C-S-H in the ITZ and matrix without RGP was mainly concentrated around 0.5, while RGP generated more C-S-H gels with Si/Ca in the range of 1-2. It has been known that C-S-H with high Si/Ca had higher cohesion strength (Kunther, et al. 2017). Combining the proportion of hydration products in Table 4.2, it can be reasonably speculated that ITZ exhibited higher performance in samples containing RGP. In addition, the dot where the Si/Ca ratio was close to 7 represented RGP according to the oxide components listed in Table 4.1. As expected, after adding 20% RGP, the number of these dots significantly increased in the ITZ and matrix. However, the existing data with a high Si/Ca ratio in ITZ and matrix without RGP may be due to the interference of silica sand in the samples. It is to be noted that although locations for EDS point mapping were carefully chosen to avoid sand grains in the microstructure, a few might have interfered resulting in outliers with high Si/Ca ratios. In addition, the Si/Na ratio of the ITZ and matrix were lower in the sample with

RGP because the cement was replaced by high-Na glass powder.

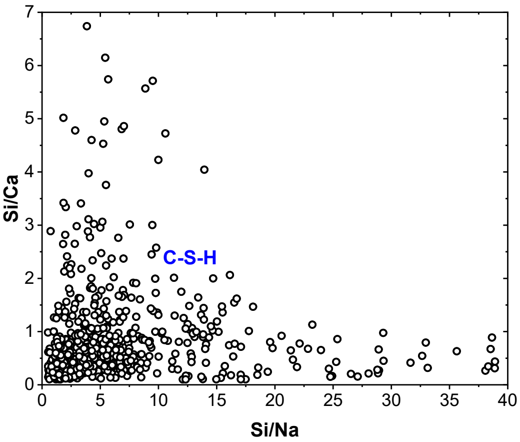

(a) ITZ without RGP

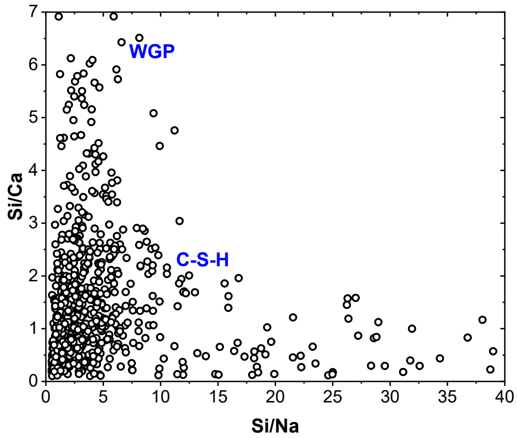

(b) ITZ with RGP

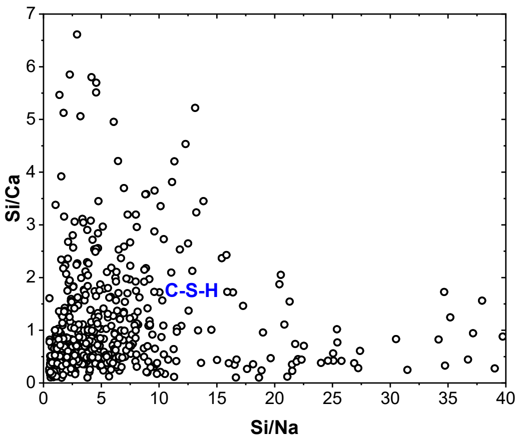

(c) Mortar matrix without RGP

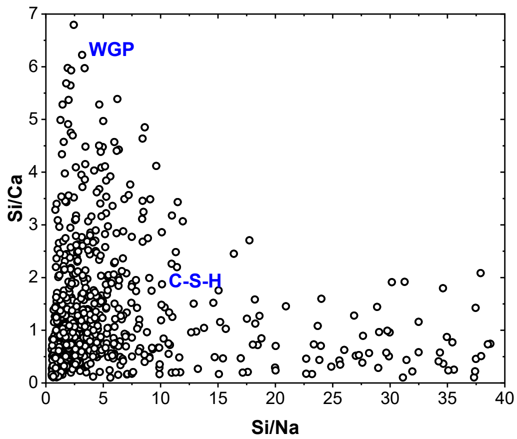

(d) Mortar matrix with RGP

Figure 4.8 Statistical analysis results of EDS mapping

4.5.2.2 XRD analysis

Specific crystals exposure to a beam of incident X-rays can cause diffraction in specific directions. Comparing the diffraction intensities in different directions with the standard powder diffraction data can determine the crystal phases in the material (Qu, et al. 2022). The mortar part of MAC with and without RGP was cut and ground into powder for XRD testing, and the corresponding XRD patterns are shown in Figure 4.9. Because the powder sample contained silica sand, there were much more quartz diffraction peaks in the XRD patterns than previous research on paste samples (Du & Tan 2017, Lu, et al. 2020). The diffraction peaks corresponding to Portlandite appeared at around 18.09°2θ， 34.14°2θ， 47.16°2θ and 50.82°2θ. Comparing the XRD spectra, the content of portlandite in the sample decreased when 20% of cement was substituted by RGP. It has to be admitted that the cement dilution reduced the peak density of portlandite. According to the change of Si/Ca ratio in Figure 4.8 and previous research results (Ismail & Al-Hashmi 2009, Omran & Tagnit-Hamou 2016), the reaction of amorphous silica in RGP with $Ca(OH)_2$ to generate C-S-H was another important reason leading to the decrease of portlandite peaks.

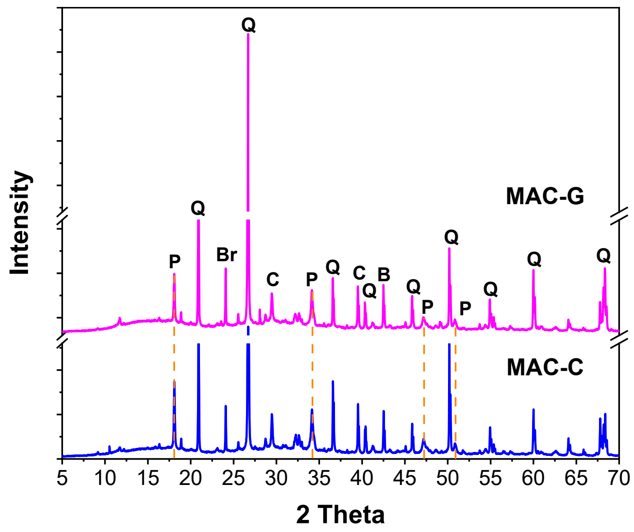

Figure 4.9 XRD patterns of cement mortar with (MAC-G) and without (MAC-C) RGP at age of 3 months

Note: Q-Quartz; P-Portlandite; B-Belite; Br-Brownmillerite; C-Calcite

4.5.2.3 FTIR analysis

Figure 4.10 shows the FTIR spectrum of samples with and without RGP in this study. Band 1 at around 3642 cm^{-1}, typical of the O-H stretching vibrations generated by portlandite ($Ca(OH)_2$) (Lodeiro, et al. 2009, Lu, et al. 2022b), indicates that RGP consumed a certain amount of portlandite to generate C-S-H gel. This is consistent with the above XRD analysis results and the conclusions observed by other researchers through SEM and TGA (Mirzahosseini & Riding 2015, Mostofinejad, et al. 2020, Ye, et al. 2022). The rest bands were mainly concentrated between 1500-500 cm^{-1} and the corresponding band assignments are listed in Table 4.3. To compare the content of components in samples, the FTIR spectra between 1300-700 cm^{-1} were separated into four independent peaks at around 785 cm^{-1}, 869 cm^{-1}, 975 cm^{-1}, 1100 cm^{-1}, with a shoulder at 1180 cm^{-1} by Gaussian mixture models (see Figure 4.11). The frequency values of the peaks and respective area fractions obtained from statistical deconvolution are shown in Table 4.4. The peaks at around 785 cm^{-1} and 975 cm^{-1} were characteristic of the stretching vibrations generated by Si-O bonds in Q^1 and Q^2 (C-S-H), respectively (Garcı´a-Lodeiro, et al. 2008). The area fractions of Q^1 and Q^2 in the cement mortar with RGP increased by 2.06% and 4.19%, respectively, compared with the sample without RGP, indicating that more C-S-H gel was generated after adding RGP. In addition, the Q^2 peak tends to shift toward higher frequencies with the improvement of the Si/Ca ratio due to the progressive depolymerisation of the silicate chains (Lodeiro, et al. 2009). The frequency shifted from 974 cm^{-1} to 980 cm^{-1} when 20% RGP was added to the sample representing more C-S-H with a high Si/Ca ratio was generated (Lodeiro, et al. 2009), which is corresponding to the results in Figure 4.8. The appearance of the peak at frequencies around 1180 cm^{-1} is attributed to silica-rich gel (Lodeiro, et al. 2009). The signal of this peak was stronger in the sample with RGP, suggesting a more condensed microstructure. The peaks at around 869 cm^{-1} and 1100 cm^{-1} corresponded to C-O (CO_3^{2-}) and S-O (mainly for ettringite), respectively (Garcı´a-Lodeiro, et al. 2008). The data in Table 4.4 shows that the area fraction of the peak corresponding to C-O increased by 0.29% in the sample containing RGP, while the figure corresponding to S-O decreased by 7.3% compared to the counterpart. The generation of ettringite and carbonation of cement paste were largely controlled by the content of soluble alkali metal oxides (mainly CaO and Na_2O) (Qu, et al. 2021). A high concentration of Na_2O could increase the pH value of the pore solution. The alkali environment accelerated the carbonisation speed of cement paste and enhance the solubility of ettringite (Qu, et al. 2021). Moreover, ettringite was formed by combining CaO with Al^{2+} and SO_4^{2-} (Li, et al. 2020, Li, et al. 2023c). RGP contained more Na_2O than CaO in Table 4.1. As a result, compared with the sample without RGP, the peak corresponding to C-O was strengthened after adding RGP, while the peak corresponding to S-O weakened.

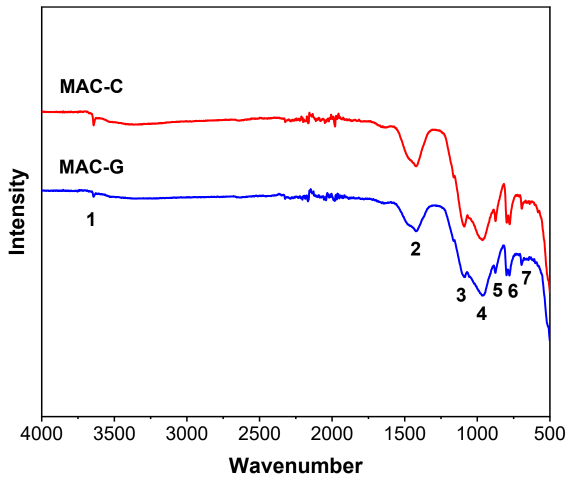

Figure 4.10 FTIR spectra of cement mortar with (MAC-G) and without (MAC-C) RGP at the age of 3 months

Table 4.3 Sample powder with and without RGP assignments

Band	Frequency (cm^{-1})	Assignment
1	3642	*v* OH ($Ca(OH)_2$)
2	1420	v_3 CO (CO_3^{2-})
3	1090	*v* Si-O
4	965	*v* Si-O (C-S-H) Q^2
5	874	v_2 CO (CO_3^{2-})

6	797	v Si-O (C-S-H) Q^1
7	693	v_2 CO (CO_3^{2-})

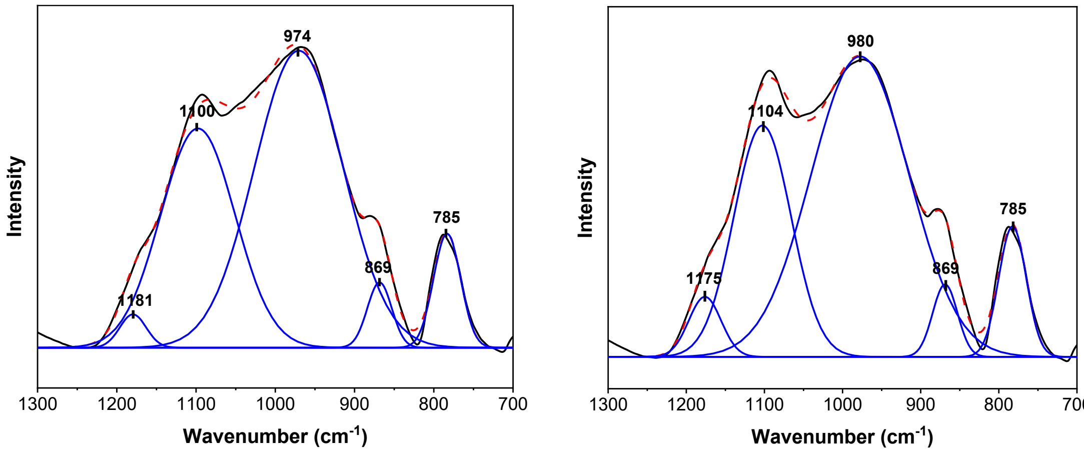

(a) Cement mortar without RGP (b) Cement mortar with RGP

Figure 4.11 Deconvolution spectra of mixtures from 700-1300 cm^{-1}

Table 4.4 Results obtained from the statistical deconvolution of FTIR spectra from 1300-700 cm^{-1}

MAC-C		MAC-G	
Frequency (cm^{-1})	Area (%)	Frequency (cm^{-1})	Area (%)
1181	1.82	1175	3.88
1100	33.79	1104	26.49
974	54.68	980	58.87
869	3.30	869	3.59
785	6.40	785	7.16

4.5.3 Nano/micromechanical properties of ITZs

4.5.3.1 Nanoindentation test results

The elastic modulus of materials can be determined from the slope of the Load vs. Indentation depth unloading curve. The frequency density distribution histograms (FDH) of elastic modulus for ITZ and the adjacent matrix for specimens with and without RGP are shown in Figure 4.12. The results show that the elastic modulus of ITZ and matrix of MAC without RGP followed an approximately normal distribution. The test results of ITZ without RGP were mainly distributed between 5 and 20 GPa, while the elastic modulus in the matrix was slightly higher, distributing between 5 and 23 GPa, which is in line with the traditional concept of the micromechanical difference between ITZ and matrix (Luo, et al. 2018, Luo, et al. 2019). Some recent studies reported an opposite conclusion (Diamond & Huang 2001, Luo, et al. 2021a). There were more CH clinkers in the ITZ, resulting in a slightly higher measured elastic modulus of the ITZ than that of the mortar matrix (Luo, et al. 2021a). However, the test results still approved the conclusion that the ITZ was the weakest part of concrete because the cohesiveness of CH clinkers can be neglected (Luo, et al. 2021a). The curing age of the MAC samples in this study was more than 3 months. Combined with the EDS mapping analysis in Figure 4.7 (a), there was almost no obvious Ca^{2+}-rich area within ITZ, indicating that the cement hydration has reached a relatively high level (Kunther, et al. 2016). Most of the nanoindentation data in Figs. 4.12 (a) and (b) can be regarded as the mechanical properties of gel products. As a result, it can be inferred that the cohesion of C-S-H in the mortar matrix was greater than that in ITZ without RGP which explains why cement composites are prone to fail along the ITZ; better cohesion imparts better strength.

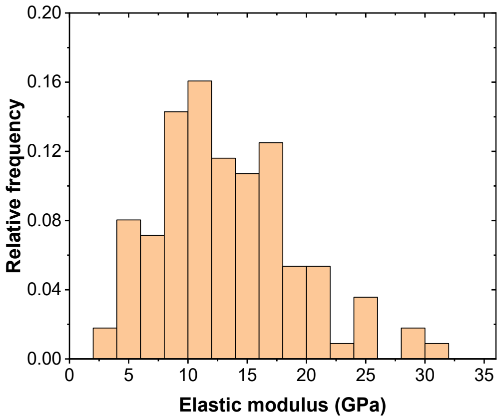

(a) ITZ without RGP

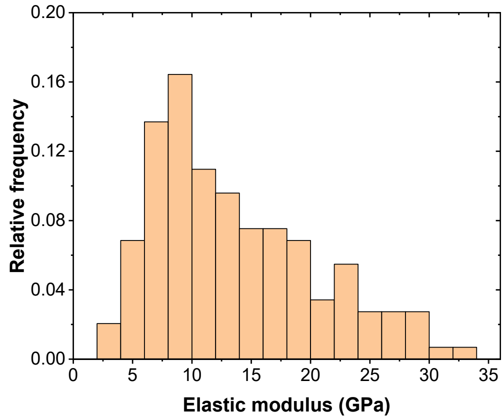

(b) Mortar matrix without RGP

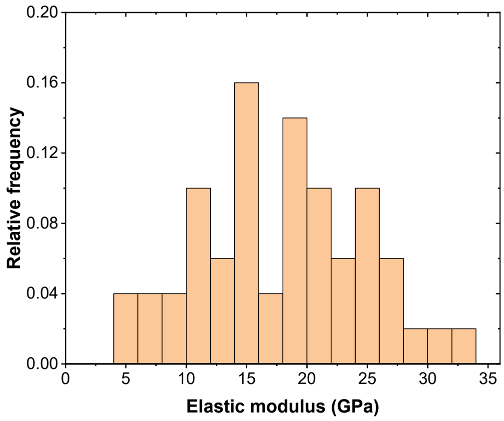

(c) ITZ with RGP

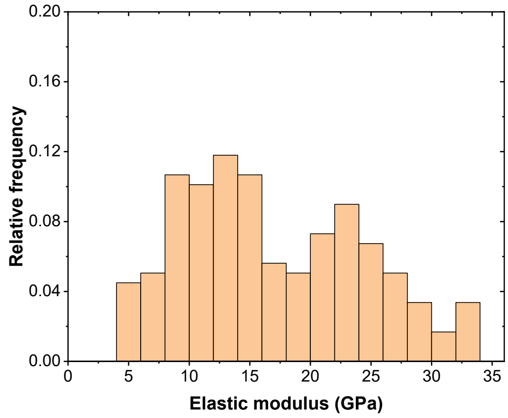

(d) Mortar matrix with RGP

Figure 4.12 Elastic modulus statistical results obtained from nanoindentation tests (Bin size =2 GPa)

It is worth noting that the elastic modulus of ITZ and matrix with RGP were distributed over a wider range and two remarkable peaks appeared. The first peak ranged from 10 GPa to 15 GPa, mainly reflecting the mechanical properties of the C-S-H gel. According to the literature, the elastic modulus of cement paste was generally between 10-20 GPa, while the elastic modulus of glass particles can be as high as 80 GPa (Bosque, et al. 2017, Khedmati, et al. 2019, Khedmati, et al. 2018). The second peaks at 19-27 GPa in Figs. 4.12 (c) and (d) could represent the mixed phase of gel and partially reacted glass particles. It can also be concluded that the heterogeneity of ITZ and matrix with RGP was more significant.

4.5.3.2 Nanoscratch results

Nanoscratch can provide far more test data than nanoindentation in a short operation time. The huge amount of data made it possible to use a very small bin size for frequency density statistical analysis, revealing more phases but not disordering the shape of the histogram (Li, et al. 2021). After trial and error, the bin size was finally determined to be 0.05 GPa. However, the tip radius and the displacement into the surface of the nanoscratch were usually higher than those of nanoindentation, which led to a higher project area than nanoindentation tests. As a result, the nanoscratch results often reflect the mixed results of multiple phases. Nevertheless, most of the test values can still represent the micromechanical properties of C-S-H due to the deliberate avoidance of large pores and aggregate in the test.

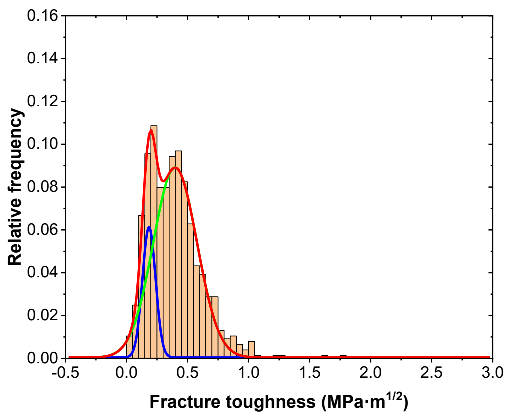

(a) ITZ without RGP

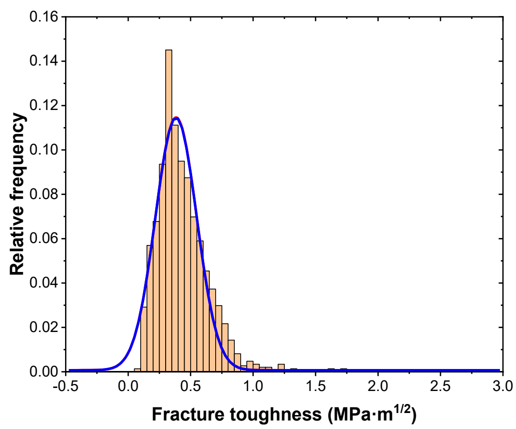

(b) Mortar matrix without RGP

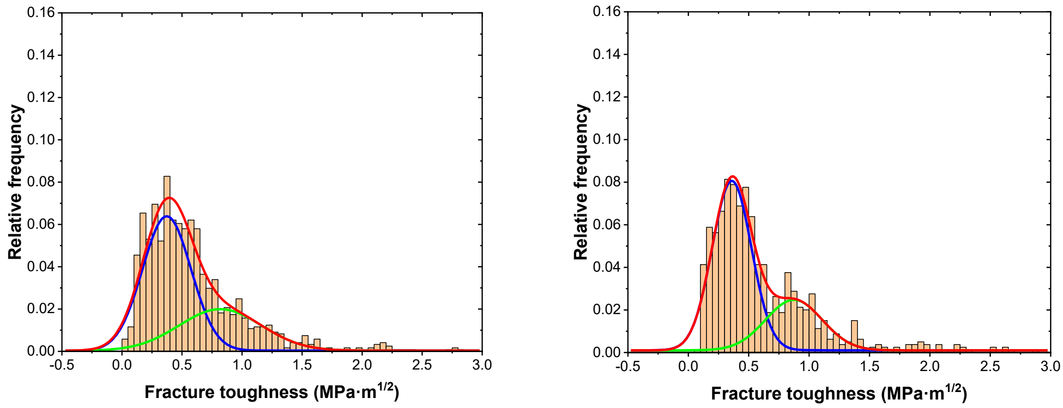

(c) ITZ with RGP (d) Mortar matrix with RGP

Figure 4.13 Fracture toughness statistical results and deconvolution analysis obtained from nanoscratch (Bin size=0.05 GPa)

Figure 4.13 shows the FDH of fracture toughness of ITZ and matrix with and without RGP obtained from nanoscratch tests. Fracture toughness quantitatively evaluates the ability of a material with natural defects to resist rapid and unlimited crack propagation (Yan, et al. 2022). The FDH of fracture toughness of ITZ without RGP can be separated into two components by the Gaussian mixture model. The expected values of fracture toughness for these two components were 0.18 MPa·m$^{1/2}$ and 0.39 MPa·m$^{1/2}$, which could be regarded as low-density C-S-H and high-density C-S-H, respectively. In contrast, there was only one independent peak in the mortar matrix without RGP. The expected value of fracture toughness of this component was 0.40 MPa·m$^{1/2}$, indicating that the gel phase in the matrix without RGP was mainly composed of high-density C-S-H with better homogeneity and cohesion strength, compared with weaker C-S-H gel structure in the ITZ. For ITZ and mortar matrix with RGP, the FDH of fracture toughness can be segmented into an independent peak with a shoulder. It can be seen from deconvolution analysis that the standard deviation of fracture toughness of ITZ and matrix with RGP was higher than their counterparts, indicated by shorter and wider distribution curves. The expected value of the peak was around 0.37 MPa·m$^{1/2}$. It can be explained that the RGP promoted the formation of C-S-H with a high Si/Ca ratio, improving the density of the ITZ and matrix, that is, the sample containing 20% RGP had more high-density C-S-H. The explanation of the shoulder with the expected value of 0.86 MPa·m$^{1/2}$ can refer to the second peak in Figs. 4.12 (c) and (d), which is the mixed phase of C-S-H and incompletely reacted RGP.

4.5.3.3 Comparison of nanoindentation and nanoscratch results

Figure 4.14 compared the nanoscratch hardness and nanoindentation hardness of samples with and without RGP. Because of the huge amount of data, the nanoscratch hardness of samples still followed an approximate normal distribution even if a very small bin size was adopted in histograms. In contrast, the nanoindentation hardness data was more discrete, and there were gaps between some values. Nevertheless, for samples without RGP, the main data of nanoindentation hardness and nanoscratch hardness can still achieve good concordance. By observing Figs. 4.14 (a) and (b), it can be reasonably identified that the hardness of ITZ and matrix without RGP ranged from 0.125 GPa to 0.375 GPa. In comparison, when 20% RGP was added to the sample, the hardness of ITZ and matrix was distributed in a wider range, which is similar to elastic modulus in Figure 4.12 and fracture toughness in Figure 4.13. In the test results of nanoscratch, the value of the first two bars of the sample with RGP was higher than that of the sample without RGP. This is due to the presence of softer C-S-H gel within the sample containing RGP although the microstructure was denser, and the unreasonable data corresponding to the large pores and cracks in the ITZ and matrix without RGP were removed in the statistical analysis. Therefore, there were more low-hardness constituents (≤ 0.1 GPa) in the nanoscratch test results of ITZ and matrix with RGP. It is worth noting that the nanoindentation hardness of ITZ and matrix with RGP was slightly higher than the nanoscratch hardness. As mentioned before, the project area of nanoindentation was much smaller than that of nanoscratch, which means nanoindentation could measure the micromechanical properties of some individual phases, such as CH or glass particles. The nanoscratch hardness was determined according to the scratch depth of the tip under a certain normal load (Rayóna, et al. 2018). The difference in test methods made it difficult for the nanoscratch to accurately reflect the hardness of glass particles. For example, when a hemispherical tip touched a small glass particle during scratching, the tip may push it aside rather than swipe directly across the glass. In this condition, the hardness of the combined phase of glass and the surrounding C-S-H would be mistaken for the hardness of the glass particles. As a result, the concordance between nanoscratch hardness and nanoindentation hardness was poor in samples containing RGP. In general, nanoindentation is likely to reflect the real micromechanical properties of materials, but this is based on a large amount of test time to produce massive test data, otherwise, it is difficult to observe the right frequency density distribution of mechanical properties (Luo, et al. 2018). For materials with high homogeneity, nanoscratch is an ideal technique which can not only ensure the accuracy of test results but also greatly shorten test time (Yin, et al. 2022).

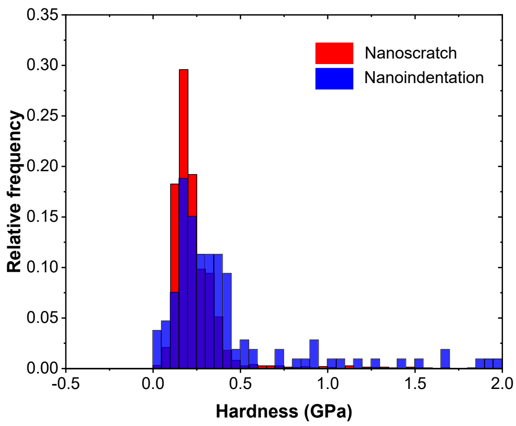

(a) ITZ without RGP

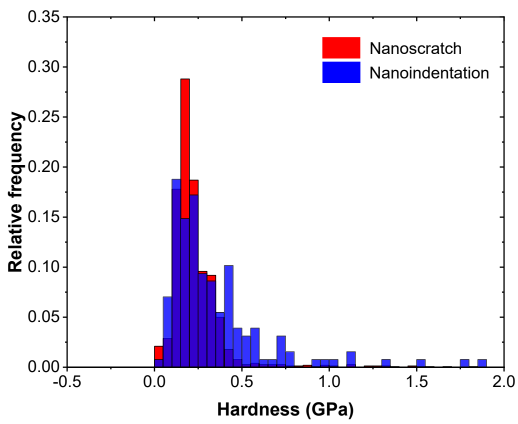

(b) Mortar matrix without RGP

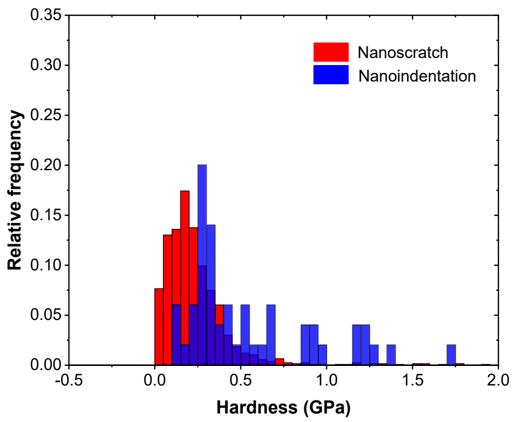

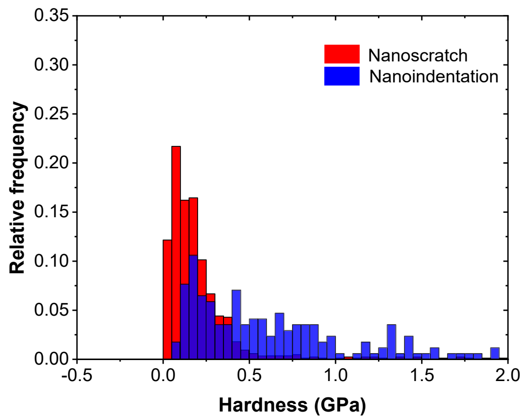

(c) ITZ with RGP (d) Mortar matrix with RGP

Figure 4.14 Comparison of nanoindentation and nanoscratch results (Bin size=0.05 GPa)

4.6 Conclusions

In this part, two groups of MAC samples were prepared to replicate concrete in a simplified manner to avoid the complexities of ITZs in large-scale concrete and improve accuracy in investigating the ITZ. Instead of increasingly scarce conventional SCMs, RGP was used to replace 20% of cement in the sample. The performance of RGP in the ITZ and the adjacent mortar matrix was observed from multiple aspects. The test results obtained from microcharacterization and nanoindentation/ nanoscratch were compared and discussed by image analysis or statistical methods. The critical findings can be listed as follows:

(1) The 20% RGP can greatly reduce the width of ITZ from 30 μm to 10 μm, featured by the reduction of unreacted cement particles and the increase of hydration products. By contrast, the matrix with RGP had more unhydrated cement particles and fewer hydration products. However, the proportion of pores and cracks was greatly reduced in the ITZ and mortar matrix containing RGP, because the RGP participated in the

pozzolanic reaction to generate more C-S-H gels, and the unreacted RGP played a role in physically filling pores.

(2) The cement hydration can be evaluated according to the uniform distribution of Ca and Si elements in EDS mapping. Moreover, the unreacted RGP can also be captured through the distribution of Si and Na elements. In the ITZs without RGP, the Si/Ca ratio of C-S-H was around 0.5. However, when 20% of cement was replaced by RGP, the proportion of C-S-H with a Si/Ca ratio ranging from 1 to 2 was significantly improved, representing a higher cohesion strength.

(3) XRD and FTIR results show that the RGP consumed the CH and generated additional C-S-H gels. In addition, the deconvolution results of the FTIR spectrum between 700 cm^{-1} and 1300 cm^{-1} indicate that the high content of soluble alkali metal oxides in the RGP improved the pH of the pore water, which accelerated the carbonisation speed of cement paste and slowed down the formation rate of ettringite.

(4) The elastic modulus of ITZ and mortar matrix without RGP were between 5-20 GPa and 5-23 GPa, respectively, and the frequency density distribution roughly presents a standard normal distribution. However, two relatively independent components appeared between 10-20 GPa and 19-27 GPa in elastic modulus FDH of ITZ and mortar matrix containing RGP, implying the C-S-H gel and mixed phase of C-S-H and unhydrated or partially hydrated RGP, respectively. The data volume of the nanoscratch was higher than nanoindentation. Low-density C-S-H and high-density C-S-H were found in fracture toughness FDH of ITZ without RGP by deconvolution analysis. In contrast, the distribution of C-S-H in the mortar matrix without RGP was uniform. The ITZ and mortar matrix with RGP can also be separated into two components according to the fracture toughness FDH: C-S-H and mixed phase of C-S-H and RGP.

(5) In the comparative analysis of nanoindentation hardness and nanoscratch hardness, nanoindentation results of ITZ and mortar matrix without RGP were consistent with the nanoscratch ones. However, the nanoindentation hardness of ITZs and mortar matrix with RGP was slightly higher than nanoscratch one because the scratch area of the nanoscratch was much higher than that of nanoindentation. Therefore, nanoscratch is more likely to reflect the mixed nano/micromechanical properties of multiple phases. For materials with high homogeneity, nanoscratch can greatly improve testing efficiency. However, for extremely inhomogeneous materials, the accuracy of nanoindentation was higher based on enough indents.

CHAPTER 5. NANOCHARACTERIZATION ON ITZS OF RAC WITH RGP

5.1 Introduction

Researchers have attempted to recycle crushed waste concrete and glass powder as substitutes for NCA and cement, respectively (Li, et al. 2023b, Tang, et al. 2019, Tang, et al. 2020b). Existing research results indicate that the old mortar on the surface of recycled coarse aggregate (RCA) is responsible for the weak bond strength with the new mortar matrix, resulting in lower mechanical and durable properties of RAC (Cabrera-Covarrubias, et al. 2021, Hu, et al. 2019).

RAC possesses more ITZs than NAC, among which, researchers mostly focus on the old ITZ adjacent to NCA and the new ITZ between the old mortar on the RCA and the new mortar (Silva, et al. 2023, Tang, et al. 2020d). Numerous existing instrumentation techniques such as SEM-based characterisation and nanoindentation provide a realistic basis for the determination of ITZ width and understanding its characteristics from multiple dimensions (Luo, et al. 2018).

Chapter 4 has demonstrated that RGP is contributed to modify microstructure and micromechanical properties of ITZs in NAC. In this chapter, modelled recycled aggregate concrete (MRAC) samples were manufactured. The use of model aggregates can alleviate the non-uniformity caused by the sharp edges and corners of the aggregate surface. This helps nanoindentation and image analysis techniques obtain more stable test data, although ignoring the interference of angular surface of NCA. The feasibility of modelled concrete for studying ITZ characteristics within RAC has been fully verified in previous studies (Luo, et al. 2021, Zhan, et al. 2020). The 20% of WGP was added to the new mortar compared with the pure cement-based new mortar. Instrument techniques combined with image analysis and statistical knowledge were used to explore the performance of old and new ITZs in MRAC from different perspectives.

5.2 Materials and mixture proportion

A MRAC sample consists of three parts: a rectangular granite block, old mortar on the surface of the stone block, and new mortar on the outermost layer of the sample. The schematic diagram of MRAC is shown in Figure 5.1. Rectangular granite blocks were seen as virgin coarse aggregate. Fine aggregate in the old and new mortar was silica sand with a fineness modulus of 1.9. General purpose Portland cement was used as the main cementitious material. In the MRAC sample with RGP, 20% of cement in the new mortar was replaced by milled waste soda-lime glass powder with average particle size of 50 μm. The particle size distribution and oxide composition of cement and RGP is shown in Figure 5.2. and Table 5.1, respectively. Considering that the interface between old and new mortar may be difficult to distinguish under an electron microscope, different water-cement ratios were designed in the preparation of new and old mortar. According to previous studies, the strength of RAC is normally lower than that of NAC under the same conditions (Lei, et al. 2018). Civil engineers usually reduce water-cement ratio of new mortar or choose cement with higher strength grade to ensure that the RAC structures meet the strength requirements (Tang, et al. 2020c). Therefore, the water-cement ratios of old and new mortars in this study were designed to be 0.45 and 0.4, respectively. The detailed mix proportion of new and old mortar is shown in Table 5.2.

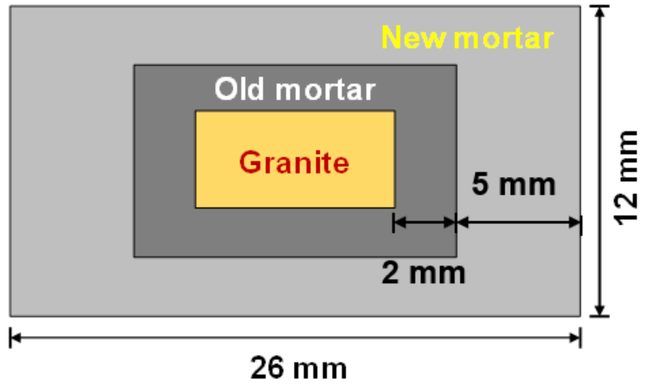

Figure 5.1 Schematic diagram of modelled recycled aggregate concrete

Table 5.1 Oxide composition of cement and RGP measured by X-ray fluorescence

Composition (%)	CaO	SiO_2	Al_2O_3	SO_3	Fe_2O_3	MgO	K_2O	Na_2O	LOI
Cement	64.9	18.6	4.1	3.0	3.1	1.6	0.5	-	4.2
RGP	10.8	68.4	0.9	0.1	0.4	1.8	0.3	13.5	3.8

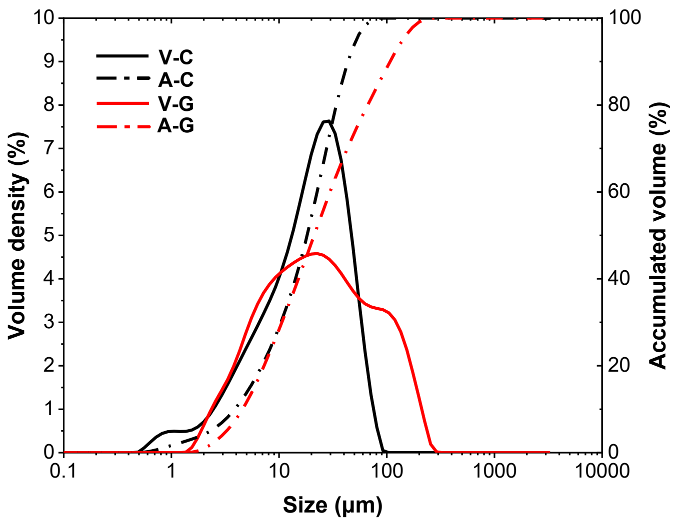

Figure 5.2 Particle size distribution of cementitious materials tested by Mastersizer 3000

Note: ‘V-C’ and ‘V-G’ represent volume density of cement and RGP respectively; ‘A-C’ and ‘A-G’ represent accumulated volume of cement and RGP respectively.

Table 5.2 Mix proportions of MRAC

Mix ID	Phases	Cement (g)	Glass (g)	Sand (g)	Water (g)	Granite
MRAC-C	Old mortar	100	0	150	45	1
	New mortar	100	0	150	40	
MRAC-G	Old mortar	100	0	150	45	1
	New mortar	80	20	150	40	

5.3 Sample preparation

According to previous experience (Li, et al. 2021, Luo, et al. 2021a, Luo, et al. 2022), the main steps of MRAC sample preparation were designed and shown in Figure 5.3. Granite gravels with appropriate size were selected and ground on 320 grits abrasive papers into 13 mm × 13 mm × 8 mm rectangular blocks. Then, the surface of the granite blocks was smoothed by 600, 800 and 1200 grits abrasive papers with each grade lasting for 15 min. 0.3 μm and 0.05 μm alumina slurry were used to polish granite blocks under a small force, and the polish process lasted for 1 hour. After grinding and polishing, granite blocks were cleaned in an ultrasonic bath for 3 min to remove alumina particles on the surface of samples. The processed granite blocks are called modelled NCA. According to the mix proportion in Table 5.2, the saturated surface-dried modelled NCA were covered with old mortar in Φ25 mm cylindrical moulds, and discharged air bubbles in the mortar by tapping. After curing in the mould for one day, samples were put in a moist environment at 23 ±

3 ℃ for 28 days. Grinding and polishing were consistent with the above-mentioned processes of modelled NCA. Then, new mortar with/without RGP was prepared and covered around the modelled RCA. After 28 days, the MRAC with old and new mortar was ground and put in Φ35 mm cylindrical moulds and poured with epoxy resin. After one day, samples were wet-cut by a low-speed diamond saw under the protection of hardened epoxy resin to expose old and new ITZs into the air. Finally, samples were coated with an additional layer of epoxy resin. The surface waiting for observation was ground and polished. It should be noted that to avoid the height difference between the aggregate and mortar caused by excessive polishing, the entire polishing time was reduced to 30 min (Lyu, et al. 2019a). Photos of MRAC manufacturing process are presented in Figure 5.4. The modelled samples were used for Backscattered electron-Energy dispersive spectrometer (BSE-EDS) tests and nanoindentation. After that, the new mortar was cut out and ground into powder for Thermogravimetric-derivative thermogravimetry (TG-DTG) and Nuclear magnetic resonance spectrometer (^{29}Si NMR) tests.

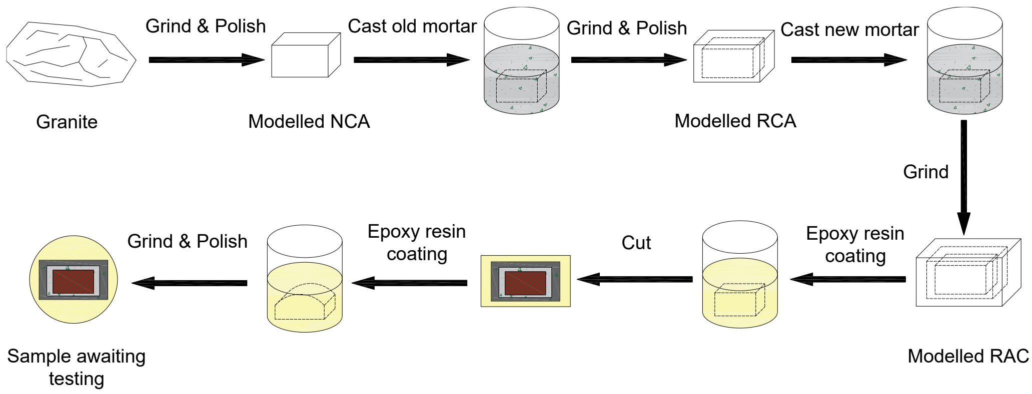

Figure 5.3 Preparation schematic of modelled recycled aggregate concrete

(a) Casting mortar

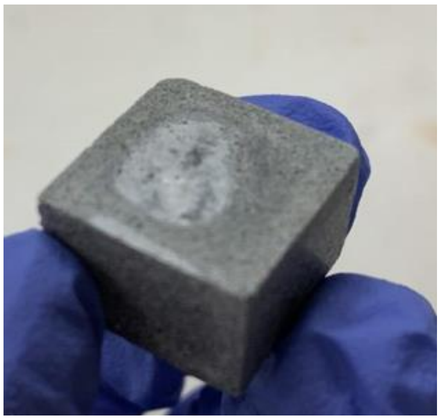

(b) Modelled RAC after surface polishing

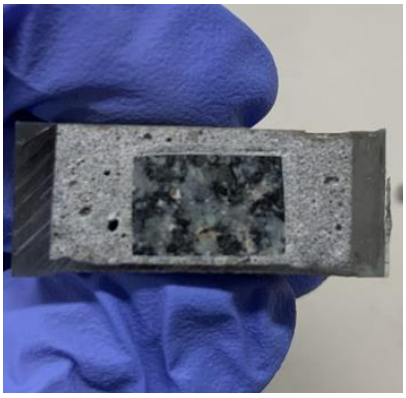

(c) Cutting modelled sample with epoxy resin

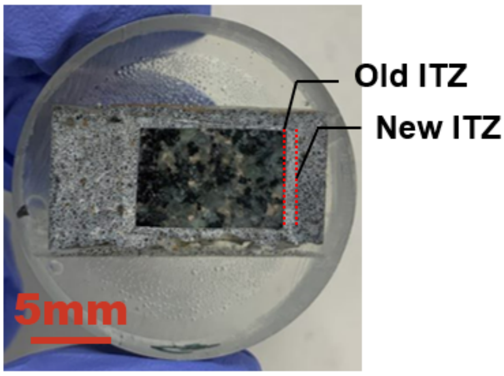

(d) modelled sample after grinding and polishing

Figure 5.4 Preparation of modelled recycled aggregate concrete

5.4 Experimental methods

5.4.1 BSE-EDS tests

A scanning electron microscope (SEM, Zeiss EVO LS15) equipped with a BSE image detector was used to randomly extract images of ITZs. The accelerating voltage and working distance were set as 15 kV and 10 mm respectively. For each ITZ, 30 BSE images at 500 × magnification were used to statistically analyse the volume fraction of constituents (Luo, et al. 2021a, Lyu, et al. 2019a). The brightness and contrast of BSE images of each ITZ were kept consistent to reduce the workload of image analysis. EDS data were acquired at accelerating voltage consistent with BSE and lower probe current. EDS mapping was used to show phase distribution. In addition, stoichiometric quantification with P/B-ZAF on Si, Ca and Na was conducted to deeply analyse the element ratio within ITZs and adjacent mortar matrix.

5.4.2 TG-DTG tests

TG tests were conducted by NETZSCH STA 449 F3 Jupiter. 20-30 mg sample powder was weighed in an alumina crucible, and then kept in a 40 °C/N_2 environment. After maintaining this environment for 30 min, the temperature in the furnace was heated to 1000 °C at a speed of 10 °C/min, and the mass loss of the sample powder between 50-1000 °C was obtained. The TG curves were derived to highlight the relative content differences of C-S-H, Portlandite and Calcite in different groups of samples.

5.4.3 ^{29}Si NMR tests

Agilent 500 MHz Nuclear Magnetic Resonance (NMR) was used to acquire solid-state ^{29}Si spectra from -50 to -150 ppm. The measurements were conducted in a 4 mm rotor at 71.4 kHz spinning rate and 30 s relaxation delays. The statistical deconvolution of ^{29}Si NMR spectra based on the Gaussian model was applied to obtain Q^0-Q^2 for unhydrated cement clinkers and C-S-H gel content analysis.

5.4.4 Nanoindentation

Nanoindentation tests on ITZs were carried out by an Agilent G200 Nano Indenter. Due to the heterogeneous structure of cement-based materials, it may be difficult to obtain accurate micromechanical properties of ITZ under shallow indentation tests (Luo, et al.

2021a). If the indentation depth is too deep, the indentation area of a single point would be too large to ensure that enough indentation points are conducted within ITZs. Comprehensively comparing the previous research data and according to the requirements in ASTM E384-17 (Standard test method for microindentation hardness of materials), the indentation depth of each testing point was set to 800 nm (Luo, et al. 2021a). The vertical spacing of testing points was 15 μm. The horizontal spacing of the testing points near the boundary between aggregate and ITZ was 8 μm, and the horizontal spacing between the remaining testing points was 7 μm. No testing points were designed at the boundary to avoid the interference of sudden change of hardness on the results.

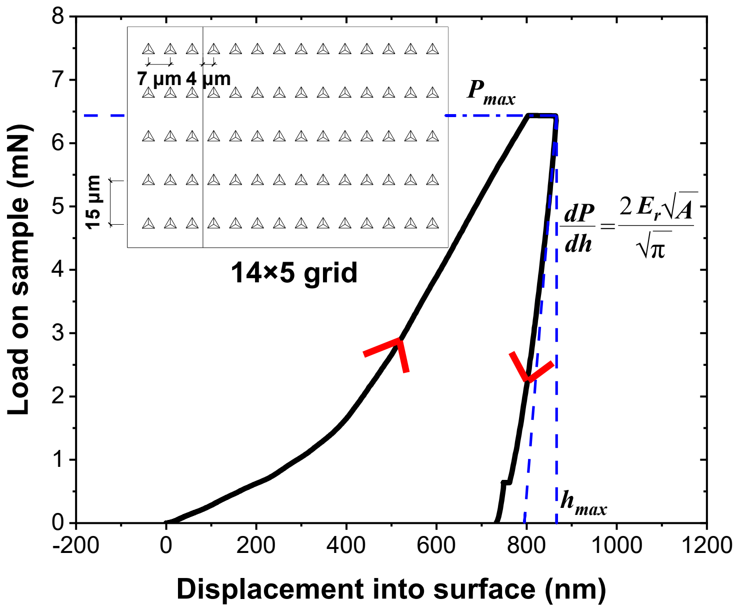

Figure 5.5 Grid nanoindentation and a typical indentation load-depth curve

The layout of the testing points and a typical depth-load curve on old ITZ are shown in Figure 5.5. The nanoindentation depth-load curve was not deformed, indicating that the flatness of the sample after polishing meets the test requirements of nanoindentation. Five of these 14×5 grid nanoindentation tests were performed for each ITZ (Luo, et al. 2021a). The nanoindentation force loading procedure was based on the depth control method.

When the indentation depth was close to 800 nm, the load was sustained at the peak value for 10 s, and then gradually unloaded to 10% of the peak load after reaching the target depth. The elastic modulus and hardness of ITZs can be calculated by indentation load (*P*), indentation depth (*h*), reduced elastic modulus (E_r), projected area (*A*) and characteristics of the diamond indenter tip (elastic modulus, E_i and Poisson's ratio, V_i) according to Eqs. (5.1) to (5.3) adopted by previous researchers (Oliver & Pharr 1992, Xiao, et al. 2013c). The Poisson's ratio of cement paste (*v*) was set as 0.2. This study focused on the cohesion strength of ITZ, so the test avoided regions close to fine aggregate and large cracks. The test results of each column were averaged as the final results.

$$H = \frac{P_{max}}{A} \tag{5.1}$$

$$S = \left.\frac{dP}{dh}\right|_{h=h_{max}} = \frac{2}{\sqrt{\pi}} E_r \sqrt{A} \tag{5.2}$$

$$\frac{1}{E_r} = \frac{1 - v^2}{E} + \frac{1 - v_i^2}{E_i} \tag{5.3}$$

5.5 Results and analysis

5.5.1 Phases distribution of ITZs

Figure 5.6 shows typical BSE images of three ITZs in this study. Compared with common SEM images, BSE is easier to distinguish between phases in cement-based materials according to grey value, even though the resolution of BSE image may be lower than SEM images (Kim, et al. 2019). Many researchers have adopted BSE images combined with image analysis techniques to investigate the constituent distribution in ITZs (Kim, et al. 2019, Lyu, et al. 2019b, Scrivener 2004).

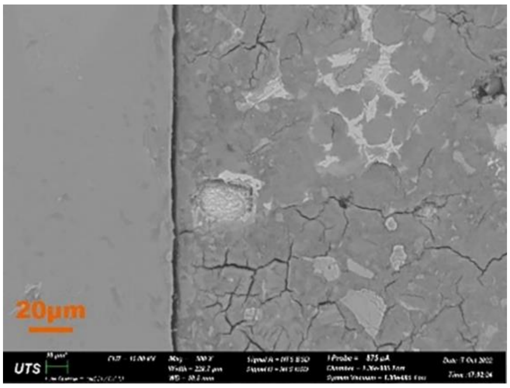

(a) Old ITZ

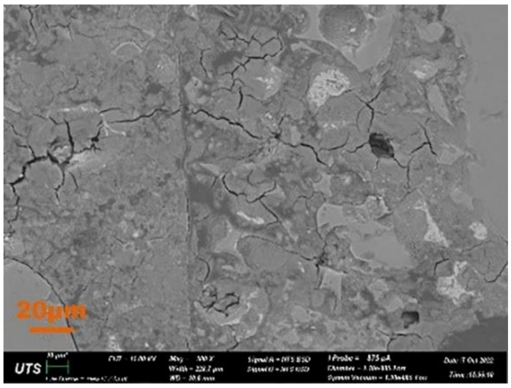

(b) New ITZ without RGP

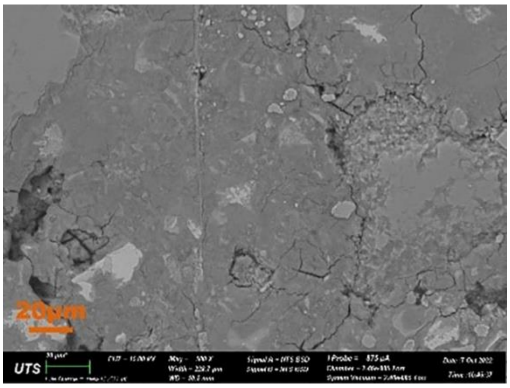

(C) New ITZ with RGP

Figure 5.6 BSE images of old and new modelled ITZs

Taking the old ITZ as an example, Figure 5.7 shows the schematic view of BSE image processing for statistical analysis. The boundary between the aggregate and the matrix can be easily captured manually and the aggregate part can be removed by Photoshop. For the remaining mortar matrix region, the image analysis software, Image Pro was used to acquire its grey value-area segmentation curve. Wong's grey value segmentation method was adopted (Wong & Buenfeld 2006, 2009, Wong, et al. 2006). The grey value threshold and different phases can be identified by the intersection between the two liner fittings at the inflection of the cumulative area curve with grey values, as shown in Figure 5.7 (b). However, it must be noted that Wong et al. declared that this method may slightly overestimate the actual grey threshold (Wong, et al. 2006). Therefore, in this study, Wong's method was used to roughly identify the grey threshold. The grey range and segmentation of each phase were finally determined by manual adjustment (Li, et al. 2021, Wong & Buenfeld 2006, Wong, et al. 2006). The image after phase segmentation is shown in Figure 5.7 (c) (red represents pores and cracks; green represents reaction products; blue represents unreacted products). The matrix within 100 μm from the aggregate boundary was continuously divided into 20 strips with a width of 5 μm. For each ITZ, 30 BSE images were selected for statistical analysis of phase volume fraction within ITZ and a part of the mortar matrix.

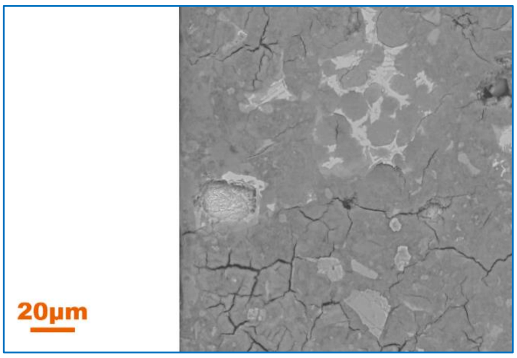

(a) Aggregate region removal

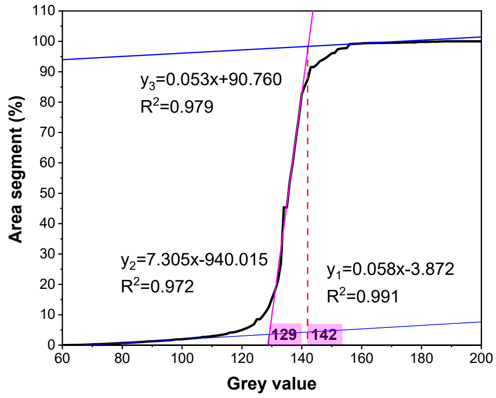

(b) Grey threshold determination

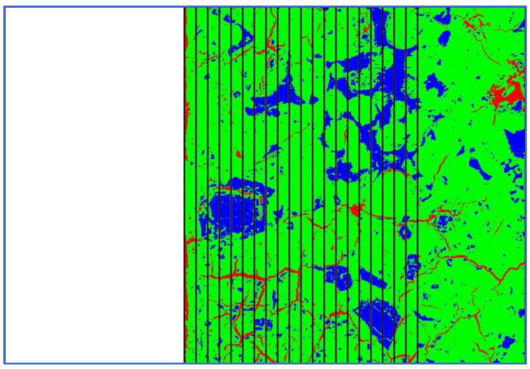

(c) Phases segmentation

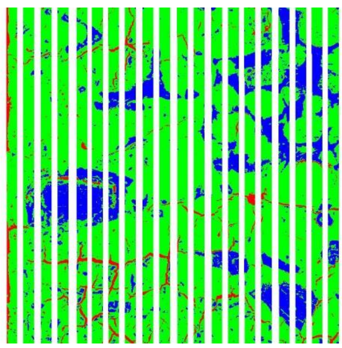

(d) Strips division

Figure 5.7 Schematic view of BSE image processing

The volume fractions of unreacted products, reaction products and pores/cracks are shown in Figure 5.8 as stacked area graphs. The ‘wall effect’ can be clearly detected by observing the volume fraction change of unreacted products from the aggregate surface to mortar matrix. The content of unreacted products in the region close to the aggregate surface was lower and the percentage gradually improved to a stable value with the increase of distance to the aggregate surface. Compared to pores and cracks, reaction and unreacted product contents have a lower variability degree at different positions (Fang & Zhang 2020). As a result, the ITZ width can be determined according to the volume fraction of unreacted products (Fang & Zhang 2020, Luo, et al. 2021a). Taking the middle of the strips as the coordinate points, the region where the content of unreacted products increased significantly was identified as ITZ. Therefore, the widths of old ITZ, new ITZ with and without RGP were 52.5, 37.5 and 22.5 μm, respectively. The width of the new ITZ without RGP was narrower than the old ITZ, probably because the lower water-cement ratio designed in the new mortar improved the properties of the matrix (Xiao, et al. 2013c). Comparing the volume fractions of reaction and unreacted products in ITZ, it is seen that the content of unreacted products in the new ITZ without RGP was 11.98%, lower than 14.60% of the old ITZ. However, the volume fractions of reaction products were similar, both around 80.5%, because of the higher proportion of pores and cracks (7.29%) within the new ITZ without RGP than about 4.33% of the old ITZ. The surface of old mortar was looser and more porous than natural granite aggregate, and it was difficult to form a dense bonding between old and new mortar (Thomas, et al. 2018). In comparison, the width, unreacted products, and void volume fractions in new ITZ containing RGP were significantly reduced to 22.5 μm, 10.27% and 4.30% respectively. Correspondingly, the proportion of reaction products increased to 85.43%, indicating that RGP can effectively reduce the volume of ITZ in RAC and improve the bonding performance between new mortar and RCA surface. By observing the volume fraction of pores and cracks in three ITZs, the volume fraction close to the aggregate surface was obviously higher than in other regions and decreased rapidly within 10 μm from the aggregate surface. This is not only due to the 'wall effect' improving local water-cement ratio, the self-shrinkage of cement paste was more obvious than aggregate because of lower elastic modulus (Luo, et al. 2021a). Some researchers have even discovered the debonding phenomenon between mortar and aggregate (Khedmati, et al. 2019, Khedmati, et al. 2018). This proves the feasibility of the image analysis technique in this work from another aspect.

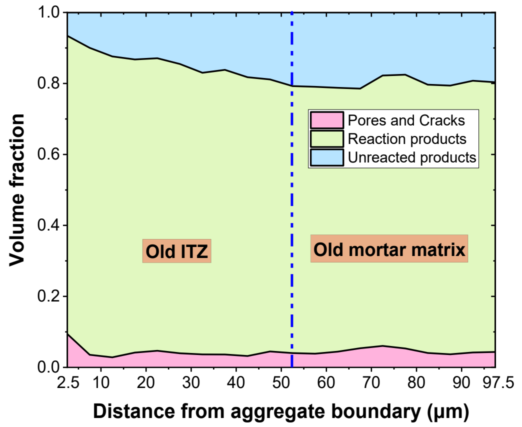

(a) Old ITZ

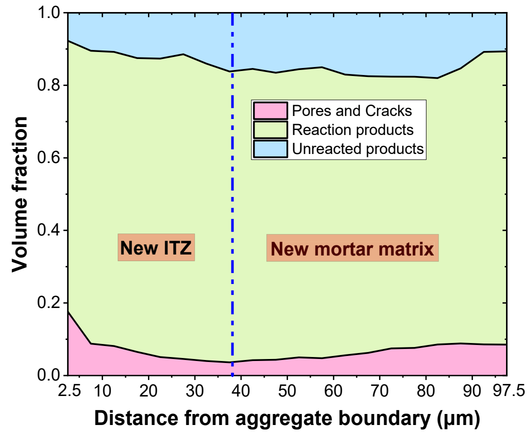

(b) New ITZ without RGP

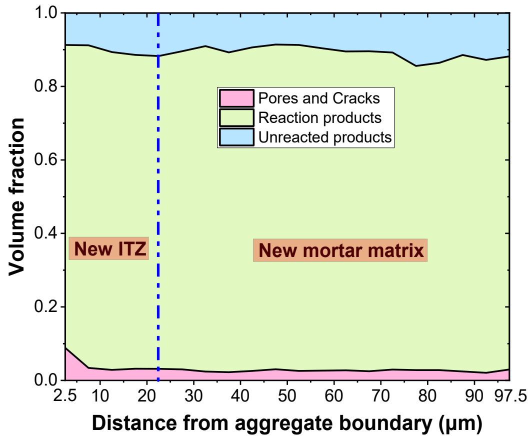

(c) New ITZ with RGP

Figure 5.8 Phases volume fraction from aggregate boundary to mortar matrix

To conduct a more detailed statistical analysis of the phases within the ITZ, the analysis of variance (ANOVA) proposed by R.A. Fisher was used to evaluate the difference significance between ITZ-mortar matrix and ITZ-ITZ. The F value in ANOVA represents the ratio of the between-group mean variance to the within-group mean variance (Camposeco-Negrete 2013). The larger F value means a significant difference between the two groups of data (Camposeco-Negrete 2013). However, the P value can more intuitively reveal the difference between two groups of data. Each F value corresponds to a P value. A P value higher than 0.05 indicates that the two groups of data are similar (Giasin & Ayvar-Soberanis 2017). Otherwise, it is believed that there is a significant difference between the two groups of data, and when the P value is less than 0.01, it can be considered that the difference between the two groups of data is extremely significant (Giasin & Ayvar-Soberanis 2017). The statistical results of the volume fraction of phases between ITZ-mortar matrix and ITZ-ITZ are shown in Table 5.3.

The data shows that the content of reaction/unreacted products between old ITZ and old mortar matrix was significantly different. This was equally evident between the new mortar matrix and the new ITZ without RGP. The volume fractions of reaction and unreacted products directly reflect the performance of ITZs (Fang & Zhang 2020). It can be inferred from the statistical results that the characteristics of pure cement-based ITZ were obviously weaker than the mortar matrix. In comparison, the content of reaction/unreacted products in the new mortar matrix and new ITZ with 20% RGP were similar, while the proportions of pores and cracks were obviously different, indicating that RGP can effectively refine the percentage of reaction and unreacted products, but the ability to reduce porosity in ITZ was insufficient. Nevertheless, it still can be seen from Figure 5.8 that the volume fraction of pores and cracks in the ITZ with RGP was lower than that of old mortar and new mortar without RGP.

Table 5.3 Difference comparison of phases between ITZ and mortar matrix

	Pores and cracks		Reaction products		Unreacted products	
	P value	F value	P value	F value	P value	F value
Old ITZ Old mortar matrix	0.68204	0.17339	2.44×10^{-4}**	20.76867	0.00202**	13.00413
New ITZ without RGP New mortar matrix without RGP	0.66176	0.19785	0.02505*	5.97313	0.00543**	9.98152
New ITZ with RGP New mortar matrix with RGP	0.01994*	6.52166	0.2609	1.3474	0.53176	0.40653

Note: The symbol '*' and '**' represent significant difference and extremely significant difference between two groups of data, respectively.

Table 5.4 presents the statistical results of phase differences among ITZs. The difference of phases between old ITZ and new ITZ without RGP was not obvious. However, the volume fraction of reaction products was significantly different in the new ITZs with and without RGP. Combining with Figure 5.8, it can be seen that the increase in the volume fraction of reaction products in the new ITZ with RGP was the result of the decrease in both the proportion of pores/cracks and unreacted products. Therefore, the difference in the content of the reaction products within the two groups of new ITZ was the most obvious.

Table 5.4 Difference comparison of phases between ITZs

	Pores and cracks		Reaction products		Unreacted products	
	P value	F value	P value	F value	P value	F value
Old ITZ New ITZ without RGP	0.065	3.8921	0.81863	0.05424	0.13371	2.48027
New ITZ without RGP New ITZ with RGP	0.2115	1.76007	0.00662**	11.13918	0.19851	1.87228

Note: The symbol '*' and '**' represent significant difference and extremely significant difference between two groups of data, respectively.

5.5.2 Chemical and mineralogical composition of ITZs

5.5.2.1 EDS element mapping analysis

Considering that soda-lime RGP was used as an additive in this study, in addition to the main elements (Al, Si, Ca) belonging to cement-based materials, the distribution of Na is also presented in Figure 5.9 by EDS mapping. The natural aggregate used in this research was granite, whose main component was silica and feldspar. The boundary between natural aggregate and old mortar can be easily distinguished by the observation of Al, Si, Na distribution in Figure 5.9 (a). Granite possesses an extremely low water absorption ratio. Free water attached below the surface of granite is easy to bleed into ITZs and form a local high water-cement ratio region with less Al, Si and Ca content near the boundary of aggregate, as shown in Figure 5.9 (a). This is an important reason why the cohesion of C-S-H in ITZ is weaker than that in the mortar matrix (Rangaraju, et al. 2010). Al was mainly distributed in some phases, such as C-A-S-H, which is consistent with the distribution of Al in previous cement paste samples (Kumar, et al. 2017, Skibsted &

Andersen 2013). In addition, Si and Ca were dispersed in ITZs uniformly in old ITZ and new ITZ without RGP, indicating that cement in these two regions had high degree of hydration. In comparison, there were obvious Si and Na rich zones in the new ITZ with RGP, which were incompletely reacted glass clinkers, and the proportion increased with the distance to the boundary of old mortar. This is consistent with the unreacted products distribution in Figure 5.8 (c) and previous studies on the fly ash clinkers distribution in ITZs of geopolymer concrete (Fang & Zhang 2020, Luo, et al. 2022). According to Chen et al. (Chen, et al. 2006) and Du et al. (Du & Tan 2017), the pozzolanic reaction involved in RGP is a long process, which may last for one year or more. However, this did not prevent the amorphous silica in small-size and parts of large-size glass clinkers from dissolving and reacting with CH to form more C-S-H gel, which improved the performance of ITZ (Mostofinejad, et al. 2020).

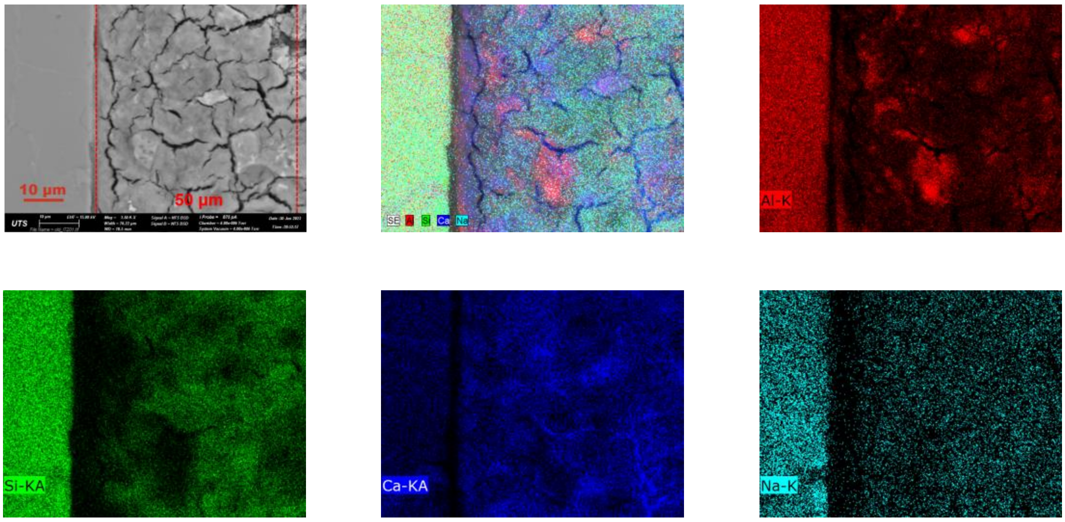

(a) Old ITZ

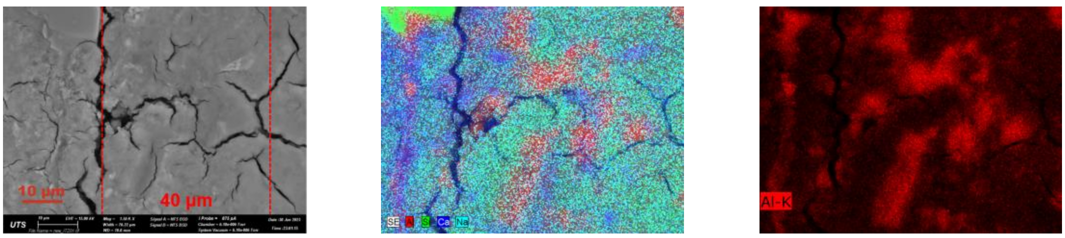

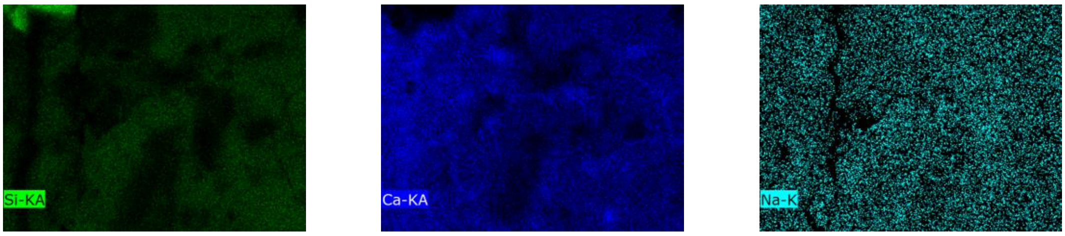

(b) New ITZ without RGP

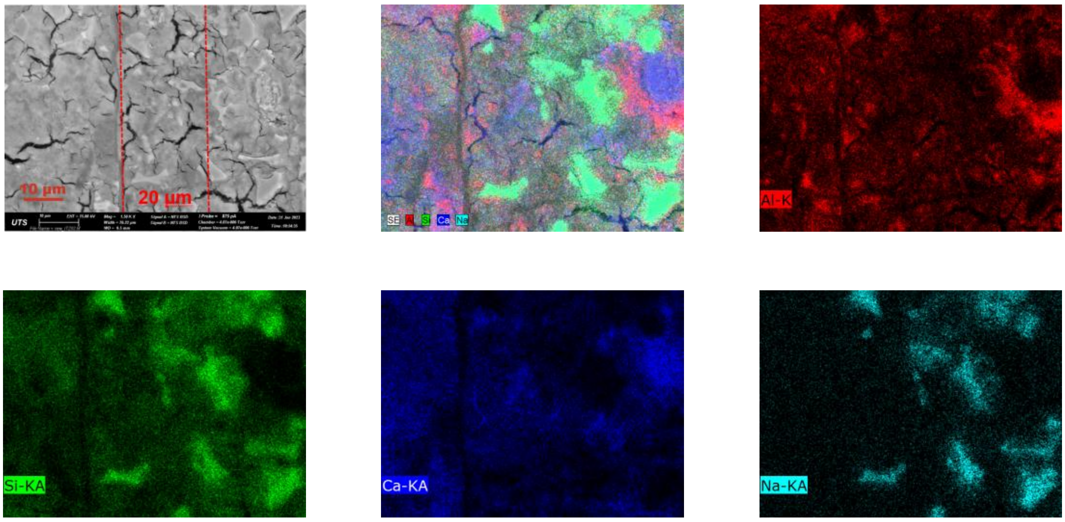

(c) New ITZ with RGP

Figure 5.9 EDS mapping analysis of ITZs

5.5.2.2 EDS element quantitative analysis

Numerous areas were randomly selected and more than 10000 points were extracted for quantitative analysis of EDS results. The Si/Ca vs. Si/Na atomic ratios of effective points in ITZs and the adjacent matrix were collected and shown in Figure 5.10. Except several data points close to 0 may represent pores or cracks, the densest point cluster determined by the naked eye within the blue ellipse represents C-S-H gel. The centre of the ellipse was marked with a red dot. It can be clearly seen from Figure 5.10 (a) that the number of effective points in the old ITZ was lower than that in other regions, indicating that the constituents in the old ITZ was relatively loose. The number of effective points in the corresponding old mortar matrix increased significantly, and the average Si/Ca ratio of

C-S-H was about 1.2, higher than that of the old ITZ (0.6 on average). It has been known that C-S-H exhibits a better performance with a higher Si/Ca ratio, which is consistent with the common knowledge that ITZ is the weakest region in concrete (Kunther, et al. 2017). Since a lower water-cement ratio was designed to prepare new mortar, the distance between cement clinkers in the new ITZ and the matrix reduced. As a result, the number of effective points in the new ITZ and the matrix without RGP were both higher than old ITZ. In addition, the average Si/Ca ratio in the two regions reached around 1.0 in Figs. 3.10 (c) and (d). When 20% of the cement in the sample was replaced by RGP, the Si/Na ratio reduced, and the Si/Ca ratio increased significantly to around 1.5 as shown in Figs. 3.10 (e) and (f). Cement dilution as well as unreacted glass clinkers were important factors for the above element ratio changes (Mejdi, et al. 2022). However, it cannot be ignored that part of the RGP participated in the pozzolanic reaction, generating more C-S-H gel with high Si/Ca ratio, which enhanced the bonding strength of ITZ (Jiang, et al. 2019). In addition, from the physical level, the rough and angular surface of the glass clinkers provided a natural place for the C-S-H nucleation reaction, which promotes the cement hydration, thereby increasing the overall Si/Ca ratio (Mirzahosseini & Riding 2015).

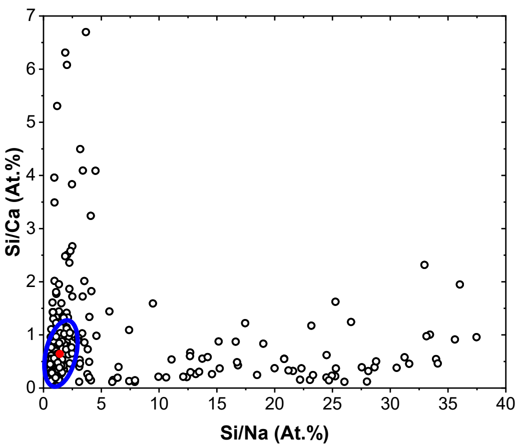

(a) Old ITZ

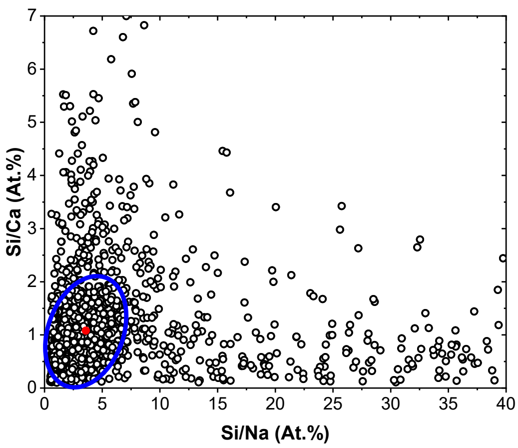

(b) Old mortar matrix

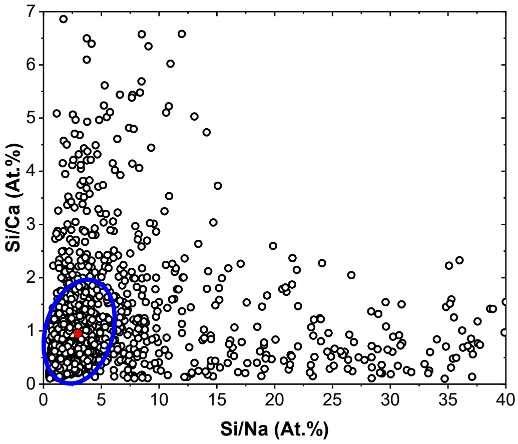

(c) New ITZ without RGP

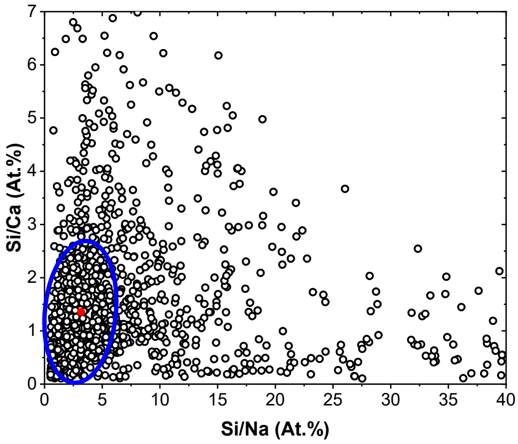

(d) New mortar matrix without RGP

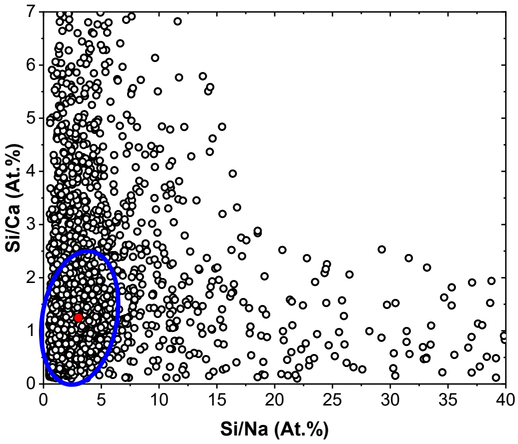

(e) New ITZ with RGP

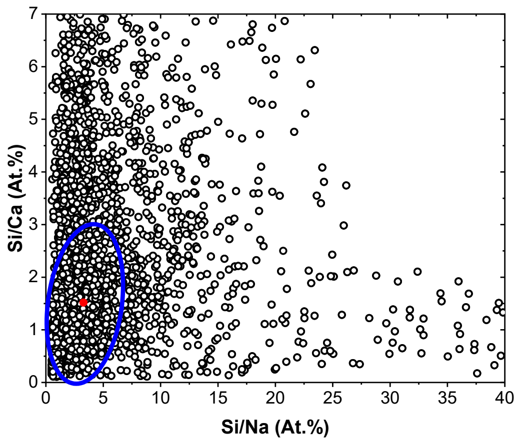

(f) New mortar matrix with RGP

Figure 5.10 Atomic proportions of element statistical results in ITZs and mortar matrix

5.5.2.3 TG-DTG analysis

The new mortar part of the sample was cut out and ground into powder for TG tests in this section and ^{29}Si NMR tests in Section 5.5.2.4. Although the chemical composition in the new ITZs cannot be understood exactly, the influence of RGP on the performance of ITZs can still be deduced indirectly through the analysis of the new mortar matrix.

Figure 5.11 shows the TG-DTG results for new mortar with and without RGP. The apparent mass loss at 100-150 ℃, 385-440 ℃ and 600-690 ℃ represent the decomposition of C-S-H/AFt, Portlandite and Calcite, respectively (Qu, et al. 2021). From the results of DTG analysis, it can be clearly found that the content of CH in the new mortar containing RGP was lower than that of the new mortar without RGP. Moreover, the C-S-H/AFt content of new mortar containing RGP was slightly higher than that of the counterpart. These results were consistent with the EDS chemical elemental analysis in section 5.5.2.2. RGP consumed CH in the mortar and generated C-S-H/AFt, which helped to improve the cohesion and density of ITZs. In addition, RGP increased the mass ratio of $CaCO_3$ in the new mortar.

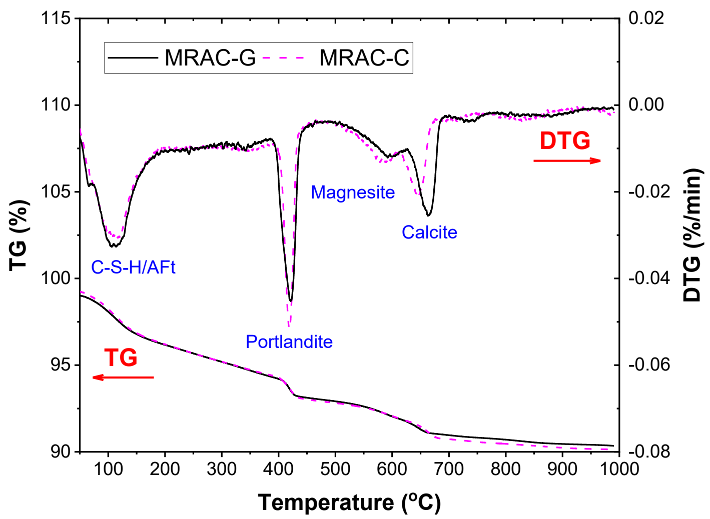

(a) TG-DTG curves

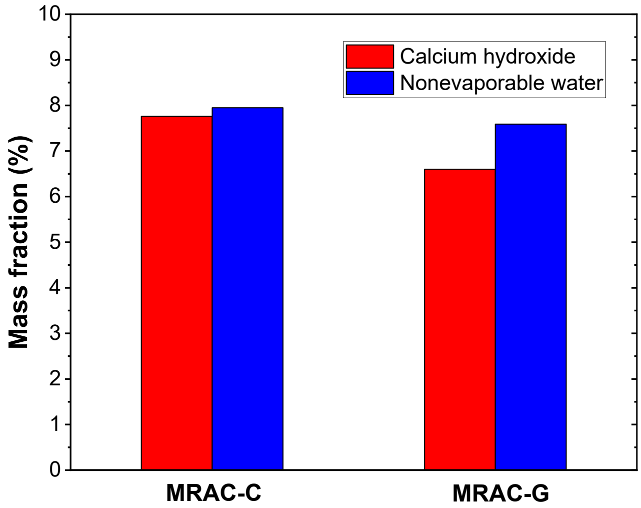

(b) Quantitative analysis of TG results

Figure 5.11 TG and DTG results of new mortar with and without RGP

To further confirm the hydration degree of the two groups of mortar, the total amount of CH (including the existing portion and the portion transformed into $CaCO_3$) and nonevaporable water were calculated by Eqs. (5.4) and (5.5) (Dong, et al. 2022, Guo, et al. 2020). The results were shown in Figure 5.11 (b).

$$CH = \frac{74}{18} \cdot \frac{M_{440} - M_{385}}{M_0} + \frac{74}{44} \cdot \frac{M_{690} - M_{600}}{M_0} \tag{5.4}$$

$$NEW = \frac{M_{1000} - M_{105}}{M_0} \tag{5.5}$$

Among the equations, M_0 represents the initial mass of the sample; M_x represents the residual mass of the sample at *x* °C; The numbers 74, 18 and 44 represent the relative molecular weight of CH, water, and CO_2 respectively.

According to Figure 5.11 (b), the mass fractions of CH and nonevaporable water in the new mortar with RGP decreased 1.16% and 0.36%, respectively, compared with the new mortar without RGP. In cement paste containing SCM, nonevaporable water is contributed by cement hydration and replacement material (Escalante-Garcia 2003). It is reported that smaller amounts of additional water were required in pozzolanic reaction than cement hydration (Escalante-Garcia 2003). The decrease of the proportion of nonevaporable in the mortar containing RGP combined with the variation of C-S-H and CH contents proved the existence of pozzolanic reaction.

5.5.2.4 ^{29}Si NMR characterisation analysis

The ^{29}Si NMR spectra and corresponding deconvolution results of samples with and without RGP are shown in Figure 5.12 and Table 5.5. The ^{29}Si NMR reflected the bonding relations between Si and O in cementitious materials (Maclaren & White 2003). A silicon chain can be represented by Q^n, and the number 'n' corresponds to the number of $(SiO_4)^{4-}$ units attached to the central $(SiO_4)^{4-}$ tetrahedral units (Maclaren & White 2003). The complex degree of the silicate chain improved with the number of units, and the chemical shift became more negative (Lu, et al. 2022a). Q^3-Q^6 corresponded to quartz and silicon-rich impurities. Here we only focus on the Si chains most directly related to Portland cement hydration, including Q^0, Q^1 and Q^2, whose chemical shifts were at around -70 ppm, -80 ppm and -85 ppm, respectively (Chen, et al. 2022). The Gaussian distribution area frictions of Q^3-Q^6 were deducted, and the remaining proportions were adjusted. Q^0 could be considered as the unreacted cement clinkers (C_2S and C_3S) (Chen, et al. 2022, Jamsheer, et al. 2018). Q^1 and Q^2 refer to the end-chain unit and middle-chain unit of C-S-H gel (Chen, et al. 2022, Jamsheer, et al. 2018).

The peaks of soda-lime glass and unreacted cement clinkers overlapped (Chen, et al. 2022). In Figure 5.12, the Q^0 peak of the sample containing RGP decreased, while the Q^1 and Q^2 peak improved compared with the sample powder without RGP, indicating that amorphous SiO_2 in RGP reacted with incompletely hydrated cement clinker to generate more C-S-H gel. In addition, RGP can also contribute to cement hydration to generate more C-S-H gel due to filler effect (Mirzahosseini & Riding 2015).

According to the relative intensities of Q^0, Q^1 and Q^2, the degree of hydration (DoH) of silicate phase, the polymerization degree (PD) of C-S-H and the mean chain length (MCL) of the silicate chain can be calculated (Chen, et al. 2022). The relative equations are as follows:

$$DoH = 100\% - Q^0 \tag{5.6}$$

$$PD = Q^1 + \frac{2 \times Q^2}{Q^1 + Q^2} \tag{5.7}$$

$$MCL = 2 \times \frac{Q^1 + Q^2}{Q^1} \tag{5.8}$$

The quantitative analysis results in Table 5.5 show that the hydration degree of silicate phase and polymerization degree of C-S-H in the sample with 20% RGP improved by 34.3% and 0.21, respectively, compared with the sample without RGP. In addition, the increase of the mean length of silicate chains in new mortar with RGP reflected the formation of denser and more stable C-S-H gel (Chen, et al. 2022). This explains why there were more hydration products and less pores/cracks in new ITZs containing RGP in image analysis. To summarize, the TG-DTG and ^{29}Si NMR test results supported the deductions in Section 5.5.1 and Section 5.5.2.1 about the functions of RGP in new ITZs.

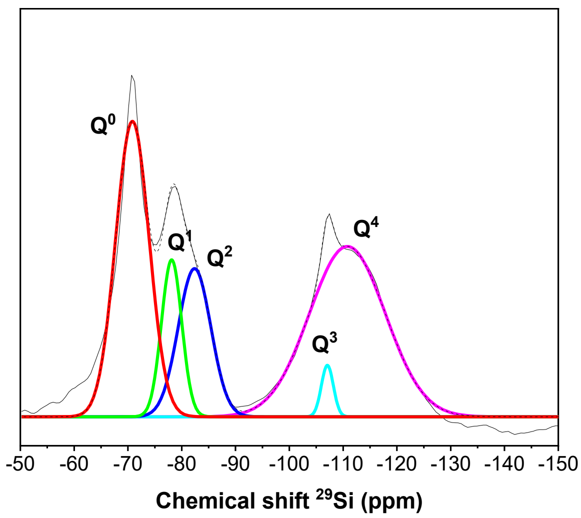

(a) New mortar without RGP

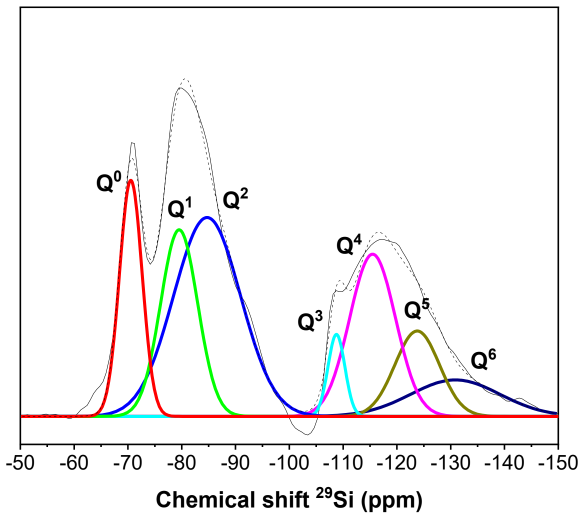

(b) New mortar with RGP

Figure 5.12 ^{29}Si NMR spectra of new mortar with and without RGP

Table 5.5 Statistical deconvolution results of 29Si NMR spectra

	Q^0	Q^1	Q^2	DoH	PD	MCL
New mortar without RGP	55.2%	17.8%	27.0%	44.8%	1.38	5.03
New mortar with RGP	20.9%	27.1%	52.0%	79.1%	1.59	5.84

5.5.3 Micromechanical properties of ITZs

The nanoindentation test results with ITZ widths identified in Section 5.5.1 are shown in Figure 5.13. The NCA adopted in this study was granite with the elastic modulus exceeding 160 GPa and the hardness over 25 GPa. It is worth noting that there was a clear drop in micromechanical properties on the edge of the modelled NCA, but not where the old mortar matrix adjacent to new ITZs. This could be explained that the elastic modulus and hardness of NCA chosen in this experiment were significantly higher than old mortar matrix. Old ITZ cannot provide enough restraint on the NCA edge. As a result, the value of the third column in Figs. 5.13 (a) and (b) NAC region was evidently lower than the first two columns. It can also be found that the average elastic modulus and hardness of old ITZ were slightly lower than old mortar matrix, and the corresponding average elastic modulus and hardness ratios were 0.86 and 0.88, respectively. This is because of the 'wall effect' leading to a high water-cement ratio and low strength of old ITZ. Among them, the elastic modulus and hardness of old ITZ at 4 μm away from the surface of NCA were obviously lower than those far away from the surface of NCA. This corresponded to the local high water-cement ratio region near the NCA boundary observed in Figure 5.9 (a).

As for MRAC without RGP, the average elastic modulus and hardness of new ITZ were 11.89 GPa and 0.29 GPa, respectively, which were slightly higher than those of the adjacent old mortar matrix (8.2 GPa and 0.2 GPa respectively). Although the 'wall effect' and release of pore water from the surface of RCA weakened the strength of the new ITZ, the lower initial water-cement ratio of the new ITZ still played a dominant role. Similar to the old ITZ, the micromechanical properties of the new ITZ were lower than those of the new mortar matrix (average elastic modulus ratio and hardness ratio were 0.69 and 0.71, respectively). In addition, the average elastic modulus and hardness of the new ITZ increased by 14.7% and 9.5%, respectively, compared with the old ITZ (10.37 GPa and

0.26 GPa), which confirmed the proposal to satisfy the strength requirements of RAC by reducing the water-cement ratio of the new mortar in real infrastructure construction.

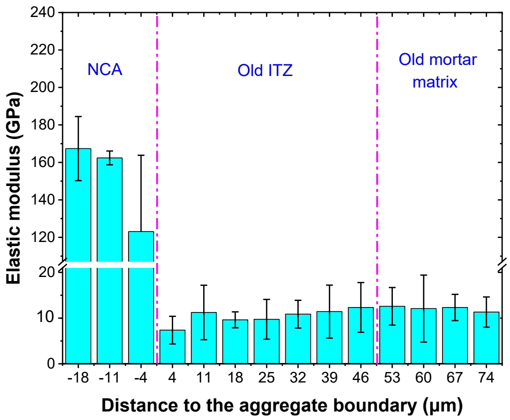

(a) Modulus of old ITZ

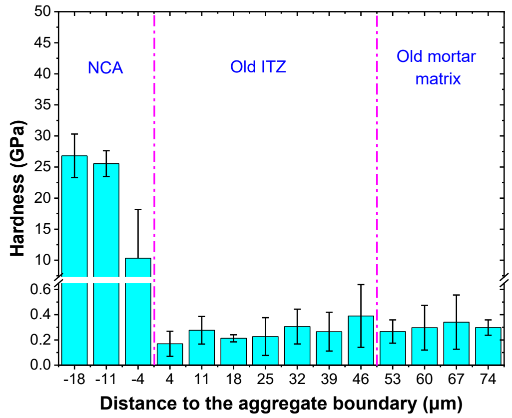

(b) Hardness of old ITZ

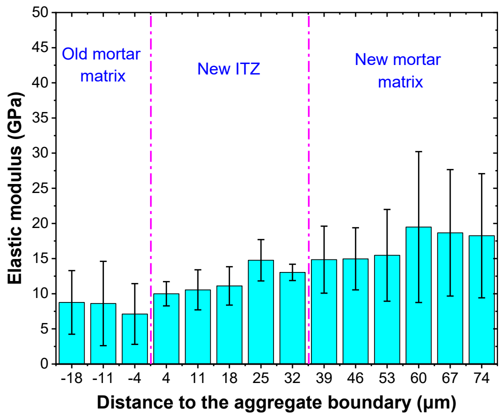

(c) Modulus of new ITZ without RGP

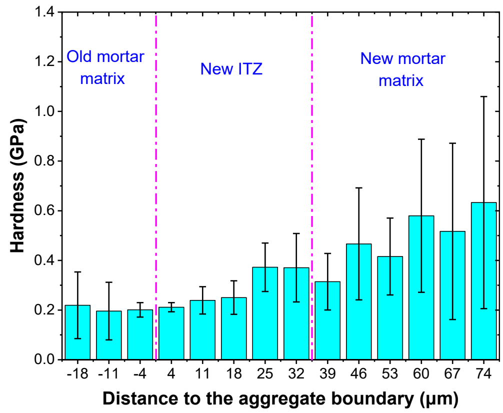

(d) Hardness of new ITZ without RGP

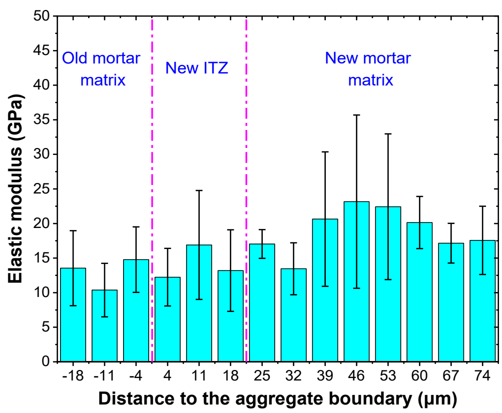

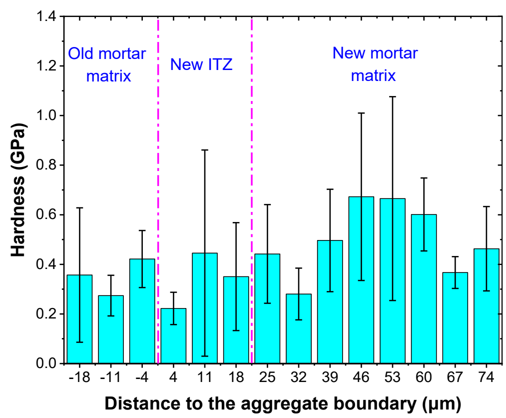

(e) Modulus of new ITZ with 20% RGP (f) Hardness of new ITZ with 20% RGP

Figure 5.13 Grid nanoindentation test results of modelled ITZs

As shown in Figs. 5.13 (e) and (f) the average elastic modulus of the new ITZ with RGP and the adjacent old mortar matrix was 14.11 GPa and 12.93 GPa, respectively. The average hardness was 0.34 and 0.35 GPa, respectively. As expected, RGP participated in the pozzolanic reaction, generating more C-S-H gels with a high Si/Ca ratio, which enhanced the strength and compactness of the new ITZ. It is worth noting that the micromechanical properties of the old mortar adjacent to the new ITZ with RGP were also enhanced compared to the old mortar adjacent to the new ITZ without RGP (average elastic modulus and hardness increased by 57.9% and 70.8% respectively). This can be partly attributed to the dissemination effect of amorphous silica in the new mortar with RGP. SiO_2 in the new mortar penetrated into the adjacent old mortar region and proceeded the pozzolanic reaction, so that the local old mortar performance was improved and achieved a tighter bond between old and new mortar. Furthermore, the 'wall effect' was also evident in the MRAC with RGP. The average elastic modulus and average hardness ratio of the new ITZ to the new mortar matrix were 0.74 and 0.68, respectively. In addition, the data fluctuation of columns in the new ITZ containing RGP was more significant than old ITZ and new ITZ without RGP. A small amount of unreacted RGP particles may still hid under the observation surface. According to Bosque et al. (2017), the nanoindentation elastic modulus of glass was up to 86.17 GPa, which was significantly higher than that of cement products. The heterogeneity of cement paste containing RGP could pose a certain degree of influence on the results of nanoindentation test.

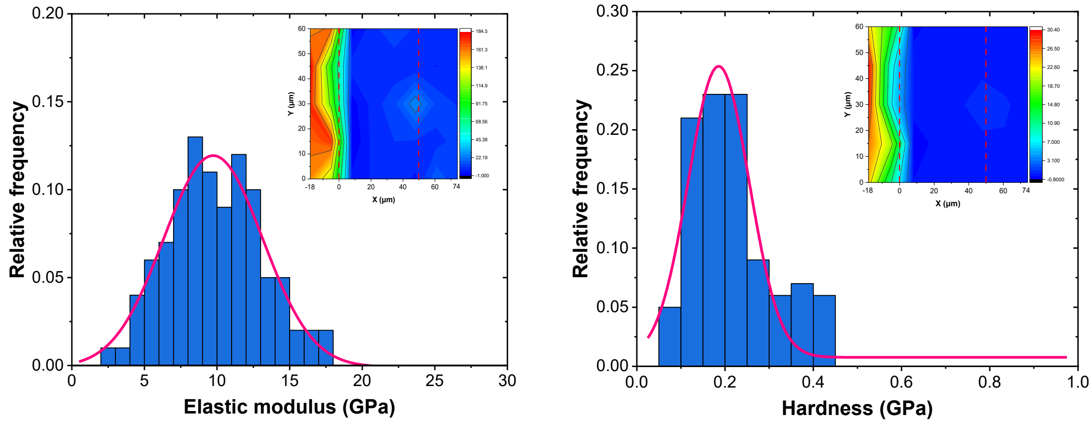

(a) Old ITZ

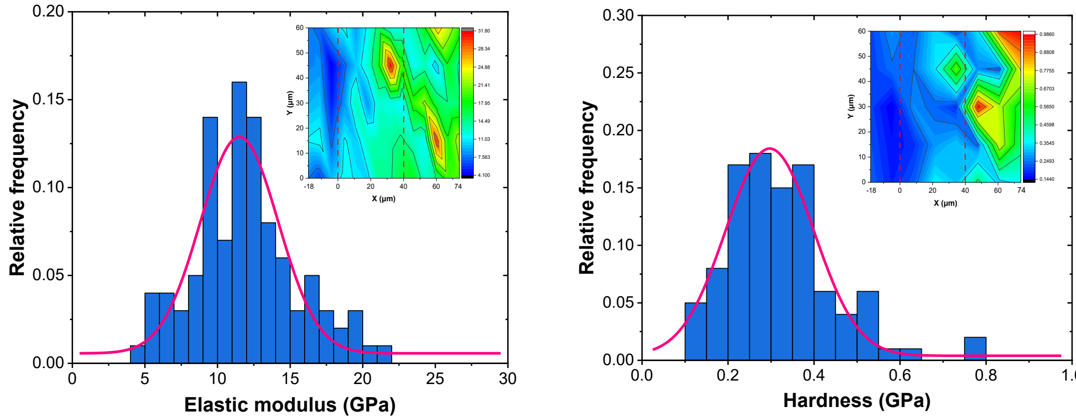

(b) New ITZ without RGP

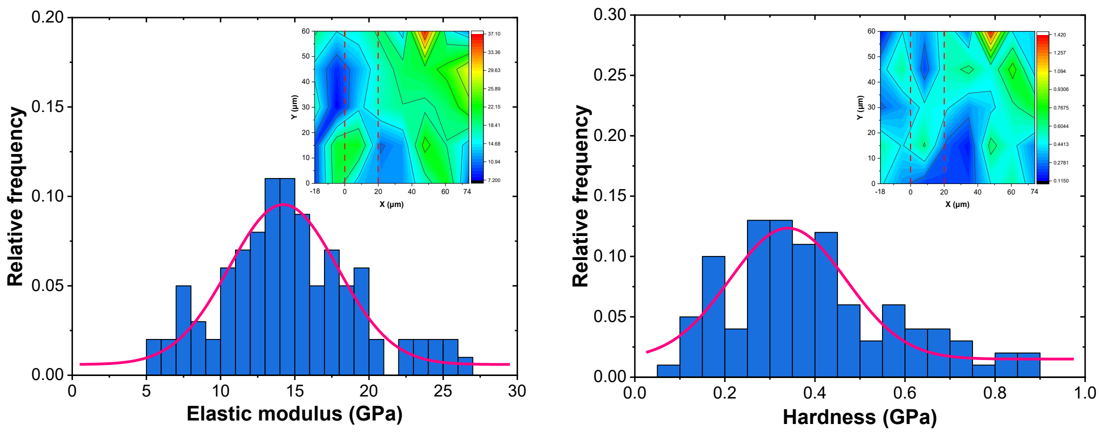

(c) New ITZ with RGP

Figure 5.14 Distribution of grid nanoindentation results in modelled ITZs

The nanoindentation test results were collected and presented in Figure 5.14 in the form of frequency distribution histograms and contour maps. The elastic modulus and hardness of ITZ roughly follows the normal distribution. Therefore, the Gaussian model was used to fit the frequency histogram of the nanoindentation test results. The elastic modulus and hardness of the old ITZ were mainly distributed around 5-15 GPa and 0.2 GPa. The elastic modulus and hardness of the new ITZ without RGP increased slightly compared with the old ITZ. The values in the new ITZ with RGP were scattered in a larger range, and the overall elastic modulus and hardness were higher than those of the old ITZ and the new ITZ without RGP. In the contour maps of new ITZs with and without RGP, there were points with higher elastic modulus and hardness than the surrounding area. In comparison, the elastic modulus and hardness of Old ITZ remained at a low level. This is because of the existence of CH and glass clinkers in the sample. By comparing Figure 5.14 (b) and (c) we can see that RGP is more effective in enhancing the micromechanical properties of peripheral C-S-H gel.

5.6 Conclusion

In this chapter, MRAC samples were fabricated to simulate regular ITZs. In order to distinguish the interface between the old and new mortar easily, the new mortar adopted a lower water-cement ratio. The performance of old and new ITZs was compared by using statistical techniques and multiscale experimental methods. Meanwhile, the improvement efficiency of RGP on the new ITZ properties was evaluated. The related conclusions can be drawn up as below:

(1) The regular natural aggregate-old mortar and old mortar-new mortar interfaces produced in this study can be clearly observed under an electron microscope. Modelled ITZ effectively reduced unnecessary workload as well as achieved

satisfactory accuracy of test results. The sample preparation procedure in this study is sufficient to meet the testing requirements for BSE and nanoindentation tests.

(2) Morphological analysis revealed that the widths of the old ITZ, the new ITZ without RGP and the new ITZ with RGP were around 50, 40, and 20 μm, respectively. The volume fraction of cracks and pores in the new ITZ without RGP was 7.29%, which was higher than 4.33% in the old ITZ, while the content of the reaction products was similar, around 80.5%. In comparison, the proportion of pores and unreacted products within the new ITZ with RGP decreased to 4.30% and 10.27%, and the content of reaction products increased to 85.43%.

(3) In the ANOVA of the phase distribution, the volume fractions difference of reaction and unreacted products were extremely significant for the old and new ITZ without RGP compared with the corresponding mortar matrix (P values lower than 0.01), while for the new ITZ with RGP, only the porosity was significantly different from that in the new mortar matrix (P value was between 0.01 and 0.05). In the comparison between different ITZs, RGP can increase the difference significance in the reaction products.

(4) The chemical and mineralogical analysis showed that the hydration of cement clinkers in the three types of ITZs reached a high level. The Si/Ca ratio in the new ITZ without RGP was around 1.0, which was slightly higher than that of the old ITZ (0.6 on average). RGP can effectively promote hydration and pozzolanic reaction from physical and chemical level to generate a large amount of C-S-H with a Si/Ca ratio of around 1.5, which provided stronger cohesion strength for the ITZ.

(5) Nanoindentation tests well reflected the influence of the ‘wall effect’ on the micromechanical properties of ITZ. The average elastic modulus and hardness of the three ITZs were lower than those of the corresponding mortar matrix. The elastic

modulus and hardness of the new ITZ without RGP were 11.89 GPa and 0.29 GPa, which were higher than old ITZ (10.37 GPa and 0.26 GPa) due to the lower water-cement ratio used in new mortar. Besides, RGP can largely improve the elastic modulus and hardness of new ITZs to 14.11 GPa and 0.34 GPa respectively.

(6) There were more exposed pores on the surface of the old mortar, which led to the fact that the bond between the old and new mortar cannot be as tight as that between old mortar and natural aggregate. Moreover, a large number of pores were formed in the new ITZ without RGP. After adding 20% RGP to the new mortar, amorphous silica improved the performance of the new ITZ as well as penetrated into the adjacent old mortar to accelerate the pozzolanic reaction. The surface structure of the old mortar was thus also improved. To evaluate the bonding strength between old and new mortar in RAC, not only the cohesion of C-S-H gel, but also the effective contact area should be considered.

CHAPTER 6. EFFECT OF PORE WATER PRESSURE ON MECHANICAL PERFORMANCE OF RAC TRIAIXAL COMPRESSION

6.1 Introduction

There have been many studies on the basic mechanical properties of RAC under compression, tension, shear and impact loads (Sunayana & Barai 2020, Tang, et al. 2020d, Wang, et al. 2021). However, concrete is generally under a multiaxial loading state, such as a triaxial compression state rather than being subjected to a simple unidirectional load during its service period (Jiang, et al. 2017, Tang, et al. 2020b). Existing research results show that when RAC is subjected to a high lateral confinement, its compressive strength, ductility and toughness all increase significantly, and the mechanical properties difference between NAC and RAC with the same water-cement ratio alleviate (Chen, et al. 2019, Folino & Xargay 2014). This is because lateral pressure weakens the adverse effect of the multi-ITZs on the compressive strength of RAC (Chen, et al. 2019). In addition, the cracks cannot propagate freely under the action of lateral confinement. The evidence is that the failure mode converted from vertical splitting failure under uniaxial compression to slip-shear failure mode (Chen, et al. 2019, Yang, et al. 2022). The triaxial compressive strength depends more on the mechanical properties of the aggregate and mortar matrix (Deng, et al. 2020). However, some researchers pointed out that excessive confining pressure would lead to new cracks in concrete, resulting in a decrease in elastic modulus (Wu, et al. 2023).

Another point worth noting is that pore water in the concrete is difficult to completely dissipate, especially for underground structures including bridge pires, dams and pile foundations (Xue, et al. 2020). The pore water pressure would emerge and increase rapidly under obvious compression deformation, and its role in promoting crack propagation in concrete and resisting compression deformation cannot be ignored (Malecot, et al. 2019, Vu, et al. 2009). Researchers have realised the significance of porosity and pore pressure to study the triaxial compression properties of concrete (Malecot, et al. 2019, Vu, et al. 2009). He et al. (He, et al. 2022) established a pore-cement paste finite element model through ANSYS. Experimental and numerical simulation results show that pores increased the deformation properties of concrete, and when the pore pressure was higher than 17 MPa, dense damage occurred around the pores (He, et al. 2022). Vu and Malecot et al. (Malecot, et al. 2019, Vu, et al. 2009) investigated the mechanical properties of dry, semi-saturated and fully saturated concrete at confining pressure of up to 600 MPa. Pore water pressure played a major role in the triaxial compressive strength and bulk stiffness of concrete (Malecot, et al. 2019, Vu, et al. 2009). When the pore pressure existed, the efficiency of confining pressure to improve the compressive strength of the concrete decreased, and the deformation capacity before failure was weakened (Malecot, et al. 2019, Vu, et al. 2009).

Up to now, no one has experimentally revealed the triaxial compressive properties of RAC in the presence of a constant pore water pressure. Wu et al. (Wu, et al. 2022) pointed out that there is a superior linear relationship between the compressive strength of RAC and the micromechanical properties of the old ITZ. Xiao et al. (Xiao, et al. 2013b) reported that the compressive strength of RAC improved with the increase of the elastic modulus of new mortar matrix by finite element simulation. However, there is still a lack of experimental data linking the microstructure, micromechanical properties and macromechanical properties of RAC under the coupling of multilevel loads. Therefore, this part statistically analysed the porosity in the old and new ITZs and adjacent paste matrix of RAC through the BSE-Image analysis technique. Nanoindentation was used to obtain the elastic modulus and hardness in the region corresponding to the BSE-Image analysis. Then, different levels of confining pressure and pore water pressure were applied to the cylindrical concrete specimens with 0%, 50% and 100% RCA replacement ratios, and the stress-strain curves were obtained. Based on the existing theoretical model, the relationship between the porosity, micromechanical properties of weak regions in RAC and macromechanical properties under multi-field coupling stress state was established.

6.2 Experimental programme

6.2.1 Materials and specimen preparation

The concrete specimens used for triaxial compression tests were $\Phi 50\times 100$ mm cylinders. According to the ratio requirement of concrete specimen diameter to coarse aggregate particle size in ASTM C192, the particle size of NCA and RCA was determined to be 5-16 mm. The main physical properties of NCA and RCA are summarized in Table 6.1. It can be seen that the density of RCA was lower, whereas water absorption and crush index were higher due to porous old mortar attached to the surface of RCA. Natural river sand with a fineness modulus of 2.80, an apparent density of 2615 kg/m^3 and water absorption of 1.44% was adopted as NFA. The particle size distribution of NFA is shown in Figure 6.1, which satisfies the requirements in ASTM C33. Ordinary Portland cement was mixed with water, naphthalene-based superplasticizer (SP), coarse and fine aggregate for concrete specimens.

Table 6.1 Physical properties of coarse aggregate

	NCA	RCA
Size (mm)	5-16	5-16

Apparent density (kg/m^3)	2791.5	2736.5
Water absorption (wt. %)	1.375	5.910
Crush index (wt. %)	17	22

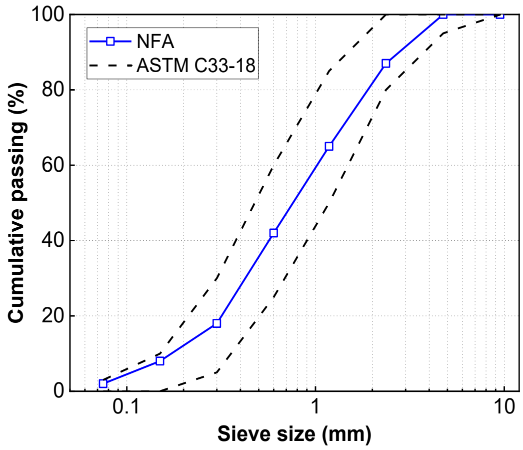

Figure 6.1 Particle size distribution of fine aggregate

Table 6.2 Concrete specimen mix proportions

Mix	Raw materials (kg/m^3)					
	NCA	RCA	NFA	Cement	Water	SP
NAC	1055	0	675	498	174	4.23
RAC50	527.5	527.5	675	498	174	4.23
RAC100	0	1055	675	498	174	4.23

RCA replacement ratio was 0%, 50% and 100%. The detailed mixture proportion of NAC and RAC are shown in Table 6.2. Considering the high-water absorption of RCA, the NCA and RCA were soaked in water for 24 h and kept in a saturated surface dry (SSD) state before the formal mixing. After all the raw materials were ready, coarse and fine aggregate was poured into a drum mixer and dry-mixed for 1 min. Then, cement was poured into the drum mixer and dry-mixed with aggregate for another 1 min. Finally, the water mixed with SP was poured into the mixer slowly and evenly. The mixer continued to work for 2-3 min until all constituents were mixed uniformly. When the mixing was done, slump tests were conducted immediately. The slump of RAC was slightly higher than that of NAC, because the RCA contained more absorbed water in the SSD state, but the slump was at 120-140 mm.

The fully mixed fresh concrete mixtures were cast in Φ50 mm × 100 mm cylinder moulds and consolidated by a vibration table for about 30s until no large bubbles emerged. The top surfaces of the concrete samples were covered with a plastic film to prevent water evaporation. After curing in the moulds for one day, the solidified concrete specimens were transferred to a standard curing room (25 ± 5 °C, 95% RH) for one year.

6.2.2 Sample preparation for microstructure and nanoindentation tests

A cylindrical concrete specimen was randomly selected and cut into small slices from the middle. Then, the concrete slice containing RCA and new mortar was placed into a Φ35 mm cylindrical mould, followed by pouring epoxy resin. After the epoxy resin was solidified, the surface of sample was ground by 120, 240, 600 and 1200 grit abrasive paper for 10 min each (Luo, et al. 2021a, Luo, et al. 2022). The sample surface was then polished by 0.3 μm and 0.05 μm alumina suspensions for 30 min each (Luo, et al. 2021a, Luo, et al. 2022). After each polishing, the sample was put into an ultrasonic bath for 2 min cleaning to remove the alumina particles attached to the surface. Finally, the processed sample was dried in a vacuum oven at 60 °C for 48 h.

6.2.3 BSE-based image analysis

NAC and RAC slice samples coated with epoxy resin were used to observe the pore structure of ITZs by a scanning electron microscope (SEM, Zeiss EVO LS15). The accelerating voltage was set as 15 kV. To enhance the conductivity of the sample, the sample was sputter-coated with a layer of 5 nm platinum. At least 30 BSE images at a magnification of 500 × were obtained at constant contrast and brightness for each ITZ.

The volume fraction of constituents in ITZs and the adjacent paste matrix can be obtained by grey level analysis by Image Pro (Wong & Buenfeld 2009, Wong, et al. 2006). The interface between aggregate and cement paste was captured and 17 strips with 5 μm in width were taken from aggregate to paste matrix. The width of ITZ was determined by the distribution of unreacted products (Luo, et al. 2021a). As a result, the porosity of ITZ and adjacent paste matrix in each BSE image can be obtained.

6.2.4 Nanoindentation tests

A Nano Indenter G200 equipped Berkovich tip was used for grid nanoindentation tests. Berkovich tip is a triangular pyramid with the same aspect ratio. Based on the geometric shape of the tip, requirements in standards (ASTM E384-17) and previous research, the indentation depth was designed to be 400 nm to satisfy results accuracy and sufficient measuring points conducted within ITZs (Luo, et al. 2020, Luo, et al. 2021b). Figs. 6.2 (a) to (c) show the indentation regions of ITZ in NAC (ITZ-NAC), Old ITZ and New ITZ in RAC (old ITZ-RAC and new ITZ-RAC). Figure 6.2 (d) illustrates test points distribution in each region. The vertical and lateral space between measuring points were 10 μm and 5 μm respectively. A total of 10 groups of 5 × 20 grid nanoindentation test areas were taken randomly along each ITZ. The test area artificially avoided areas near fine aggregate and cracks. When the indentation depth reached 400 nm, the tip was maintained at the maximum load for 10 s and then unloaded to 10% of the peak load. The elastic modulus and hardness of ITZs can be obtained by nanoindentation tests.

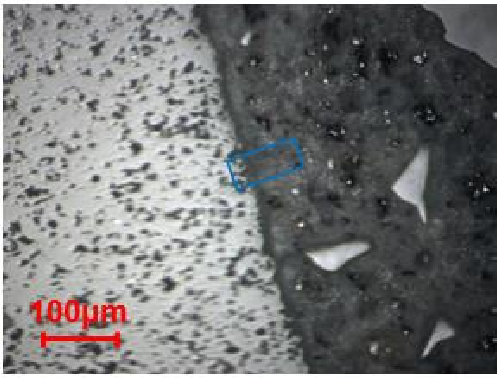

(a) ITZ-NAC

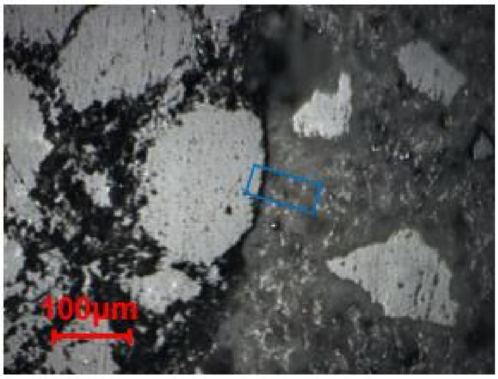

(b) Old ITZ-RAC

(c) New ITZ-RAC

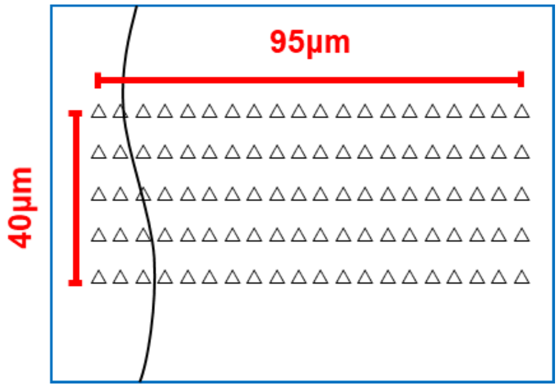

(d) Layout of testing points

Figure 6.2 Schematic of grid nanoindentation tests on ITZs

6.2.5 Triaxial and pore pressure test

A triaxial multi-field coupled testing system (RTX-1000) was used to test the compression performance of concrete under different confining pressure and pore water pressure. The system has two Linear Variable Differential Transformers (LVDTs) and one circumferential LVDT (all with ± 2.5 mm range), for measuring axial and radial strains respectively. The system has an independent servo-controlled axial pressure actuator, confining pressure actuator and pore pressure actuator, which can apply 1000 kN of axial load and 70 MPa of confining and pore pressure respectively.

Considering the output power of the apparatus and the stability of the concrete specimen, the maximum confining pressure was set to 14 MPa to obtain a stable stress-strain curve.

In order to ensure sufficient lateral confinement to prevent pore water from seeping out from the sides of the specimen, the maximum pore water pressure was set to 13 MPa. As a result, four different levels of confining pressure ($\sigma_c = \sigma_1 = \sigma_2 = 0$, 3, 7, 14 MPa) and four different level of pore pressure ($\sigma_p = 0$, 5, 9, 13 MPa) were designed in this experiment. The specific pressure parameters are shown in Table 6.3. Each group of tests was repeated once. Both ends of concrete specimens were ground flat with the error less than 1 mm by a grinder. To prevent the oil from being pressed into the concrete specimen, a heat shrink tube was wrapped and tightly attached to the surface of the specimen. The holes on the surface of the concrete specimen were sealed with the same water-cement ratio mortar. The triaxial compression apparatus and a sample covered with a heat shrink tube and installed LVDTs is shown in Figure 6.3.

Table 6.3 Testing parameters for compression

Mix	σ_c (MPa)	σ_p (MPa)	Specimen	σ_c (MPa)	σ_p (MPa)
NAC-0	0	0	RAC50-14-5	14	5
NAC-3	3	0	RAC50-14-13	14	13
NAC-7	7	0	RAC100-0	0	0
NAC-14	14	0	RAC100-3	3	0
NAC-14-5	14	5	RAC100-7	7	0
NAC-14-9	14	9	RAC100-14	14	0
NAC-14-13	14	13	RAC100-14-5	14	5
RAC50-0	0	0	RAC100-14-9	14	9
RAC50-7	7	0	RAC100-14-13	14	13

RAC50-14	14	0

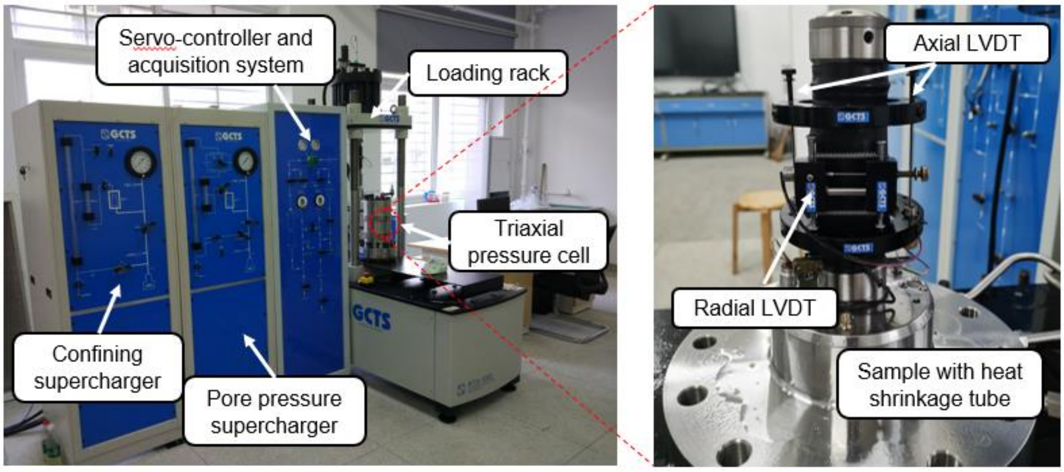

Figure 6.3 Triaxial testing apparatus

Stress states of concrete specimens and the loading procedure in the experiment are shown in Figure 6.4 and Figure 6.5 respectively. The uniaxial compression test ($\sigma_c = \sigma_p = 0$) was carried out at first. To ensure full contact between the loading panel and the top surface of specimen at the initial stage of the stress-strain curve, the specimen was loaded to 4 kN (approximately 10% of the peak load) and maintained for 20 s. The strain control method was adopted at the rate of 0.02%/min until radial strain reached 2% in the subsequent compression process. For triaxial compression tests ($\sigma_c \neq 0$; $\sigma_p = 0$), concrete specimens were fixed by a 4 kN axial load. Subsequently, silicone oil was injected into the triaxial pressure cell. The axial pressure and confining pressure were simultaneously raised to the target value at 0.2 MPa/s and maintained the concrete specimen under a hydrostatic pressure condition for 20 s. Finally, the axial load was applied at 0.02%/min until the radial strain reaching 2%. Regarding coupled test of confining pressure and pore water pressure ($\sigma_c \neq 0$; $\sigma_p \neq 0$), to make the internal pore pressure uniform, concrete specimens were vacuum-saturated for 24 hr before the formal test. Preloading and hydrostatic pressure condition steps were same with triaxial compression tests. Pure water was injected from the top of the concrete specimen to the bottom at designed pore water pressure as shown in Figure 6.6. After loading the pore water pressure, the water outlet was closed and maintained for 4 h to ensure a stable pore water pressure. Finally, the axial load continued rising at a rate of 0.02%/min until the radial strain reaching 2% and the stress-strain curves were obtained. It should be noted that confining pressure and pore water pressure were monitored in real time to ensure they are maintained at designed value during compression.

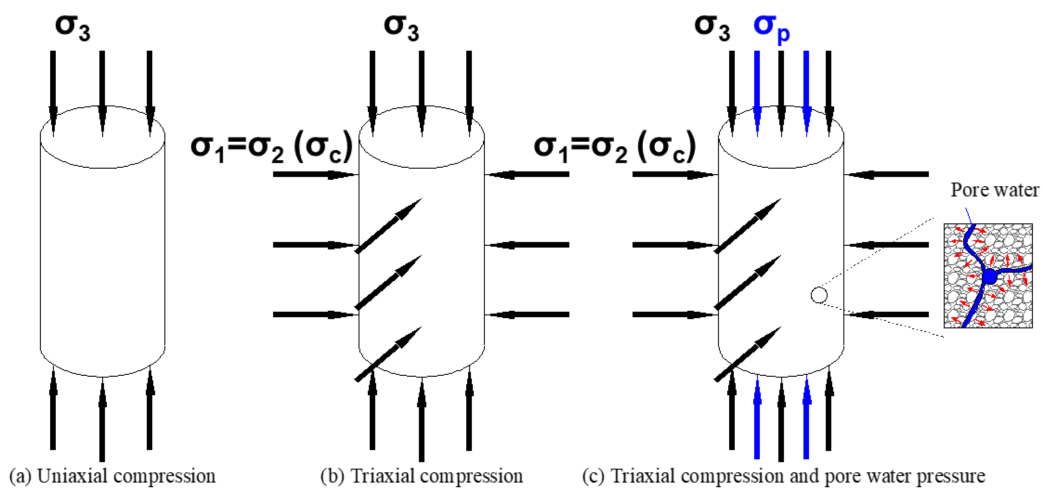

Figure 6.4 Stress states of concrete specimens

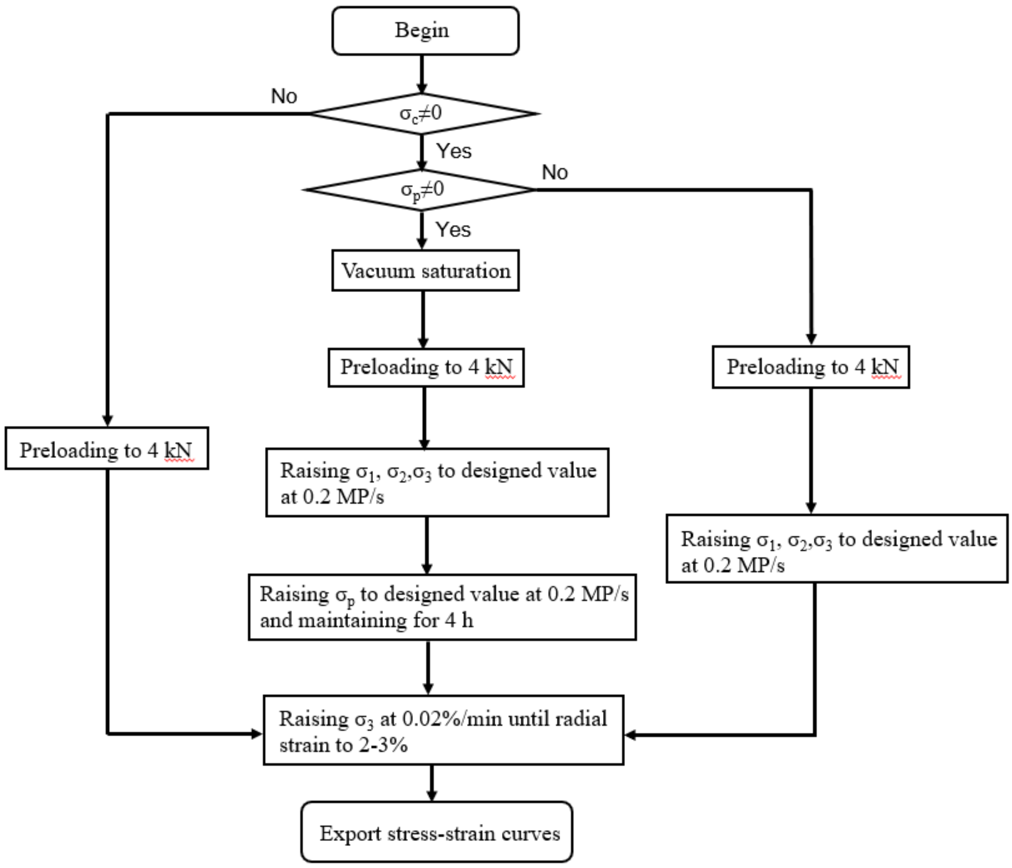

Figure 6.5 Flow chart of loading scheme

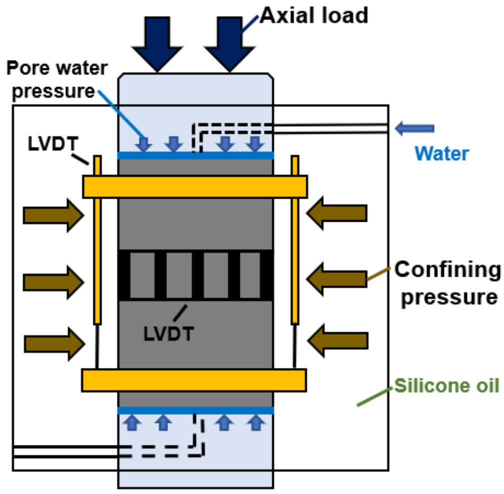

Figure 6.6 Schematic diagram of loading methods

6.3 Results and discussions

6.3.1 ITZs identification

The ITZ width of concrete can be identified from the area in the BSE images where the content of unreacted products or reaction products changes significantly. Figs. 6.7 (a) to (c) are the BSE images of three ITZs in this study. According to the grey threshold theory proposed by Wong et al. (Wong & Buenfeld 2006, 2009, Wong, et al. 2006), the unreacted product with the highest grey value was captured and replaced by white areas. The cement paste was divided into 17 consecutive 5 μm-width bands starting from the interface. According to previous identification results, the ITZ width of concrete was between 15-50 μm (Diamond & Huang 2001, Rangaraju, et al. 2010, Scrivener, et al. 2004). Therefore, it can be speculated that the segmented region contains the entire ITZ and part of paste matrix. For each type of ITZ, at least 30 different BSE images were used to statistical analyse the variation of unreacted product content at different distances from the aggregate boundary. The statistical results are shown in Figure 6.8.

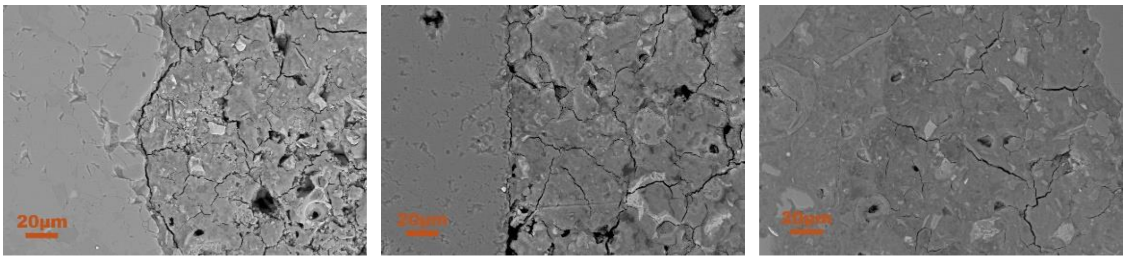

(a) Cement paste-NAC (b) Old cement paste-RAC (c) New cement paste-RAC

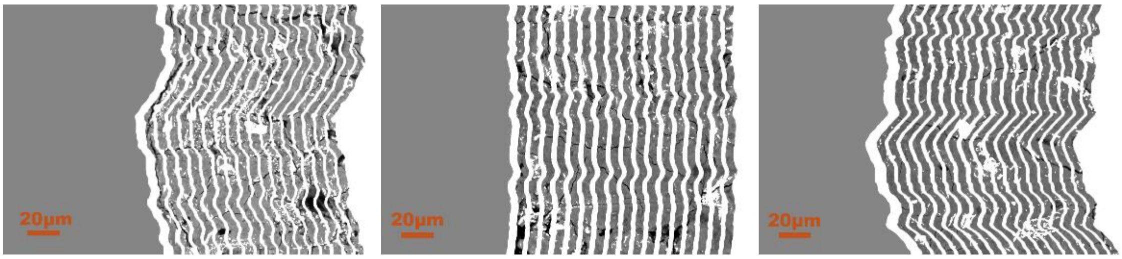

(d) Processed ITZ-NAC (e) Processed Old ITZ-RAC (f) Processed New ITZ-RAC

Figure 6.7 Segmentation of unreacted products in ITZs and adjacent matrix

The trend of unreacted product content in Cement paste-NAC and Old cement paste-RAC with the distance from the aggregate boundary was similar. The volume fraction improved rapidly and then maintained at a stable value. As a result, it can be deduced that the width of the ITZ-NAC and Old ITZ-RAC was 17.5 μm. Due to the uneven and porous structure of the old mortar on the surface of RCA, the 'wall effect' in the new ITZ was not obvious. The content of unreacted products increased rapidly within 2.5-7.5 μm from the old mortar boundary, and then entered a slow rising stage with the increase of the distance. According to the volume fraction of unreacted products, the width of the New ITZ-RAC was about 27.5 μm. Furthermore, it is evident that the unreacted product content in the Cement paste-NAC was higher compared to that of the New cement paste-RAC, despite the fact that the mixture design of the two pastes was the same (see Table 6.2). The reason is probably that when the RAC was at SSD condition, the absorbed water in the RCA promoted the hydration of the unhydrated cement clinkers in the old mortar during long-term curing, and at the same time, function like an internal curing agent, the desorbed water from the RCA promoted the hydration reaction in the adjacent new cement paste. Due to the longest curing age, the content of unreacted products in the Old cement paste-RAC was the lowest.

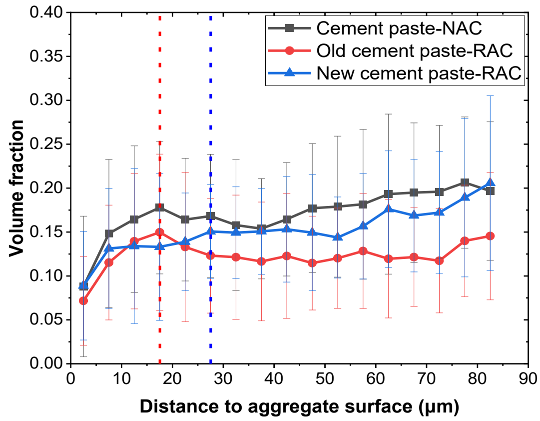

Figure 6.8 Statistical results of unreacted products distribution in different ITZs

In addition to the volume fraction of unreacted products, the width of ITZs can also be identified according to the micromechanical properties. In general, the elastic modulus of ITZ is lower than that of paste matrix. Figure 6.9 shows the elastic modulus distribution of three cement paste adjacent to aggregate in this research. Similar to the distribution of unreacted products, the 'wall effect' was obvious in Cement paste-NAC and Old cement paste-RAC. The width of the ITZ-NAC and Old ITZ-RAC can be roughly identified as 12.5 μm and 22.5 μm, respectively. The elastic modulus of the new ITZ, which the width was about 32.5 μm in RAC, higher than that of the ITZ-NAC and the Old ITZ-RAC.

Based on the results of image analysis and nanoindentation, the width of the ITZ-NAC, the Old ITZ-RAC and the New ITZ-RAC are finally determined as 15 μm, 20 μm and 30 μm, respectively.

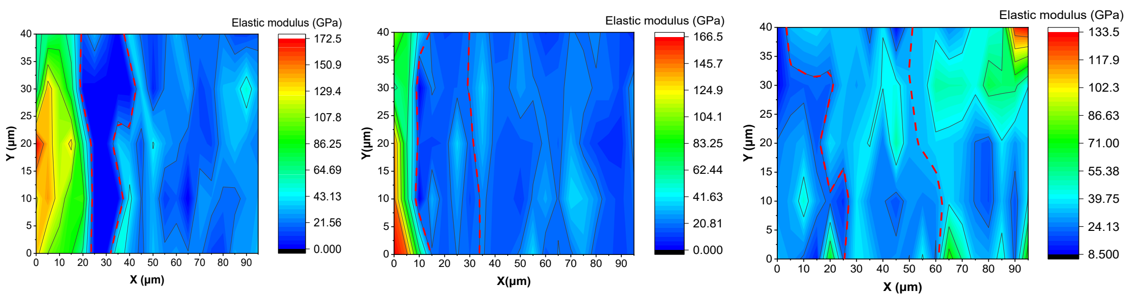

(a) Cement paste-NAC (b) Old cement paste-RAC (c) New cement paste-RAC

Figure 6.9 Elastic modulus contour map of different cement pastes adjacent to aggregate

6.3.2 Nano/micromechanical properties of ITZs

Figure 6.10 shows the nanoindentation test results of NAC and RAC. Average values and standard deviations of ITZs and adjacent paste matrix are listed in Table 6.4. The elastic modulus of the new ITZ and paste matrix were found to be higher than those of the corresponding regions in the NAC, despite having the same water-cement ratio design value. The similar difference was also observed in the unreacted products (see Figure 6.8). The elastic modulus of the new ITZ and the new paste matrix in RAC were 23.97 GPa and 24.54 GPa, which were 65.8% and 46.6% higher, respectively, than those in the corresponding regions in NAC. This probably because both the NCA and RCA were in an SSD state before the formal preparation of concrete. Due to the porous and cracked structure of old mortar, water retention capacity was better than NCA. During the curing process, the free water on the surface of NCA could cause an increase in the water-cement ratio of the ITZ, leading to a reduction in the elastic modulus. The absorbed water in RCA may function as an internal curing agent and old mortar in RAC continued to hydrate during the long-term curing process, which enhanced the bonding performance with the new paste. Bosque et al. (2017) also pointed out that the micromechanical properties of ITZ were closely related to the type of interface. The elastic modulus of ITZ bonded to rough-surfaced aggregate such as asphalt, clay or recycled aggregate was higher than that of ITZ bonded to smooth-surface aggregate including glass and plastic. The elastic modulus of Old ITZ-RAC was similar to that of ITZ-NAC, both about 14.45 GPa. However, the elastic modulus of Old paste matrix-RAC was 18.52 GPa, which was 10.6%

higher than that of the Paste matrix-NAC. In comparison, the hardness of each region was similar, but the numerical difference was consistent with the elastic modulus.

Table 6.4 Micromechanical properties of ITZs and adjacent paste matrix

Indent regions	Micromechanical properties	
	Elastic modulus (GPa)	Hardness (GPa)
ITZ-NAC	14.46 ±2.85	0.81 ±0.28
Paste matrix-NAC	16.74 ±1.06	1.01 ±0.19
Old ITZ-RAC	14.44 ±0.46	0.67 ±0.07
Old paste matrix-RAC	18.52 ±4.44	1.07 ±0.44
New ITZ-RAC	23.97 ±1.84	0.85 ±0.14
New paste matrix-RAC	24.54 ±3.25	1.16 ±0.55

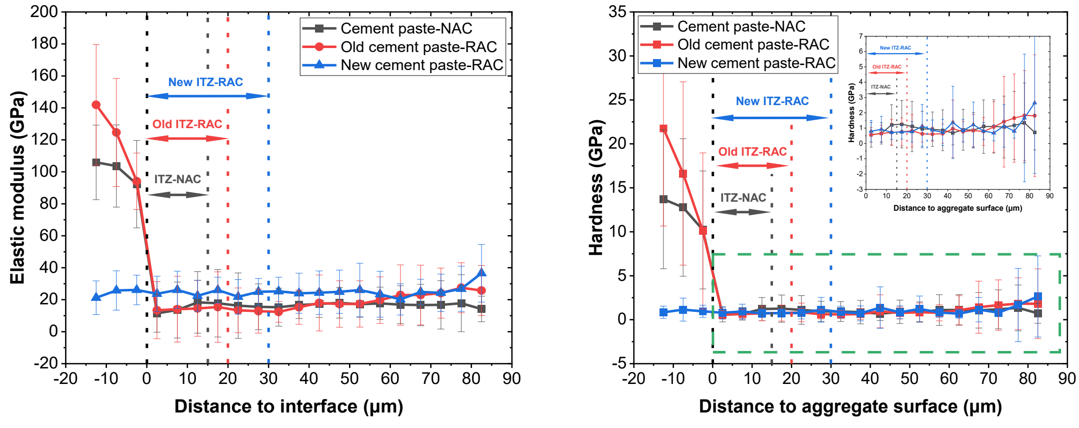

(a) Elastic modulus (b) Hardness

Figure 6.10 Nanoindentation test results of different ITZs and corresponding adjacent matrix

6.3.3 Porosity and pore diameter distribution within ITZs

Figure 6.11 shows the variation of pores and cracks volume fraction from ITZ to paste matrix in NAC and RAC. It is evident that the "wall effect" of the ITZ-NAC and Old ITZ-RAC in contact with NCA was the most prominent. The volume fraction of pores and cracks reached 18.7% at a distance of 2.5 μm from the aggregate boundary, followed by rapidly dropping to a stable value. The porosity of the old ITZ and old paste matrix in RAC was higher than that of the corresponding regions in NAC. In comparison, the volume fraction of pores and cracks in the New cement paste-RAC constantly showed a stable and slightly decreasing trend with the distance from the aggregate boundary.

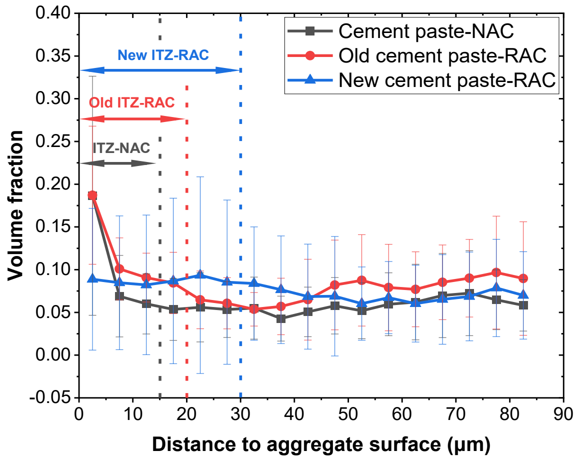

Figure 6.11 Proportion statistical results of pores and cracks distribution in ITZs and adjacent matrix

The pores and cracks of the ITZ and the paste matrix within 50 μm from the outside of the ITZ were captured according to the grey threshold. The equivalent circle diameter was calculated based on the area of pores and cracks. The cumulative porosity of ITZ and adjacent paste matrix in NAC and RAC was shown in Figure 6.12. As seen in Figure 6.12

(a), most of pores in ITZ-NAC were larger than those in Paste matrix-NAC. In contrast, there was no significant difference in Old cement paste-RAC and New cement paste-RAC in each equivalent diameter range (see Figure 6.12 (b) and (c)).

For a more detailed comparison of the pore size distribution in the ITZ and paste matrix, the proportion of pores and cracks with an equivalent diameter of 0.1-10 μm was shown in Figure 6.13. According to Figure 6.13, no matter ITZ or paste matrix, there were three obvious peaks at 0.25 μm, 0.65 μm and 1.5 μm. Pores and cracks with equivalent diameter of approximately 0.25 μm, 0.65 μm and 1.5 μm are considered in this study as slight defects, moderate defects and severe defects, which are segmented by green, light blue and orange in Figure 6.13. It can be seen that ITZ-NAC and Paste matrix-NAC possessed the lowest proportion of slight defects, which were 38.5% and 41.1%, respectively. However, the proportions of moderate defects (7.9% for ITZ-NAC and 7.1% for Paste matrix-NAC) and severe defects (10.3% for ITZ-NAC and 9.6% for Paste matrix-NAC) were the highest. Despite the same water-cement ratio, the proportion of slight defects in New cement paste-RAC was higher than that of Cement paste-NAC, and the proportion of moderate and severe defects was lower than that of Cement paste-NAC. The percentages of three types of defects were 44.9%, 5.6% and 8.0% respectively for New ITZ-RAC and 45.0%, 5.6% and 7.7% respectively for New paste matrix-RAC. As explained earlier, the bleeding phenomenon of NCA resulted in a higher proportion of large size pores and cracks in the ITZ and adjacent paste matrix. It was also pointed out in the Pope et al.'s research (1992) that the porosity in the concrete ITZ depended on the relative humidity in the aggregate surface. Furthermore, it is important to note that natural aggregate lacks the secondary hydration function found in old mortar. The continuous, long-term hydration of old mortar actually enhanced the bond with new mortar. Due to longer curing age, Old ITZ-RAC had the highest percentage of slight defects, while the lowest percentages of moderate and severe defects, which were 46.4%, 5.2% and 7.0%, respectively. Similarly, the proportions of the three kinds of defects in Old paste matrix-RAC were 46.6%, 5.3% and 7.8%, respectively.

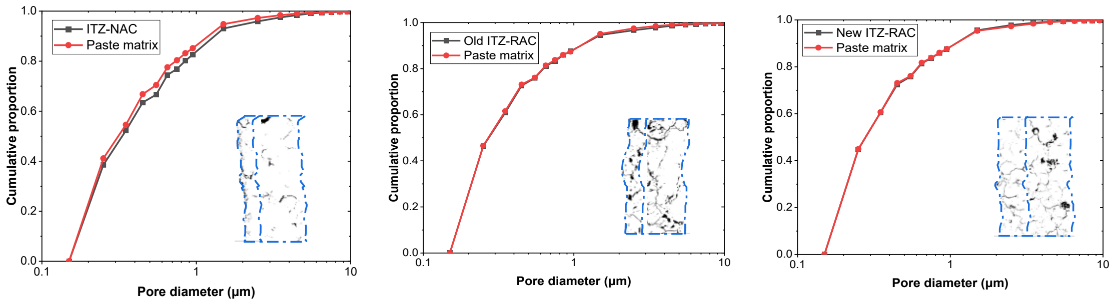

(a) Cement paste-NAC (b) Old cement paste-RAC (c) New cement paste-RAC

Figure 6.12 Equivalent porosity of different ITZs and adjacent matrix

The average percentages of pores and cracks, unreacted products and reacted products in the ITZ and corresponding paste matrix obtained through image analysis are listed in Table 6.5. For pores and cracks in ITZ and paste matrix, consistent with the above results, the average volume fraction of ITZ-NAC was 1.83% higher than New ITZ-RAC. However, as the distance from the aggregate boundary increases, the influence of free water attached to the aggregate surface weakened, and the average volume fraction of pores and cracks in Paste matrix-NAC was 1.21% lower than that in New paste matrix-RAC. The average volume fractions of pore and cracks in the old ITZ and old paste matrix in RAC were the highest, which were 11.58% and 7.6%, respectively. This is mainly related to the water-cement ratio of the old mortar and the cracks created in the old mortar during the crushing process. For unreacted products, the proportion in the ITZ was consistently lower compared to paste matrix. Among them, the old cement paste in RAC had the lowest difference because of the longer curing age. The reaction product content in ITZ was always lower than paste matrix, but in the new cement paste of RAC, the reaction product volume fraction of new ITZ reached 78.36%, which was higher than

76.52% in new paste matrix. A small amount of incompletely hydrated cement clinkers in the old paste matrix secondary hydrated during the curing process, which promoted the hydration degree in the New ITZ-RAC.

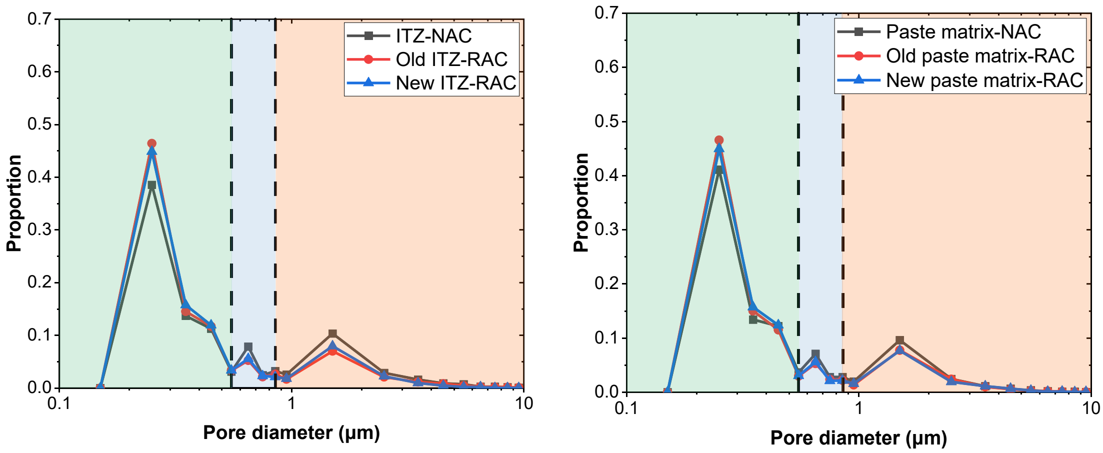

(a) ITZs (b) Paste matrix

Figure 6.13 Equivalent pore diameter distribution of different ITZs and adjacent matrix

Note: green, light blue and orange areas represent slight defects, moderate defects and severe defects respectively.

Table 6.5 Contents of pores and cracks, unreacted products and reaction products within ITZs and adjacent paste matrix

Regions	Constituents proportion		
	Pores and Cracks	Unreacted products	Reaction products
ITZ-NAC	10.52% ±5.77%	13.37% ±3.30%	76.12% ±2.54%
Paste matrix-NAC	5.77% ±0.75%	17.94% ±1.57%	76.29% ±2.22%
Old ITZ-RAC	11.58% ±4.16%	11.90% ±3.01%	76.51% ±1.54%
Old paste matrix-RAC	7.60% ±1.36%	12.49% ±0.89%	79.91% ±1.87%

New ITZ-RAC	8.69% ±0.36%	12.95% ±1.92%	78.36% ±1.89%
New paste matrix-RAC	6.98% ±0.69%	16.50% ±1.86%	76.52% ±1.99%

6.3.4 Failure modes of RAC under confining pressure and pore water pressure

The failure modes of concrete specimens under various stress states are shown in Figure 6.14. The RCA replacement ratio had no significant effect on the failure patterns of the specimens. Under uniaxial compression, NAC-0 and RAC50-0 and RAC100-0 were damaged most severely. Multiple longitudinal main cracks appeared on the surface of the concrete specimen, showing a radial splitting failure mode. For the concrete specimens damaged by triaxial compression, the damage severity was obviously alleviated. The longitudinal crack with branches was replaced by an oblique crack. At this time, the concrete specimen presented a shear failure mode, which is consistent with existing knowledge (He & Zhang 2014, Xu, et al. 2021b). Under the confining pressure combined with pore water pressure condition, the damage degree of concrete specimens was further reduced when the target radial strain was reached. At this time, there were no obvious main cracks on the surface of three groups of concrete, because the internal friction between cement particles was weakened by pore water, and many fine cracks appeared on the concrete surface.

NAC-0 NAC-3 NAC-7 NAC-14 NAC-14-5 NAC-14-9 NAC-14-13

Figure 6.14 Failure modes of RAC under triaxial compression and pore water pressure

6.3.5 Stress-strain curves analysis

The measured stress-strain curves of NAC and RAC under different stress states are shown in Figure 5.15. The corresponding stress parameters, peak strength, axial peak strain, radial peak strain, maximum volumetric strain and elastic modulus are given in Table 6.6. The elastic modulus was obtained according to ASTM C469 as follows:

$$E = \frac{40\% f_c - \sigma_1(0.005\%)}{\varepsilon_1(40\% f_c) - 0.005\%} \tag{6.1}$$

Where, $\sigma_1(0.005\%)$ and $\varepsilon_1(40\% f_c)$ represents the axial stress when the axial strain is 0.005% and the axial strain when the axial stress reaches $40\% f_c$, respectively.

Table 6.6 Mechanical properties of NAC and RAC obtained from stress-strain curves

Specimens	σ_c	σ_p	f_c (MPa)	S.D.	ε_{3p}	ε_{1p} or ε_{2p}	ε_{vp} (%)	E	S.D.

	(MPa)	(MPa)			(%)	(%)		(GPa)	
NAC-0	0	0	29.36	1.66	0.101	-0.159	0.0485	30.35	1.36
NAC-3	3	0	61.38	1.93	0.381	-0.466	0.1285	35.71	1.24
NAC-7	7	0	76.99	2.31	0.911	-0.611	0.2794	35.51	2.21
NAC-14	14	0	124.31	1.34	0.973	-0.430	0.3982	42.10	1.07
NAC-14-5	14	5	100.79	1.68	0.924	-0.559	0.2784	53.09	3.03
NAC-14-9	14	9	74.98	3.21	0.784	-0.789	0.0642	60.54	2.15
NAC-14-13	14	13	52.9	1.12	0.273	-0.248	0.2168	67.82	1.69
RAC50-0	0	0	33.35	2.58	0.099	-0.372	0.0252	40.59	2.16
RAC50-7	7	0	93.81	1.62	0.899	-0.768	0.2118	30.96	3.56
RAC50-14	14	0	125.87	2.06	1.070	-0.411	0.4781	38.72	2.45
RAC50-14-5	14	5	103.1	1.24	0.998	-0.744	0.1551	52.93	2.36
RAC50-14-13	14	13	71.5	2.33	0.312	-0.551	0.1214	65.68	1.87
RAC100-0	0	0	37.26	2.15	0.120	-0.638	0.0365	42.51	1.69
RAC100-3	3	0	71.68	1.98	0.348	-0.259	0.1282	48.61	2.15
RAC100-7	7	0	98.95	2.13	0.569	-0.188	0.2934	40.90	1.57
RAC100-14	14	0	128.42	1.19	1.263	-0.130	0.4541	45.69	2.36
RAC100-14-5	14	5	97.7	0.96	1.472	-1.104	0.3227	41.97	3.14
RAC100-14-9	14	9	94.44	1.25	1.841	-1.213	0.51	28.84	3.41
RAC100-14-13	14	13	98.03	2.16	2.23	-1.784	0.1373	61.48	2.21

Note: σ_c represents confining pressure; σ_p represents pore water pressure; f_c represents compressive strength; ε_{3p} represents axial peak strain; ε_{1p} and ε_{2p} represent radial peak strain; ε_{vm} represents the maximum volumetric strain; E represents elastic modulus; S.D. represents standard deviation.

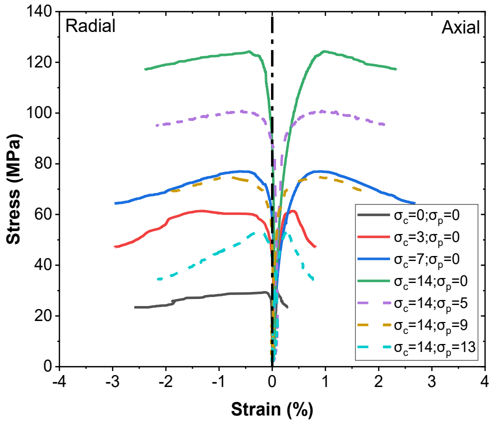

(a) NAC

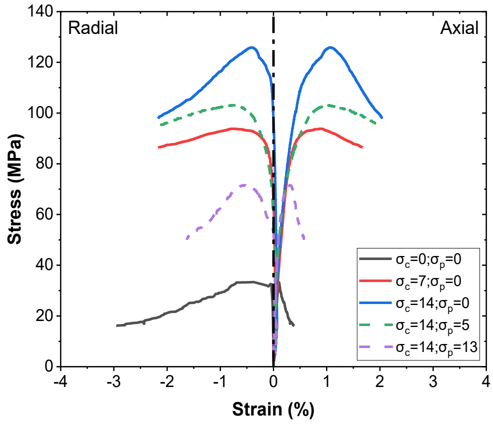

(b) RAC50

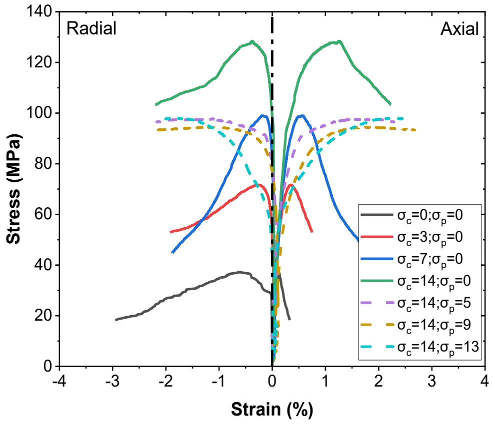

(c) RAC100

Figure 6.15 Stress-strain curves of concrete samples under triaxial compression

6.3.5.1 Influence of confining pressure on the stress-strain curves

It is easy to be conscious of the contribution of lateral confinement to the compressive strength and ductility of concrete samples from stress-strain curves in Figure 6.15. Under uniaxial compression, the concrete specimen quickly entered the descending section after reaching the peak stress. During the entire compression process, the axial deformation of the specimens was small, while after fully failure, the radial strain increased rapidly as the stress decreased due to the lack of lateral confinement. In comparison, the triaxial compression strength of concrete specimens increased significantly compared to uniaxial compression. For example, Figure 6.15 (a) shows that the compressive strength of the

NAC specimen improved from 29.36 MPa under uniaxial compression to 124.31 MPa when the confining pressure was 14 MPa. This phenomenon can be attributed to the fact that the lateral positive confinement restrained the lateral deformation and crack propagation. In addition, lateral pressure enhanced the internal friction between the coarse aggregate, fine aggregate and C-S-H gel, which improved the external force required for the shear-slip failure of the specimens.

It can also be seen from the rising section of the stress-strain curve that after the initial linear growth, the stress rising rate of the concrete specimens under triaxial compression gradually slowed down with the strain, and this plasticity stage become more apparent with the increase of confining pressure. Correspondingly, the peak axial strain of concrete specimens increased with the confining pressure. For NAC, it increased from 0.101% under uniaxial compression to 0.973% when the confining pressure was 14 MPa. After passing the peak point, unlike the uniaxial compression, the stress-strain curve of concrete specimens under high confining pressure had a gentler descending section, showing an obvious plastic failure characteristic. However, compared with the axial stress and axial deformation, the variation law of the radial peak strain and elastic modulus of concrete specimens with confining pressure was not obvious. Similar observations were also found in the studies of Chen et al. (2019) and Folino et al. (2014). This may be attributed to the combined effect of lateral confinement and plasticization of concrete specimens under high confining pressure.

6.3.5.2 Influence of RCA replacement ratio and ITZs on the stress-strain curves

The uniaxial compressive strength of RAC50 and RAC100 were 33.35 MPa and 33.76 MPa, respectively, which were higher than that of NAC. This trend continued to triaxial compression (125.87 MPa for RAC50-14 and 128.42 MPa for RAC100-14 vs. 124.31

MPa for NAC-14). According to Vargas et al. (2017), when concrete specimens is under compression, ITZ often experiences stress concentration, which determines the compressive strength of concrete. However, the nanoindentation test results in Table 6.4 show that the micromechanical properties of the old and new ITZs and adjacent cement paste of RAC were higher than those of the corresponding regions in NAC. In addition, by comparing the porosity in Table 6.5, the porosity of the old ITZ-RAC was similar to that of ITZ-NAC, while the porosity of the new ITZ-RAC was lower than that of ITZ-NAC. As a result, the uniaxial and triaxial compressive strength of RAC was higher than that of NAC.

For the stress-strain curves of the RAC, another noteworthy difference from the NAC occurred in the descending section. The descending sections of the stress-strain curves for RAC50-14, RAC100-7 and RAC100-14 are steeper than the descending sections of NAC at the same stress states. From the nanoindentation test results from Table 6.4, ITZ-RAC and Paste matrix-RAC showed better micromechanical properties than ITZ-NAC and Paste matrix-NAC. Therefore, RAC showed more brittle damage characteristics under triaxial compression, although the lateral confinement increased its plastic deformation capacity compared to uniaxial compression.

6.3.5.3 Influence of pore water pressure and ITZs on the stress-strain curves

Similar to the confining pressure, the pore water pressure can also significantly change the concrete triaxial compressive stress-strain trend. For NAC and RAC50, the peak stress and axial peak strain of specimens gradually decreased, whereas the elastic modulus increased with pore water pressure as shown in Figs. 6.15 (a) and (b). As explained earlier, pore water weakened the internal friction that contributed prominently to concrete triaxial compressive strength. The slip between the failure surface was easier by the lubricating effect of pore water. In addition, the infiltration of pore water under compression contributed more to the propagation of initial microcracks, resulting in a decrease in compressive strength. RAC100 is different from NAC and RAC50. Under 5 MPa pore water pressure, the triaxial compressive strength of RAC100 decreased to around 98 MPa and maintained at this value when the pore water pressure improved to 9 MPa and 13 MPa as shown in Figure 6.15 (c). However, the axial peak strain increased with pore water pressure. This stress-strain form is similar to the changing pattern of stress-strain curves of concrete with different saturations under high confining pressure by Vu and Malecot et al. (2019, 2009). It can be seen that pore water pressure had a great influence on the ultimate stress of low strength concrete. For RAC100, the micromechanical properties of old and new ITZs and paste matrix were better than those corresponding regions within NAC. Moreover, RAC had less severe defects which reduce mechanical properties. During compression, the supporting effect of pore water pressure became more pronounced, improving the axial peak strain of RAC before destruction.

6.3.5.4 Detailed mechanical properties analysis

In order to further compared the influence of confining pressure and pore water pressure on the mechanical properties of NAC and RAC, peak stress, peak strain and elastic modulus were normalised. The corresponding data are shown in Figure 6.16. It can be seen from Figure 6.16 (a) that as the confining pressure increased, the normalised axial stress increased gradually, and the improving rate of NAC and RAC was similar. However, when pore water pressure existed, the normalised axial stress of NAC decreased gradually with pore water pressure. The normalised axial stress of RAC50 also showed a decreasing trend with pore water pressure, but the descending rate was slightly lower than that of NAC, because NAC had higher severe defects (see Figure 6.13). For RAC100, when it suffered pore water pressure, the normalised axial stress dropped rapidly from 3.45, without pore water pressure, to 2.62, and no longer changed significantly with the increase of pore water pressure. This is because RAC possessed better micromechanical properties and microstructure performance according to data in Section 3.2 and 3.3. In this condition, the supporting effect of pore water was more prominent, but the promoting effect on cracks expansion was not obvious.

As shown in Figure 6.16 (b), due to the positive lateral confinement, the normalised axial strain of NAC and RAC50 increased gradually with the confining pressure, while the pore water pressure accelerated the expansion of microcracks, so that the normalised axial strain gradually decreased. It should be noted that due to better micromechanical properties of RAC100, the supporting effect of pore water pressure was more obvious, which improved the normalised axial peak strain to 18.58 under the 14 MPa confining pressure and 13 MPa pore water pressure. In contrast, the variation law of normalised radial strain under different confining pressure and pore water pressure was not clear in Figure 6.16 (c). Only RAC100 showed an increasing trend in the normalised radial strain when the pore water pressure existed.

The normalised elastic modulus did not vary obviously under different confining pressure, and the values of the three types of concrete were ranged between 0.7 and 1.4, as shown in Figure 6.16 (d). However, with the increase of pore water pressure, the normalised elastic modulus of concrete specimens increased gradually except for RAC100-14-9. As explained earlier, the pore water pressure enhanced the initial stiffness of concrete specimens under compression.

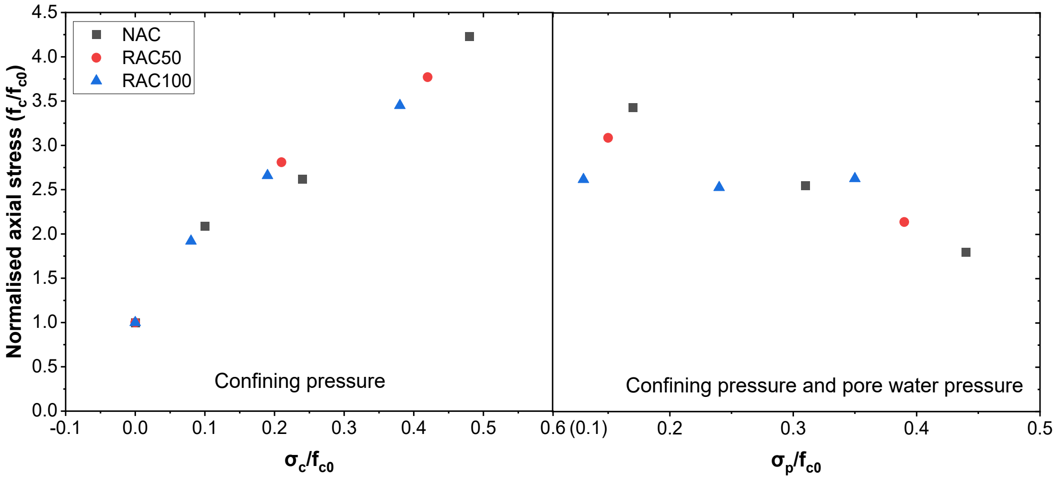

(a) Contribution of confining pressure and pore water pressure to peak stress

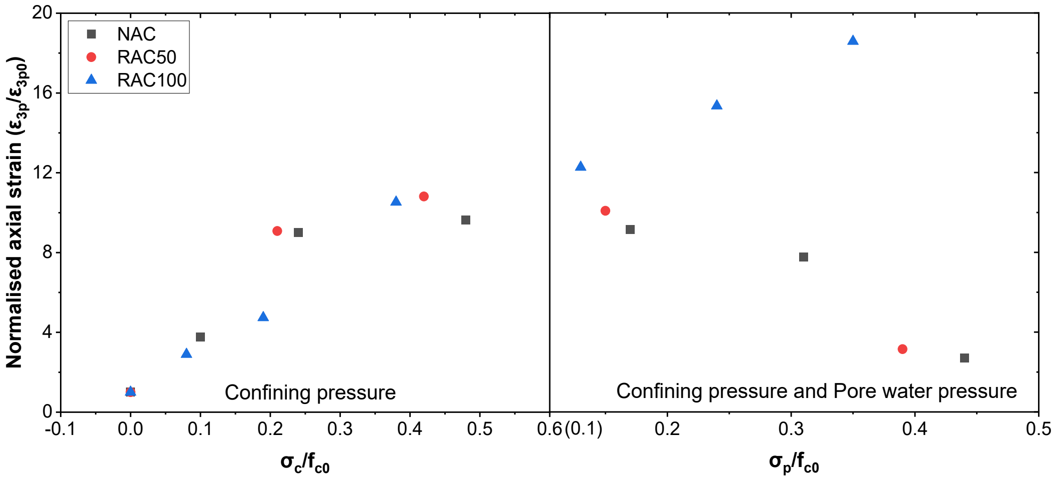

(b) Contribution of confining pressure and pore water pressure to axial strain

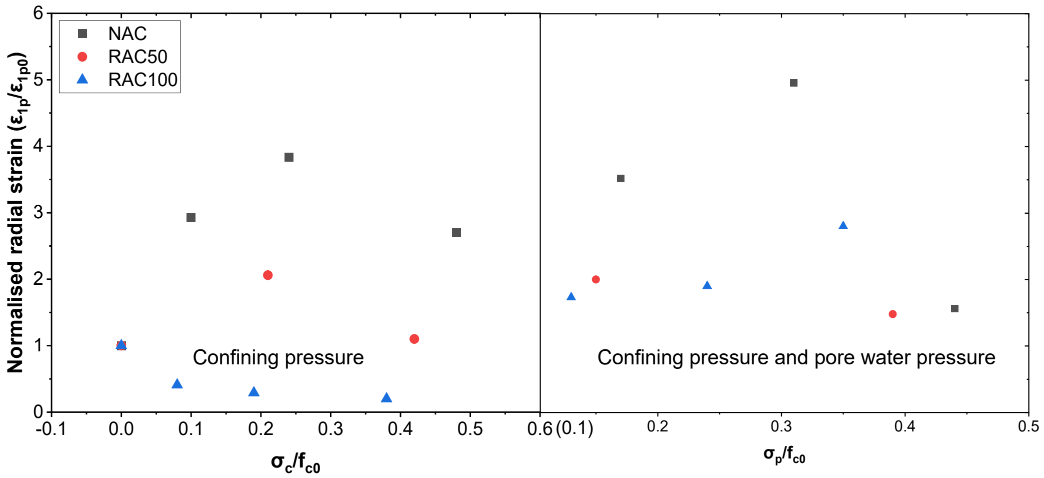

(c) Contribution of confining pressure and pore water pressure to radial strain

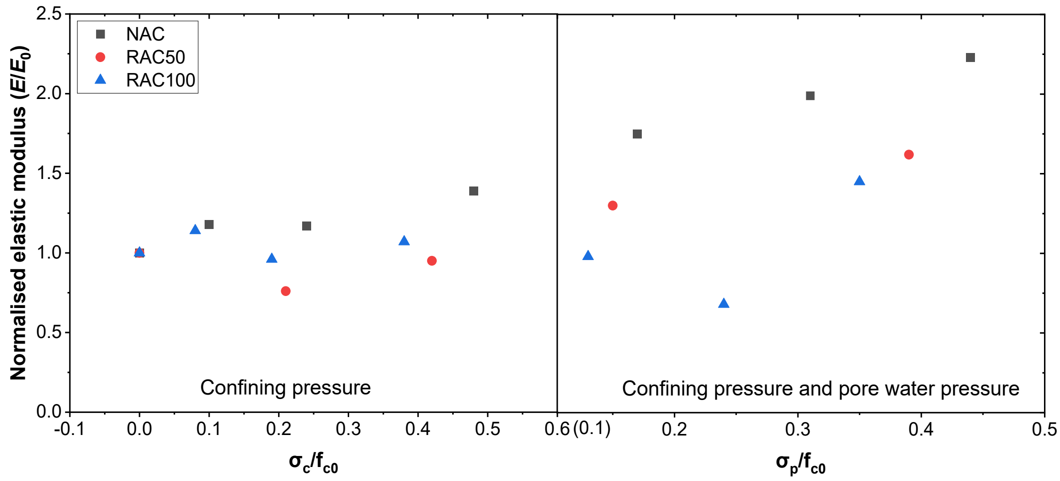

(d) Contribution of confining pressure and pore water pressure to elastic modulus

Figure 6.16 Limit state of RAC under triaxial compression and pore water pressure

6.3.6 Axial stress-volumetric strain analysis

The volumetric strain of concrete specimens can be calculated according to the equation $\varepsilon_v = \varepsilon_1 + \varepsilon_2 + \varepsilon_3$. The relationship curves of volumetric strain and axial stress of NAC and RAC under different stress states are shown in Figure 6.17. The maximum volumetric strains of both NAC and RAC gradually increased with confining pressure, mainly because the lateral confinement enhanced the plastic deformation ability of concrete before failure. However, when a 13 MPa pore pressure existed, the maximum volumetric strain of NAC, RAC50 and RAC100 decreased from 0.3982%, 0.4781% and 0.4541%, without pore water pressure, to 0.2168%, 0.1214% and 0.1373%, respectively. This is because the pore water pressure promoted crack propagation and accelerated the collapse of the specimen. It is noteworthy that the maximum volumetric strain of RAC100-14-9 increased compared to RAC100-14-5. This is because RAC100 had a higher uniaxial compressive strength. Pore water was trapped within the pore structure and the supporting effect was more significant, which enhanced the compressive deformation capacity of RAC specimens.

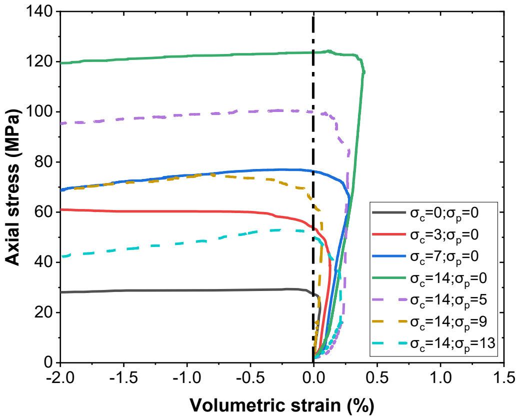

(a) NAC

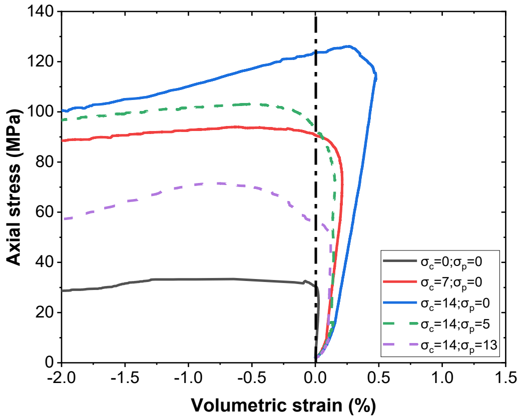

(b) RAC50

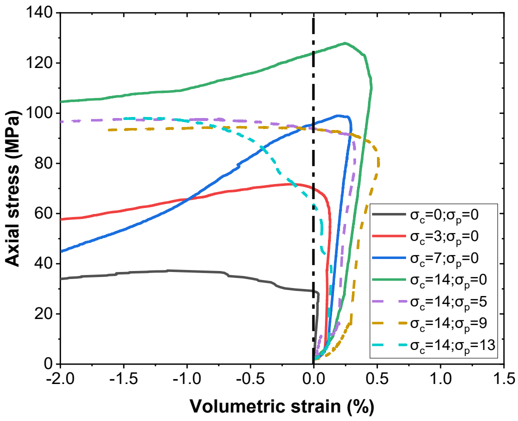

(c) RAC100

Figure 6.17 Axial stress-volumetric strain curves of concrete samples under triaxial compression

The contribution of confining pressure and pore water pressure to the normalised maximum volumetric strain is shown in Figure 6.18. It can be clearly seen that with the increase of confining pressure, the normalised volumetric strain increased gradually, while the growth rate of NAC was slower. When subjected to pore water pressure, the normalised volumetric strain decreased to 4-8 compared to uniaxial compression, except for RAC100-14-9 (σ_p/f_{c0}=0.24). As explained earlier, the RAC100 had a higher uniaxial compressive strength. 9 MPa of pore water pressure provided better support for the RAC skeleton. Therefore, the deformation capacity of RAC100-14-9 was enhanced.

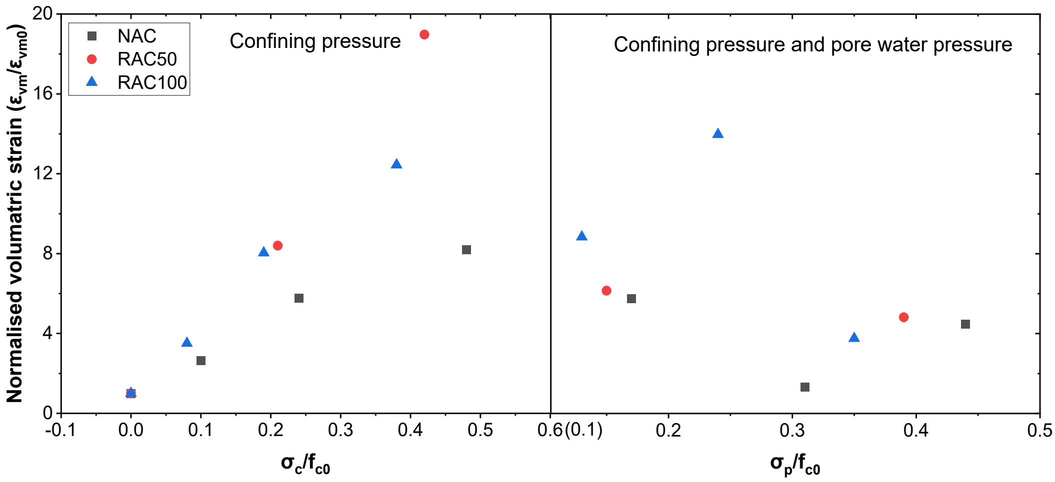

Figure 6.18 Limit volumetric strain of RAC under triaxial compression and pore water pressure

6.4 Failure criteria

6.4.1 Triaxial compression

6.4.1.1 Mohr-Coulomb failure criterion

The Mohr-Coulomb failure criterion has been widely used to describe the failure surface of concrete under triaxial compression. It assumes that the triaxial compressive strength of concrete has a linear relationship with the confining pressure. The expression is as follows (Li, et al. 2022a):

$$\frac{f_c}{f_{c0}} = k\frac{\sigma_c}{f_{c0}} + 1 \tag{6.2}$$

where, f_c and f_{c0} are the triaxial compressive strength and uniaxial compressive strength of concrete, respectively. σ_c is the confining pressure. k is a parameter related to the internal friction angle, which needs to be obtained by regression analysis on experimental data. According to Li et al. (2022a), recycled aggregate would not affect the internal frication angle of concrete under triaxial compression. Therefore, the relationship between the triaxial compressive strength and confining pressure of NAC and RAC can be expressed by the same linear equation:

$$\frac{f_c}{f_{c0}} = 6.96\frac{\sigma_c}{f_{c0}} + 1 \tag{6.3}$$

The experimental data and fitting curve are shown in Figure 6.19. The triaxial compressive strength and confining pressure of NAC and RAC showed a strong linear relationship (R^2=0.953).

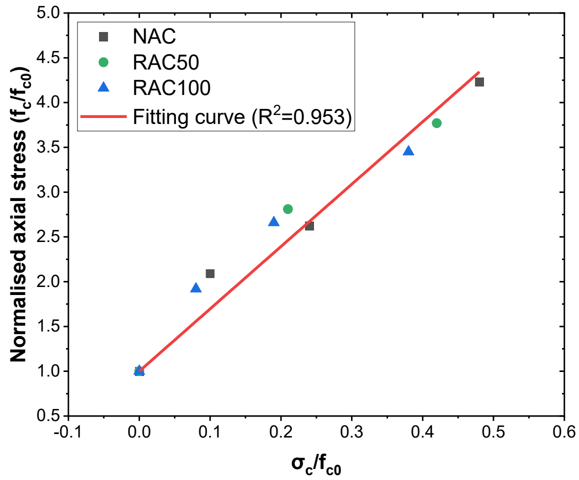

Figure 6.19 Mohr-Coulomb failure criteria for RAC under triaxial compression

6.4.1.2 William-Warnke failure criterion

The William-Warnke failure criterion is another three-parameter model. It can be used to describe the relationship between the principal shear stress and mean principle stress of concrete in triaxial compression as shown in Eqs. (6.4) to (6.6) (Wu, et al. 2023).

$$\frac{\tau_m}{f_{c0}} = a_1 + b_1\left(\frac{\sigma_m}{f_{c0}}\right) - c_1\left(\frac{\sigma_m}{f_{c0}}\right)^2 \tag{6.4}$$

$$\sigma_m = \frac{1}{3}(\sigma_1 + \sigma_2 + \sigma_3) \tag{6.5}$$

$$\tau_m = \frac{1}{\sqrt{15}}\sqrt{(\sigma_1-\sigma_2)^2+(\sigma_1-\sigma_3)^2+(\sigma_2-\sigma_3)^2} \tag{6.6}$$

where τ_m and σ_m represent the principal shear stress and mean principal stress of concrete specimens, respectively. a_1, b_1 and c_1 are the corresponding parameters. Through the regression analysis of the experimental data in the present study, the expression of the William-Warnke failure criterion of NAC and RAC can be written as Eq. (6.7).

$$\frac{\tau_m}{f_{c0}} = -0.045 + 0.806\left(\frac{\sigma_m}{f_{c0}}\right) + 0.109\left(\frac{\sigma_m}{f_{c0}}\right)^2 \tag{6.7}$$

The testing data and the fitting curve are shown in Figure 6.20. It can be seen that the fitting performance of the William-Warnke failure criterion can achieve a better fitting results than Mohr-Coulomb failure criterion. The rising rate of principal shear stress of NAC with confining pressure is close to that of RAC50 and RAC100.

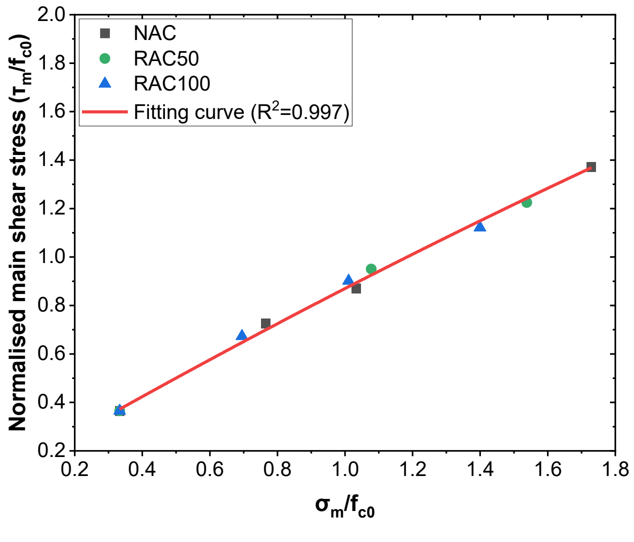

Figure 6.20 William-Warnke failure criteria for RAC under triaxial compression

6.4.1.3 Power-Law failure criterion

The Power-Law failure criterion is a two-parameter exponential model as shown in Eq. (6.8) (Jiang, et al. 2023).

$$\frac{f_c}{f_{c0}} = a_2\left(\frac{\sigma_c}{f_{c0}}\right)^{b_2} + 1 \tag{6.8}$$

where, a_2 and b_2 are parameters, which are calculated to be 5.13 and 0.70 respectively through the experimental data. Therefore, the Power-Law failure criterion equation of NAC and RAC can be written as:

$$\frac{f_c}{f_{c0}} = 5.13\left(\frac{\sigma_c}{f_{c0}}\right)^{0.7} + 1 \tag{6.9}$$

It can be seen from Figure 6.21 that the Power-Law failure criterion can achieve a satisfying fitting performance (R^2=0.989) on the limit states of NAC and RAC under triaxial compression, which is consistent with the conclusion of Wu et al. (2023).

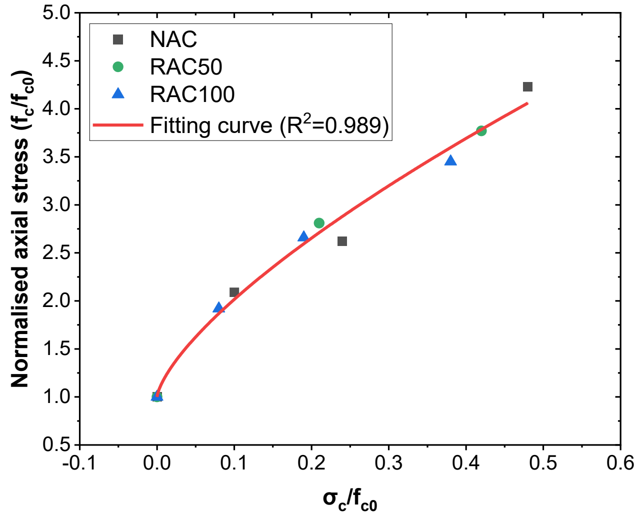

Figure 6.21 Power-Law failure criteria for RAC under triaxial compression

6.4.2 Triaxial compression with pore water pressure

At present, there are few failure criterion theoretical models suitable for analysing the coupling effect of confining pressure and pore water pressure on RAC. Based on experimental data, as shown in Figure 6.16 (a), it can be roughly concluded that the triaxial compressive strength of NAC and RAC50 under the 14 MPa confining pressure decreased linearly with the increase of pore water pressure. Therefore, we assume that the triaxial compressive strength and pore water pressure of NAC and RAC50 have the following relationship:

$$f_c = k_2\sigma_p + f_{c14} \tag{6.10}$$

where, f_c and f_{c14} are the triaxial compressive strength and triaxial compressive strength with a confining pressure of 14 MPa, respectively. σ_p is the pore water pressure. The fitting curves of NAC and RAC50 can be obtained from the experimental data as Eqs. (6.11) to (6.12).

NAC $$f_c(NAC) = -5.42\sigma_p + f_{c14}(NAC) \tag{6.11}$$

RAC50 $$f_c(RAC50) = -4.23\sigma_p + f_{c14}(RAC50) \tag{6.12}$$

For RAC100, we can refer to the theoretical model Eq. (6.13) proposed by Malecot et al. (2019).

$$\sigma_{c-sat} = \sigma_{cp0} - \lambda\phi_{air}^{1/3} - \kappa\phi_{cap}^{1/3} \tag{6.13}$$

where, $\sigma_{c\text{-}sat}$ and σ_{cp0} are the triaxial compressive strength of saturated concrete specimen and dry concrete specimen, respectively. Φ_{air} and Φ_{cap} are entrained air porosity and capillary porosity, respectively. λ and κ are parameters.

In concrete, ITZs accounts for about 20%-30% of the total volume of cement paste (Scrivener 2004). Here, we take 25%. RAC100 possesses two kinds of ITZs as old ITZ and new ITZ, which are assumed to account for 50% of the total cement paste volume. According to Jayasuriya et al. (2018), the ratio of old mortar to new mortar is assumed to be 1:9. Combined with the micromechanical test data in this study, Eq. (6.13) is modified to the following Eq. (6.14) considering ITZ porosity and mortar porosity.

$$f_c(RAC100) = f_{c14}(RAC100) - \tag{6.14}$$

$$\alpha(\varphi_{old\ ITZ} + \varphi_{new\ ITZ}) \times 0.5 - \beta(\frac{1}{10}\varphi_{old\ mortar} + \frac{9}{10}\varphi_{new\ mortar}) \times 0.5$$

where, $\varphi_{old\ ITZ}$ and $\varphi_{new\ ITZ}$ are the porosity of old and new ITZ in RAC, respectively. $\varphi_{old\ mortar}$ and $\varphi_{new\ mortar}$ are the porosity of old and new mortar in RAC respectively. α and β are the parameters, which were calibrated as 210 and 235 respectively. The experimental data and fitting curves of three groups of concrete specimens are shown in Figure 6.22.

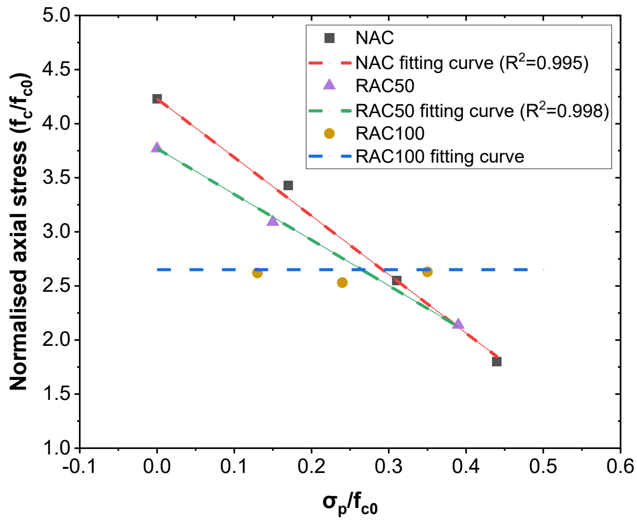

Figure 6.22 Failure criteria for RAC under triaxial compression with pore water pressure

6.5 Stress-strain model

6.5.1 Uniaxial compression

The stress-strain curves of NAC and RAC under uniaxial compression can be simply divided into ascending and descending sections. Tang et al. (2019) made a comprehensive comparison of the existing stress-strain empirical models of RAC specimens under uniaxial compression, and concluded that the model proposed by Collins and Mitchell (1991) is close to the experimental data. The experimental model can be express as:

$$\frac{\sigma_3}{f_{c0}} = \begin{cases} \dfrac{A_1\left(\dfrac{\varepsilon_3}{\varepsilon_{3p0}}\right)}{A_1 - 1 + \left(\dfrac{\varepsilon_3}{\varepsilon_{3p0}}\right)^{A_1}} & 0 \le \dfrac{\varepsilon_3}{\varepsilon_{3p0}} < 1 \\ \dfrac{A_1\left(\dfrac{\varepsilon_3}{\varepsilon_{3p0}}\right)}{A_1 - 1 + \left(\dfrac{\varepsilon_3}{\varepsilon_{3p0}}\right)^{A_1 B_1}} & \dfrac{\varepsilon_3}{\varepsilon_{3p0}} \ge 1 \end{cases} \tag{6.15}$$

Therefore, this study corrected the parameters of Collins and Mitchell model to predict the NAC and RAC uniaxial compression experimental data in Figure 6.15. For NAC, RAC50 and RAC100, parameter A_1 is 2.89, and parameter B_1 is 0.84. The fitting results are shown in Figure 6.23. It can be seen that the modified Collins and Mitchell model slightly underestimates the stress of the later decline section of NAC. A satisfactory fitting performance are achieved for the other sections and curves.

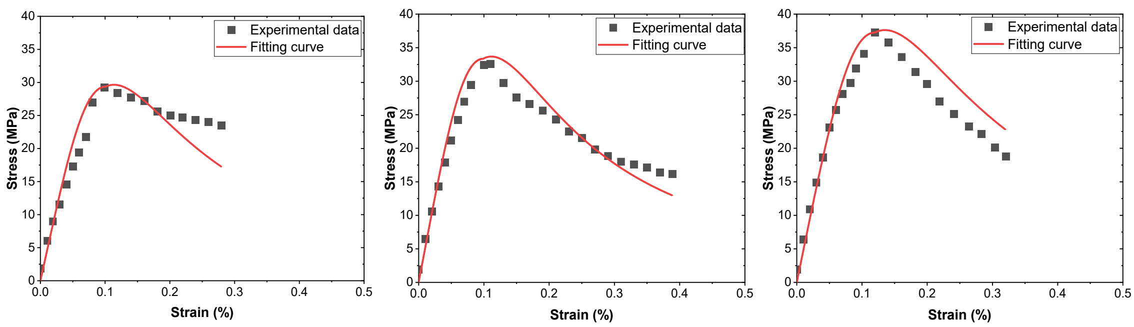

(a) NAC-0 (b) RAC50-0 (c) RAC100-0

Figure 6.23 Stress-strain fitting curves of NAC and RAC under uniaxial compression

6.5.2 Triaxial compression

For the stress-strain curves of NAC and RAC under triaxial compression, the model Eq. (6.16) proposed by Guo and Zhang (1982) was selected.

$$0 \le \frac{\varepsilon_3}{\varepsilon_{3p}} < 1 \tag{6.16}$$

$$\frac{\sigma_3}{f_c} = \begin{cases} A_2\left(\frac{\varepsilon_3}{\varepsilon_{3p}}\right) + (3-2A_2)\left(\frac{\varepsilon_3}{\varepsilon_{3p}}\right)^2 + (A_2-2)\left(\frac{\varepsilon_3}{\varepsilon_{3p}}\right)^3 & \frac{\varepsilon_3}{\varepsilon_{3p}} \geq 1 \\ \dfrac{\left(\frac{\varepsilon_3}{\varepsilon_{3p}}\right)}{B_2\left(\frac{\varepsilon_3}{\varepsilon_{3p}}-1\right)^2 + \left(\frac{\varepsilon_3}{\varepsilon_{3p}}\right)} & \end{cases}$$

The parameters were determined by regression analysis, in which A_2 and B_2 for NAC were 3.36 and 0.19; A_2 and B_2 for RAC50 and RAC100 were 3.41 and 0.74, respectively. The fitting results are shown in Figs. 6.24. It can be seen that, there is a certain difference between the fitting results and test data in the descending sections of NAC-3, NAC-14 and RAC50-7. However, the fitting results of rest curves have a satisfying degree of agreement.

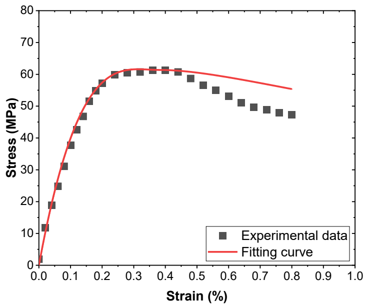

(a) NAC-3

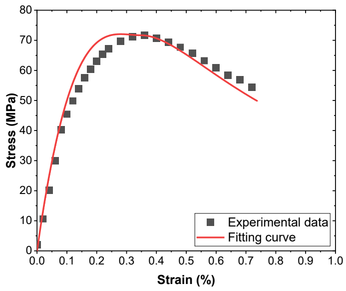

(b) RAC100-3

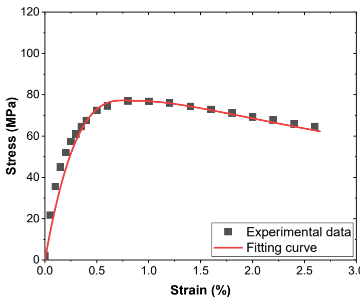

(c) NAC-7

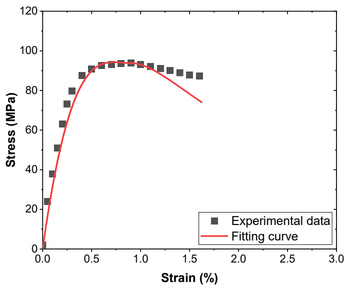

(d) RAC50-7

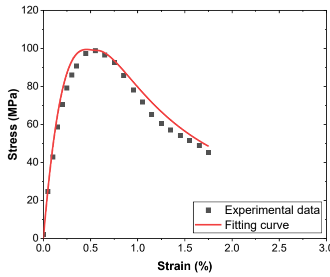

(e) RAC100-7

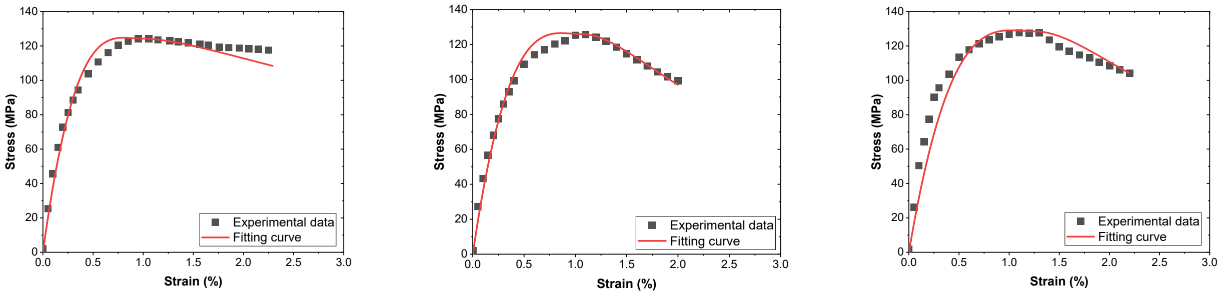

(f) NAC-14 (g) RAC50-14 (h) RAC100-14

Figure 6.24 Stress-strain fitting curves of NAC and RAC under triaxial compression

6.5.3 Triaxial compression with pore water pressure

It has been known in the analysis of the stress-strain curves in Figure 6.15 that the pore water pressure reduced the compressive strength of the concrete specimens under a fixed confining pressure and improved the elastic modulus. This characteristic is also reflected in the fitting analysis of stress-strain curves. As shown in Figure 6.25, the triaxial compressive stress-strain model Eq. (5-16) (Fitting curve-T in Figure 6.25) overestimates the compressive strength and underestimates the elastic modulus when concrete specimens were subjected to pore water pressure. Chen et al. (2019) proposed a new empirical model, which was originally developed from Euro Code CEB-FIP (1990) and Guo and Zhang (1982) model to predict the RAC stress-strain relationship. The Chen's model (2019) can be expressed as:

$$\frac{\sigma_3}{f_c} = \begin{cases} \dfrac{A_3\left(\dfrac{\varepsilon_3}{\varepsilon_{3p}}\right) - \left(\dfrac{\varepsilon_3}{\varepsilon_{3p}}\right)^2}{1 + (A_3 - 2)\left(\dfrac{\varepsilon_3}{\varepsilon_{3p}}\right)} & 0 \le \dfrac{\varepsilon_3}{\varepsilon_{3p}} < 1 \\[2ex] \dfrac{\dfrac{\varepsilon_3}{\varepsilon_{3p}}}{B_2\left(\dfrac{\varepsilon_3}{\varepsilon_{3p}} - 1\right)^2 + \left(\dfrac{\varepsilon_3}{\varepsilon_{3p}}\right)} & \dfrac{\varepsilon_3}{\varepsilon_{3p}} \ge 1 \end{cases} \tag{6.17}$$

It can be seen that the stress-strain model Eq. (6.17) (Fitting curve-C in Figure 6.25) has a better fitting performance on peak stress and slop of ascending sections. In Eq. (6.17), for NAC-14-5, NAC-14-9, RAC50-14-5, RAC100-14-5, RAC100-14-9, RAC100-14-13, the parameters A_3 and B_3 are 10.629 and 0.112. For NAC-14-13 and RAC50-14-13, the descending section of stress-strain curves are steeper. As a result, the parameters A_3 and B_3 are 3.254 and 0.592.

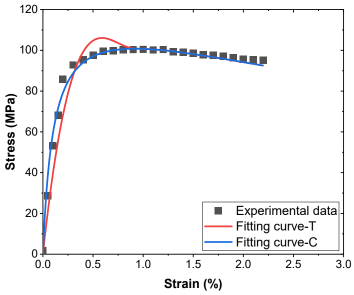

(a) NAC-14-5

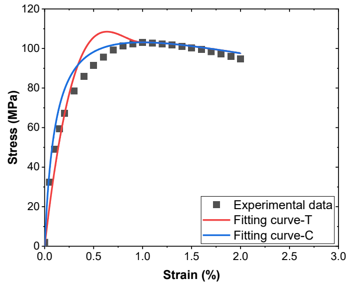

(b) RAC50-14-5

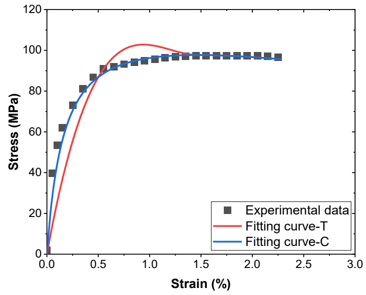

(c) RAC100-14-5

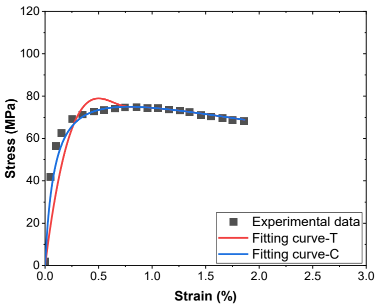

(d) NAC-14-9

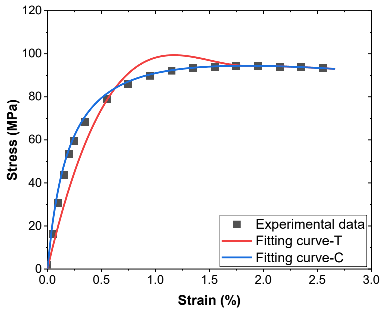

(e) RAC50-14-9

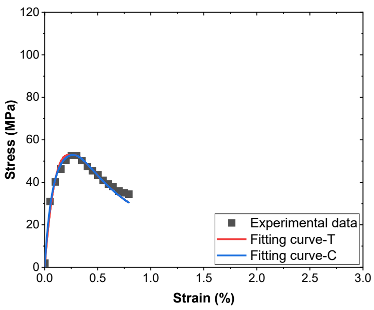

(f) NAC-14-13

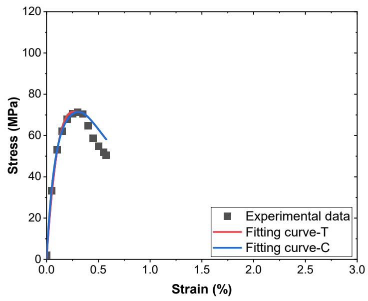

(g) RAC50-14-13

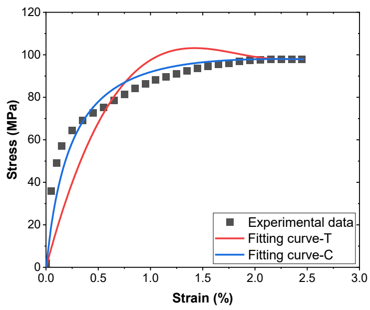

(h) RAC100-14-13

Figure 6.25 Stress-strain fitting curves of NAC and RAC under triaxial compression with pore water pressure

6.6 Conclusions

In this chapter, concrete specimens were made with RCA replacement ratio of 0%, 50% and 100%. BSE-Image analysis technique and nanoindentation were used to determine the ITZ width. The constituent composition and micromechanical properties of ITZs and adjacent paste matrix were compared. Subsequently, the 0-14 MPa confining pressure and 0-13 MPa pore water pressure were applied to NAC and RAC specimens, and the stress-strain curves under different stress states were obtained. The following conclusions can be drawn up:

(1) The micromechanical properties of ITZ are related to the characteristics of contact surface. Due to the rough surface of the old mortar and one year of continuous secondary hydration, the elastic modulus of New ITZ-RAC was 9.51 GPa, higher than that of ITZ-NAC with the same water-cement ratio. The micromechanical properties of adjacent paste matrix were less affected by the characteristics of contact surface, but the elastic modulus of New paste matrix-RAC was still 7.8 GPa higher than that of Paste matrix-NAC. The elastic modulus of Old ITZ-RAC was close to that of ITZ-NAC, about 14.44 GPa.

(2) Compared with New ITZ-RAC, ITZ-NAC had fewer small pores (0.2-0.3 μm) and more large pores (1-2 μm). The porosities of ITZ-NAC and Old ITZ-RAC were similar (10.52% and 11.58%, respectively), whereas the porosity of New ITZ-RAC in contact with old mortar was lower (8.69%).

(3) The compressive strength, axial peak strain and maximum volumetric strain of NAC and RAC increased gradually with the increase of confining pressure. The failure

pattern converted from radial splitting failure mode under uniaxial compression to shear-slip failure mode. Due to the higher elastic modulus and hardness of New ITZ-RAC and New paste matrix-RAC, RAC exhibited higher post-peak brittle failure characteristics. The variation law of elastic modulus and radial peak strain of concrete specimens with confining pressure was not obvious.

(4) When subjected to pore water pressure, NAC and RAC had decreased compressive strength and maximum volumetric strain, but increased elastic modulus with pore water pressure. For RAC100 with higher micromechanical properties, the supporting effect of pore water was more prominent. As a result, the axial peak strain of RAC100 increased with pore water pressure. However, NAC and RAC50 showed the adverse trend.

(5) Willam-Warnke failure criterion can well describe the relationship between principal normal stress and principal shear stress of NAC and RAC. The relationship between the peak stress and pore water pressure of NAC and RAC50 can be described by linear descending functions. However, the normalised axial stress of RAC100 dropped to about 2.6 and did not change obviously with pore water pressure. Its value can be described by the modified equation proposed by Malecot et al.

(6) The stress-strain model can well predict the stress-strain curves of NAC and RAC under uniaxial and triaxial compression. However, the triaxial compression model overestimated the peak stress and underestimated the elastic modulus when subjected to pore water pressure. In contrast, the empirical model proposed by Chen et al. can achieve a satisfactory fitting performance for the coupling state of confining pressure and pore water pressure.

CHAPTER 7. EFFECT OF PORE WATER PRESSURE ON TRIAIXAL COMPRESSION PERFORMANCE OF RECYCLED AGGREGATE/ GLASS SAND CONCRETE

7.1 Introduction

Waste crushed concrete and glass cullet can be used as coarse and fine aggregate respectively for concrete, namely RCA and RGS (Arabi, et al. 2019, Chen, et al. 2006). To understand the performance of sustainable concrete mixed with RCA and RGS, it is necessary to explore the constituent distribution and micromechanical properties within ITZ between aggregate and cement paste matrix, because ITZ is the weakest region where determines the mechanical properties and durability of concrete (Bravo, et al. 2017, Jayasuriya, et al. 2018, Tang, et al. 2022). The different surface morphologies and chemical activity of natural sand, old cement paste and RGS lead to differences in the microscopic performance of ITZs (Arabi, et al. 2019, Zhao, et al. 2013). Existing studies illustrate that better microscopic properties of ITZs resulted in a better mechanical property of concrete specimens (Bilondi, et al. 2018, Thomas, et al. 2018).

Up to now, no researcher has comprehensively evaluated the microscopic properties of ITZs and macroscopic mechanical properties of sustainable concrete containing RCA and RGS under complicated stress states. In this chapter, 4 groups of sustainable concrete specimens were produced by adjusting the contents of RCA and RGS. The micromechanical properties and microstructure of ITZs in sustainable concrete were evaluated by nanoscratch and BSE-based image analysis techniques. A triaxial multi-field coupled testing system (RTX-1000) was used to apply a confining pressure of 0-14 MPa and a pore water pressure of 0-13 MPa to Φ50×100 mm cylindrical concrete specimens, and the corresponding stress-strain curves were obtained. Finally, empirical models were calibrated and used to predict ultimate conditions and stress-strain curves of sustainable concrete under various stress states.

7.2 Experimental programme

7.2.1 Raw materials

Considering the size of concrete specimens (Φ50×100 mm) used for triaxial compression tests, the maximum particle size of coarse aggregate adopted to prepare concrete is 16 mm to meet the requirements of ASTM C-192. As shown in Figure 7.1, NCA, RCA, NFA and RGS were selected as aggregate for concrete in this study. The basic properties of aggregate are listed in Table 7.1. As expected, the apparent density of RCA was lower than that of NCA, whereas the water absorption and crushing index were higher than that of NCA because of the old mortar attached to the surface of RCA. The apparent density of NFA was lower than that of NCA and its water absorption ratio was close to that of NCA. The water absorption of RGS can be ignored, and the apparent density was the lowest among the four aggregate, which was 2530 kg/m^3. The particle size distribution curves of NFA and RGS are shown in Figure 7.2. General purpose Portland cement, tap water and Naphthalene-base superplasticizer were mixed together for concrete.

(a) Natural coarse aggregate (b) Recycled coarse aggregate

(c) Natural fine aggregate (d) Recycled glass sand

Figure 7.1 Coarse and fine aggregate for preparing concrete specimens

Table 7.1 Physical and mechanical properties of coarse and fine aggregate

	NCA	RCA	NFA	RGS
Size (mm)	5-16	5-16	0.15-4.75	0.15-4.75
Apparent density (kg/m^3)	2791.5	2736.5	2615	2530
Water absorption (wt. %)	1.375	5.91	1.44	~0
Crush index (wt. %)	17	22	-	-
Fineness modulus	-	-	2.80	2.61

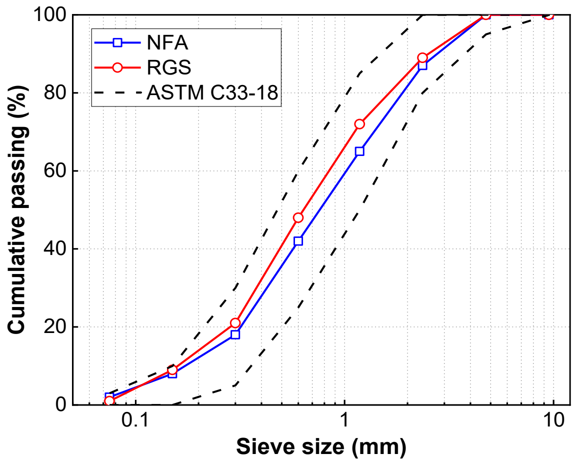

Figure 7.2 Particle size distribution of fine aggregate

7.2.2 Mixture design and specimen preparation

RCA had an obviously higher water absorption ratio, therefore, NCA and RCA were soaked in water for one day and allowed to a SSD state before preparing concrete. The detailed mixture proportion of concrete specimens in this study is shown in Table 7.2. The numbers following RA and RG represent the replacement ratio of RCA and RGS respectively. The coarse and fine aggregate was poured into a drum mixer and mixed for 1 minute, followed by cement and mixed together for another 1 minute. With the mixer running continuously, tap water mixed with superplasticizer was slowly added and then continued to operate for 2 minutes until the ingredients were even distributed. The slump value of each group of concrete mixtures was tested as soon as the mixer stopped and the test results are listed in the last column of Table 7.2. The slumps of NAC and RA50 were similar because NCA and RCA were in an SSD state before mixing. The slump of the fresh concrete mixture decreased significantly with RGS content improving because the sharp and angular surface of RGS increased the friction between particles. Fresh concrete mixture was added into Φ50×100 mm cylindrical moulds and vibrated until no large bubbles emerged. After curing in the mould for one day, the specimens were transferred to a standard environment for one year. The upper and lower surfaces of concrete specimens were smoothed to an error lower than 0.1 mm. The holes on the surface of specimens were sealed by cement paste with the same water-cement ratio, and then triaxial compression with pore water pressure experiments were conducted.

Table 7.2 Mixture proportion of NAC and RAC specimens

Mix. ID	Raw materials (kg/m^3)							Slump (mm)
	NCA	RCA	NFA	RGS	Cement	Water	SP	
NAC	1055	0	675	0	498	174	4.23	120
RA50	527.5	527.5	675	0	498	174	4.23	126
RA50RG50	527.5	527.5	337.5	337.5	498	174	4.23	105
RA50RG100	527.5	527.5	0	675	498	174	4.23	70

7.2.3 ITZs microscopic properties tests

7.2.3.1 Sample preparation

A thin concrete slice containing ITZs was cut out from the middle of the cylinder concrete specimen and subsequently was impregnated by epoxy resin. After the epoxy resin solidified, 120, 240, 600 and 1200 grit abrasive paper was used to grind the sample surface. Each grit of abrasive paper was ground for 10 minutes. 0.3 μm and 0.05 μm aluminium were used to polish the sample surface and each particle size of aluminium was polished for 30 minutes. To eliminate the interference of residual aluminium particles in pores and cracks on subsequent BSE-based image analysis and nanoscratch tests, the sample was placed in an ultrasonic bath for 2 minutes of cleaning. Finally, samples were dried in a vacuum oven at 60 °C for 48 h.

7.2.3.2 BSE-based image analysis

The surface of the sample impregnated by epoxy resin was coated with a layer of 6 nm gold. A scanning electron microscope (SEM, Zeiss EVO LS15) was used to acquire BSE images. For each ITZ, 30 BSE images with a magnification of 500 times were extracted. The contrast and brightness of each ITZ were kept consistent to facilitate image analysis.

Typical BSE images of ITZs and image analysis are shown in Figure 7.3. 15 of 5 μm-width strips were segmented from the aggregate or old mortar boundaries to paste matrix. It is reported that the ITZ width of concrete was approximately between 15-50 μm (Corr, et al. 2007, Pope & Jennings 1992, Scrivener, et al. 2004). As a result, it can be reasonably inferred that the divided cement paste area contained the entire ITZ and part of paste matrix. According to the grey threshold determination method proposed by Wong et al., (2006, 2009, 2006) the constituents in the cement paste can be divided into hydration products, unhydrated clinkers, pores and cracks, which are represented by green, white and black areas respectively in Figure 7.3 (f). By statistically analysing the areas of different coloured regions, the variation law of constituent proportions with the distance from the aggregate boundary can be obtained.

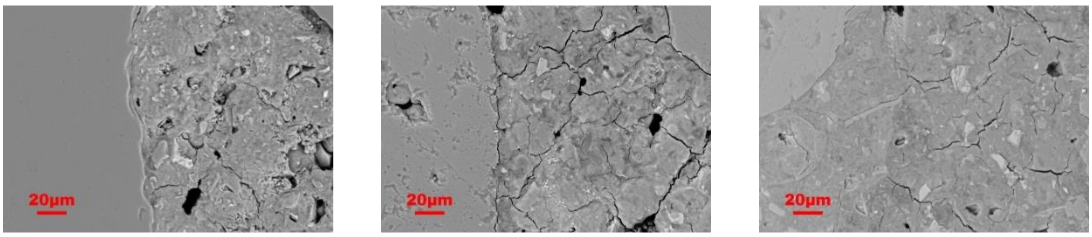

(a) ITZ-NCA (b) Old ITZ-RCA (c) New ITZ-RCA

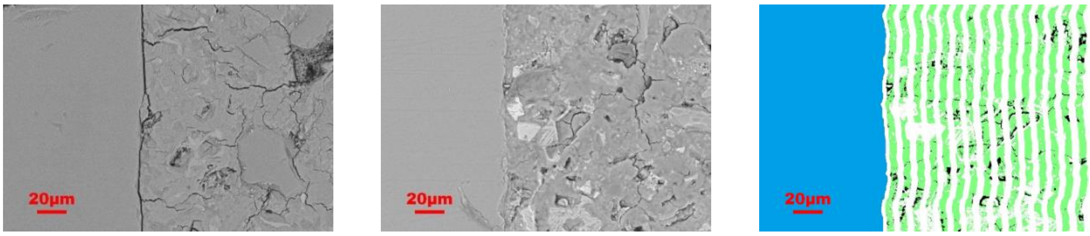

(d) ITZ-NFA (e) ITZ-Glass (f) Phases segmentation

Figure 7.3 Different ITZs and image analysis

7.2.3.3 Nanoscratch tests

Nanoscratch tests were performed by an Agilent G200 Nano Indenter installed with a hemispherical tip, as shown in Figure 7.4. The tip is controlled by normal force and lateral force. Here, twice repetitive unidirectional nanoscratch with a constant normal load of 4 mN testing mode was chosen. The scratch started from the aggregate perpendicular to the interface and ended at the paste matrix. The length of each scratch path was 150 μm, of which the aggregate part was 50 μm and the cement paste part was 100 μm. Based on ASTM G171-03 and previous experience, the minimum spacing between scratches was 20 μm to avoid interference from overlap on test data. Nanoscratch hardness can be calculated by Eqs. (7.1)-(7.3) and used to identify ITZ width and phases.

$$HS_p = \frac{8F_{Nmax}}{\pi w^2} \tag{7.1}$$

$$w = \begin{cases} 2\sqrt{r^2 - (r-d)^2} & d \le d_{gt} \\ w_{gt} + 2\tan\left(\frac{\alpha}{2}\right) \times \left(d - d_{gt}\right) & d > d_{gt} \end{cases} \tag{7.2}$$

$$d_{gt} = r\left(1 - \sin\left(\frac{\alpha}{2}\right)\right) \tag{7.3}$$

Where HS_p is nanoscratch hardness. F_{Nmax} is the maximum normal force, which is set by 4 mN in this study. The parameter r means radius of the hemispherical tip and the value is 5 μm. Another parameter d represents nanoscratch depth. Prescratch scan and postscratch scan with a low load were conducted before and after the formal scratch to acquire surface topography along the scratch path. The scratch depth (d) can be calculated by prescratch depth subtracting from the formal scratch depth. w_{gt} and d_{gt} denote geometric transition depth and corresponding scratch width, which are 2500 nm and 5 μm, respectively. α means the apex angle of the hemispherical tip, which is 60°.

20 scratches were conducted for each type of ITZ and a datum was acquired for every millimetre of scratch. To avoid error when the tip was pressed into and pulled out from the sample, the data from the middle 80 μm scratch path (20 μm for aggregate and 60 μm for cement paste) were used for statistical analysis.

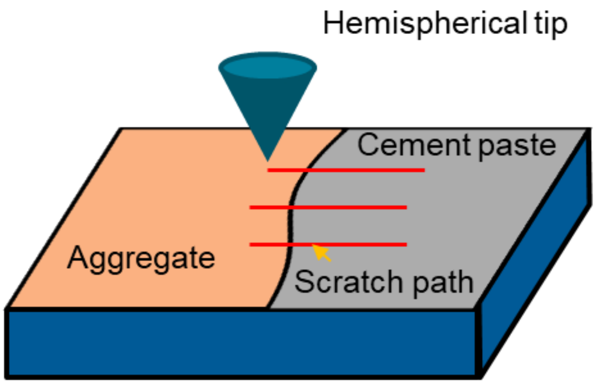

Figure 7.4 Schemes of nanoscratch test

7.2.4 Triaxial compression with pore water pressure tests

7.2.4.1 Apparatus description

RTX-1000 multi-field coupling testing apparatus was used to apply confining pressure, pore water pressure and obtain stress-strain curves of concrete specimens under compression. The load of the system was provided by servo hydraulic pressure, which can apply a maximum confining pressure and pore water pressure of 70 MPa. The concrete specimen for triaxial compression with pore water pressure is shown in Figure

7.5. During the test, the concrete specimens were put in a high-pressure triaxial chamber, where silicone oil was injected into to provide confining pressure. Pure water was injected into the sub-surface of the concrete specimen from the channel in the lower loading cap and discharged from the top surface of the specimen along the channel in the upper loading cap to provide pore water pressure. During the compression, the confining pressure and pore water pressure remained constant. The concrete specimen was covered by a heat shrinkage tube to prevent silicone oil from entering the specimen. An axial LVDT was installed on each side of the concrete specimen, and a circumferential LVDT was installed on the middle to obtain the axial and circumferential strains during the compression process.

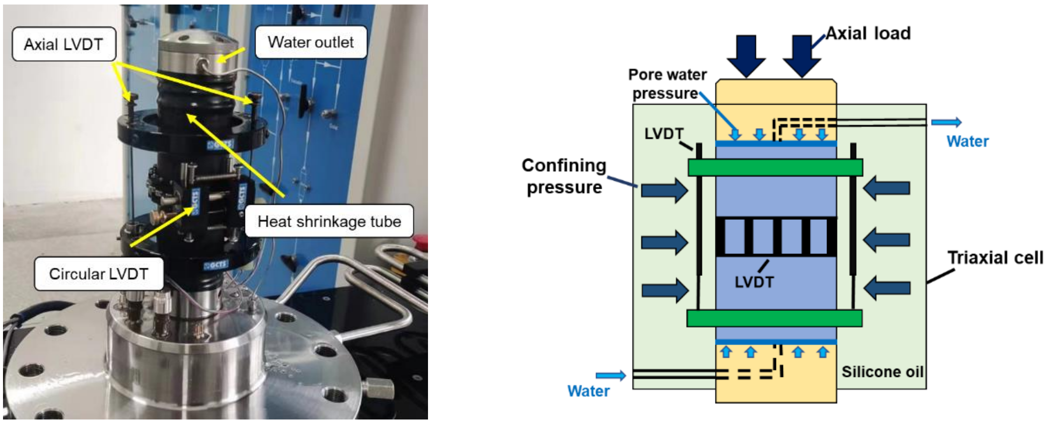

(a) Concrete specimen awaiting test (b) Scheme of multiple loads

Figure 7.5 Concrete specimen multi-field coupling stress-strain curves experimental setup

7.2.4.2 Loading procedure

Four groups of concrete specimens were used to test the stress-strain behaviours under different stress states. Confining pressure of 0-14 MPa and pore water pressure of 0-13 MPa were applied to concrete specimens and the detailed loading parameters are listed in Table 7.3. Tests were repeat twice for each condition. The loading path of sustainable concrete specimens under three stress states are illustrated in Figure 7.6. For uniaxial compression, a preload of 4 kN was applied to fix the specimen before the formal loading. The upper loading cap was then controlled by a strain of 0.02%/min until the circumferential strain of the specimen reached 2-3%. For triaxial compression, a preload of 4 kN was applied as the former loading path. Subsequently, the confining pressure and axial pressure increased simultaneously at a rate of 0.2 MPa/s to the designed value of the confining pressure, so that the specimen was at hydrostatic pressure state. Finally, the axial load was improved with an axial strain of 0.02%/min until the circumferential strain reached 2-3%. For triaxial compression tests with pore water pressure, in order to ensure uniform pore water pressure, the concrete specimen was vacuum-saturated in advance. The following two steps were the same as normal triaxial compression. Pore water pressure was applied at 0.2 MPa/s to concrete specimens under hydrostatic pressure state, and maintained it for 4 hours after reaching the target value. Finally, the axial load was improved at 0.02%/min until the circumferential strain reached 2-3% and the stress-strain curve was obtained.

Table 7.3 Loading parameters of triaxial compression with pore water pressure

Specimen	σ_c	σ_p	Specimen	σ_c	σ_p
NAC-0	0	0	RA50RG50-0	0	0
NAC-3	3	0	RA50RG50-14	14	0
NAC-7	7	0	RA50RG50-14-5	14	5
NAC-14	14	0	RA50RG50-14-13	14	13
NAC-14-5	14	5	RA50RG100-0	0	0
NAC-14-9	14	9	RA50RG100-3	3	0

NAC-14-13	14	13	RA50RG100-7	7	0
RA50-0	0	0	RA50RG100-14	14	0
RA50-7	7	0	RA50RG100-14-5	14	5
RA50-14	14	0	RA50RG100-14-9	14	9
RA50-14-5	14	5	RA50RG100-14-13	14	13
RA50-14-13	14	13			

Note: σ_c and σ_p represents confining pressure and pore water pressure respectively.

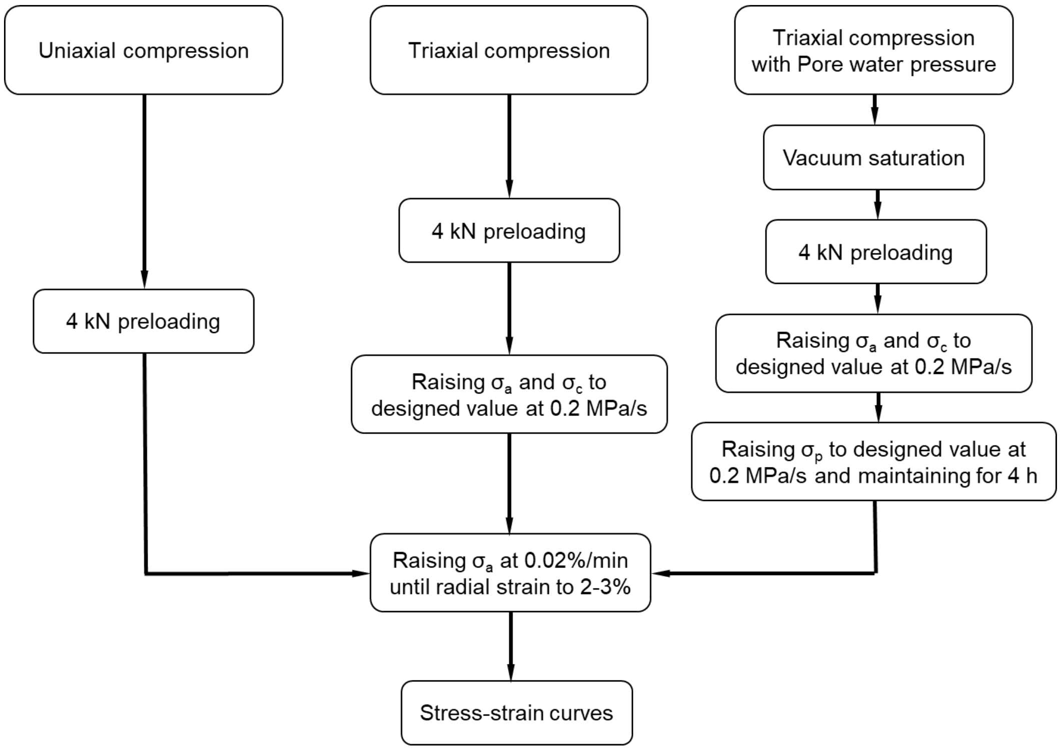

Figure 7.6 Loading path of compression tests

Note: σ_a, σ_c and σ_p represents axial load, confining pressure and pore water pressure respectively.

7.3 Results and discussions

7.3.1 Nanoscratch results analysis

7.3.1.1 ITZ thickness identification

Figure 7.7 is a SEM image of nanoscratch paths. It can be clearly seen that the scratching paths did not overlap, indicating that the minimum spacing of 20 μm is reasonable. Cement paste has a softer texture than natural aggregate, as a result, the scratch paths were more visible on cement paste. Figure 7.8 (a) shows the scratch hardness distribution from NCA to paste matrix. The hardness of NCA was approximately 17.5 GPa. However, the value decreased gradually near the boundary. Xiao and Li et al. (2012, 2013c) also found a similar phenomenon in the nanoindentation hardness tests of RAC. This is because the strength of cement paste was much lower than that of NCA and cannot provide sufficient support for the boundary of NCA, leading to a lower measured hardness at this region than the normal value (Luo, et al. 2021a). Due to the 'wall effect' of NCA, there were more pores and fewer unreacted clinkers within the cement paste close to the aggregate boundary (Hosan, et al. 2021). Therefore, the scratch hardness was lower than the paste matrix. As the distance from the aggregate boundary increased, the scratch hardness of the paste matrix stabilised at around 1 GPa. Based on this, the test area was divided into three parts (NCA, Paste I and Paste II) based on scratch hardness distribution. Letters A-H were used to mark the boundaries of each part, as shown in Figure 7.8 (a).

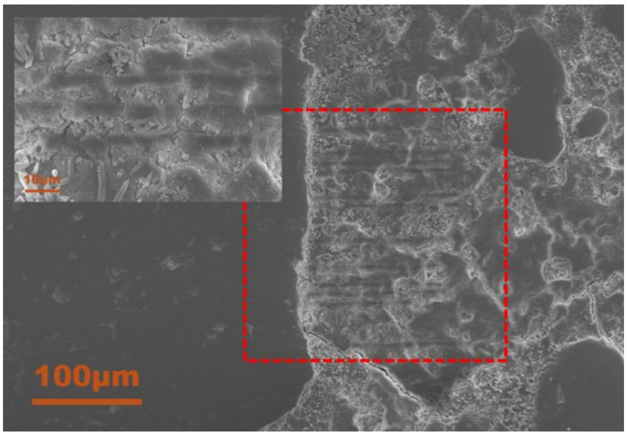

Figure 7.7 Residual path after nanoscratch

The simplified scratch hardness distribution is shown in Figure 7.8 (b). The yellow and brown horizontal solid lines represent the average hardness of aggregate and Paste II respectively, where the yellow solid line was obtained from the hardness value between points A and B. Point D was the actual boundary of NCA, and the hardness of point D was much lower than the normal hardness of NCA. Therefore, point D was moved up to the average line. Point I was located at the middle of E and F, and its hardness value was an average of the test results between E and F. Xu et al. (Xu, et al. 2015) and Wei et al. (Wei, et al. 2021) proved that micromechanical properties such as hardness and fracture toughness can be used for ITZ width quantification. Here, symmetric targets of A, D, G, H and the two average value lines were drawn with I as the centre point. Two 'S' shape curves can be constructed for fitting key points. The tangent line was then drawn along the waist of the 'S' curve, passing through point I and intersecting the average value lines. The horizontal distances of the intersection points were W_3 and W_4 respectively. ITZ width can be calculated by the following Eq (7.4) (Wei, et al. 2021):

$$W_{ITZ} = W_1 + W_2 = \frac{1}{2}W_3 + \frac{1}{2}W_4 \tag{7.4}$$

The calculated results are shown in Figure 7.8 (d). In the previous, some researchers quantified the ITZ width by nanoindentation or image analysis techniques (Lyu, et al. 2019a, Sidorova, et al. 2014). However, the spacing between indentation points and the width of the strips used for image analysis were generally above 5 μm (Lyu, et al. 2019a, Sidorova, et al. 2014). This resulted in a minimum accuracy of 2.5 μm for the ITZ with quantification by the above two methods. In comparison, nanoscratch can obtain continuous micromechanical properties, and the calculated ITZ width had better accuracy (Wei, et al. 2021). As shown in Figure 7.8 (d), there were still obvious differences in the width of ITZ-NCA, New ITZ-RCA, ITZ-NFA and ITZ-Glass even with the same mixture ratio due to chemical activity and specific surface area of aggregate (Bosque, et al. 2017). ITZ-NCA and Old ITZ-RCA had similar widths, about 13 μm. New ITZ-RCA and ITZ-Glass had the largest width, reaching 27.91 μm and 30.77 μm respectively. ITZ-NFA had the smallest with, only 9.18 μm. The detailed microscopic properties of ITZs are discussed in the following sections.

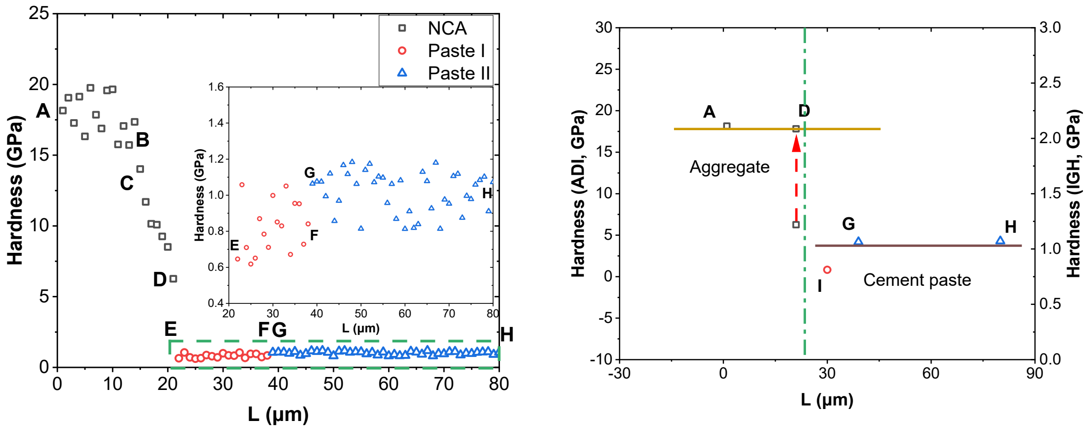

(a) Scratch hardness distribution

(b) Simplification of key scratch hardness

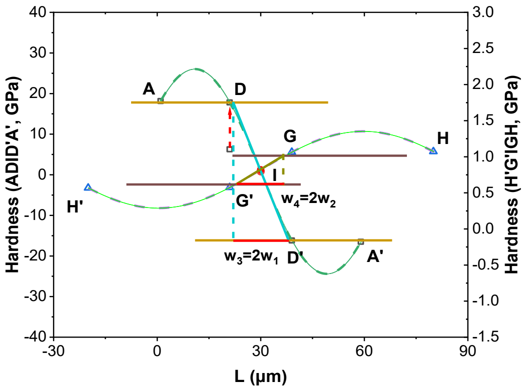

(c) Illustration of ITZ width identification

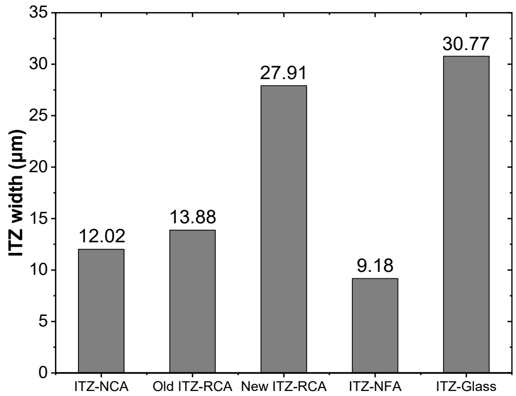

(d) Comparison of different ITZ width

Figure 7.8 ITZ width identification process and results by scratch hardness

7.3.1.2 Nanoscratch hardness frequency density analysis

The Gaussian mixture model can be used to fit the frequency distribution histogram of scratch hardness in ITZs and analyse the contribution of phases to the micromechanical properties of ITZs. Some researchers pointed out that the scratch depth and hemispherical tip size caused the scratch hardness to hardly reflect a single phase but a combination of multiple phases (Li, et al. 2021). Here, we can still infer the hydration degree and phase content within ITZs based on the minimum number of peaks (*k*) required for deconvolution and the frequency density of peaks. A narrow bin size for the frequency density histogram can reduce the interference caused by phase overlap within ITZs. However, a too-narrow bin size would cause the shape of the histogram disordered due to insufficient data. After trying, the bin size was finally determined to be 0.1 GPa.

The minimum component numbers required for peak fitting of the scratch hardness frequency density distribution histogram of ITZ-NCA, Old ITZ-RCA and New ITZ-RCA were 7, 3 and 7 respectively (*k*=7, 3 and 7 respectively), as shown in Figure 7.9. These separated components included three main peaks (indicated by green, blue and cyan respectively), and other sub-peaks with lower proportions. The scratch hardness corresponding to the sub-peaks was higher, generally above 1 GPa, which is a result of mixed phase of calcium silicate hydrate (C-S-H) gel and calcium hydroxide (CH) or unhydrated clinkers (Hoover & Ulm 2015b). It can be seen that the sub-peaks containing CH and unhydrated clinkers were almost absent in Old ITZ-RCA because the old mortar attached to the RCA surface had the longest curing age and higher hydration degree. For the three main peaks (k_1, k_2 and k_3), k_1 corresponds to the smallest scratch hardness, which is mainly affected by pores and cracks; k_2 mainly represents low-density C-S-H and high-density C-S-H; k_3 mainly represents high-density C-S-H and partial CH. Pores and cracks do not create bond strength with C-S-H. It is worth noting that the bonding between CH and C-S-H is also relatively loose (Khedmati, et al. 2019). Therefore, judging the bond strength within ITZ was mainly based on the ratio of k_2. In Figure 7.9, the k_2 of ITZ-NCA and New ITZ-RCA were similar, and the frequency density reached above 0.1. However, the proportion of k_2 in Old ITZ-RCA was lower as well as the proportion of k_1 was higher because the crushing process for waste concrete produced a large number of cracks within Old ITZ-RCA.

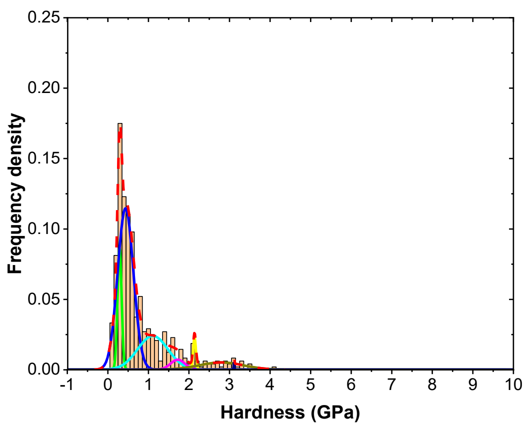

(a) ITZ-NCA (k=7)

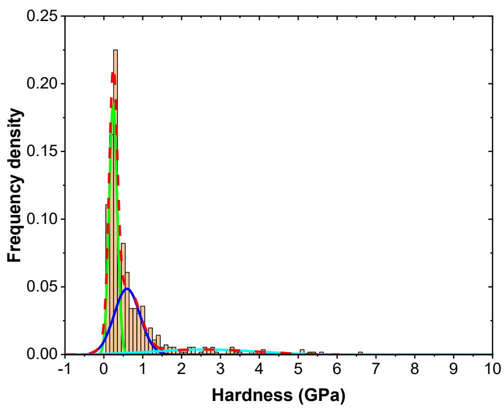

(b) Old ITZ-RCA (k=3)

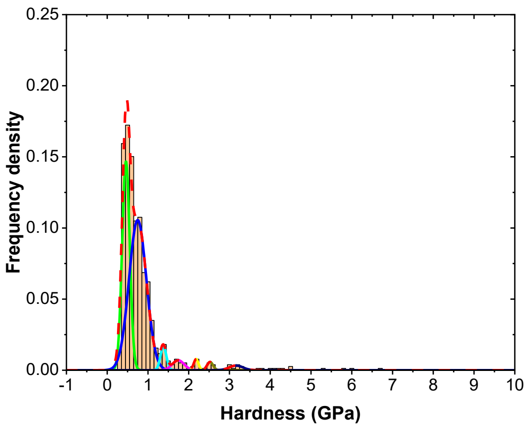

(c) New ITZ-RCA (k=7)

Figure 7.9 Scratch hardness frequency density distribution histogram of ITZs bonded to coarse aggregate

As shown in Figure 7.10, there were not many sub-peaks in the scratch hardness frequency distribution histogram of ITZ-NFA and ITZ-Glass, because the high specific surface area of fine aggregate made ITZ less likely to accumulate unhydrated clinkers. k_3 was not even present within ITZ-Glass because RGS contained active SiO_2 and consumed CH in the pozzolanic reaction (Du & Tan 2017). However, the proportion of k_1 of ITZ-Glass was prominent and even exceeded that of Old ITZ-RCA, indicating that there were many pores and cracks in ITZ-Glass and the bonding performance was loose.

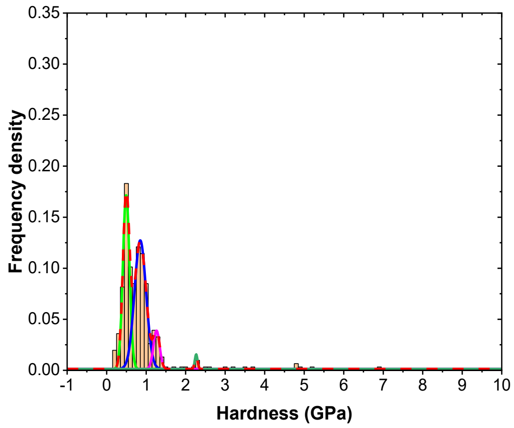

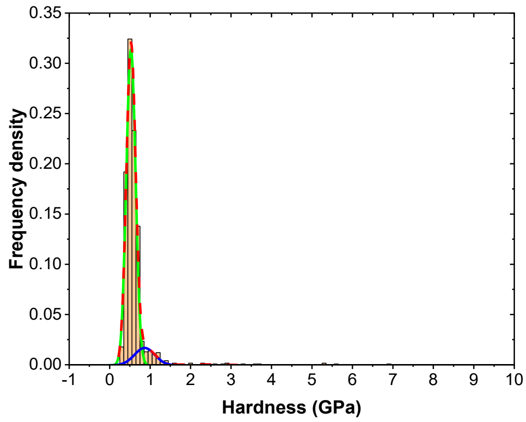

(a) ITZ-NFA (*k*=4) (b) ITZ-Glass (*k*=2)

Figure 7.10 Scratch hardness frequency density distribution histogram of ITZs bonded to fine aggregate

The cumulative fitting curves of ITZ scratch hardness density distribution histogram is shown in Figure 7.11. For ITZ in contact with coarse aggregate, Old ITZ-RCA had the smallest scratch hardness and New ITZ-RCA had the highest scratch hardness. As explained earlier, the crushing process of waste concrete created more micro-cracks within the old ITZ. Moreover, due to long-term curing, the unhydrated clinkers in the old mortar continued to hydrate, enhancing the bond between old and new mortar. In addition, it can be observed a shoulder at the descending stage of ITZ-NCA, Old ITZ-RCA and New ITZ-RCA curves, which is caused by the mixed phase of C-S-H and CH. In comparison, there was not a shoulder at the descending stage of ITZ-Glass curve but a single peak, because pores and cracks occupied a large proportion within ITZ-Glass. The individual peak was caused by the mixed phase of pores and low-density C-S-H gel.

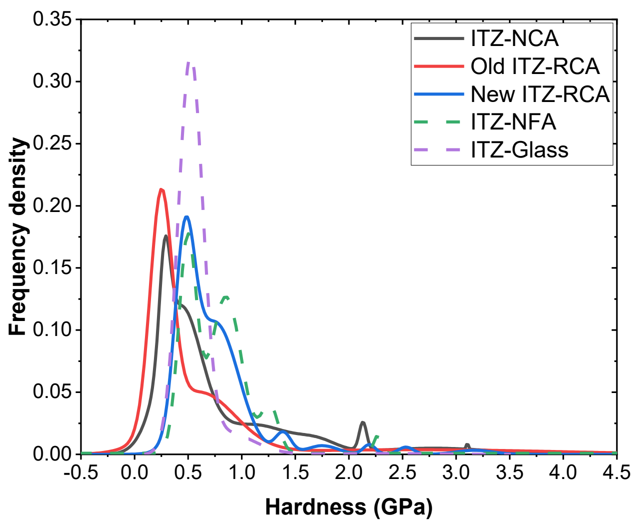

Figure 7.11 Cumulative scratch hardness density distribution of ITZs

7.3.2 Phase proportion and distribution from BSE-based image analysis

The statistical results for the proportion of phases within ITZs and adjacent matrix are shown in Figure 7.12. Based on ITZ width identified in Section 7.3.1.1, the ITZ and paste matrix is divided by a dash-dot line. It can be found that the phase proportion changed most significantly within ITZs and maintained at a stable value in the paste matrix. There was a negative correlation between the content of pores and reaction products with the distance to aggregate surface. In ITZ-NCA and Old ITZ-RCA, the proportion of pores and cracks decreased rapidly between the first and second strip and was accompanied by a rapid increase in the proportion of reaction products. Meanwhile, the proportion of unreacted products gradually increased to a stable value. The porosity within ITZ-NCA was lower than that of Old ITZ-RCA and the content of unreacted products was opposite. This explained that the scratch hardness of ITZ-NCA in Section 7.3.1.2 was higher than that of Old ITZ-RCA. The variation of phases proportion in New ITZ-RCA was not obvious, indicating that the 'wall effect' of the old mortar was ignorable. In fact, this is reasonable. The surface of old mortar was rough and porous, limiting water accumulation compared to natural sand and gravel surfaces (Zhang, et al. 2019). In addition, due to long-term curing, the incompletely reacted clinkers on the surface of the old mortar were further hydrated, which promoted the consistency of the phases in New ITZ-RCA. The variation law of pores, cracks and reaction products in ITZ-NFA showed a similar phenomenon to ITZ-NCA and Old ITZ-RCA, while the content of unreacted products gradually decreased instead of steadily increasing. The apparent density of NFA was close to that of NCA, as shown in Table 7.1, which results in easy accumulation of free water on the surface of NFA when fresh cement paste was not completely solidified. However, the specific surface area of NFA was higher and had little influence on the distribution of unreacted clinkers in ITZs. The proportion of pores and cracks in ITZ-Glass was significantly higher than the above four ITZs, which determined the worst bonding performance between RGS and cement paste. Correspondingly, the content of the reaction product dropped from 0.86 for 5 μm-strip to 0.76 for 15 μm-strip and then increased to around 0.83 in the paste matrix. Active SiO_2 in the surface of RGS participated in the pozzolanic reaction, resulting in a higher content of reaction production near the RGS surface. However, ITZ-Glass still had the highest porosity and a lower proportion of reaction products.

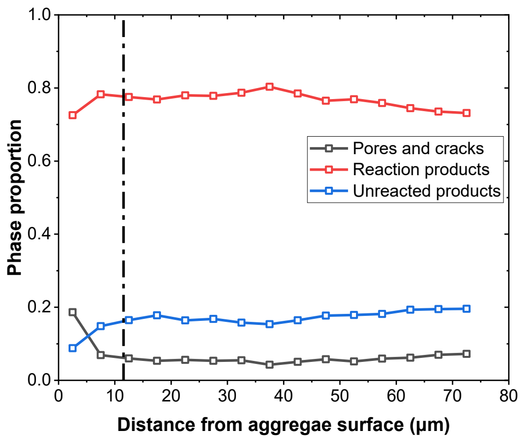

(a) ITZ-NCA

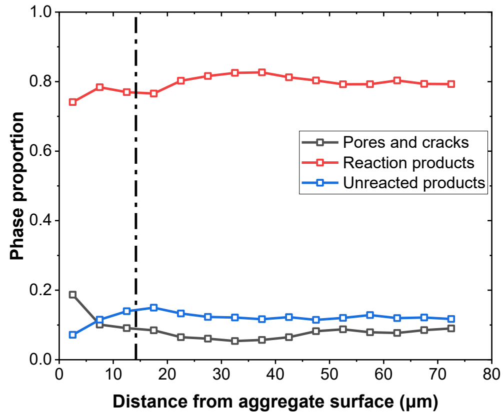

(b) Old ITZ-RCA

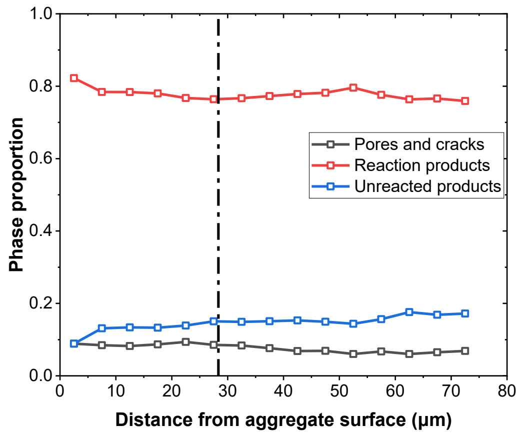

(c) New ITZ-RCA

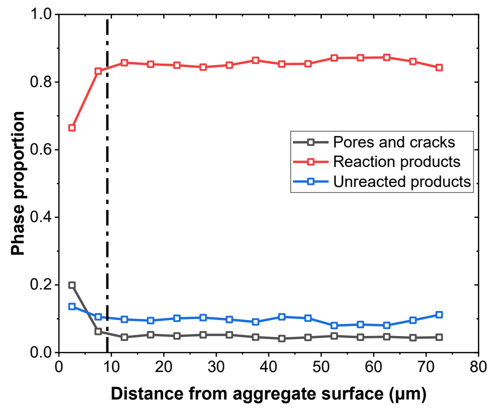

(d) ITZ-NFA

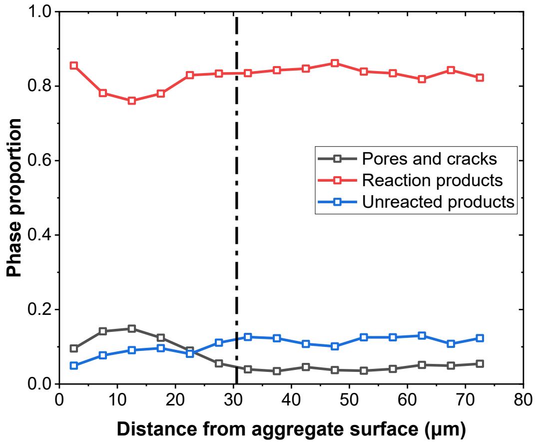

(e) ITZ-Glass

Figure 7.12 Phases contents distribution within ITZs and adjacent matrix

The pore structure of ITZs is an important feature for judging the mechanical properties and permeability of concrete. Figure 7.13. shows the equivalent circle diameter of pores distribution in ITZs based on image analysis technique. It can be easily found that three peaks appeared at 0.25 μm, 0.65 μm and 1.5 μm. In general, the proportion of pores with equivalent diameters below 1 μm in ITZ-NCA was lower than that in Old ITZ-RCA and New ITZ-RCA, while the opposite was true for pores with equivalent diameters above 1 μm, especially the equivalent diameter of 1.5 μm, which accounted for 0.104 in ITZ-NCA. The proportion of pore with the equivalent diameter of 1.5 μm in Old ITZ-RCA and New ITZ-RCA was only 0.080. The difference in pore size was more pronounced for ITZs in contact with fine aggregate. ITZ-Glass had the highest proportion of pores with an equivalent diameter of 0.25 μm, reaching 0.461, whereas for ITZ-NFA was 0.384. In comparison, the proportion of pores with equivalent diameters of 1.5-4.5 μm in ITZ-Glass was lower than that in ITZ-NFA. Combined with Figure 7.12, it can be concluded that ITZ-Glass had the highest porosity and the equivalent diameter of the pores was mainly concentrated between 0.2-0.3 μm.

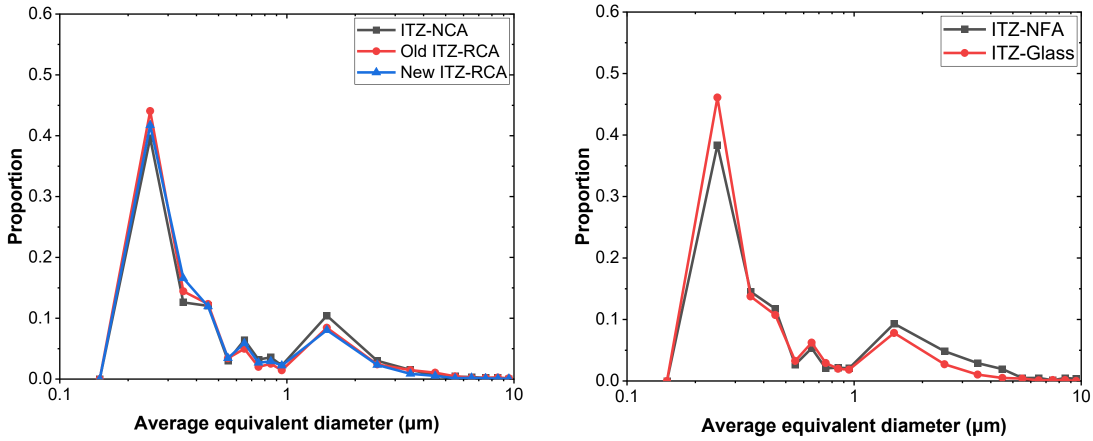

(a) ITZs in contact with coarse aggregate (b) ITZs in contact with fine aggregate

Figure 7.13 Pore size distributions within ITZs

7.3.3 Triaxial compression with pore water pressure

7.3.3.1 Failure patterns

NAC-0 NAC-3 NAC-7 NAC-14 NAC-14-5 NAC-14-9 NAC-14-13

RA50-0 RA50-7 RA50-14 RA50-14-5 RA50-14-13

RA50RG5	RA50RG5	RA50RG5	RA50RG5
0-0	0-14	0-14-5	0-14-13

RA50RG1	RA50RG1	RA50RG1	RA50RG1	RA50RG1	RA50RG1	RA50RG1
00-0	00-3	00-7	00-14	00-14-5	00-14-9	00-14-13

Figure 7.14 Failure patterns of RAC with RGS under triaxial compression and pore water pressure

It can be seen from Figure 7.14 that the failure patterns of each group of concrete specimens changed with the stress states in a similar manner. The concrete specimens experienced circumferential expansion during the compression process and generated vertical cracks when there was no confining pressure and pore water pressure. The circumferential splitting failure mode finally appeared. When the specimen was subjected to confining pressure, numerous vertical cracks transformed into a single oblique crack and exhibited a shear failure mode. Pore water pressure had little effect on the failure mode of concrete specimens. It is worth noting that a small number of vertical cracks appeared on the surface of RA50-14-13 instead of a single oblique crack. This is probably due to the cancellation of pore water pressure and confining pressure, resulting in a uniaxial compression-like failure mode for the concrete specimen.

7.3.3.2 Stress-strain curves analysis

The stress-strain curves of four groups of concrete specimens are shown in Figure 7.15. For uniaxial compression, the axial stress-strain curves of NAC and RA50 reached the peak value almost without axial deformation and rapidly entered the descending part. On the contrary, the lateral deformation was more obvious, and the peak radial strain was -0.159% and -0.372% respectively. This corresponds to the uniaxial compression failure mode of NAC and RA50 in Figure 7.14. When the concrete specimens contained 50% and 100% RGS, the peak stress decreased and the plastic deformation capacity improved. This is because the higher porosity within ITZ-Glass provided more space for axial deformation before failure.

When concrete specimens were subjected to triaxial compression, the peak stress was significantly enhanced compared to uniaxial compression, because circumferential confinement increased the internal friction angle of concrete specimens. The axial peak strain of NAC, RA50RG50 and RA50RG100 gradually increased with confining pressure and the descending part became gentle, showing a plastic failure characteristic. This is because the pores and cracks in concrete specimens closed after applying confining pressure, which limited the expansion of new cracks during compression. RA50 behaved differently in triaxial compression. Although the peak axial strain of RA50 at confining pressure of 7 MPa and 14 MPa improved compared to uniaxial compression, the RA50-14 showed some brittle characteristics in the descending part. According to the analysis in Section 7.3.1 and 7.3.2, the scratch hardness of ITZs in RA50 was higher and had a dense microstructure, making it prone to brittle failure.

Furthermore, when pore water pressure existed, the peak stress and axial peak strain of concrete specimens were reduced. The pore water acted as a lubricant in concrete and weakened the internal friction between phases. In addition, pore water promoted the expansion of cracks in concrete specimens during compression. When the pore water pressure reached 13 MPa, the four groups of concrete specimens showed obvious brittle failure characteristics.

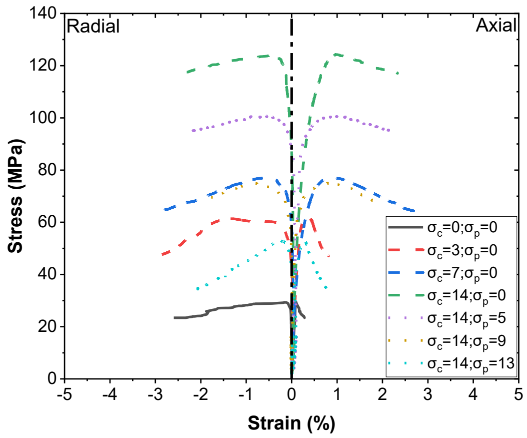

(a) NAC

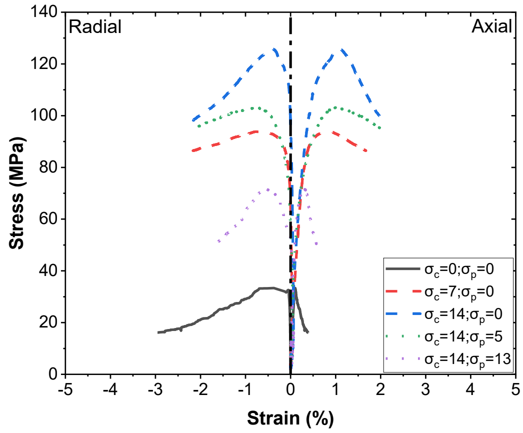

(b) RA50

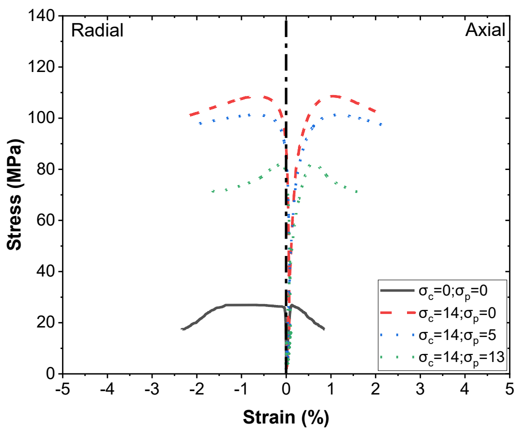

(c) RA50RG50

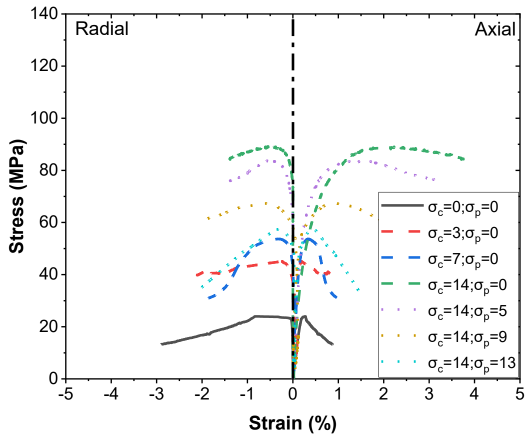

(d) RA50RG100

Figure 7.15 Stress-strain curves of sustainable concrete specimens under confining pressure and pore water pressure

7.3.3.3 Axial stress-volumetric strain curves analysis

The volumetric strain of concrete specimens during compression can be calculated according to the following formula:

$$\varepsilon_v = \varepsilon_a + 2 \times \varepsilon_c \tag{7.5}$$

Where, ε_a and ε_c represents axial and circumferential strain respectively.

The axial stress-volumetric strain curves of the four groups of concrete specimens are shown in Figure 7.16. The positive volumetric strain means that the specimen was in a compression state and vice versa. The maximum volumetric strain was directly related to the stress state and the pore structure of ITZs. The micromechanical properties and microstructure of ITZs in NAC and RA50 were better than the latter two groups of specimens. As a result, NAC and RA50 quickly transformed into an expansion deformation state after experiencing a brief compression process under uniaxial compression. When the NFA in concrete specimens was replaced by RGS, the compression deformation under uniaxial compression was more obvious. Especially for RA50RG100, the maximum volumetric strain under uniaxial compression increased to 0.1206% compared to 0.0485% of NAC.

The confining pressure limited the circumferential expansion of concrete specimens. Therefore, the compression deformation increased significantly. When the confining pressure was 14 MPa, the maximum volumetric strain of NAC, RA50, RA50RG50 and RA50RG100 reached 0.3982%, 0.4781%, 0.312% and 1.1518% respectively. Among them, Figure 7.16 (d) shows that when RA50RG100 was subjected to a confining pressure of 14 MPa, the specimen was always in a compression state until failure. The high porosity within ITZ-Glass provided enough space for compressive deformation. In addition, the triaxial compressive strength of RA50RG100 was obviously lower than the former three groups of specimens (the triaxial compressive strength of RA50RG100-14 was only 89.19 MPa), resulting in the loss of bearing capacity before expansion deformation occurred.

When pore water pressure existed, the maximum volumetric strain of NAC and RA50 reduced under triaxial compression, mainly due to the supporting function of pore water before the crack propagation. The maximum volumetric strain of RA50RG50 gradually increased with pore water pressure, which is probably because of its low triaxial compressive strength. In the process of improving pore water pressure, more cracks were generated in concrete specimens, thereby increasing the axial deformation. When the pore water pressure was low (σ_p=5 MPa), RA50RG100 was still in a compressed state until failure, while for the pore water pressure of 9 MPa and 13 MPa, the expansion deformation reappeared because the pore water pressure offset the influence of confining pressure.

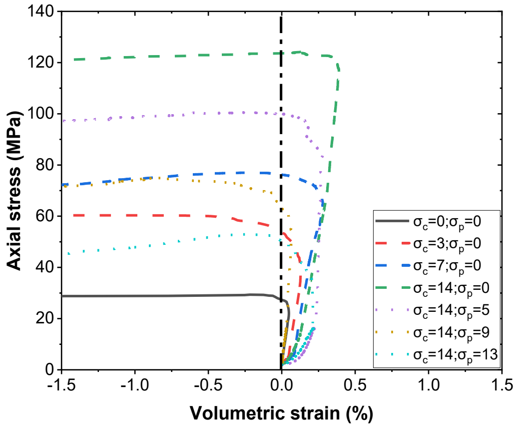

(a) NAC

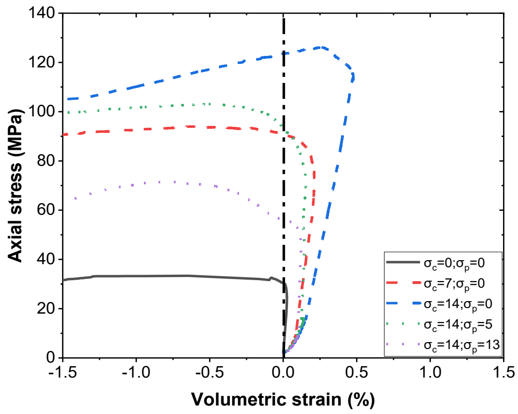

(b) RA50

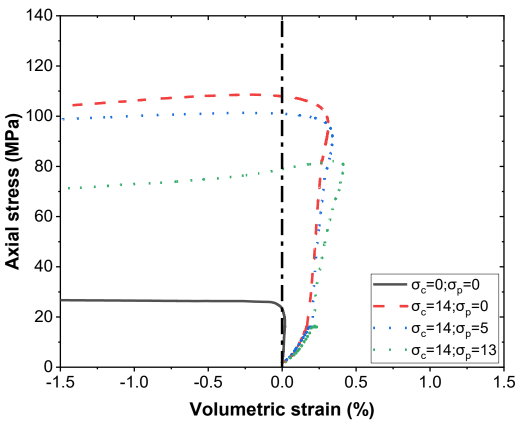

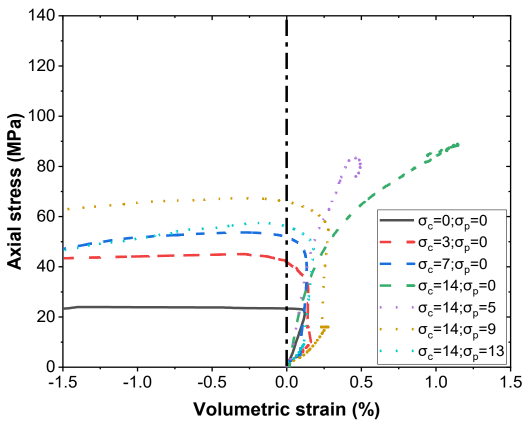

(c) RA50RG50 (d) RA50RG100

Figure 7.16 Axial stress-volumetric strain curves of sustainable concrete specimens under confining pressure and pore water pressure

7.3.3.4 Ultimate condition

The representative mechanical data of concrete specimens were extracted from the Figure 7.15 and 7.16 and listed in Table 7.4. The elastic modulus was defined as the slope of the stress-strain curve between axial strain of 0.005% and 40% of peak stress according to ASTM C469. To highlight the changes in the mechanical properties of concrete specimens with confining pressure and pore water pressure, the data in Table 7.4 were normalised and shown in Figure 7.17.

Table 7.4 Testing results extracted from stress-strain curves

Specimens	σ_c (MPa)	σ_p (MPa)	f_c (MPa)	S.D.	ε_{ap} (%)	ε_{cp} (%)	ε_{vm} (%)	E (GPa)	S.D.
NAC-0	0	0	29.36	1.66	0.101	-0.159	0.0485	30.35	1.36
NAC-3	3	0	61.38	1.93	0.381	-0.466	0.1285	35.71	1.24
NAC-7	7	0	76.99	2.31	0.911	-0.611	0.2794	35.51	2.21
NAC-14	14	0	124.31	1.34	0.973	-0.430	0.3982	42.10	1.07
NAC-14-5	14	5	100.79	1.68	0.924	-0.559	0.2784	53.09	3.03
NAC-14-9	14	9	74.98	3.21	0.784	-0.789	0.0642	60.54	2.15
NAC-14-13	14	13	52.9	1.12	0.273	-0.248	0.2168	67.82	1.69
RA50-0	0	0	33.35	2.58	0.099	-0.372	0.0252	40.59	2.16
RA50-7	7	0	93.81	1.62	0.899	-0.768	0.2118	30.96	3.56

RA50-14	14	0	125.87	2.06	1.070	-0.411	0.4781	38.72	2.45
RA50-14-5	14	5	103.1	1.24	0.998	-0.744	0.1551	52.93	2.36
RA50-14-13	14	13	71.5	2.33	0.312	-0.551	0.1214	65.68	1.87
RA50RG50-0	0	0	26.92	1.63	0.129	-0.661	0.0515	29.84	1.71
RA50RG50-14	14	0	108.59	5.07	1.044	-0.630	0.312	43.48	5.85
RA50RG50-14-5	14	5	101.33	5.53	1.179	-0.738	0.341	50.37	5.79
RA50RG50-14-13	14	13	82.19	5.57	0.592	-0.111	0.423	42.77	3.43
RA50RG100-0	0	0	23.97	1.49	0.280	-0.842	0.1206	12.61	3.11
RA50RG100-3	3	0	45.05	4.16	0.185	-0.234	0.2379	28.75	3.62
RA50RG100-7	7	0	53.68	2.39	0.335	-0.311	0.1342	34.51	1.14
RA50RG100-14	14	0	89.19	3.73	2.246	-0.549	1.1518	23.14	4.40
RA50RG100-14-5	14	5	83.67	5.79	1.611	-0.566	0.4973	30.26	4.74
RA50RG100-14-9	14	9	67.31	5.82	0.929	-0.628	0.2792	65.69	3.71
RA50RG100-14-13	14	13	57.61	1.79	0.418	-0.278	0.1802	38.16	4.03

Note: σ_c and σ_p represent confining pressure and pore water pressure respectively; f_c represents compressive strength of concrete specimens under various stress states; ε_{ap} and ε_{cp} represent axial peak strain and circumferential peak strain respectively; ε_{vm} respenent the maximum volumetric strain; E represents elastic modulus; S.D. means standard diviations.

7.3.3.4.1 Peak stress and elastic modulus

It can be seen from Figure 7.17 (a) that the compressive strength of concrete specimens gradually increased with confining pressure. For a confining pressure ratio of 0.5, the triaxial compressive strength can be increased by more than 4 times than the uniaxial compressive strength. However, the improving efficiency on the peak stress reduced with the content of RGS. Circumferential confinement improved the microstructure of concrete and enhanced the internal friction between phases. Some studies pointed out that concrete with lower strength had a more obvious improvement ratio in triaxial compression (Chen, et al. 2017, Deng, et al. 2017, Meng, et al. 2017). The test results in this study contradict some previous conclusions because the bonding strength between cement paste and RGS was weaker than normal ITZs (see Figure 7.10). When cracks extended to RGS, they were more likely to propagate along ITZ-Glass rather than penetrating RGS directly. When pore water pressure existed, the situation was opposite. The relative peak stress of NAC and RA50 decreased faster with pore water pressure. This is probably because ITZ-NCA and ITZ-NFA contained more unhydrated clinkers, and their ability to resist the effect of pore water pressure on crack expansion was not as good as ITZ-Glass with less CH and unhydrated clinkers, especially when numerous pores were compressed by circumferential confinement. As shown in Figure 7.17 (b) both confining pressure and pore water pressure can increase the elastic modulus of concrete specimens. Confining pressure posed the concrete microstructure denser, whereas the supporting effect of pore water improved the initial stiffness of concrete specimens under compression.

7.3.3.4.2 peak strain and maximum volumetric strain

As shown in Figure 7.17 (c)-(e) relative deformation also has a close relationship with confining pressure and pore water pressure. The axial peak strain of NAC and RA50 increased rapidly with confining pressure and then slowed down. At a relative confining pressure of 0.3, the relative axial peak strain of RA50RG100 remained constant. However, as the relative confining pressure approached 0.6, the relative axial strain increased significantly. This increase is also attributed to the high porosity present in the ITZ-Glass. The supporting effect of pore water reduced the axial peak strain, which was more obvious for concrete specimens with higher micromechanical properties. Similar phenomena were also reflected in the maximum volumetric strain. The strengthening effect of confining pressure on the ductility and the supporting effect of pore water pressure caused the relative volumetric strain in Figure 7.17 (c) to increase at first and then decrease. In comparison, the change pattern between circumferential peak strain, confining pressure and pore water pressure was not obvious, because it was affected by many accidental factors, including the irregular expansion of specimens. The circumferential peak strain of RA50RG50 and RA50RG100 was not significantly different from that of uniaxial compression, whereas the circumferential peak strain of NAC under triaxial compression with and without pore water pressure was more than twice that of uniaxial compression. This provides further evidence that RGS increased the porosity of concrete specimens and allowed for more axial compression space.

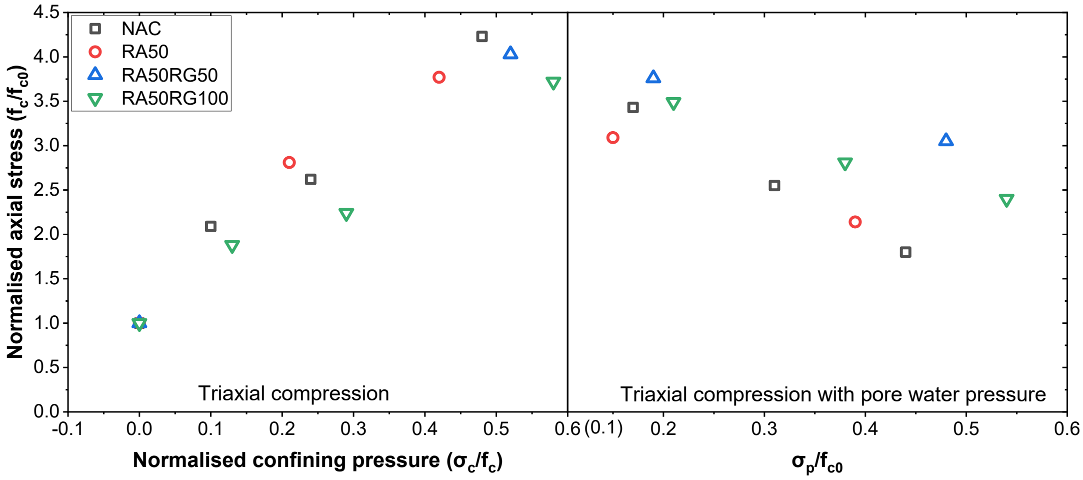

(a) Relative axial peak stress at triaxial compression with pore water pressure

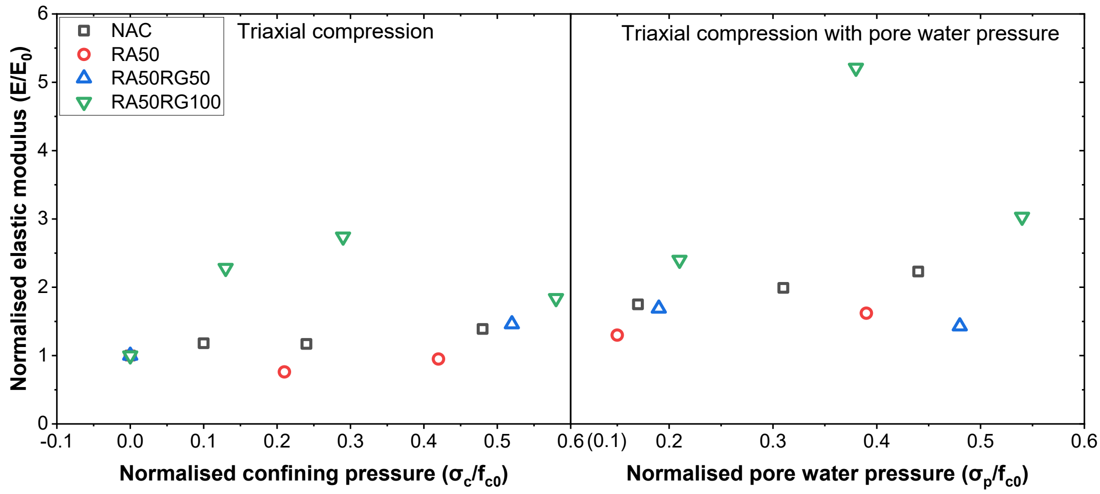

(b) Relative elastic modulus at triaxial compression with pore water pressure

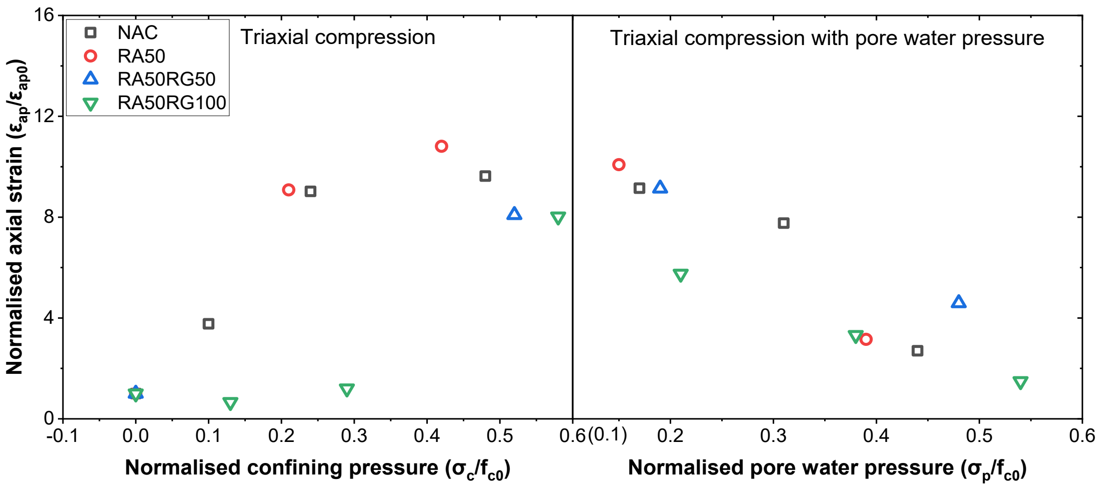

(c) Relative axial peak strain at triaxial compression with pore water pressure

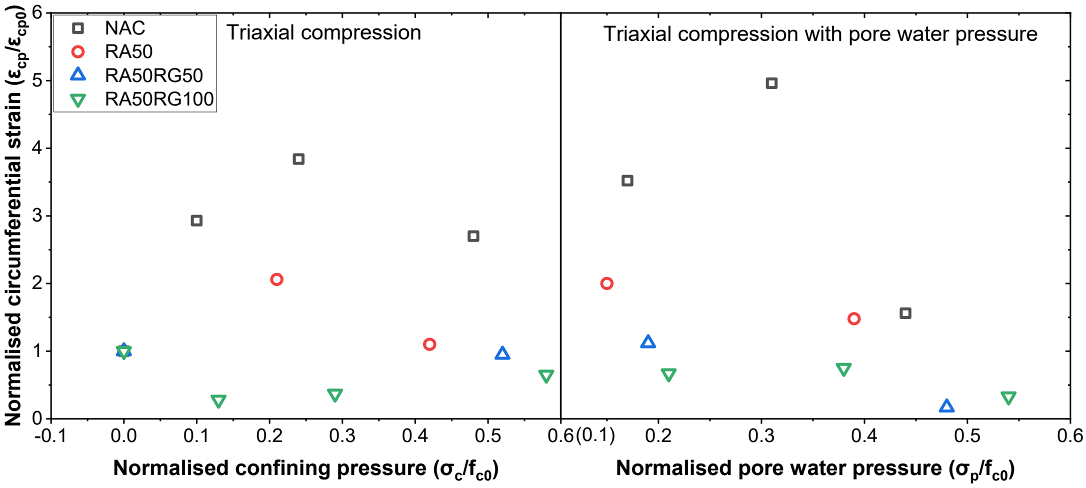

(d) Relative circumferential peak strain at triaxial compression with pore water pressure

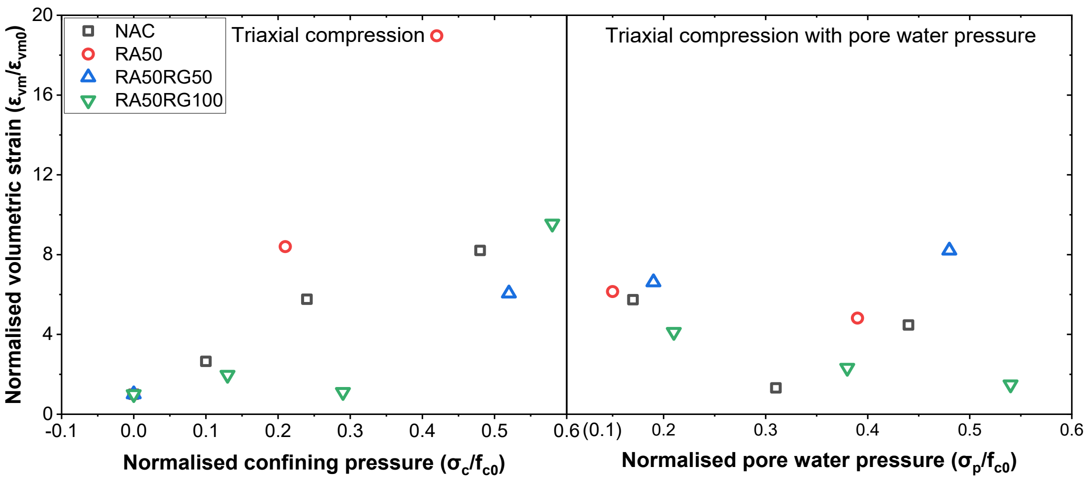

(e) Relative volumetric strain at triaxial compression with pore water pressure

Figure 7.17 Ultimate states of sustainable concrete specimens under various stress states

7.4 Failure criteria

7.4.1 Failure criteria for triaxial compression

7.4.1.1 Mohr-Coulomb failure criterion

Mohr-Coulomb failure criterion is a classic linear theory considering normal stress and maximum shear stress. It was first proposed and applied to analyse the failure surface of clay. Nowadays, it has been widely used to describe the critical state of concrete materials under uniaxial and triaxial compression. The criterion can be described as below (Li, et al. 2022a):

$$\frac{f_c}{f_{c0}} = a_1 \frac{\sigma_c}{f_{c0}} + 1 \tag{7.6}$$

Where, f_{c0} and f_c represent uniaxial compressive strength and triaxial compressive strength respectively; σ_c represents confining pressure; a_1 can be calculated by $\frac{1+sin\varphi}{1-sin\varphi}$ and φ means the internal friction angle of concrete (Li, et al. 2022a). Confining pressure improves the strength and ductility of concrete specimens by improving the internal friction angle of concrete. The strengthening efficiency of the confining pressure on concrete specimens becomes more obvious as a_1 increases. The Mohr-Coulomb equations for concrete containing RCA and RGS can be obtained by regression analysis of the data in this study:

NAC and RA50

$$\frac{f_c}{f_{c0}} = 6.93 \frac{\sigma_c}{f_{c0}} + 1 \tag{7.7}$$

RA50RG50 and RA50RG100

$$\frac{f_c}{f_{c0}} = 5.13 \frac{\sigma_c}{f_{c0}} + 1 \tag{7.8}$$

The fitting results of Mohr-Coulomb failure criterion on the test data is shown in Figure 7.18. Meanwhile, the existing experimental data (Chen, et al. 2019, Folino & Xargay 2014, Meng, et al. 2017) on RAC triaxial compression are also presented in Figure 7.18. It can be seen that the a_1 value of Mohr-Coulomb failure criterion is in a reasonable range. RCA would not change the internal friction angle of concrete, which is consistent with conclusions in other research (Chen, et al. 2019). The a_1 values of RA50RG50 and RA50RG100 were lower than those of NAC and RA50 because the higher porosity in ITZ-Glass weakened the efficiency of the confining pressure in improving the internal friction of phases in concrete.

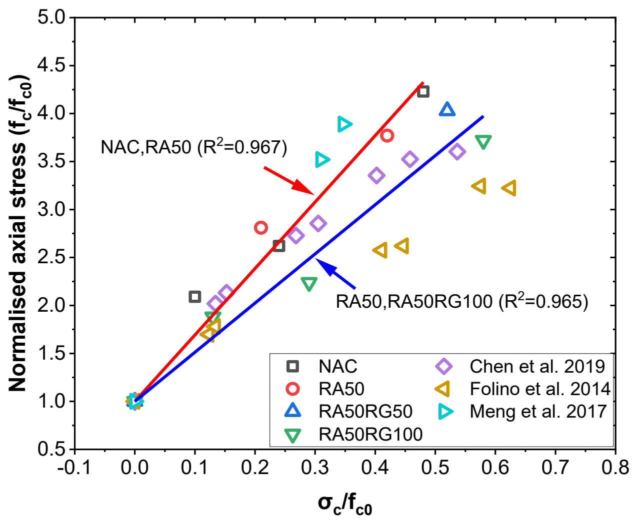

Figure 7.18 Fitting performance of Mohr-Coulomb failure criterion under triaxial compression

7.4.1.2 William-Warnke failure criterion

William-Warnke failure criterion is a five-parameter model widely used in finite element software such as failure surface analysis by ANSYS. When the confining pressure is low, it can be simplified to a three-parameter model as Eq. (7.9) (Wu, et al. 2023).

$$\frac{\tau_m}{f_{c0}} = a_2 + b_2\left(\frac{\sigma_m}{f_{c0}}\right) - c_2\left(\frac{\sigma_m}{f_{c0}}\right)^2 \tag{7.9}$$

Where a_2, b_2 and c_2 are parameters; σ_m and τ_m are principal axial stress and principal shear stress, which can be calculated by $\sigma_m=(\sigma_1+\sigma_2+\sigma_3)/3$ and $\tau_m=\frac{1}{\sqrt{15}}[(\sigma_1-\sigma_2)^2+(\sigma_1-\sigma_3)^2+(\sigma_2-\sigma_3)^2]^{0.5}$, respectively. σ_1, σ_2 and σ_3 are principal stress in three directions. The William-Warnke failure criterion for concrete specimens in this study are displayed in Eqs. (7.10) and (7.11).

NAC and RA50

$$\frac{\tau_m}{f_{c0}} = 0.091 + 0.857\left(\frac{\sigma_m}{f_{c0}}\right) - 0.071\left(\frac{\sigma_m}{f_{c0}}\right)^2 \tag{7.10}$$

RA50RG50 and RA50RG100

$$\frac{\tau_m}{f_{c0}} = 0.186 + 0.546\left(\frac{\sigma_m}{f_{c0}}\right) + 0.045\left(\frac{\sigma_m}{f_{c0}}\right)^2 \tag{7.11}$$

The fitting curves and test data in this study are shown in Figure 7.19. Similarly, existing triaxial compression test data (Chen, et al. 2019, Folino & Xargay 2014, Meng, et al. 2017) on RAC was also collected and presented in Figure 7.19. The William-Warnke failure curves obtained based on the data in this study are within a reasonable range. A satisfying fitting result can be achieved for both concrete specimens with and without RGS.

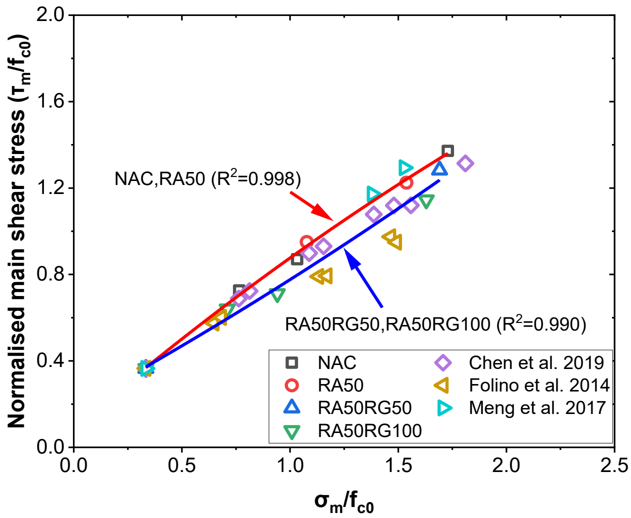

Figure 7.19 Fitting performance of William-Warnke failure criterion under triaxial compression

7.4.1.3 Power-Law failure criterion

The power-law failure criterion suggests that the peak stress of concrete has a nonlinear relationship with the increase rate of confining pressure, initially increasing rapidly and then slowing down (Jiang, et al. 2023). It can be expressed as:

$$\frac{f_c}{f_{c0}} = a_3 \left(\frac{\sigma_c}{f_{c0}}\right)^{b_3} + 1 \tag{7.12}$$

Where, a_3 and b_3 are parameters. f_c, f_{co} and σ_c are consistent with the symbols in Mohr-Coulomb failure criterion.

Based on test data in this study, the parameters were calibrated and Power-Law failure criteris for concrete specimens can be expressed as Eqs. (7.13) and (7.14).

NAC and RA50

$$\frac{f_c}{f_{c0}} = 5.398 \left(\frac{\sigma_c}{f_{c0}}\right)^{0.744} + 1 \tag{7.13}$$

RA50RG50 and RA50RG100

$$\frac{f_c}{f_{c0}} = 4.979 \left(\frac{\sigma_c}{f_{c0}}\right)^{0.959} + 1 \tag{7.14}$$

The Power-Law failure curves for concrete specimens with and without RGS was plotted in Figure 7.20. In addition, existing data provided by other researchers (Chen, et al. 2019, Folino & Xargay 2014, Meng, et al. 2017) in triaxial compression experiments of RAC were presented together. It can be seen that the failure surfaces of NAC and RA50 satisfied the Power-Law failure criterion with the fitting correlation coefficient R^2 of 0.989, whereas the fitting curve of RA50RG50 and RA50RG100 were closer to a straight line.

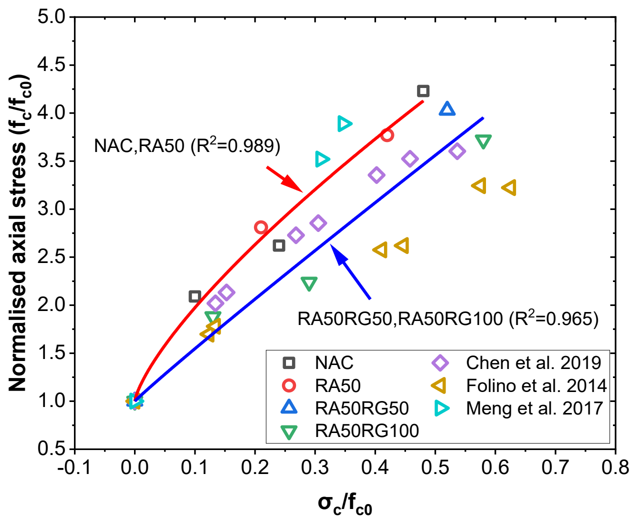

Figure 7.20 Fitting performance of Power-Law failure criterion under triaxial compression

A comprehensive comparison shows that the William-Warnke failure criterion had the best fitting performance on test data in this study. The fitting correlation coefficient R^2 for concrete specimens with and without RGS are both higher than 0.99. Moreover, the William-Warnke failure curve proposed from this experiment is closer to RAC triaxial compression data obtained by other researchers.

7.4.2 Failure criteria for triaxial compression with pore water pressure

At present, there is still a lack of test data on the triaxial compressive strength of concrete materials under a constant pore water pressure. This study drew on Mohr-Coulomb failure criterion and Power-Law failure criterion and proposed a new failure criterion model to describe the strength surface of RAC with and without RGS. The failure criterion can be expressed as:

$$f_c = k_4\sigma_p + b_4 \tag{7.15}$$

$$\frac{f_c}{f_{c0}} = a_5 \left(\frac{\sigma_c}{f_{c0}}\right)^{b_5} + c_5 \tag{7.16}$$

Coefficients k_4, b_4, a_5, b_5 and c_5 can be calculated based on test data. The verified failure criteria are shown in Eqs. (7.17)-(7.20):

NAC and RA50 $$f_c = -4.87\sigma_p + 4.02 \tag{7.17}$$

NAC and RA50 $$f_c = -2.49\sigma_p + 3.96 \tag{7.18}$$

RA50RG50 and RA50RG100 $$\frac{f_c}{f_{c0}} = -5.24\left(\frac{\sigma_c}{f_{c0}}\right)^{1.09} + 3.99 \tag{7.19}$$

RA50RG50 and RA50RG100 $$\frac{f_c}{f_{c0}} = -3.35\left(\frac{\sigma_c}{f_{c0}}\right)^{1.46} + 3.89 \tag{7.20}$$

The verification of proposed failure criteria and test data of concrete specimens under triaxial compression with pore water pressure are shown in Figure 7.21. It can be found that normalised axial stress of NAC and RA50 decreased faster than RA50RG50 and RA50RG100 with pore water pressure. The peak stress of NAC and RA50 was closer to a linear relationship with normalised pore water pressure. The power function can achieve a better fitting results for RAC containing RGS, but the fitting correlation coefficient R2 did not exceed 0.9.

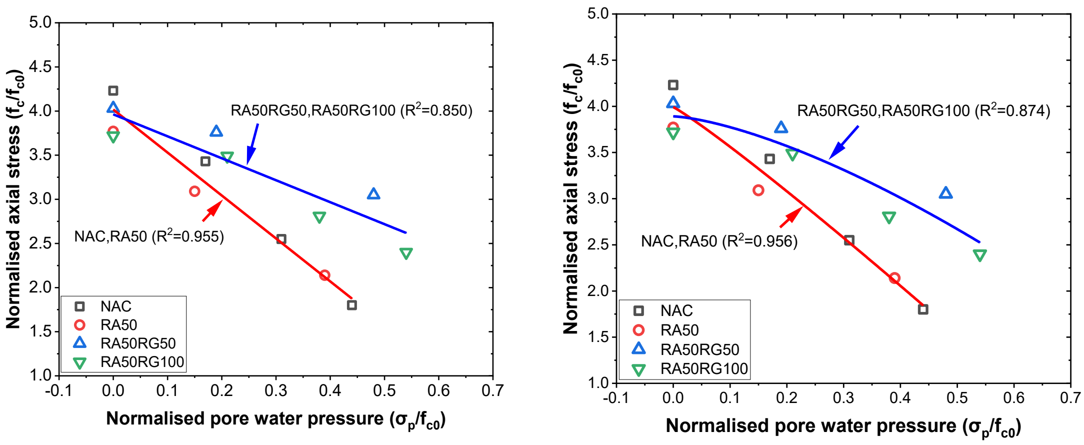

(a) Linear fitting (b) Power function fitting

Figure 7.21 Fitting performance under triaxial compression with pore water pressure

7.5 Stress-strain model

The stress-strain behaviour of NAC and RAC under uniaxial and triaxial compression has been studied by many researchers (Xu, et al. 2021b, Xue, et al. 2023). Based on the test data, empirical models were proposed, including CEB-FIP model, Collins and Mitchell's model and Binici's model etc (Tang, et al. 2019). However, due to the lack of test data, to the authors' knowledge no model has been proven to predict the stress-strain trends of RAC with RGS under triaxial compression and pore water pressure. By comparing existing models, Collins and Mitchell's model (Eq. (7.21)) (Collins & Mitchell 1991), Guo and Zhang's model (Eq. (7.22)) (1982) and Chen's model (Eq. (7.23)) (2019) were selected to fit experimental data of uniaxial compression, triaxial compression and triaxial compression combined with pore water pressure respectively. From the analysis in Section 4, it can be known that RGS could change the internal friction angle of concrete specimens. Therefore, the concrete specimens were divided into two groups, which are discussed in Section 7.5.1 and 7.5.2 respectively.

Uniaxial compression

$$\frac{\sigma_a}{f_{c0}}=\begin{cases}\dfrac{A_1\left(\dfrac{\varepsilon_a}{\varepsilon_{ap0}}\right)}{A_1-1+\left(\dfrac{\varepsilon_a}{\varepsilon_{ap0}}\right)^{A_1}} & 0\le\dfrac{\varepsilon_a}{\varepsilon_{ap0}}<1\\ \dfrac{A_1\left(\dfrac{\varepsilon_a}{\varepsilon_{ap0}}\right)}{A_1-1+\left(\dfrac{\varepsilon_a}{\varepsilon_{ap0}}\right)^{A_1B_1}} & \dfrac{\varepsilon_a}{\varepsilon_{ap0}}\ge 1\end{cases}\tag{7.21}$$

Triaxial compression

$$\frac{\sigma_a}{f_c}=\begin{cases}A_2\left(\dfrac{\varepsilon_a}{\varepsilon_{ap}}\right)+(3-2A_2)\left(\dfrac{\varepsilon_a}{\varepsilon_{ap}}\right)^2+(A_2-2)\left(\dfrac{\varepsilon_a}{\varepsilon_{ap}}\right)^3 & 0\le\dfrac{\varepsilon_a}{\varepsilon_{ap}}<1\\ \dfrac{\left(\dfrac{\varepsilon_a}{\varepsilon_{ap}}\right)}{B_2\left(\dfrac{\varepsilon_a}{\varepsilon_{ap}}-1\right)^2+\left(\dfrac{\varepsilon_a}{\varepsilon_{ap}}\right)} & \dfrac{\varepsilon_a}{\varepsilon_{ap}}\ge 1\end{cases}\tag{7.22}$$

Pore water pressure

$$\frac{\sigma_a}{f_c}=\begin{cases}\dfrac{A_3\left(\dfrac{\varepsilon_a}{\varepsilon_{ap}}\right)-\left(\dfrac{\varepsilon_a}{\varepsilon_{ap}}\right)^2}{1+(A_3-2)\left(\dfrac{\varepsilon_a}{\varepsilon_{ap}}\right)} & 0\le\dfrac{\varepsilon_a}{\varepsilon_{ap}}<1\\ \dfrac{\dfrac{\varepsilon_a}{\varepsilon_{ap}}}{B_2\left(\dfrac{\varepsilon_a}{\varepsilon_{ap}}-1\right)^2+\left(\dfrac{\varepsilon_a}{\varepsilon_{ap}}\right)} & \dfrac{\varepsilon_a}{\varepsilon_{ap}}\ge 1\end{cases}\tag{7.23}$$

7.5.1 NAC and RA50

Based on test data, A_1 and B_1 in Eq. (7.21) were calibrated as 3.52 and 1.05 respectively for NAC and RA50 under uniaxial compression. For NAC and RA50 under triaxial compression, the model Eq. (7.22) considered the ductility enhancement under the influence of confining pressure, which is shown on the stress-strain curve with a higher peak strain and a gentle descending part. The parameters A_2 and B_2 were determined as 3.52 and 0.25 respectively by regression analysis. The situation was even more special under triaxial compression combined with pore water pressure. This is shown by an increase in the elastic modulus and a decrease in the peak stress. Moreover, when the pore water pressure reached 13 MPa, the post-peak curve of the concrete specimen become steeper, close to the stress-strain curve under uniaxial compression. Traditional uniaxial and triaxial compression empirical models are not suitable for this situation. By comparison, Chen et al. (2019) proposed a model which was modified from CEB-FIP model (1990) and Guo and Zhang's model (1982) for studying the mechanical properties of RAC can achieve a better prediction of stress-strain curves of concrete specimens under triaxial compression combined with pore water pressure. The parameters A_3 and B_3 for NAC and RA50 under triaxial compression with pore water pressure of 5 MPa and 9 MPa were determined as 9.69 and 0.11 respectively. When pore water pressure reached 13 MPa, A_3 and B_3 were 4.35 and 0.59 respectively.

The comparison of test data and above models is shown in Figs. 7.22-7.24. The empirical model selected in this study can achieve a satisfying predicting results for stress-strain development trends of NAC and RA50 under various stress states, especially in the rising part of the curves. Due to the multi-phase and heterogeneous nature of concrete materials, numerous accidental conditions may occur after cracks generated, and therefore, deviations between the prediction results and experimental data occurred in the descending part of the curve.

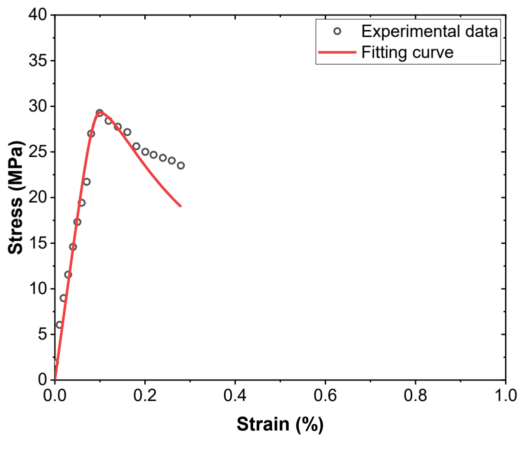

(a) NAC-0

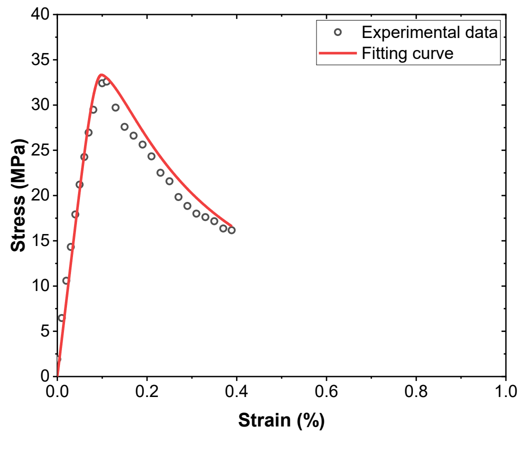

(b) RA50-0

Figure 7.22 Comparison of experimental results and fitting curves of NAC and RA50 under uniaxial compression

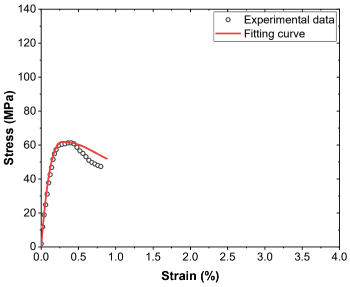

(a) NAC-3

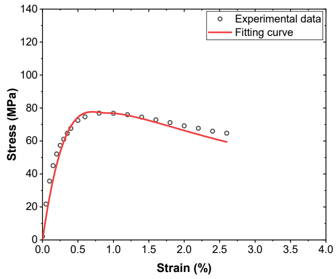

(b) NAC-7

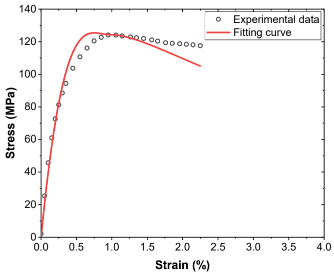

(c) NAC-14

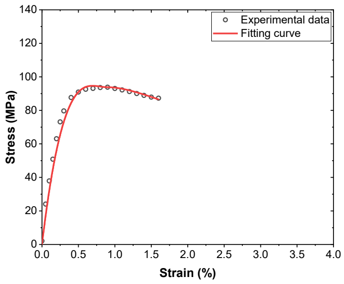

(d) RA50-7

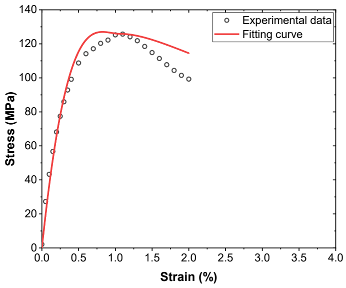

(e) RA50-14

Figure 7.23 Comparison of experimental results and fitting curves of NAC and RA50 under triaxial compression

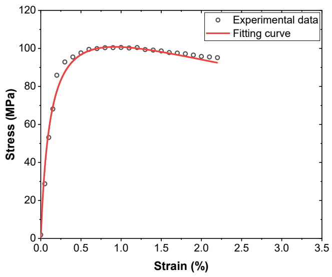

(a) NAC-14-5

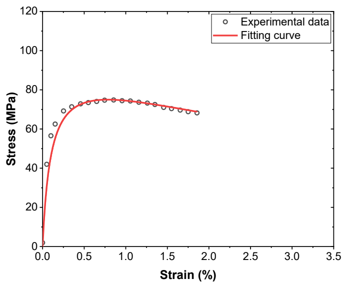

(b) NAC-14-9

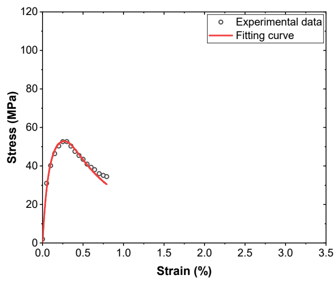

(c) NAC-14-13

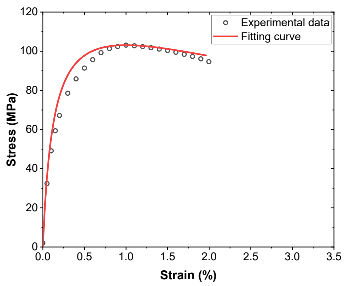

(d) RA50-14-5

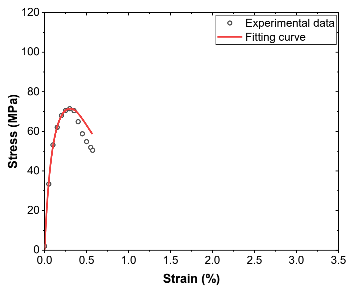

(e) RA50-14-13

Figure 7.24 Comparison of experimental results and fitting curves of NAC and RA50 under triaxial compression with pore water pressure

7.5.2 RA50RG50 and RA50RG100

The ductility of RAC containing RGS was better than ordinary NAC and RAC. As shown in Figure 7.25, when uniaxial compression empirical model Eq. (7.21) was used to fit the experimental data, deformities appeared in the descending part of the curve. The higher porosity within ITZ-Glass enhanced the plastic deformation characteristics of the specimen. As a result, the descending section of the stress-strain curves is flatter than the uniaxial compression stress-strain curves of ordinary concrete specimens which is close to the triaxial compression case without considering the peak stress. After switching to the triaxial compression model Eq. (7.22), the fitting curve returns to normal. However, there were still differences between the predicted results and the experimental data in the descending part of the curve. This may be related to the poor bonding performance between RGS and cement paste. The high porosity and weak cohesion strength in ITZ-Glass increased the discreteness of the data after the specimens damaged. For RA50RG50 and RA50RG100 under uniaxial compression, A_2 and B_2 in Eq. (7.22) were determined as 1.49 and 1.51 respectively. Under triaxial compression, the model Eq. (7.22) was still used to fit the experimental data. Parameters A_2 and B_2 were calibrated as 3.63 and 0.15 respectively for RA50RG50 and RA50RG100. The fitting curves and experimental data under triaxial compression were presented in Figure 7.26. When concrete specimens were subjected to triaxial compression combined with pore water pressure of 5 MPa and 9 MPa, the parameters A_3 and B_3 in Eq. (7.23) were determined as 10.78 and 0.18. High pore water pressure improved the steepness of the descending part of the stress-strain curve. As a result, when pore water pressure rose to 14 MPa, A_3 and B_3 were 4.44 and 0.27 respectively. Similar to NAC and RA50, the empirical models had satisfying fitting performance for the rising part of stress-strain curves, but there were deviations in the descending part, as shown in Figure 7.27.

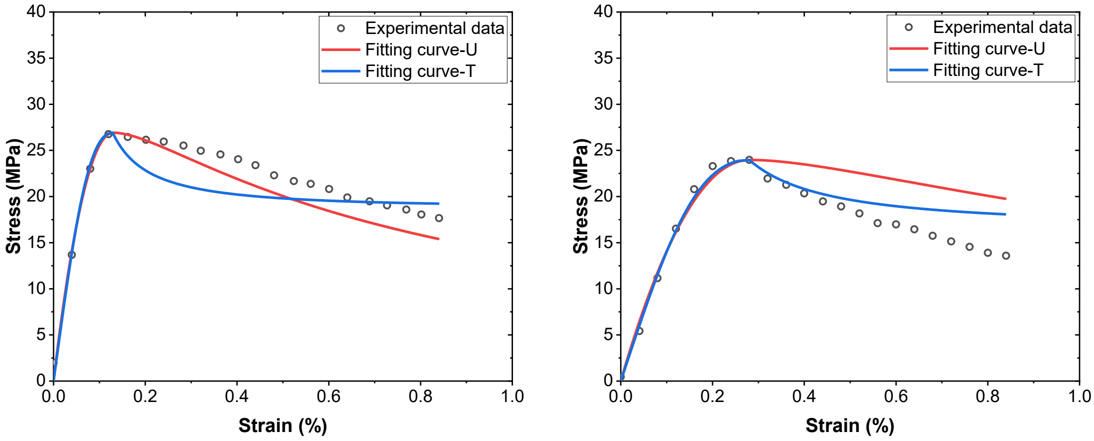

(a) RA50RG50-0 (b) RA50RG100-0

Figure 7.25 Comparison of experimental data and fitting curves of RA50RG50 and RA50RG100 under uniaxial compression

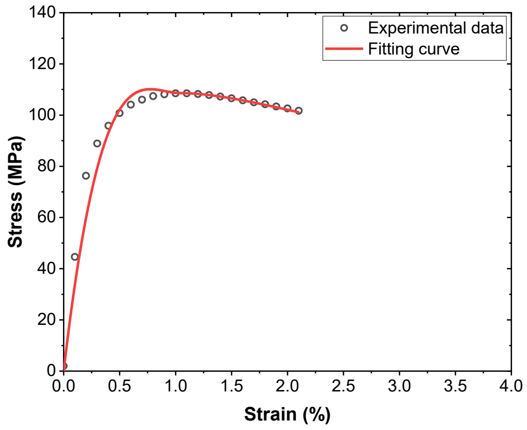

(a) RA50RG50-14

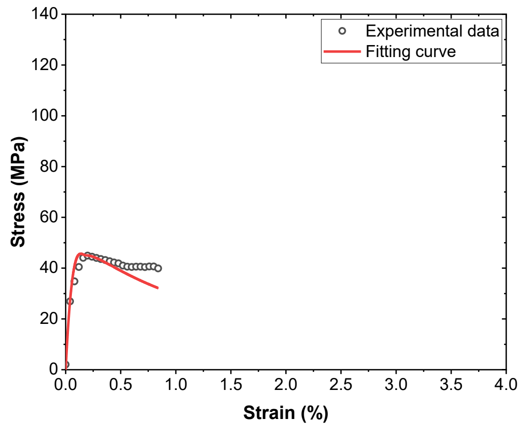

(b) RA50RG100-3

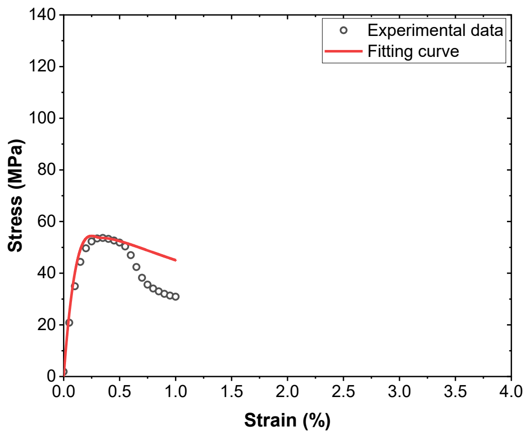

(c) RA50RG100-7

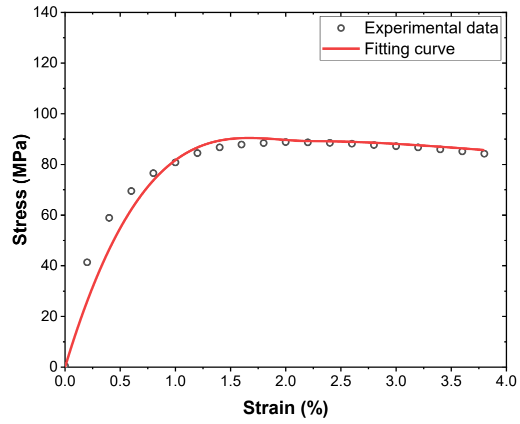

(d) RA50RG100-14

Figure 7.26 Comparison of experimental data and fitting curves of RA50RG50 and RA50RG100 under triaxial compression

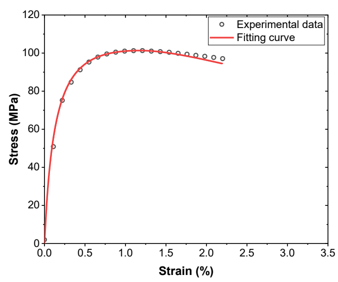

(a) RA50RG50-14-5

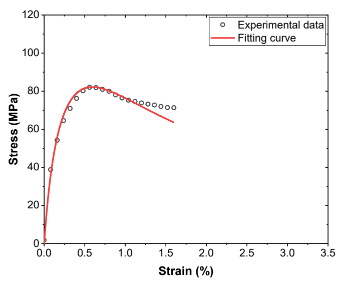

(b) RA50RG50-14-13

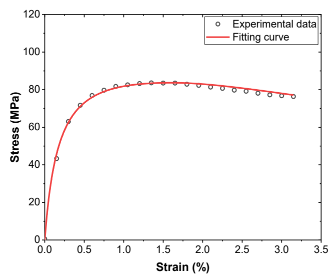

(c) RA50RG100-14-5

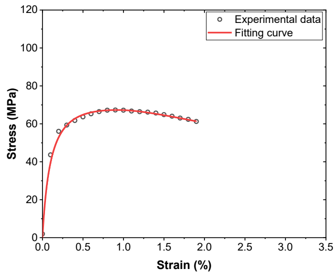

(d) RA50RG100-14-9

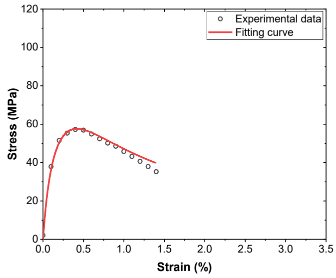

(e) RA50RG100-14-13

Figure 7.27 Comparison of experimental data and fitting curves of RA50RG50 and RA50RG100 under triaxial compression with pore water pressure

7.6 Conclusion

Triaxial compressive properties of sustainable concrete with RCA and RGS under the influence of pore water pressure were analysed and discussed based on stress-strain curves. Nanoscratch and BSE-based image analysis technique were used to identify characteristics of ITZs in concrete samples, which is contributed to explain the mechanism of the sustainable concrete specimen performance under various complicated stress states. The following conclusions can be drawn up from this study:

(1) Nanoscratch is a more precise method for determining the ITZ width than traditional techniques like nanoindentation and image analysis. In the study, the widths of New ITZ-RCA and ITZ-Glass were the largest, measuring at 27.91 μm and 30.77 μm respectively. ITZ-NCA, Old ITZ-RCA, and ITZ-NFA had smaller widths at around 10 μm.

(2) The microscopic properties of ITZ are not only related to the mixture ratio of cement paste, but also closely related to the chemical activity and specific surface area of aggregate. For coarse aggregate, the scratch hardness of New ITZ-RCA was higher than that of ITZ-NCA because the rough surface of the old mortar weakened the

influence of ‘wall effect’, and the incompletely hydrated particles in the old mortar enhanced the cohesion with new ITZ. For fine aggregate, ITZ-Glass contained fewer unhydrated clinkers, less CH, and had a higher porosity, resulting in low scratch hardness.

(3) Under triaxial compression, the confining pressure significantly enhanced the peak stress, axial peak strain and maximum volumetric strain of concrete specimens. When pore water pressure existed, the elastic modulus was improved and the ductility was reduced due to the supporting effect of pore water pressure. Meanwhile, because of the promotion effect of pore water pressure on crack expansion, peak stress decreased and the descending part of stress-strain curves became steeper.

(4) RCA would not weaken the mechanical properties of concrete specimens under triaxial compression and pore water pressure. However, when NFA was replaced by RGS, the peak stress decreased significantly and the peak strain improved under various stress states. The enhancement efficiency of confining pressure on the peak stress of sustainable concrete with RGS was diminished. When the confining pressure reached 14 MPa and pore water pressure was 0-5 MPa, concrete specimens were destroyed in the compressive state.

(5) The William-Warnke failure criterion is suitable for fitting the failure surface of sustainable concrete with RCA and RGS under triaxial compression. For triaxial compression combined with pore water pressure condition, power function can be used to describe the relationship between peak stress and normalised pore water pressure.

(6) Three empirical models were selected and used to predict the stress-strain curves of sustainable concrete under various stress states. High pore water pressure made the

triaxial compressive stress-strain curves be more like that under uniaxial compression. As a result, a modified uniaxial compression empirical model combined with triaxial compression model needs to be used. For stress-strain curves of RA50RG50 and RA50RG100 under uniaxial compression, a triaxial compression model achieved a better fitting performance.

CHAPTER 8. CONCLUSIONS AND RECOMMENDATIONS

8.1 Summary and conclusions

In this thesis, the microscopic properties of ITZs in sustainable concrete with RCA, RGS and RGP are investigated in depth and detail. BSE-based image analysis was used to statistically analyse the distribution patterns of hydration products, unhydrated products, pores and cracks within ITZs. Nanoindentation and nanoscratch were used to test the elastic modulus, hardness and fracture toughness of different types of ITZs. Subsequently, considering the promotion of the sustainable concrete materials in actual engineering construction, triaxial compression tests with pore water pressure was conducted and stress-strain curves were obtained. The mechanical properties of the sustainable concrete under complicated stress states were analysed based on stress-strain curves, and the failure mechanism was explained according to the microscopic characterisation of ITZs.

For the ITZs microscopic characterisation, the critical findings can be listed as follows:

(1) Nanoindentation, nanoscratch and BSE-based image analysis technique can be used to identify ITZ width. The quantitative accuracy of ITZ width by nanoscratch is higher than nanoindentation and BSE-based image analysis because nanoscratch can obtain continuous test data and less affected by rough aggregate surface. Among the ITZs discussed in this thesis, ITZ-NCA and Old ITZ-RCA were close in width. The width of New ITZ-RCA was higher than that of Old ITZ-RCA. ITZ-NFA had the smallest width due to the higher specific surface area. When NFA was replaced by RGS, the width of ITZ-Glass increased significantly compared to ITZ-NFA, indicating the weakest cohesion strength between cement paste and RGS. In addition, replacing Portlandite cement with 20% RGP is contributed to reduce the width of ITZ-NCA and New ITZ-RCA.

(2) The constituent composition within ITZs is closely related to curing age and chemical activity of aggregate. The old mortar on the surface of RCA had the longest curing time, so the content of unhydrated products in Old ITZ-RCA was lower. However, the crushing and saving process produced more cracks within Old ITZ-RCA. The early porosity of New ITZ-RCA reached 7.29%. After one year of curing, the volume fraction of cracks and pores in New ITZ-RCA decreased, the proportion of hydration products increased. The 20% RGP can reduce the proportion of pores, cracks and unhydrated products as well as improve the content of hydration products. Due to almost zero water absorption and high specific surface area, free water easily accumulated on the surface of RGS, resulting in a high porosity in ITZ-Glass. Meanwhile, the pozzolanic activity of glass consumed CH and created more hydration products near the surface of RGS.

(3) The micromechanical properties of ITZ were lower than those of the adjacent paste matrix. In this thesis, the elastic modulus and hardness of New ITZ-RCA were not obviously different from adjacent paste matrix, indicating that the ‘wall effect’ was not obvious in New ITZ-RCA. RGP can improve the micromechanical properties of cement paste contact with NCA and old mortar. On the one hand, RGP consumed CH and generated more high-density C-S-H. On the other hand, the incompletely reacted glass clinker filled the pores, thus showing higher mechanical properties in the nanoindentation test results. New ITZ-RCA without RGP could have higher cohesion strength than ITZ-NCA after a long-term curing. ITZ-Glass had the weakest micromechanical properties because of the higher proportion of pores and low-density C-S-H.

(4) Nanoscratch combined with deconvolution analysis can obtain the proportion of phases in ITZs and the frequency density histograms of scratch hardness and fracture

toughness. To avoid the interference of asymmetry on the test results, the hemispherical tip was equipped when conducting nanoscratch tests rather than the Berkovich tip in nanoindentation tests. The project area of the hemispherical tip was larger and it is difficult to reflect a single phase. In most cases, the peaks by using Gaussian mixture model to deconvolute the frequency density histograms of scratch hardness and fracture toughness represent a component of multiple phases. Among the ITZs discussed in this thesis, the composition within Old ITZ-RCA and ITZ-Glass was relatively uniform. Old ITZ-RCA experienced a longer curing period. For ITZ-Glass, the pozzolanic effect of glass accelerated the consumption of unhydrated products.

(5) Quantitative analysis of EDS mapping shows that the Si/Ca ratio of C-S-H in ITZ-NCA and New ITZ-RCA without RGP was between 0.5 and 1. 20% RGP can effectively promote hydration and pozzolanic reaction from physical and chemical level to generate more high-density C-S-H with a Si/Ca ratio of around 1.5. TGA, XRD and NMR results confirmed that RGP consumed CH in ITZs and created more C-S-H gels. In addition to active SiO_2, RGP also contained a large amount of alkali metal oxides. The deconvolution results of the FTIR spectrum between 700 cm^{-1} and 1300 cm^{-1} indicate that the alkali metal oxides in RGP dissolved in pore water, accelerating the carbonisation of the cement paste and slowing down the formation of ettringite.

For macro-mechanical properties of sustainable concrete with RCA and RGS under coupling effect of confining pressure and pore water pressure, the following conclusions can be drawn up:

(1) When sustainable concrete specimens were under triaxial compression, the failure mode changed from circumferential splitting failure for uniaxial compression to oblique shear shear failure. The contents of RCA and RGS would not have a significant impact on the failure mode of sustainable concrete specimens. Under the coupling effect of confining pressure and pore water pressure, the concrete specimens still showed an oblique shear failure mode. It is worth noting that when the pore water pressure was high, the concrete specimens would show a failure mode similar to uniaxial compression condition due to the offset effect of confining pressure and pore water pressure.

(2) The peak stress, peak strain and maximum volumetric strain on the stress-strain curves of sustainable concrete specimens increased with confining pressure. The post-peak ductility of stress-strain curves also gradually increased with confining pressure because the lateral confinement improved the internal friction angle of concrete specimens. In comparison, the change pattern of elastic modulus due to the influence of confining pressure was not obvious. Pore water pressure has a supporting effect on pores and a promotion effect on crack expansion. The supporting effect increased the initial stiffness of concrete specimens, whereas the promotion effect on crack expansion reduced the peak stress and axial peak strain of stress-strain curves.

(3) RCA did not reduce the mechanical properties of sustainable concrete specimens under complicated stress states. The peak stress of concrete specimens decreased with increasing RGS content and the axial peak strain of specimens with RGS was higher than NAC and RAC because the higher porosity within the ITZ-Glass reduced the improving efficiency of confining pressure on the compressive strength of concrete and provided more compression space. When the confining pressure was higher than 14 MPa and there was not enough pore water pressure, RA50RG100 remained in

compressive deformation until destruction. The micromechanical properties of ITZs in RCA were high. Therefore, it showed more obvious post-peak brittle damage characteristics at various stress states. In comparison, the ductile damage characteristics of concrete specimens with RGS were more pronounced at triaxial compression with pore water pressure.

(4) Mohr-Coulomb failure criterion, Power-Law failure criterion and William-Warnke failure criterion can be used to describe the critical state of sustainable concrete with RCA and RGS under triaxial compression with pore water pressure. Comparison with test data from other researchers, the parameters of failure criteria obtained from regression analysis based on the data in this thesis are within reasonable limits. The William-Warnke failure criterion can achieve the best fitting results for sustainable concrete with RCA and RGS under triaxial compression. The relationship between the normalised peak stress and pore water pressure of sustainable concrete with RCA and RGS can be described by descending linear function and power function. RAC100 had a special situation under triaxial compression combined with pore water pressure. The normalised peak stress of RA100 dropped to 2.6 when pore water pressure was 5 MPa and maintained at this value with the increase of pore water pressure. This peak stress can be calculated by the modified function proposed by Malecot et al.

(5) Existing empirical models can be used to predict stress-strain curves of sustainable concrete under uniaxial compression and triaxial compression. RAC with RGS exhibited strong ductile deformation under uniaxial compression. If the traditional uniaxial compression empirical model was used, abnormal fitting curve was obtained. As a result, the stress-strain curve of RAC with RGS under uniaxial compression should be fitted by a triaxial compression empirical model. Traditional triaxial

compression models overestimated peak stress and underestimated elastic modulus when pore water pressure existed. Modifying and combining the uniaxial compression empirical model and triaxial compression empirical model can achieve satisfying fitting results for the sustainable concrete specimens under confining pressure with pore water pressure.

8.2 Recommendations for future work

In this thesis, the cohesion performance of ITZs in sustainable concrete with RCA, RGS and RGP was evaluated in depth from component distribution, micromechanical properties and chemical composition. In order to promote the application of sustainable concrete materials in the actual engineering construction, the macro-mechanical properties of concrete containing RCA and RGS under coupling confining pressure and pore water pressure were studied. The mechanical performance of sustainable concrete specimens under various complicated stress states were explained by microscopic characterisation techniques for ITZs in concrete. However, there is still much meaningful work to be done on material optimisation and durability of sustainable concrete materials under complicated stress states, which are recommended as follows:

(1) In addition to RCA, recycled fine aggregate and recycled powder are produced in the curing process. The study of the bonding properties of cement paste to recycled fine aggregate and the influence of recycled powder on ITZs can help maximise the use of C&D waste. Recycled fine aggregate and recycled powder deserve more attention in the future.

(2) RGP has been shown to function as a precursor for geopolymer composites. Studying the cohesion performance of ITZs in RGP-based geopolymer recycled aggregate concrete is contributed to maximise the utilization of waste concrete and glass. In

addition, ITZ strengthening methods, such as carbonization, can also be tried in future research.

(3) Ordinary RCA and transparent soda-lime glass were used as raw materials in this thesis. However, the original water-cement ratio, age and source of the RCA; the particle size and chemical composition of the glass can all have a significant impact on the micro- and macro-level properties of sustainable concrete. To enhance the generalizability of this research, more experiments on the effects of raw materials deserve carrying out.

(4) This thesis conducted mechanical property tests of sustainable concrete specimens under complicated stress states and discussed the effects of RCA and RGS replacement ratio on the mechanical properties of specimens under coupling of confining pressure and pore water pressure, but the test data is limited. In the future, more concrete specimens can be used for mechanical property tests under different level of confining pressure and pore water pressure. Based on the test data, a more precise predictive model considering ITZ porosity and micromechanical properties for the macro-mechanical properties of sustainable concrete under complicated stress states can be established. This helps predict the safety of sustainable concrete materials used in structural elements.

(5) The durability of sustainable concrete materials under complicated stress states is also worth exploring. For example, the triaxial compressive properties of concrete containing RCA and RGS under high temperature, the permeability performance under lateral active confinement, and the anti-deformation ability under the coupling effect of confining pressure and pore water pressure, etc. If sustainable concrete materials can still maintain satisfactory durability under these complicated stress

conditions, it can be speculated that structure elements constructed by sustainable concrete materials can work normally after experiencing aggressive environments.

REFERENCES

Abbas, A., Fathifazl, G., Fournier, B., Isgor, O.B., Zavadil, R., Razaqpur, A.G. & Foo, S., 2009, 'Quantification of the residual mortar content in recycled concrete aggregates by image analysis', *Materials Characterization*, vol. 60, pp. 716-728.

Akono, A.-T. & Ulm, F.-J., 2014, 'An improved technique for characterizing the fracture toughness via scratch test experiments', *Wear*, vol. 313, pp. 117-124.

Akono, A.-T. & Ulm, F.-J., 2017, 'Microscopic Toughness of Viscous Solids via Scratching: From Amorphous Polymers to Gas Shale', *Journal of Nanomechanics and Micromechanics*, vol. 7, no. 3, pp. 04017009.

Ali, E.E. & Al-Tersawy, S.H., 2012, 'Recycled glass as a partial replacement for fine aggregate in self compacting concrete', *Construction and Building Materials*, vol. 35, pp. 785-791.

Aliabdo, A.A., Elmoaty, A.E.M.A. & Fawzy, A.M., 2018, 'Experimental investigation on permeability indices and strength of modified pervious concrete with recycled concrete aggregate', *Construction and Building Materials*, vol. 193, pp. 105-127.

Arabi, N., Meftah, H., Amara, H., Kebaïli, O. & Berredjem, L., 2019, 'Valorization of recycled materials in development of self-compacting concrete: Mixing recycled concrete aggregates – Windshield waste glass aggregates', *Construction and Building Materials*, vol. 209, pp. 364-376.

Arulrajah, A., Disfani, M.M., Haghighi, H., Mohammadinia, A. & Horpibulsuk, S., 2015, 'Modulus of rupture evaluation of cement stabilized recycled glass/recycled concrete aggregate blends', *Construction and Building Materials*, vol. 84, pp. 146-155.

ASTM 2005. ‘G171-03: Standard test method for scratch hardness of materials using a diamond stylus’, *West Conshohocken*, *PA, USA: American Society for Testing and Materials International*.

ASTM 2013, ‘C1567-13: Standard test method for determining the potential alkali-silica reactivity of combinations of cementitious materials and aggregate (accelerated mortar-bar method’, *West Conshohocken*, *PA, USA: American Society for Testing and Materials International*.

ASTM 2019, ‘C511-19: Standard specification for mixing rooms, moist cabinets, moist rooms, and water stroage tanks used in the testing of hydraulic cements and concretes’, *West Conshohocken*, *PA, USA: American Society for Testing and Materials International*.

ASTM 2019, ‘C192-19: Standard practice for making and curing concrete test specimens in the laboratory’, *West Conshohocken*, *PA, USA: American Society for Testing and Materials International*.

AS 2010, ‘AS 3972: General purpose and blended cements’, *Sydney, Australia, Australian Standard*.

AS 2014, ‘AS 1141.60.1: Methods for sampling and testing aggregates potential alkali-silica reactivity-Accelerated mortar bar method’, *Sydney, Australia, Australian Standard*.

Bilondi, M.P., Toufigh, M.M. & Toufigh, V., 2018, 'Using calcium carbide residue as an alkaline activator for glass powder–clay geopolymer', *Construction and Building Materials*, vol. 183, pp. 417-428.

Bisht, K., Kabeer, K.I.S.A. & Ramana, P.V., 2020, 'Gainful utilization of waste glass for production of sulphuric acid resistance concrete', *Construction and Building Materials*, vol. 235, pp. 117486.

Bogas, J.A., Brito, J.d. & Ramos, D., 2016, 'Freeze-thaw resistance of concrete produced with fine recycled concrete aggregates', *Journal of Cleaner Production*, vol. 115, pp. 294-306.

Bosque, I.F.S.d., Zhu, W., Howind, T., Matías, A., Rojas, M.I.S.d. & Medina, C., 2017, 'Properties of interfacial transition zones (ITZs) in concrete containing recycled mixed aggregate', *Cement and Concrete Composites*, vol. 81, pp. 25-34.

Brand, A.S., Roesler, J.R. & Salas, A., 2015, 'Initial moisture and mixing effects on higher quality recycled coarse aggregate concrete', *Construction and Building Materials*, vol. 79, pp. 83-89.

Bravo, M., Brito, J.d., Evangelista, L. & Pacheco, J., 2017, 'Superplasticizer's efficiency on the mechanical properties of recycled aggregates concrete: Influence of recycled aggregates composition and incorporation ratio', *Construction and Building Materials*, vol. 153, pp. 129-138.

Cabrera-Covarrubias, F.G., Gómez-Soberón, J.M., Rosas-Casarez, C.A., Almaral-Sánchez, J.L. & Bernal-Camacho, J.M., 2021, 'Recycled Mortars with Ceramic Aggregates. Pore Network Transmutation and Its Relationship with Physical and Mechanical Properties', *Materials*, vol. 14, no. 1543, pp. 14061543.

Camposeco-Negrete, C., 2013, 'Optimization of cutting parameters for minimizing energy consumption in turning of AISI 6061 T6 using Taguchi methodology and ANOVA', *Journal of Cleaner Production*, vol. 53, pp. 195-203.

Candappa, D.C., Sanjayan, J.G. & Setunge, S., 2001, 'Complete triaxial stress-strain curves of high-strength concrete', *Journal of Materials in Civil Engineering*, vol. 13, no. 3, pp. 209-215.

Carvalho, E.P. & Carrasco, E.V.M., 2010, 'Influence of test specimen on experimental characterization of timber–concrete composite joints', *Construction and Building*

Materials, vol. 24, pp. 1313-1322.

CE, M., 1990, 'Design of Concrete Structures', *CEB-FIP Model Code*, vol. pp.

Chen, C.H., Huang, R., Wu, J.K. & Yang, C.C., 2006, 'Waste E-glass particles used in cementitious mixtures', *Cement and Concrete Research*, vol. 36, pp. 449-456.

Chen, D., Yu, X., Shen, J., Liao, Y. & Zhang, Y., 2017, 'Investigation of the curing time on the mechanical behavior of normal concrete under triaxial compression', *Construction and Building Materials*, vol. 147, pp. 488-496.

Chen, J.J., Thomas, J.J., Taylor, H.F.W. & Jennings, H.M., 2004, 'Solubility and structure of calcium silicate hydrate', *Cement and Concrete Research*, vol. 34, pp. 1499-1519.

Chen, L., Zhang, Y., Wang, L., Ruan, S., Chen, J., Li, H., Yang, J., Mechtcherine, V. & Tsang, D.C.W., 2022, 'Biochar-augmented carbon-negative concrete', *Chemical Engineering Journal*, vol. 431, pp. 133946.

Chen, Y., Chen, Z., Xu, J., Lui, E.M. & Wu, B., 2019, 'Performance evaluation of recycled aggregate concrete under multiaxial compression', *Construction and Building Materials*, vol. 229, pp. 116935.

Collins, M.P. & Mitchell, D., 1991, 'Prestressed Concrete Structures', *Prentice Hall, Englewood Cliffs, NJ*.

Corinaldesi, V. & Moriconi, G., 2009, 'Influence of mineral additions on the performance of 100% recycled aggregate concrete', *Construction and Building Materials*, vol. 23, pp. 2869-2876.

Corr, D., Accardi, M., Graham-Brady, L. & Shah, S., 2007, 'Digital image correlation analysis of interfacial debonding properties and fracture behavior in concrete', *Engineering Fracture Mechanics*, vol. 74, pp. 109-121.

Deng, Z., Wang, Y., Sheng, J. & Hu, X., 2017, 'Strength and deformation of recycled aggregate concrete under triaxial compression', *Construction and Building Materials*, vol. 156, pp. 1043-1052.

Deng, Z., Huang, H., Ye, B., Xiang, P. & Li, C., 2020, 'Mechanical Performance of RAC under True-Triaxial Compression after High Temperatures', *Journal of Materials in Civil Engineering*, vol. 32, no. 8, pp. 04020194.

Diamond, S. & Huang, J., 2001, 'The ITZ in concrete-a different view based on image analysis and SEM observations', *Cement and Concrete Composites*, vol. 23, pp. 179-188.

Dimitriou, G., Savva, P. & Petrou, M.F., 2018, 'Enhancing mechanical and durability properties of recycled aggregate concrete', *Construction and Building Materials*, vol. 158, pp. 228-235.

Djerbi, A., 2018, 'Effect of recycled coarse aggregate on the new interfacial transition zone concrete', *Construction and Building Materials*, vol. 190, pp. 1023-1033.

Dong, W., Li, W. & Tao, Z., 2021, 'A comprehensive review on performance of cementitious and geopolymeric concretes with recycled waste glass as powder, sand or cullet', *Resources, Conservation & Recycling*, vol. 172, pp. 105664.

Dong, W., Li, W., Guo, Y., Wang, K. & Sheng, D., 2022, 'Mechanical properties and piezoresistive performances of intrinsic graphene nanoplate/cement-based sensors subjected to impact load', *Construction and Building Materials*, vol. 327, pp. 126978.

Du, H. & Tan, K.H., 2017, 'Properties of high volume glass powder concrete', *Cement and Concrete Composites*, vol. 75, pp. 22-29.

El-Hassan, H., Kianmehr, P. & Zouaoui, S., 2019, 'Properties of pervious concrete incorporating recycled concrete aggregates and slag', *Construction and Building Materials*, vol. 212, pp. 164-175.

Escalante-Garcia, J.I., 2003, 'Nonevaporable water from neat OPC and replacement materials in composite cements hydrated at different temperatures', *Cement and Concrete Research*, vol. 33, pp. 1883-1888.

Fang, G. & Zhang, M., 2020, 'The evolution of interfacial transition zone in alkali-activated fly ash-slag concrete', *Cement and Concrete Research*, vol. 129, pp. 105963.

Fang, G., Wang, Q. & Zhang, M., 2021, 'Micromechanical analysis of interfacial transition zone in alkali-activated fly ash-slag concrete', *Cement and Concrete Composites*, vol. 119, pp. 103990.

Fang, G., Chen, J., Dong, B. & Liu, B., 2023, 'Microstructure and micromechanical properties of interfacial transition zone in green recycled aggregate concrete', *Journal of Building Engineering*, vol. 66, pp. 105860.

Folino, P. & Xargay, H., 2014, 'Recycled aggregate concrete – Mechanical behavior under uniaxial and triaxial compression', *Construction and Building Materials*, vol. 56, pp. 21-31.

Fu, C., Ling, Y. & Wang, K., 2020, 'An innovation study on chloride and oxygen diffusions in simulated interfacial transition zone of cementitious material', *Cement and Concrete Composites*, vol. 110, pp. 103585.

Gaël, B., Christelle, T., Gilles, E., Sandrine, G. & Tristan, S.-F., 2016, 'Determination of the proportion of anhydrous cement using SEM image analysis', *Construction and Building Materials*, vol. 126, pp. 157-164.

Gao, C., Huang, L., Yan, L., Kasal, B. & Li, W., 2016, 'Behavior of glass and carbon FRP tube encased recycled aggregate concrete with recycled clay brick aggregate', *Composite Structures*, vol. 155, pp. 245-254.

Garcı´a-Lodeiro, I., Ferna´ndez-Jime´nez, A., Blanco, M.T. & Palomo, A., 2008, 'FTIR study of the sol–gel synthesis of cementitious gels: C–S–H and N–A–S–H', *Journal of Sol-Gel Science Technology*, vol. 45, pp. 63-72.

Gebremariam, A.T., Vahidi, A., Maio, F.D., Moreno-Juez, J., Vegas-Ramiro, I., Łagosz, A., Mróz, R. & Rem, P., 2021, 'Comprehensive study on the most sustainable concrete design made of recycled concrete, glass and mineral wool from C&D wastes', *Construction and Building Materials*, vol. 273, pp. 121697.

Gesoglu, M., Güneyisi, E., Öz, H.Ö., Taha, I. & Yasemin, M.T., 2015, 'Failure characteristics of self-compacting concretes made with recycled aggregates', *Construction and Building Materials*, vol. 98, pp. 334-344.

Ghorbani, B., Arulrajah, A., Narsilio, G., Horpibulsuk, S. & Bo, M.W., 2021, 'Dynamic characterization of recycled glass-recycled concrete blends using experimental analysis and artificial neural network modeling', *Soil Dynamics and Earthquake Engineering*, vol. 142, pp. 106544.

Giasin, K. & Ayvar-Soberanis, S., 2017, 'An Investigation of burrs, chip formation, hole size, circularity and delamination during drilling operation of GLARE using ANOVA', *Composite Structures*, vol. 159, pp. 745-760.

Golewski, G.L., 2022, 'Fracture Performance of Cementitious Composites Based on Quaternary Blended Cements', *Materials*, vol. 15, no. 6023, pp. 15176023.

Golewski, G.L., 2023, 'Combined Effect of Coal Fly Ash (CFA) and Nanosilica (nS) on the Strength Parameters and Microstructural Properties of Eco-Friendly Concrete', *Energies*, vol. 16, no. 452, pp. 16010452.

Golewski, G.L. & Szostak, B., 2022, 'Strength and microstructure of composites with cement matrixes modified by fly ash and active seeds of C-S-H phase', *Struct. Eng. Mech.*, vol. 82, no. 4, pp. 543-556.

Guo, L., Wu, J. & Wang, H., 2020, 'Mechanical and perceptual characterization of ultra-high-performance cement-based composites with silane-treated graphene nano-platelets', *Construction and Building Materials*, vol. 240, pp. 117926.

Guo, Z., Zhang, X., Zhang, D. & Wang, R., 1982, 'Experimental investigation of stress-strain curves for concrete', *China. J. Build. Struct.*, vol. 3, no. 1, pp. 1-12.

Hager, I., Sitarz, M. & Mr´oz, K., 2021, 'Fly-ash based geopolymer mortar for high-temperature application – Effect of slag addition', *Journal of Cleaner Production*, vol. 316, pp. 128168.

Han, J. & Yan, P., 2021, 'Influence of segregation on the permeability of self-consolidating concrete', *Construction and Building Materials*, vol. 269, pp. 121277.

He, T., Wang, T., Xie, D. & Daemen, J.J.K., 2022, 'The mechanism of pores enhancing the deformation of completion cement under confining pressure', *Cement and Concrete Composites*, vol. 125, pp. 104322.

He, Z. & Zhang, J., 2014, 'Strength characteristics and failure criterion of plain recycled aggregate concrete under triaxial stress states', *Construction and Building Materials*, vol. 54, pp. 354-362.

He, Z., Zhang, J., Cao, W. & Wang, L., 2015, 'Multiaxial mechanical properties of plain recycled aggregate concrete', *Magazine of Concrete Research*, vol. 67, no. 8, pp. 401-413.

Hea, S., Li, Z. & Yang, E.-H., 2019, 'Quantitative characterization of anisotropic properties of the interfacial transition zone (ITZ) between microfiber and cement paste', *Cement and Concrete Research*, vol. 122, pp. 136-146.

Head, M.K. & Buenfeld, N.R., 2006, 'Measurement of aggregate interfacial porosity in complex, multi-phase aggregate concrete: Binary mask production using backscattered electron, and energy dispersive X-ray images', *Cement and*

Concrete Research, vol. 36, pp. 337-345.

Heukamp, F.H., Ulm, F.-J. & Germaine, J.T., 2001, 'Mechanical properties of calcium-leached cement pastes triaxial stress states and the influence of the pore pressures', *Cement and Concrete Research*, vol. 31, pp. 767-774.

Hjorth, J., Skibsted, J. & Jakobsen, H.J., 1988, '29Si MAS NMR studies of portland cement components and effects of microsilica on the hydration reaction', *Cement and Concrete Research*, vol. 18, no. 5, pp. 789-798.

Hoover, C.G. & Ulm, F.-J., 2015a, 'Experimental chemo-mechanics of early-age fracture properties of cement paste', *Cement and Concrete Research*, vol. 75, pp. 42-52.

Hoover, C.G. & Ulm, F.J., 2015b, 'Experimental chemo-mechanics of early-age fracture properties of cement paste', *Cement and Concrete Research*, vol. 75, pp. 42-52.

Hosan, A., Shaikh, F.U.A., Sarker, P. & Aslani, F., 2021, 'Nano- and micro-scale characterisation of interfacial transition zone (ITZ) of high volume slag and slag-fly ash blended concretes containing nano SiO_2 and nano $CaCO_3$', *Construction and Building Materials*, vol. 269, pp. 121311.

Hosseini, S., Brake, N.A., Nikookar, M., Günaydın-Sen, O. & Snyder, H.A., 2021, 'Mechanochemically activated bottom ash-fly ash geopolymer', *Cement and Concrete Composites*, vol. 118, pp. 103976.

Hu, Y., Tang, Z., Li, W., Li, Y. & Tam, V.W.Y., 2019, 'Physical-mechanical properties of fly ash/GGBFS geopolymer composites with recycled aggregates', *Construction and Building Materials*, vol. 226, pp. 139-151.

Huang, Y., Ding, Q., Wang, Y., Liao, Z. & Yin, X., 2022, 'Evolution of thermal parameters ofwet-screened dam concrete after different freeze–thaw deterioration', *Structural Concrete*, vol. 23, pp. 2185-2197.

Hutchinson, T.C. & Chen, Z., 2006, 'Improved Image Analysis for Evaluating Concrete

Damage', *Journal of Computing in Civil Engineering*, vol. 20, no. 3, pp. 210-216.

Igarashi, S.-i., Watanabe, A. & Kawamura, M., 2005, 'Evaluation of capillary pore size characteristics in high-strength concrete at early ages', *Cement and Concrete Research*, vol. 35, pp. 513-519.

Ismail, Z.Z. & AL-Hashmi, E.A., 2009, 'Recycling of waste glass as a partial replacement for fine aggregate in concrete', *Waste Management*, vol. 29, pp. 655-659.

Jamsheer, A.F., Kupwade-Patil, K., Büyüköztürk, O. & Bumajdad, A., 2018, 'Analysis of engineered cement paste using silica nanoparticles and metakaolin using 29Si NMR, water adsorption and synchrotron X-ray Diffraction', *Construction and Building Materials*, vol. 180, pp. 698-709.

Jayasuriya, A., Adams, M.P. & Bandelt, M.J., 2018, 'Understanding variability in recycled aggregate concrete mechanical properties through numerical simulation and statistical evaluation', *Construction and Building Materials*, vol. 178, pp. 301-312.

Jiang, J., Xiao, P. & Li, B., 2017, 'True-triaxial compressive behaviour of concrete under passive confinement', *Construction and Building Materials*, vol. 156, pp. 584-598.

Jiang, X., Li, Q., Yin, X. & Xu, S., 2023, 'Investigation on triaxial compressive mechanical properties of ultra high toughness cementitious composites with high strain capacity', *Cement and Concrete Research*, vol. 170, pp. 107185.

Jiang, Y., Ling, T.-C., Mo, K.H. & Shi, C., 2019, 'A critical review of waste glass powder – Multiple roles of utilization in cement-based materials and construction products', *Journal of Environmental Management*, vol. 242, pp. 440-449.

Jiao, Y., Zhang, Y., Guo, M., Zhang, L., Ning, H. & Liu, S., 2020, 'Mechanical and fracture properties of ultra-high performance concrete (UHPC) containing waste glass sand as partial replacement material', *Journal of Cleaner Production*, vol.

277, pp. 123501.

Katz, A., 2003, 'Properties of concrete made with recycled aggregate from partially hydrated old concrete', *Cement and Concrete Research*, vol. 33, pp. 703-711.

Ke, G., Li, W., Li, R., Li, Y. & Wang, G., 2018, 'Mitigation Effect of Waste Glass Powders on Alkali–Silica Reaction (ASR) Expansion in Cementitious Composite', *International Journal of Concrete Structures and Materials*, vol. 12, no. 7, pp. 1063-1076.

Khedmati, M., Kim, Y.R. & Turner, J.A., 2019, 'Investigation of the interphase between recycled aggregates and cementitious binding materials using integrated microstructuralnanomechanical-chemical characterization', *Composites Part B*, vol. 158, pp. 218-229.

Khedmati, M., Kim, Y.-R., Turner, J.A., Alanazi, H. & Nguyen, C., 2018, 'An integrated microstructural-nanomechanical-chemical approach to examine material-specific characteristics of cementitious interphase regions', *Materials Characterization*, vol. 138, pp. 154-164.

Kim, Y., Hanif, A., Usman, M. & Park, W., 2019, 'Influence of bonded mortar of recycled concrete aggregates on interfacial characteristics – Porosity assessment based on pore segmentation from backscattered electron image analysis', *Construction and Building Materials*, vol. 212, pp. 149-163.

Kim, Y., Hanif, A., Kazmi, S.M.S., Munir, M.J. & Park, C., 2018, 'Properties enhancement of recycled aggregate concrete through pretreatment of coarse aggregates e Comparative assessment of assorted techniques', *Journal of Cleaner Production*, vol. 191, pp. 339-349.

Kocaba, V., Gallucci, E. & Scrivener, K.L., 2012, 'Methods for determination of degree of reaction of slag in blended cement pastes', *Cement and Concrete Research*, vol.

42, pp. 511-525.

Kong, Y., Wang, P., Liu, S., Zhao, G. & Peng, Y., 2016, 'SEM Analysis of the Interfacial Transition Zone between Cement-Glass Powder Paste and Aggregate of Mortar under Microwave Curing', *Materials*, vol. 9, no. 9, pp. 733-745.

Kumar, A., Walder, B.J., Mohamed, A.K., Hofstetter, A., Srinivasan, B., Rossini, A.J., Scrivener, K., Emsley, L. & Bowen, P., 2017, 'The Atomic-Level Structure of Cementitious Calcium Silicate Hydrate', *The Journal of Physical Chemistry C*, vol. 121, pp. 17188-17196.

Kunther, W., Dai, Z. & Skibsted, J., 2016, 'Thermodynamic modeling of hydrated white Portland cement–metakaolin–limestone blends utilizing hydration kinetics from 29Si MAS NMR spectroscopy', *Cement and Concrete Research*, vol. 86, pp. 29-41.

Kunther, W., Ferreiro, S. & Skibsted, J., 2017, 'Influence of the Ca/Si ratio on the compressive strength of cementitious calcium–silicate–hydrate binders', *Journal of Materials Chemistry A*, vol. 5, pp. 17401.

Lee, G., Poon, C.S., Wong, Y.L. & Ling, T.C., 2013, 'Effects of recycled fine glass aggregates on the properties of dry–mixed concrete blocks', *Construction and Building Materials*, vol. 38, pp. 638-643.

Lei, B., Li, W., Tang, Z., Tam, V.W.Y. & Sun, Z., 2018, 'Durability of recycled aggregate concrete under coupling mechanical loading and freeze-thaw cycle in salt-solution', *Construction and Building Materials*, vol. 163, pp. 840-849.

Li, B., Dai, S., Zhan, Y., Xu, J., Guo, X., Yang, Y. & Chen, Y., 2022a, 'Strength criterion of recycled aggregate concrete under triaxial Compression: Model calibration', *Construction and Building Materials*, vol. 320, pp. 126210.

Li, L., Liu, Q., Dao, V. & Wu, M., 2023a, 'Dimensional change of cement paste subjected to carbonation in CO2 sequestration and utilization context: A critical review on the mechanisms', *Journal of CO2 Utilization*, vol. 70, pp. 102444.

Li, L., Lu, J., Shen, P., Sun, K., Pua, L.E.L., Xiao, J. & Poon, C.S., 2023b, 'Roles of recycled fine aggregate and carbonated recycled fine aggregate in alkali-activated slag and glass powder mortar', *Construction and Building Materials*, vol. 364, pp. 129876.

Li, P., Li, W., Yu, T., Qu, F. & Tam, V.W.Y., 2020, 'Investigation on early-age hydration, mechanical properties and microstructure of seawater sea sand cement mortar', *Construction and Building Materials*, vol. 249, pp. 118776.

Li, P., Li, W., Wang, K., Zhou, J.L., Castel, A., Zhang, S. & Shah, S.P., 2023c, 'Hydration of Portland cement with seawater toward concrete sustainability: Phase evolution and thermodynamic modelling', *Cement and Concrete Composites*, vol. 138, pp. 105007.

Li, W., Xiao, J., Sun, Z., Kawashima, S. & Shah, S.P., 2012, 'Interfacial transition zones in recycled aggregate concrete with different mixing approaches', *Construction and Building Materials*, vol. 35, pp. 1045-1055.

Li, W., Luo, Z., Gan, Y., Wang, K. & Shah, S.P., 2021, 'Nanoscratch on mechanical properties of interfacial transition zones (ITZs) in fly ash-based geopolymer composites', *Composites Science and Technology*, vol. 214, pp. 109001.

Li, W., Qu, F., Dong, W., Mishra, G. & Shah, S.P., 2022b, 'A comprehensive review on self-sensing graphene/cementitious composites: A pathway toward next-generation smart concrete', *Construction and Building Materials*, vol. 331, pp. 127284.

Lim, J.C. & Ozbakkaloglu, T., 2014, 'Stress–strain model for normal- and light-weight concretes under uniaxial and triaxial compression', *Construction and Building*

Materials, vol. 71, pp. 492-509.

Lin, K.L., Shiu, H.S., Shie, J.L., Cheng, T. & Hwang, C.L., 2012, 'Effect of composition on characteristics of thin film transistor liquid crystal display (TFT-LCD) waste glass-metakaolin-based geopolymers', *Construction and Building Materials*, vol. 36, pp. 501-507.

Ling, T.C., Poon, C.S. & Kou, S.C., 2012, 'Influence of recycled glass content and curing conditions on the properties of self-compacting concrete after exposure to elevated temperatures', *Cement and Concrete Composites*, vol. 34, pp. 265-272.

Liu, H., Liu, C., Bai, G. & Zhu, C., 2020, 'Impact of chloride intrusion on the pore structure of recycled aggregate concrete based on the recycled aggregate porous interface', *Construction and Building Materials*, vol. 259, pp. 120397.

Liu, J., Qiu, Q., Chen, X., Xing, F., Han, N., He, Y. & Ma, Y., 2017, 'Understanding the interacted mechanism between carbonation and chloride aerosol attack in ordinary Portland cement concrete', *Cement and Concrete Research*, vol. 95, pp. 217-225.

Liu, J., Ma, K., Shen, J., Zhu, J., Long, G., Xie, Y. & Liu, B., 2023, 'Influence of recycled concrete aggregate enhancement methods on the change of microstructure of ITZs in recycled aggregate concrete', *Construction and Building Materials*, vol. 371, pp. 130772.

Lodeiro, I.G., Macphee, D.E., Palomo, A. & Fernández-Jiménez, A., 2009, 'Effect of alkalis on fresh C–S–H gels. FTIR analysis', *Cement and Concrete Research*, vol. 39, pp. 147-153.

Lothenbach, B., Scrivener, K. & Hooton, R.D., 2011, 'Supplementary cementitious materials', *Cement and Concrete Research*, vol. 41, pp. 1244-1256.

Lu, B., Shi, C., Cao, Z., Guo, M. & Zheng, J., 2019, 'Effect of carbonated coarse recycled concrete aggregate on the properties and microstructure of recycled concrete', *Journal of Cleaner Production*, vol. 233, pp. 421-428.

Lu, B., Drissi, S., Liu, J., Hu, X., Song, B. & Shi, C., 2022a, 'Effect of temperature on CO2 curing, compressive strength and microstructure of cement paste', *Cement and Concrete Research*, vol. 157, pp. 106827.

Lu, C., Zhang, Z., Hu, J., QijunYu & Shi, C., 2022b, 'Effects of anionic species of activators on the rheological properties and early gel characteristics of alkali-activated slag paste', *Cement and Concrete Research*, vol. 162, pp. 106968.

Lu, J., Shen, P., Zheng, H., Zhan, B., Ali, H.A., He, P. & Poon, C.S., 2020, 'Synergetic recycling of waste glass and recycled aggregates in cement mortars: Physical, durability and microstructure performance', *Cement and Concrete Composites*, vol. 113, pp. 103632.

Lu, X. & Hsu, C.-T.T., 2006, 'Behavior of high strength concrete with and without steel fiber reinforcement in triaxial compression', *Cement and Concrete Research*, vol. 36, pp. 1679-1685.

Luo, Z., Li, W., Wang, K. & Shah, S.P., 2018, 'Research progress in advanced nanomechanical characterization of cementbased materials', *Cement and Concrete Composites*, vol. 94, pp. 277-295.

Luo, Z., Li, W., Tam, V.W.Y., Xiao, J. & Shah, S.P., 2019, 'Current progress on nanotechnology application in recycled aggregate concrete', *Journal of Sustainable Cement-Based Materials*, vol. 8, no. 2, pp. 79-96.

Luo, Z., Li, W., Gan, Y., Mendu, K. & Shah, S.P., 2020, 'Applying grid nanoindentation and maximum likelihood estimation for N-AS-H gel in geopolymer paste: Investigation and discussion', *Cement and Concrete Research*, vol. 135, pp. 106112.

Luo, Z., Li, W., Wang, K., Castel, A. & Shah, S.P., 2021a, 'Comparison on the properties of ITZs in fly ash-based geopolymer and Portland cement concretes with equivalent flowability', *Cement and Concrete Research*, vol. 143, pp. 106392.

Luo, Z., Li, W., Wang, K., Shah, S.P. & Sheng, D., 2022, 'Nano/micromechanical characterisation and image analysis on the properties and heterogeneity of ITZs in geopolymer concrete', *Cement and Concrete Research*, vol. 152, pp. 106677.

Luo, Z., Li, W., Gan, Y., He, X., Castel, A. & Sheng, D., 2021b, 'Nanoindentation on micromechanical properties and microstructure of geopolymer with nano-SiO2 and nano-TiO2', *Cement and Concrete Composites*, vol. 117, pp. 103883.

Lyu, K., Garboczi, E.J., She, W. & Miao, C., 2019a, 'The effect of rough vs. smooth aggregate surfaces on the characteristics of the interfacial transition zone', *Cement and Concrete Composites*, vol. 99, pp. 49-61.

Lyu, K., She, W., Chang, H. & Gu, Y., 2020, 'Effect of fine aggregate size on the overlapping of interfacial transition zone (ITZ) in mortars', *Construction and Building Materials*, vol. 248, pp. 118559.

Lyu, K., She, W., Miao, C., Chang, H. & Gu, Y., 2019b, 'Quantitative characterization of pore morphology in hardened cement paste via SEM-BSE image analysis', *Construction and Building Materials*, vol. 202, pp. 589-602.

MacLaren, D.C. & White, M.A., 2003, 'Cement: Its Chemistry and Properties', *Journal of Chemical Education*, vol. 80, no. 6.

Maddalena, R., Roberts, J.J. & Hamilton, A., 2018, 'Can Portland cement be replaced by low-carbon alternative materials? A study on the thermal properties and carbon emissions of innovative cements', *Journal of Cleaner Production*, vol. 186, pp. 933-942.

Mahmood, A.H., Afroz, S., Kashani, A., Kim, T. & Foster, S.J., 2022, 'The efficiency of recycled glass powder in mitigating the alkali-silica reaction induced by recycled glass aggregate in cementitious mortars', *Materials and Structures*, vol. 55, no. 6.

Malecot, Y., Zingg, L., Briffaut, M. & Baroth, J., 2019, 'Influence of free water on concrete triaxial behavior: The effect of porosity', *Cement and Concrete Research*, vol. 120, pp. 207-216.

Medina, C., Zhu, W., Howind, T., Rojas, M.I.S.d. & Frías, M., 2014, 'Influence of mixed recycled aggregate on the physical - mechanical properties of recycled concrete', *Journal of Cleaner Production*, vol. 68, pp. 216-225.

Mejdi, M., Wilson, W., Saillio, M., Chaussadent, T., Divet, L. & Tagnit-Hamou, A., 2019, 'Investigating the pozzolanic reaction of post-consumption glass powder and the role of portlandite in the formation of sodium-rich C-S-H', *Cement and Concrete Research*, vol. 123, pp. 105790.

Mejdi, M., Wilson, W., Saillio, M., Chaussadent, T., Divet, L. & Tagnit-Hamou, A., 2022, 'Hydration and microstructure of glass powder cement pastes – A multi-technique investigation', *Cement and Concrete Research*, vol. 151, pp. 106610.

Meng, E., Yu, Y., Yuan, J., Qiao, K. & Su, Y., 2017, 'Triaxial compressive strength experiment study of recycled aggregate concrete after high temperatures', *Construction and Building Materials*, vol. 155, pp. 542-549.

Mirzahosseini, M. & Riding, K.A., 2015, 'Influence of different particle sizes on reactivity of finely ground glass as supplementary cementitious material (SCM)', *Cement and Concrete Composites*, vol. 56, pp. 95-105.

Mohammadi, I. & South, W., 2016, 'The influence of the higher limestone content of General Purpose cement according to high-strength concrete test results and construction field data', *Materials and Structures*, vol. 49, no. 11, pp. 4621-4636.

Mostofinejad, D., Hosseini, S.M., Nosouhian, F., Ozbakkaloglu, T. & Tehrani, B.N., 2020, 'Durability of concrete containing recycled concrete coarse and fine aggregates and milled waste glass in magnesium sulfate environment', *Journal of Building Engineering*, vol. 29, pp. 101182.

Mouret, M., Ringot, E. & Bascoul, A., 2001, 'Image analysis: a tool for the characterisation of hydration of cement in concrete ± metrological aspects of magnification on measurement', *Cement and Concrete Composites*, vol. 23, pp. 201-206.

Nassar, R.-U.-D. & Soroushian, P., 2012, 'Strength and durability of recycled aggregate concrete containing milled glass as partial replacement for cement', *Construction and Building Materials*, vol. 29, pp. 368-377.

Navarrete, I., Vargas, F., Martinez, P., Paul, A. & Lopez, M., 2021, 'Flue gas desulfurization (FGD) fly ash as a sustainable, safe alternative for cement-based materials', *Journal of Cleaner Production*, vol. 283, pp. 124646.

Nehdi, M.L., Najjar, M.F., Soliman, A.M. & Azabi, T.M., 2017, 'Novel steel fibre-reinforced preplaced aggregate concrete with superior mechanical performance', *Cement and Concrete Composites*, vol. 82, pp. 242-251.

Nuruzzaman, M., Sarker, P.K. & Shaikh, F.U.A., 2023, 'The interfacial transition zone microstructure of ground ferronickel slag incorporated self-compacting concrete investigated by nanoindentation', *Journal of Building Engineering*, vol. 71, pp. 106437.

Oliver, W.C. & Pharr, G.M., 1992, 'Improved technique for determining hardness and elastic modulus using load and displacement sensing indentation experiments', *Journal of Materials Research*, vol. 7, no. 6, pp. 1564-1583.

Omary, S., Ghorbel, E. & Wardeh, G., 2016, 'Relationships between recycled concrete aggregates characteristics and recycled aggregates concretes properties', *Construction and Building Materials*, vol. 108, pp. 163-174.

Omran, A. & Tagnit-Hamou, A., 2016, 'Performance of glass-powder concrete in field applications', *Construction and Building Materials*, vol. 109, pp. 84-95.

Omran, A.F., D.-Morin, E., Harbec, D. & Tagnit-Hamou, A., 2017, 'Long-term performance of glass-powder concrete in large-scale field applications', *Construction and Building Materials*, vol. 135, pp. 43-58.

Otsuki, N., Miyazato, S.-i. & Yodsudjai, W., 2003, 'Influence of Recycled Aggregate on Interfacial Transition Zone, Strength, Chloride Penetration and Carbonation of Concrete', *Journal of Materials in Civil Engineering*, vol. 15, no. 5, pp. 443-451.

Pan, Z., Tao, Z., Murphy, T. & Wuhrer, R., 2017, 'High temperature performance of mortars containing fine glass powders', *Journal of Cleaner Production*, vol. 162, pp. 16-26.

Park, S.B., Lee, B.C. & Kim, J.H., 2004, 'Studies on mechanical properties of concrete containing waste glass aggregate', *Cement and Concrete Research*, vol. 34, pp. 2181-2189.

Pathan, Q.A.A., Qureshi, A.S. & Mangi, S.A., 2022, 'Ageing factor for fly ash cement concrete (FACC)', *Environmental Science and Pollution Research*, vol. 29, pp. 32238-32245.

Pedro, D., Brito, J.d. & Evangelista, L., 2017, 'Structural concrete with simultaneous incorporation of fine and coarse recycled concrete aggregates: Mechanical, durability and long-term properties', *Construction and Building Materials*, vol. 154, pp. 294-309.

Pope, A.W. & Jennings, H.M., 1992, 'The influence of mixing on the microstructure of the cement paste/aggregate interfacial zone and on the strength of mortar', *Journal of Materials Science*, vol. 27, pp. 6452-6462.

Qu, F., Li, W., Wang, K., Zhang, S. & Sheng, D., 2021, 'Performance deterioration of fly ash/slag-based geopolymer composites subjected to coupled cyclic preloading and sulfuric acid attack', *Journal of Cleaner Production*, vol. 321, pp. 128942.

Qu, F., Li, W., Guo, Y., Zhang, S., Zhou, J.L. & Wang, K., 2022, 'Chloride-binding capacity of cement-GGBFS-nanosilica composites under seawater chloride-rich environment', *Construction and Building Materials*, vol. 342, pp. 127890.

Rangaraju, P.R., Olek, J. & Diamond, S., 2010, 'An investigation into the influence of inter-aggregate spacing and the extent of the ITZ on properties of Portland cement concretes', *Cement and Concrete Research*, vol. 40, pp. 1601-1608.

Rayóna, E., Arrieta, M.P., Pasíes, T., López, J. & Jordá, J.L., 2018, 'Enhancing the mechanical features of clay surfaces by the absorption of nano-SiO2 particles in aqueous media. Case of study on Bronze Age clay objects', *Cement and Concrete Composites*, vol. 93, pp. 107-117.

Ren, X., Zeng, S. & Li, J., 2015, 'A rate-dependent stochastic damage–plasticity model for quasi-brittle materials', *Computational Mechanics*, vol. 55, pp. 267-285.

Ren, Y., Yu, Z., Huang, Q. & Ren, Z., 2018, 'Constitutive model and failure criterions for lightweight aggregate concrete: A true triaxial experimental test', *Construction and Building Materials*, vol. 171, pp. 759-769.

Richardson, I.G., 2008, 'The calcium silicate hydrates', *Cement and Concrete Research*, vol. 38, pp. 137-158.

Schwarz, N. & Neithalath, N., 2008, 'Influence of a fine glass powder on cement hydration: Comparison to fly ash and modeling the degree of hydration', *Cement and Concrete Research*, vol. 38, pp. 429-436.

Scrivener, K.L., 2004, 'Backscattered electron imaging of cementitious microstructures: understanding and quantification', *Cement and Concrete Composites*, vol. 26, pp. 935-945.

Scrivener, K.L., Crumbie, A.K. & Laugesen, P., 2004, 'The Interfacial Transition Zone (ITZ) Between Cement Paste and Aggregate in Concrete', *Interface Science*, vol. 12, pp. 411-421.

Shao, Y., Lefort, T., Moras, S. & Rodriguez, D., 2000, 'Studies on concrete containing ground waste glass', *Cement and Concrete Research*, vol. 30, pp. 91-100.

Shi, C., Wang, D., & Behnood, A., 2012, 'Review of Thaumasite Sulfate Attack on Cement Mortar and Concrete', *Journal of Materials in Civil Engineering*, vol. 24, 12, pp. 1450-1460.

Sidorova, A., Vazquez-Ramonich, E., Barra-Bizinotto, M., Roa-Rovira, J.J. & Jimenez-Pique, E., 2014, 'Study of the recycled aggregates nature's influence on the aggregate–cement paste interface and ITZ', *Construction and Building Materials*, vol. 68, pp. 677-684.

Silva, S.R.d., Brito, J.d. & Andrade, J.J.d.O., 2023, 'Synergic effect of recycled aggregate, fly ash, and hydrated lime in concrete production', *Journal of Building Engineering*, vol. 70, pp. 106370.

Skibsted, J. & Andersen, M.D., 2013, 'The Effect of Alkali Ions on the Incorporation of Aluminum in the Calcium Silicate Hydrate (C–S–H) Phase Resulting from Portland Cement Hydration Studied by 29Si MAS NMR', *Journal of the American Ceramic Society*, vol. 96, no. 2, pp. 651-656.

Sunayana, S. & Barai, S.V., 2020, 'Shear Behavior of Fly-Ash-Incorporated Recycled Aggregate Concrete Beams', *ACI Materials Journal*, vol. 117, no. 1, pp. 289-303.

Tam, V.W.Y., K.Wang & Tam, C.M., 2008, 'Assessing relationships among properties of demolished concrete, recycled aggregate and recycled aggregate concrete using regression analysis', *Journal of Hazardous Materials*, vol. 152, pp. 703-714.

Tamanna, N., Tuladhar, R. & Sivakugan, N., 2020, 'Performance of recycled waste glass sand as partial replacement of sand in concrete', *Construction and Building Materials*, vol. 239, pp. 117804.

Tan, K.H. & Du, H., 2013, 'Use of waste glass as sand in mortar: Part I – Fresh, mechanical and durability properties', *Cement and Concrete Composites*, vol. 35, pp. 109-117.

Tang, Y., Fang, S., Chen, J., Ma, L., Li, L. & Wu, X., 2020a, 'Axial compression behavior of recycled-aggregate-concrete-filled GFRP–steel composite tube columns', *Engineering Structures*, vol. 216, pp. 110676.

Tang, Z., Hu, Y., Tam, V.W.Y. & Li, W., 2019, 'Uniaxial compressive behaviors of fly ash/slag-based geopolymeric concrete with recycled aggregates', *Cement and Concrete Composites*, vol. 104, pp. 103375.

Tang, Z., Li, W., Tam, V.W.Y. & Yan, L., 2020b, 'Mechanical performance of CFRP-confined sustainable geopolymeric recycled concrete under axial compression', *Engineering Structures*, vol. 224, pp. 111246.

Tang, Z., Li, W., Tam, V.W.Y. & Xue, C., 2020c, 'Advanced progress in recycling municipal and construction solid wastes for manufacturing sustainable construction materials', *Resources, Conservation & Recycling*, vol. 6, pp. 100036.

Tang, Z., Li, W., Tam, V.W.Y. & Luo, Z., 2020d, 'Investigation on dynamic mechanical properties of fly ash/slag-based geopolymeric recycled aggregate concrete', *Composites Part B*, vol. 185, pp. 107776.

Tang, Z., Li, W., Peng, Q., Tam, V.W.Y. & Wang, K., 2022, 'Study on the failure mechanism of geopolymeric recycled concrete using digital image correlation method', *Journal of Sustainable Cement-Based Materials*, vol. 11, no. 2, pp. 113-126.

Terro, M.J., 2006, 'Properties of concrete made with recycled crushed glass at elevated temperatures', *Building and Environment*, vol. 41, pp. 633-639.

Thomas, J., Thaickavil, N.N. & Wilson, P.M., 2018, 'Strength and durability of concrete containing recycled concrete aggregates', *Journal of Building Engineering*, vol. 19, pp. 349-365.

Ulsen, C., Contessotto, R., Macedo, R.d.S. & Kahn, H., 2022, 'Quantification of the cement paste and phase’s association in fine recycled aggregates by SEM-based image analysis', *Construction and Building Materials*, vol. 320, pp. 126206.

Vargas, P., Restrepo-Baena, O. & Tobón, J.I., 2017, 'Microstructural analysis of interfacial transition zone (ITZ) and its impact on the compressive strength of lightweight concretes', *Construction and Building Materials*, vol. 137, pp. 381-389.

Vu, X.D., Briffaut, M., Malecot, Y., Daudeville, L. & Ciree, B., 2015, 'Influence of the Saturation Ratio on Concrete Behavior under Triaxial Compressive Loading', *Science and Technology of Nuclear Installations*, pp. 976387.

Vu, X.H., Daudeville, L. & Malecot, Y., 2011, 'Effect of coarse aggregate size and cement paste volume on concrete behavior under high triaxial compression loading', *Construction and Building Materials*, vol. 25, pp. 3941-3949.

Vu, X.H., Malecot, Y., Daudeville, L. & Buzaud, E., 2009, 'Experimental analysis of concrete behavior under high confinement: Effect of the saturation ratio', *International Journal of Solids and Structures*, vol. 46, pp. 1105-1120.

Wang, B., Yan, L., Fu, Q. & Kasal, B., 2021, 'A Comprehensive Review on Recycled Aggregate and Recycled Aggregate Concrete', *Resources, Conservation & Recycling*, vol. 171, pp. 105565.

Wang, H., Nie, D., Li, P., Wang, D., Wang, C., Liu, W. & Du, S., 2023, 'Effect of recycled concrete aggregate with different degrees of initial alkali–aggregate reaction damage on the mechanical behavior and porosity of self-compacting recycled aggregate concrete', *Construction and Building Materials*, vol. 363, pp. 129797.

Wang, H., Long, G., Tang, Z., Xie, Y., Ma, G., Tang, C., Liu, S. & Ren, X., 2022, 'The volume stability of cement-based materials under different extreme environments in the plateau: Experimental evolution', *Journal of Building Engineering*, vol. 62, pp. 105370.

Wang, X., Wang, K., Han, J. & Taylor, P., 2015, 'Image analysis applications on assessing static stability and flowability of self-consolidating concrete', *Cement and Concrete Composites*, vol. 62, pp. 156-167.

Wang, Y., Nanukuttan, S., Bai, Y. & Basheer, P.A.M., 2017, 'Influence of combined carbonation and chloride ingress regimes on rate of ingress and redistribution of chlorides in concretes', *Construction and Building Materials*, vol. 140, pp. 173-183.

Wang, Y., Wang, Y., Zhao, Y., Li, G., Lyu, Y. & Li, H., 2020, 'Experimental study on ultra-high performance concrete under triaxial compression', *Construction and Building Materials*, vol. 263, pp. 120255.

Wei, Y., Kong, W., Wang, Y. & Sha, A., 2021, 'Multifunctional application of nanoscratch technique to characterize cementitious materials', *Cement and Concrete Research*, vol. 140, pp. 106318.

Wilson, W., Sorelli, L. & Tagnit-Hamou, A., 2018, 'Unveiling micro-chemo-mechanical properties of C–(A)–S–H and other phases in blended-cement pastes', *Cement and Concrete Research*, vol. 107, pp. 317-336.

Wong, H.S. & Buenfeld, N.R., 2006, 'Euclidean Distance Mapping for computing microstructural gradients at interfaces in composite materials', *Cement and Concrete Research*, vol. 36, pp. 1091-1097.

Wong, H.S. & Buenfeld, N.R., 2009, 'Determining the water–cement ratio, cement content, water content and degree of hydration of hardened cement paste: Method development and validation on paste samples', *Cement and Concrete Research*, vol. 39, pp. 957-965.

Wong, H.S., Head, M.K. & Buenfeld, N.R., 2006, 'Pore segmentation of cement-based materials from backscattered electron images', *Cement and Concrete Research*, vol. 36, pp. 1083-1090.

Wong, H.S., Zobel, M., Buenfeld, N.R. & Zimmerman, R.W., 2009, 'Influence of the interfacial transition zone and microcracking on the diffusivity, permeability and sorptivity of cement-based materials after drying', *Magazine of Concrete Research*, vol. 61, no. 8, pp. 571-589.

Wu, K., Luo, S., Zheng, J., Yan, J. & Xiao, J., 2022, 'Influence of carbonation treatment on the properties of multiple interface transition zones and recycled aggregate concrete', *Cement and Concrete Composites*, vol. 127, no. 104402.

Wu, Y., Liu, C., Bai, G., Liu, H., Meng, Y. & Wang, Z., 2023, '3D printed concrete with recycled sand: Pore structures and triaxial compression properties', *Cement and Concrete Composites*, vol. 139, pp. 105048.

Xiao, J., Li, W., Fan, Y. & Huang, X., 2012, 'An overview of study on recycled aggregate concrete in China (1996–2011)', *Construction and Building Materials*, vol. 31, pp. 364-383.

Xiao, J., Li, W., Corr, D.J. & Shah, S.P., 2013a, 'Simulation Study on the Stress Distribution in Modeled Recycled Aggregate Concrete under Uniaxial Compression', *Journal of Materials in Civil Engineering*, vol. 25, no. 4, pp. 504-518.

Xiao, J., Li, W., Corr, D.J. & Shah, S.P., 2013b, 'Effects of interfacial transition zones on the stress–strain behavior of modeled recycled aggregate concrete', *Cement and Concrete Research*, vol. 52, pp. 82-99.

Xiao, J., Li, W., Sun, Z., Lange, D.A. & Shah, S.P., 2013c, 'Properties of interfacial transition zones in recycled aggregate concrete tested by nanoindentation', *Cement and Concrete Composites*, vol. 37, pp. 276-292.

Xiao, R., Ma, Y., Jiang, X., Zhang, M., Zhang, Y., Wang, Y., Huang, B. & He, Q., 2020, 'Strength, microstructure, efflorescence behavior and environmental impacts of waste glass geopolymers cured at ambient temperature', *Journal of Cleaner Production*, vol. 252, pp. 119610.

Xiaohui Wang, Jacobsen, S., He, J., Zhang, Z., Lee, S.F. & Lein, H.L., 2009, 'Application of nanoindentation testing to study of the interfacial transition zone in steel fiber reinforced mortar', *Cement and Concrete Research*, vol. 39, pp. 701-715.

Xie, P., Beaudoin, J.J. & Brousseau, R., 1991, 'Effect of aggregate size on transition zone properties at the portland cement paste interface', *Cement and Concrete Research*, vol. 21, pp. 999-1005.

Xie, X., Feng, Q., Chen, Z., Jiang, L. & Lu, W., 2019, 'Diffusion and distribution of chloride ions in carbonated concrete with fly ash', *Construction and Building Materials*, vol. 218, pp. 119-125.

Xu, J., Corr, D.J. & Shah, S.P., 2015, 'Nanomechanical investigation of the effects of nanoSiO2 on C–S–H gel/cement grain interfaces', *Cement and Concrete Composites*, vol. 61, pp. 7-17.

Xu, J., Chen, Z., Xiao, Y., Demartino, C. & Wang, J., 2017a, 'Recycled Aggregate Concrete in FRP-confined columns: A review of experimental results', *Composite Structures*, vol. 174, pp. 277-291.

Xu, J.J., Chen, W.G., Demartino, C., Xie, T.Y., Yu, Y., Fang, C.F. & Xu, M., 2021a, 'A

Bayesian model updating approach applied to mechanical properties of recycled aggregate concrete under uniaxial or triaxial compression', *Construction and Building Materials*, vol. 301, pp. 124274.

Xu, L., Deng, F. & Chi, Y., 2017b, 'Nano-mechanical behavior of the interfacial transition zone between steel-polypropylene fiber and cement paste', *Construction and Building Materials*, vol. 145, pp. 619-638.

Xu, Z., Li, J., Wu, P. & Wu, C., 2021b, 'Experimental investigation of triaxial strength of ultra-high performance concrete after exposure to elevated temperature', *Construction and Building Materials*, vol. 295, pp. 123689.

Xuan, D., Zhan, B. & Poon, C.S., 2017, 'Durability of recycled aggregate concrete prepared with carbonated recycled concrete aggregates', *Cement and Concrete Composites*, vol. 84, pp. 214-221.

Xue, H., Zhu, H., Guo, M., Shao, S., Zhang, S. & Zhang, Y., 2023, 'Modeling for predicting triaxial mechanical properties of recycled aggregate concrete considering the recycled aggregate replacement', *Construction and Building Materials*, vol. 368, pp. 130447.

Xue, W., Yao, Z., Jing, W., Tang, B., Kong, G. & Wu, H., 2019, 'Experimental study on permeability evolution during deformation and failure of shaft lining concrete', *Construction and Building Materials*, vol. 195, pp. 564-573.

Xue, W., Liu, X., Jing, W., Yao, Z., Gao, C. & Li, H., 2020, 'Experimental study and mechanism analysis of permeability sensitivity of mechanically damaged concrete to confining pressure', *Cement and Concrete Research*, vol. 134, pp. 106073.

Yan, X., Zhao, H., Shen, Y. & Ding, H., 2022, 'Material removal mechanism and penetration depth modeling of CF/PEEK composites under nano-scratching', *Composites Science and Technology*, vol. 227, pp. 109566.

Yang, X., Shen, A., Guo, Y., Zhou, S. & He, T., 2018, 'Deterioration mechanism of interface transition zone of concrete pavement under fatigue load and freeze-thaw coupling in cold climatic areas', *Construction and Building Materials*, vol. 160, pp. 588-597.

Yang, Y., Wu, C., Liu, Z. & Zhang, H., 2022, '3D-printing ultra-high performance fiber-reinforced concrete under triaxial confining loads', *Additive Manufacturing*, vol. 50, pp. 102568.

Ye, T., Xiao, J., Zhao, W., Duan, Z. & Xu, Y., 2022, 'Combined use of recycled concrete aggregate and glass cullet in mortar: Strength, alkali expansion and chemical compositions', *Journal of Building Engineering*, vol. 55, pp. 104721.

Yin, Y., Zhao, Y., Koey, K.E., Tan, Q., Zhang, M. & Huang, H., 2022, 'In-situ synthesized age-hardenable high-entropy composites with superior wear resistance', *Composites Part B*, vol. 235, pp. 109795.

Yio, M.H.N., Wong, H.S. & Buenfeld, N.R., 2017, 'Representative elementary volume (REV) of cementitious materials from three-dimensional pore structure analysis', *Cement and Concrete Research*, vol. 102, pp. 187-202.

Yue, G., Ma, Z., Liu, M., Liang, C. & Ba, G., 2020, 'Damage behavior of the multiple ITZs in recycled aggregate concrete subjected to aggressive ion environment', *Construction and Building Materials*, vol. 245, pp. 118419.

Zaetang, Y., Sata, V., Wongsa, A. & Chindaprasirt, P., 2016, 'Properties of pervious concrete containing recycled concrete block aggregate and recycled concrete aggregate', *Construction and Building Materials*, vol. 111, pp. 15-21.

Zein, A.R.E., Vanhove, Y., Djelal, C., Madec, O. & Gotteland, P., 2021, 'Evaluation of internal bleeding in concrete foundation from the Terzaghi's effective stress postulate', *Materials and Structures*, vol. 54, no. 231.

Zeng, S., Ren, X. & Li, J., 2013, 'Triaxial Behavior of Concrete Subjected to Dynamic Compression', *Journal of Structural Engineering*, vol. 139, no. 9, pp. 1582-1592.

Zhan, B., Xuan, D., Poon, C.S. & Scrivener, K.L., 2020, 'Characterization of interfacial transition zone in concrete prepared with carbonated modeled recycled concrete aggregates', *Cement and Concrete Research*, vol. 136, pp. 106175.

Zhang, H., Liu, W., Lin, X., Su, S. & Zhao, B., 2021, 'To ameliorate the performance of recycled aggregate concrete (RAC) by pre-treating aggregate in sulfoaluminate cement slurry and water glass solution', *Journal of Building Engineering*, vol. 44, pp. 103364.

Zhang, H., Xu, X., Liu, W., Zhao, B. & Wang, Q., 2022, 'Influence of the moisture states of aggregate recycled from waste concrete on the performance of the prepared recycled aggregate concrete (RAC) – A review', *Construction and Building Materials*, vol. 326, pp. 126891.

Zhang, S., Liu, R., Lu, C., Gao, Y., Xu, J., Yao, L. & Chen, Y., 2023, 'Application of digital image correlation to study the influence of the water/ cement ratio on the interfacial transition zone in cement-based materials', *Construction and Building Materials*, vol. 367, pp. 130167.

Zhang, W., Wang, S., Zhao, P., Lu, L. & Cheng, X., 2019, 'Effect of the optimized triple mixing method on the ITZ microstructure and performance of recycled aggregate concrete', *Construction and Building Materials*, vol. 203, pp. 601-607.

Zhao, H., Poon, C.S. & Ling, T.C., 2013, 'Utilizing recycled cathode ray tube funnel glass sand as river sand replacement in the high-density concrete', *Journal of Cleaner Production*, vol. 51, pp. 184-190.

Zhu, X., Chen, X., Zhang, N., Wang, X. & Diao, H., 2021, 'Experimental and numerical research on triaxial mechanical behavior of self-compacting concrete subjected to freeze–thaw damage', *Construction and Building Materials*, vol. 288, pp. 123110.

Zhu, X., Zhang, Y., Chen, L., Wang, L., Ma, B., Li, J., Poon, C.S. & Tsang, D.C.W., 2023, 'Bonding mechanisms and micro-mechanical properties of the interfacial transition zone (ITZ) between biochar and paste in carbon-sink cement-based composites', *Cement and Concrete Composites*, vol. 139, pp. 105004.

Zidol, A., Tognonvi, M.T. & Tagnit-Hamou, A., 2021, 'Concrete Incorporating Glass Powder in Aggressive Environments', *ACI Materials Journal*, vol. 118, no. 2, pp. 43-51.

Zingg, L., Malecot, Y., Briffaut, M., Baroth, J. & Pla, S., 2016, 'A Radial Strain Sensor for the Characterization of Concrete Under Triaxial Loading', *Experimental Mechanics*, vol. 56, pp. 703-711.